

WL-TR-93-3063

AD-A277 516



AN EXPERIMENTAL STUDY OF
PILOT/VEHICLE DYNAMICS
USING A TILT ROTOR FLYING MACHINE

DAVID B. DOMAN

JUNE 1993

FINAL REPORT : MAY 1992 to JUNE 1993

DTIC
ELECTE
MAR 29 1994
S E D

APPROVED FOR PUBLIC RELEASE; DISTRIBUTION IS UNLIMITED.

FLIGHT DYNAMICS DIRECTORATE
WRIGHT LABORATORY
AIR FORCE MATERIEL COMMAND
WRIGHT PATTERSON AFB OH 45433-7562

DISCONTINUED 1

94-09321



94 3 25 007

**Best
Available
Copy**

REPORT DOCUMENTATION PAGE

Form Approved
OMB No. 0704-0188

Public reporting burden for this collection of information is estimated to average 1 hour per response, including the time for reviewing instructions, searching existing data sources, gathering and maintaining the data needed, and completing and reviewing the collection of information. Send comments regarding this burden estimate or any other aspect of this collection of information, including suggestions for reducing this burden, to: Washington Headquarters Services, Directorate for Information Operations and Reports, 1215 Jefferson Davis Highway, Suite 1204, Arlington, VA 22202-4302, and to the Office of Management and Budget, Paperwork Reduction Project (0704-0188), Washington, DC 20503.

1. AGENCY USE ONLY (Leave blank)		2. REPORT DATE JUNE 1993	3. REPORT TYPE AND DATES COVERED FINAL 5/92 - 6/93	
4. TITLE AND SUBTITLE An Experimental Study of Pilot/Vehicle Dynamics Using A Tilt Rotor Flying Machine			5. FUNDING NUMBERS	
6. AUTHOR(S) DAVID B. DOMAN				
7. PERFORMING ORGANIZATION NAME(S) AND ADDRESS(ES) Flight Dynamics Directorate Wright Laboratory Air Force Materiel Command Wright Patterson AFB OH 45433-7562			8. PERFORMING ORGANIZATION REPORT NUMBER WL-TR-93-3063	
9. SPONSORING / MONITORING AGENCY NAME(S) AND ADDRESS(ES) Flight Dynamics Directorate Wright Laboratory Air Force Materiel Command Wright Patterson AFB OH 45433-7562			10. SPONSORING / MONITORING AGENCY REPORT NUMBER	
11. SUPPLEMENTARY NOTES A Thesis Submitted To The Faculty Of Purdue University				
12a. DISTRIBUTION / AVAILABILITY STATEMENT Approved For Public Release; Distribution Is Unlimited.			12b. DISTRIBUTION CODE	
13. ABSTRACT (Maximum 200 words) A laboratory Tilt Rotor Flying Machine (TROFM) is designed and built for the purpose of conducting an experimental study of the effects of command systems on human pilot behavior. The aircraft is mounted on a two-axis pivot stand which gives the fuselage 2 degrees of freedom; pitch and yaw. Analytical models are derived using Lagrangian and Newtonian techniques. Identification of the aircraft characteristics is based on a nonparametric Discrete Fourier Transform technique and a maximum likelihood parameter estimation scheme. Attitude command, rate command and unaugmented systems are designed and implemented in real time using a digital computer. An investigation of the effects of command systems, displays and tasks on human pilot behavior is conducted. Pilot and pilot-vehicle describing functions are obtained from time histories of dynamic tracking tasks where the pilot attempts to track a random appearing input. Correlations between Cooper-Harper ratings and quantitative descriptions of pilot behavior are made. The experimental results compare favorably to the classical theory of man-machine system dynamics which is based on the cross-over model. The results of this study indicate that desirable controlled elements in man-machine systems have the characteristics of a simple tracker.				
14. SUBJECT TERMS Pilot Models Manual Control Vehicle Dynamics Human Pilot Dynamics Handling Qualities Pilot Dynamics System Identification			15. NUMBER OF PAGES 293	
			16. PRICE CODE	
17. SECURITY CLASSIFICATION OF REPORT UNCLASSIFIED	18. SECURITY CLASSIFICATION OF THIS PAGE UNCLASSIFIED	19. SECURITY CLASSIFICATION OF ABSTRACT UNCLASSIFIED	20. LIMITATION OF ABSTRACT UL	

TABLE OF CONTENTS

	Page
LIST OF TABLES	vi
LIST OF FIGURES	vii
1. INTRODUCTION	1
2. EQUATIONS OF MOTION	4
2.1 Coordinate Systems	5
2.2 Kinetic Energy	13
2.3 Lagrange's Equation	18
2.4 Linearization of Equations of Motion	18
2.4.1 Generalized Forces	19
2.4.2 Linearization using Taylor Series	23
2.5 Newtonian Equations of Motion	25
2.6 Comparison of Linear Lagrangian and Newtonian Models	33
3. SYSTEM IDENTIFICATION	35
3.1 System Identification Methods	35
3.1.1 Continuous Frequency Response	35
3.1.2 Method of One Frequency at a Time (Continuous)	36
3.1.3 Discrete Frequency Response	38
3.1.4 Method of One Frequency at a Time (Discrete)	39
3.1.5 Frequency Sweep Method	41
3.1.6 Maximum Likelihood Parameter Estimation	42
3.1.7 Pseudo Random Binary Sequences (PRBS)	43
3.2 Actuators	44
3.2.1 Main Rotor	44
3.2.2 Tilt Servo	44
3.3 Identification of State Space Model	47
3.3.1 Main Motor (Rotor) Identification	49
3.3.2 Tilt Servo	54

	Page
3.3.3 Drag Torque, Thrust and Rotor Speed	57
3.3.4 Pitch to Rotor Speed Transfer Function	66
3.3.5 Yaw Axis Friction Coefficient	67
3.3.6 Gyroscopic Couples	70
3.3.7 Back Substitution of Results into Analytical Model	71
3.4 Results	71
4. CONTROL SYSTEM DESIGN	77
4.1 Discrete Models of Sampled Data Systems	77
4.2 Digital Compensator Design by Emulation	79
4.3 Digital Filter Programming	79
4.4 Open Loop System	80
4.5 Attitude Command Systems	81
4.5.1 Yaw Axis	81
4.5.2 Pitch Axis	92
4.6 Rate Command Systems	98
4.6.1 Kalman Filter	102
4.6.2 Pitch Rate Command System	109
4.6.3 Yaw Rate Command System	116
4.6.4 Effect of Kalman Filter in Feedback Loop	117
5. MAN IN THE LOOP EXPERIMENTS	127
5.1 Apparatus and Procedure	128
5.1.1 Control Systems	128
5.1.2 Joystick	128
5.1.3 Pilot	131
5.1.4 Experiment #1	131
5.1.5 Experiments #2 and #3	131
5.1.6 Instrument Display	134
5.1.7 Visual Target	138
5.2 Discussion	142
5.2.1 Experiments #2 and #3	142
5.2.2 Open Loop Pilot-Vehicle Describing Functions	143
5.2.3 One Third Law	146
5.2.4 Pilot Describing Functions	147
5.2.5 Product Rule	149
5.3 Results	150
5.3.1 Experiment #1	150
5.3.2 Experiments #2 and #3	152

	Page
5.3.3 Pilot Compensation and Handling Qualities	173
6. CONCLUSIONS	181
7. RECOMMENDATIONS FOR FUTURE RESEARCH	183
REFERENCES	184
 APPENDICES	
Appendix A: Schematics of Electronic Circuits	186
Appendix B: Runlog for Piloted Experiments	191

Accession For	
NTIS CRA&I	<input checked="" type="checkbox"/>
DTIC TAB	<input type="checkbox"/>
Unannounced	<input type="checkbox"/>
Justification	
By	
Distribution /	
Availability Codes	
Dist	Avail and/or Special
A-1	

LIST OF TABLES

Table	Page
3.1 List of important physical parameters.	72
5.1 Signal composition of a) Low b) Medium s c) High bandwidth forcing functions.	135
5.2 Results of Experiment #1.	151
5.3 Handling qualities ratings for instrument display and visual scene with identical tasks.	153
5.4 Actual single and multi-axis HQRs with product rule estimates of multi-axis HQR (* Not used in regression).	162
 Appendix	
Table	
B.1 Handling qualities ratings for instrument display and visual scene.	204
B.2 Experimental results and least squares estimates of extended crossover model parameters.	206
B.3 Best fit pilot describing function parameters and slope of pilot magnitude curve at the open loop pilot-vehicle crossover frequency.	213

LIST OF FIGURES

Figure	Page
1.1 Schematic of Tilt Rotor Flying Machine (TROFM).	2
2.1 Diagram of the inertial reference frame.	6
2.2 Orientation of the mast body-axis system with respect to the inertial frame.	7
2.3 Orientation of pipe body-axis system with respect to the inertial frame.	8
2.4 Orientation of the tilt body-axis system with respect to the inertial frame.	10
2.5 Relationship between the rotor body system and the inertial frame.	11
2.6 Free body diagram of the pitch axis.	26
2.7 Free body diagram of the yaw axis.	28
2.8 Free body diagram of the roll (tilt) axis.	29
2.9 Free body diagram of the main rotor and motor armature.	31
3.1 Determining amplitude ratio and phase angle from an X-Y plot of output sinusoid versus input sinusoid.	37
3.2 Typical chirp waveform	41
3.3 Typical PRBS and PRBS signal generator consisting of digital components.	45
3.4 Main rotor angular velocity control system.	46
3.5 Block diagram of tilt servo angular position control system.	47
3.6 Flow chart of the system identification process used to determine the state space model of the TROFM.	48
3.7 Main motor (rotor) response* to a chirp input. (* DC offsets caused by rate limit subtracted out.)	50

Figure	Page
3.8 Main motor frequency response.	51
3.9 Block diagram of rate limited main motor model.	53
3.10 Block diagram of linear main motor model.	54
3.11 Actual and nonlinear simulated response of main rotor speed to a chirp input.	55
3.12 Cause of main rotor speed rate limit.	56
3.13 Response of tilt servo to chirp input.	58
3.14 Tilt servo frequency response.	59
3.15 Rotor force F_R as a function of main rotor speed $ \dot{\beta} $	60
3.16 Sketch of apparatus used to measure forces.	61
3.17 Free body diagram of system	62
3.18 Lateral force F_{SG_1} for $\Phi_1 = 20^\circ$ as a function of $\dot{\beta}$	64
3.19 Lateral force F_{SG_2} for $\Phi_2 = -20^\circ$ as a function of $\dot{\beta}$	64
3.20 Main Rotor Drag torque as a function of $\dot{\beta}$	65
3.21 Frequency response of $\Theta(s)/\dot{\beta}$ determined by OAT, DFT and maximum likelihood methods.	68
3.22 Pitch axis response to a chirp $\dot{\beta}_{com}$	69
3.23 Response of control design model to PRBS inputs.	74
3.24 Response of refined model and actual system to PRBS inputs.	76
4.1 General sampled data system.	78
4.2 Open loop command system block diagram.	81
4.3 Bode plot of open loop pitch system $\Theta(j\omega)/\dot{\beta}_{com}(j\omega)$	82
4.4 Bode plot of open loop yaw system $\Psi(j\omega)/\Phi_{com}(j\omega)$	83
4.5 Closed loop continuous yaw attitude command system.	84

Figure	Page
4.6 Bode plot of open loop continuous uncompensated and compensated yaw attitude command system $\Psi(j\omega)/e_\psi(j\omega)$	86
4.7 Bode plot of closed loop continuous compensated yaw attitude command system $\Psi(j\omega)/\Psi_{com}(j\omega)$	87
4.8 Closed loop sampled data yaw attitude command system.	88
4.9 Bode plot of open loop discrete compensated yaw attitude command system $\Psi(e^{j\omega T})/e_\psi(e^{j\omega T})$	90
4.10 Bode plot of closed loop discrete compensated yaw attitude command system $\Psi(e^{j\omega T})/\Psi_{com}(e^{j\omega T})$	91
4.11 Simulated and actual yaw attitude command system step responses. . .	93
4.12 Simulated* and actual yaw attitude command system step responses.(* Refined yaw axis model.)	94
4.13 Sampled data pitch attitude command system.	95
4.14 Bode plot of open loop continuous compensated and uncompensated pitch attitude command system $\Theta(j\omega)/e_\theta(j\omega)$	96
4.15 Bode plot of closed loop continuous compensated pitch attitude command system $\Theta(j\omega)/\Theta_{com}(j\omega)$	97
4.16 Sampled data pitch attitude command system.	97
4.17 Bode plot of open loop discrete compensated pitch attitude command system $\Theta(e^{j\omega T})/e_\theta(e^{j\omega T})$	99
4.18 Bode plot of closed loop discrete compensated pitch attitude command system $\Theta(e^{j\omega T})/\Theta_{com}(e^{j\omega T})$	100
4.19 Simulated and actual step responses for pitch attitude command system.	101
4.20 Kalman filtered state estimates, actual measurements and residuals with $\pm 2\sigma(\hat{y})$ lines from a PRBS test.	106
4.21 Block diagram of hypothetical continuous pitch rate command system .	109
4.22 Bode plot of hypothetical open loop continuous compensated and uncompensated pitch rate command system $\dot{\Theta}(j\omega)/e_{\dot{\theta}}(j\omega)$	111

Figure	Page
4.23 Bode plot of hypothetical closed loop continuous compensated pitch rate command system $\dot{\Theta}(j\omega)/\dot{\Theta}_{com}(j\omega)$	112
4.24 Block diagram of hypothetical sampled data pitch rate command system	113
4.25 Bode plot of hypothetical open loop discrete compensated pitch rate command system $\dot{\Theta}(e^{j\omega T})/e_{\dot{\Theta}}(e^{j\omega T})$	114
4.26 Bode plot of hypothetical closed loop discrete compensated pitch rate command system $\dot{\Theta}(e^{j\omega T})/\dot{\Theta}_{com}(e^{j\omega T})$	115
4.27 Block diagram of hypothetical continuous yaw rate command system . .	116
4.28 Bode plot of hypothetical open loop continuous compensated and uncompensated yaw rate command system $\Psi(j\omega)/e_{\Psi}(j\omega)$	118
4.29 Bode plot of hypothetical closed loop continuous compensated yaw rate command system $\Psi(j\omega)/\Psi_{com}(j\omega)$	119
4.30 Block diagram of hypothetical sampled data yaw rate command system .	120
4.31 Bode plot of hypothetical open loop discrete compensated yaw rate command system $\dot{\Psi}(e^{j\omega T})/e_{\dot{\Psi}}(e^{j\omega T})$	121
4.32 Bode plot of hypothetical closed loop discrete compensated yaw rate command system $\dot{\Psi}(e^{j\omega T})/\dot{\Psi}_{com}(e^{j\omega T})$	122
4.33 Block diagram of actual rate command system implementation.	123
4.34 Bode plot of closed loop discrete pitch rate command system with and without Kalman filter. $\dot{\Theta}(e^{j\omega T})/\dot{\Theta}_{com}(e^{j\omega T})$	124
4.35 Bode plot of closed loop discrete yaw rate command system with and without Kalman filter. $\dot{\Psi}(e^{j\omega T})/\dot{\Psi}_{com}(e^{j\omega T})$	125
4.36 Step responses of SISO simulated, online Kalman filtered rate estimate, and differentiated attitude measurements for a) pitch rate b) yaw rate command systems.	126
5.1 Basic structure of a continuous pilot in the loop tracking system.	127
5.2 Simplified block diagrams of, open loop, rate and attitude command systems.	129

Figure	Page
5.3 Cooper-Harper rating chart	132
5.4 Diagram of the apparatus used in Experiment #1	133
5.5 Forcing function signal composition	136
5.6 Typical forcing function time histories	137
5.7 Diagram of the instrument panel	139
5.8 Diagram of the x-y plotter with target	140
5.9 Block diagram of a sampled data system	143
5.10 Block diagram of single loop sampled data pilot-vehicle tracking system.	144
5.11 Diagram of the magnitude fitting procedure.	145
5.12 Visual versus instrument HQRs for a) pitch axis b) yaw axis tasks. . . .	155
5.13 HQR as a function of command system and forcing function bandwidth using instrument display for single axis pitch task.	156
5.14 HQR as a function of command system and forcing function bandwidth using instrument display for single axis yaw task.	157
5.15 HQR as a function of command system and forcing function bandwidth using instrument display for multi-axis tasks.	157
5.16 HQR as a function of command system and forcing function bandwidth using visual scene for single axis pitch task.	158
5.17 HQR as a function of command system and forcing function bandwidth using visual scene for single axis yaw task.	159
5.18 HQR as a function of command system and forcing function bandwidth using visual scene for multi-axis tasks.	159
5.19 Product rule for visual scene.	161
5.20 One third law for the visual scene with low bandwidth forcing functions.	164
5.21 One third law for visual scene with medium bandwidth forcing functions.	165

Figure	Page
5.22 One third laws for the visual scene with fast bandwidth forcing functions.	165
5.23 One third laws for the instrument display with low bandwidth forcing functions.	166
5.24 One third laws for the instrument display with medium bandwidth forcing functions.	166
5.25 One third laws for the instrument display with fast bandwidth forcing functions.	167
5.26 Open loop pilot-vehicle describing function for a low bandwidth single axis pitch forcing function with instrument display and attitude command system.	168
5.27 Open loop pilot-vehicle describing function for a low bandwidth single axis yaw forcing function with instrument display and attitude command system.	169
5.28 Pilot describing function for a low bandwidth single axis pitch forcing function with instrument display and attitude command system.	169
5.29 Pilot describing function for a low bandwidth single axis yaw forcing function with instrument display and attitude command system.	170
5.30 Open loop pilot-vehicle describing function for a high bandwidth single axis pitch forcing function with instrument display and rate command system.	171
5.31 Open loop pilot-vehicle describing function for a low bandwidth single axis yaw forcing function with instrument display and rate command system.	171
5.32 Pilot describing function for a high bandwidth single axis pitch forcing function with instrument display and rate command system.	172
5.33 Pilot describing function for a low bandwidth single axis yaw forcing function with instrument display and rate command system.	172
5.34 Open loop pilot-vehicle describing function for a high bandwidth single axis yaw forcing function with instrument display and open loop command system.	173

Figure	Page
5.35 Pilot describing function for a high bandwidth single axis yaw forcing function with instrument display and open loop command system. . . .	174
5.36 HQR as a function of slope of pilot Bode magnitude curve at the open loop pilot-vehicle crossover frequency for the multi-axis visual cases . . .	176
5.37 HQR as a function of slope of pilot Bode magnitude curve at the open loop pilot-vehicle crossover frequency for the single axis visual cases. . .	177
5.38 Normalized performance as a function of slope of pilot Bode magnitude curve at the open loop pilot-vehicle crossover frequency for the single axis instrument cases.	178
5.39 Normalized performance as a function of slope of pilot Bode magnitude curve at the open loop pilot-vehicle crossover frequency for the single axis visual cases.	179
5.40 Normalized performance as a function of slope of pilot Bode magnitude curve at the open loop pilot-vehicle crossover frequency for the multi-axis visual cases.	180
 Appendix	
Figure	
A.1 Schematic of angular displacement sensors.	187
A.2 Schematic of connections to Copley Model 201 Amplifier.	188
A.3 PWM circuit for tilt servo.	189
A.4 Stepper motor logic circuit.	190
B.1 Definition of linearly interpolated crossover frequency and phase margin.	203
B.2 Open loop pilot-vehicle and pilot describing functions.	217

1. INTRODUCTION

A laboratory Tilt Rotor Flying Machine (TROFM) was designed and built for the purpose of conducting an experimental study of the effects of command systems, displays and tasks on human pilot behavior. The aircraft is mounted on a two axis pivot stand which gives the fuselage two degrees of freedom; pitch and yaw. Figure 1.1 shows a diagram of the TROFM. Rotation of the mast is referred to as yawing motion and is denoted Ψ . Angular displacement of the pipe about the pivot point is called pitch which is denoted Θ . The main rotor is tilted by a Futaba 9102 servo. Tilt or roll angle is denoted Φ . Main rotor speed is the primary pitch axis controller while the rotor tilt angle is used for yaw axis control.

The angles Ψ , Θ and Φ are measured by potentiometers (1 K Ω \pm %1 linearity) configured as voltage dividers powered by a 10 V, 200 mA power supply with %0.5 ripple. A potentiometric joystick is also configured as a voltage divider and shares the sensor power supply. The rotor is driven by a Maxon 18 VDC motor which is powered by a Copley model 201 Pulse Width Modulated (PWM) amplifier. The motor has a DC tachometer mounted on its base for rotor velocity measurements. The rotor is a 12 inch fixed (#6) pitch model airplane propeller.

Sensors and actuators are interfaced to a Mac IIsi digital computer via a National Instruments NB-MIO-16 A/D, D/A board. The board has 12 bit accuracy, 9 μ sec A/D conversion time and a maximum sampling rate of 100,000 samples/sec. Two analog output channels are used to send commands to the actuators and six differential analog inputs are used to sample sensor and joystick signals. The pilot in the loop experiments make use of a custom built X-Y plotter which uses four digital I/O lines on the NB-MIO-16 board to drive two stepper motors

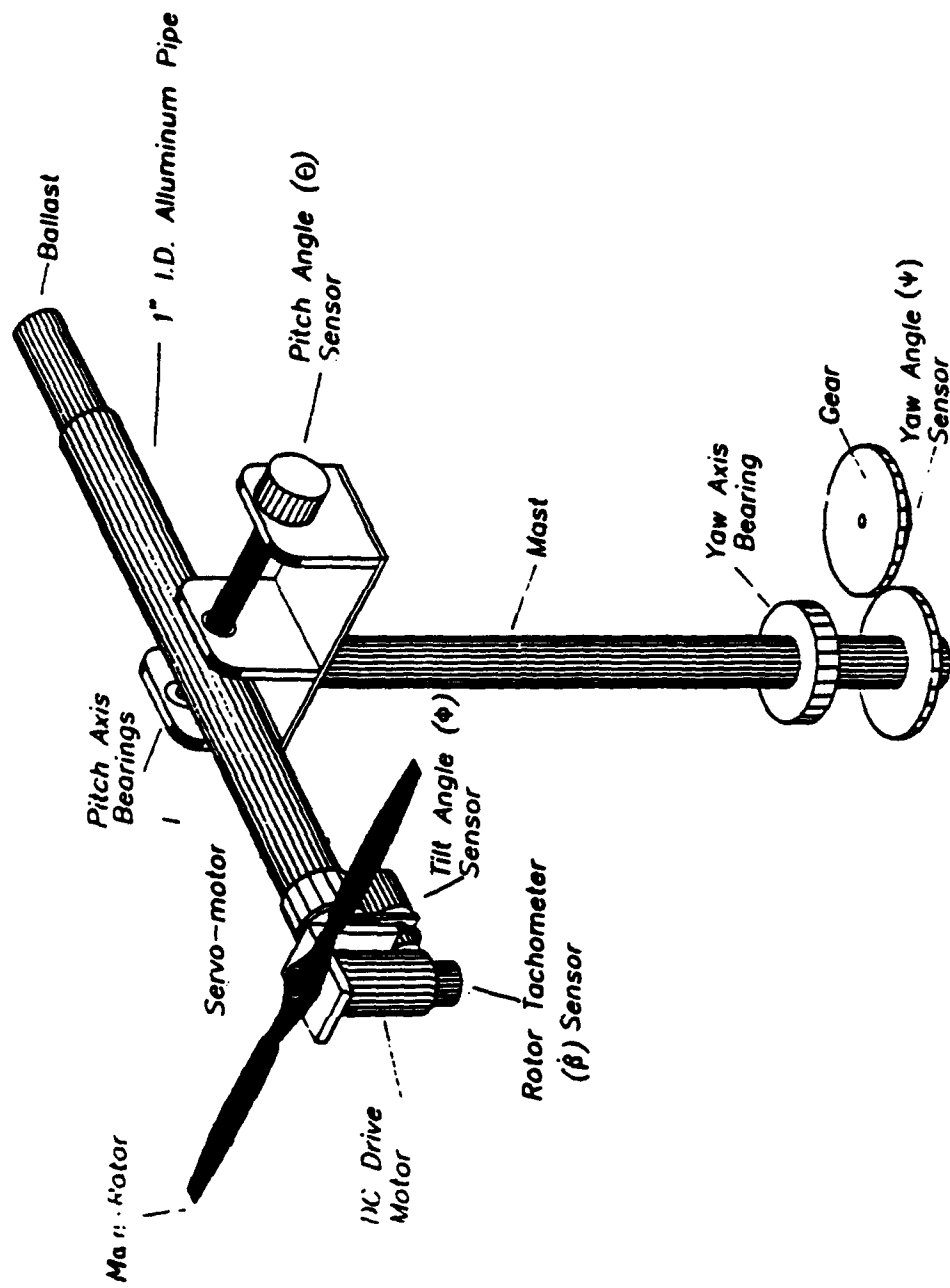


Figure 1.1 Schematic of Tilt Rotor Flying Machine (TROFM).

Analytical models are derived using Lagrangian and Newtonian techniques. Identification of the aircraft characteristics is based on a non-parametric Discrete Fourier Transform technique and a maximum likelihood parameter estimation scheme. Classical control design techniques are used to design continuous compensators for rate and attitude command systems. Digital filters are designed to emulate the continuous compensators and are implemented in real time on the digital computer. Rate command, attitude command and open loop (unaugmented) systems are developed. The attitude command system use feedback from the pitch and yaw sensors to maintain a desired attitude specified by the position of the pilot's joystick. The rate command system uses rate estimates for feedback to maintain angular rates specified by the position of the joystick. The rate estimates are generated by a digital Kalman filter which is based on a complete linear dynamic model of the TROFM because rate sensors are unavailable, attitude sensors are too noisy to be differentiated, and the model does not account for non-linear phenomena and unknown disturbances.

A study of the effects of command systems, displays and tasks on human pilot behavior is conducted. Loren P. Dean, general aviation pilot used the Cooper-Harper rating scale [2] to evaluate the flying qualities of the TROFM using three command systems for two types of tasks and two different display types. Pilot and pilot-vehicle describing functions are obtained from time histories of dynamic tracking tasks where the pilot attempts to track a random appearing input. Compensatory instrument displays and a visual pursuit scene are used for the dynamic tracking tasks. Correlations between the Cooper-Harper ratings and quantitative descriptions of pilot behavior are made. The experimental results are compared to the classical theory of man-machine system dynamics which is based on the crossover model [9].

2. EQUATIONS OF MOTION

In order to develop control laws for a physical system, a mathematical model of the motion of the system must be developed. For simple systems a Newtonian approach is advisable, but for more complex systems a Lagrangian approach is more suitable, since it allows one to directly obtain the differential equations of motion of a physical system from its kinetic energy expression.

The physical system of interest is a Tilt Rotor Flying Machine (TROFM) whose angular position is controlled by an aerodynamic actuator or rotor. The TROFM is free to rotate in pitch and yaw about a fixed point. The pitch angle is controlled by the lift generated by the rotor and the yaw angle is controlled by tilting the rotor in the direction of desired rotation. A schematic of the machine is shown in Figure 1.1.

An idealization of the TROFM consists of four rigid bodies:

- 1 M. Mast assembly
- 2 P. Pipe, ballast, tilt servo , tilt angle transducer, idler wheels and mounting bracket.
- 3 T. Tilt mechanism, i.e. friction wheel, motor mount, motor stator.
- 4 R. Rotor, motor armature.

One inertially fixed and four body fixed coordinate axis systems are defined. In order to use Lagrange's equations, the kinetic energy of the entire system must be expressed in inertial coordinates; therefore, relations between the body axis systems and an inertial frame were developed.

2.1 Coordinate Systems

An inertial coordinate system (Figure 2.1) i with origin at the top of the mast is defined. The \hat{i}_x, \hat{i}_y and \hat{i}_z unit vectors are earth fixed and defined positive North, East and toward the center of the earth respectively.

A Cartesian coordinate system is defined which rotates with the mast and whose origin is at the top of the mast. The mast is free to rotate an angle Ψ about the \hat{i}_z axis. The mast body axis system is denoted m and is shown in Figure 2.2.

A vector quantity v may be written

$$\begin{aligned} v &= m_x \hat{m}_x + m_y \hat{m}_y + m_z \hat{m}_z \\ &= i_x \hat{i}_x + i_y \hat{i}_y + i_z \hat{i}_z \end{aligned} \quad [2.1]$$

where $\hat{m}_x, \hat{m}_y,$ and \hat{m}_z are unit vectors coincident with the body fixed axes of the mast. The scalars m_x, m_y, m_z and i_x, i_y, i_z are the x, y and z components of the vector v measured with respect to the m and i coordinate systems respectively. It is convenient to make use of linear algebra when showing relationships between vectors and deriving expressions for the kinetic energy of a rigid body; therefore, matrix notation is introduced. The relationship between m_x, m_y, m_z and i_x, i_y, i_z is given by

$$\begin{bmatrix} m_x \\ m_y \\ m_z \end{bmatrix}_m = \begin{bmatrix} \cos(\Psi) & -\sin(\Psi) & 0 \\ \sin(\Psi) & \cos(\Psi) & 0 \\ 0 & 0 & 1 \end{bmatrix} \begin{bmatrix} i_x \\ i_y \\ i_z \end{bmatrix}_i \quad [2.2]$$

A pipe or p coordinate axis system is defined which rotates with the second rigid body about an origin fixed at the top of the mast. This axis system is free to rotate an angle Ψ about \hat{i}_z and an angle Θ about \hat{m}_y . The relationship between the p and i coordinate system is illustrated in Figure 2.3.

A vector quantity v may be written

$$\begin{aligned} v &= p_x \hat{p}_x + p_y \hat{p}_y + p_z \hat{p}_z \\ &= i_x \hat{i}_x + i_y \hat{i}_y + i_z \hat{i}_z \end{aligned} \quad [2.3]$$

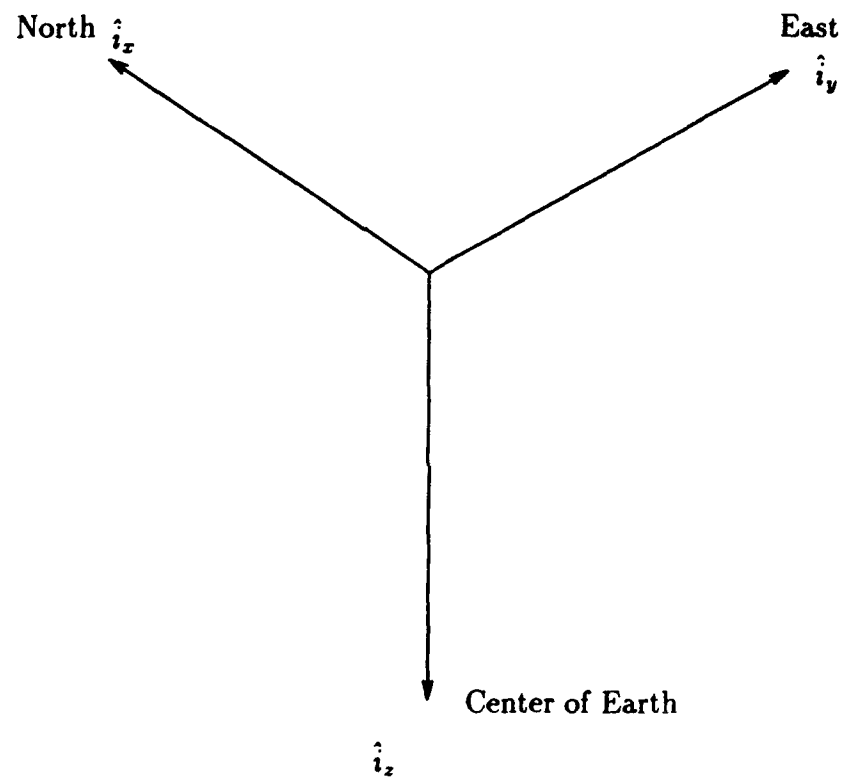


Figure 2.1 Diagram of the inertial reference frame.

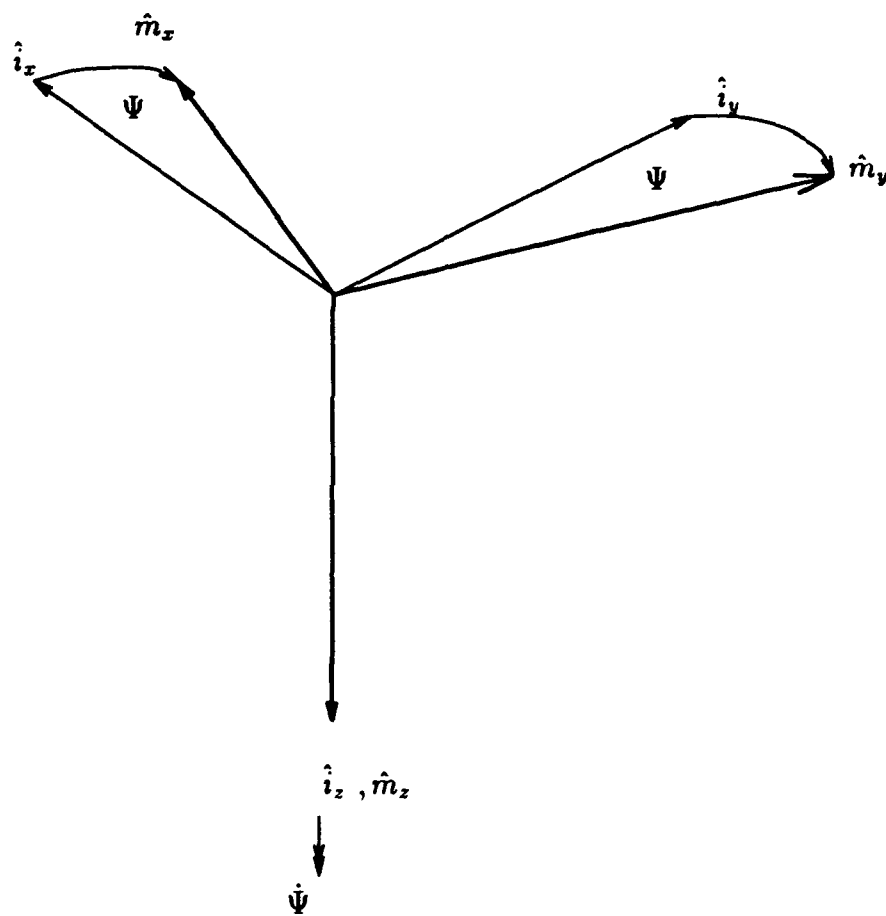


Figure 2.2 Orientation of the mast body-axis system with respect to the inertial frame.

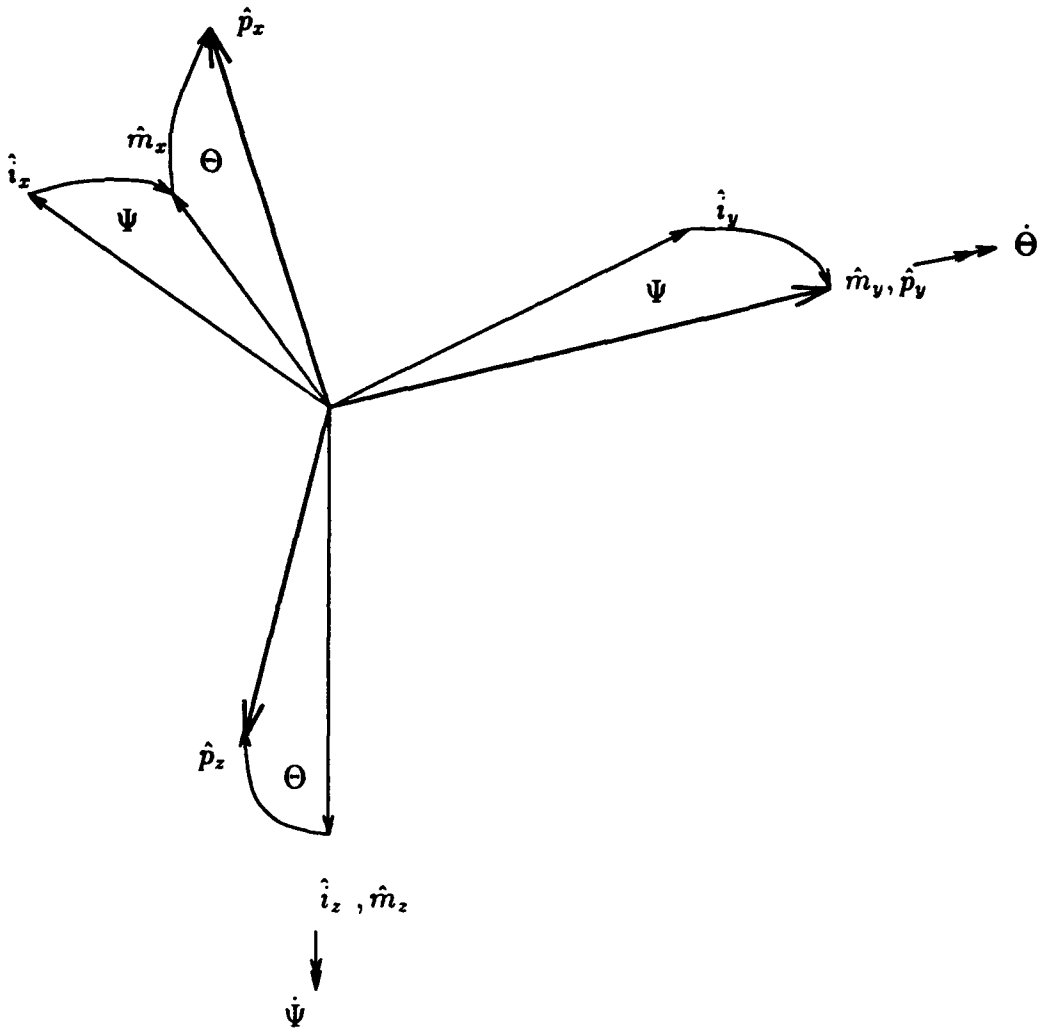


Figure 2.3 Orientation of pipe body-axis system with respect to the inertial frame.

The following equation shows the mathematical relationship between the x, y, and z components of v measured with respect to the p body-axis system and the x, y and z components of v measured with respect to the inertial frame.

$$\begin{bmatrix} p_x \\ p_y \\ p_z \end{bmatrix}_p = \begin{bmatrix} \cos(\Theta) \cos(\Psi) & \cos(\Theta) \sin(\Psi) & -\sin(\Theta) \\ -\sin(\Psi) & \cos(\Psi) & 0 \\ \sin(\Theta) \cos(\Psi) & \sin(\Theta) \sin(\Psi) & \cos(\Theta) \end{bmatrix} \begin{bmatrix} i_x \\ i_y \\ i_z \end{bmatrix}_i \quad [2.4]$$

Next a coordinate system t (Figure 2.4) is defined which rotates with the tilt mechanism and has an origin located at the top of the mast. The axis system is free to rotate an angle Ψ about \hat{i}_x , an angle Θ about \hat{m}_y and an angle Φ about the \hat{p}_x axis.

The following matrix transforms components of vectors reckoned with respect to the inertial frame to components reckoned with respect to the tilt body-axis system:
 $T^i \text{ to } t =$

$$\begin{bmatrix} \cos(\Theta) \cos(\Psi) & \cos(\Theta) \sin(\Psi) & -\sin(\Theta) \\ \sin(\Phi) \sin(\Theta) \cos(\Psi) - \cos(\Phi) \sin(\Psi) & \sin(\Phi) \sin(\Theta) \sin(\Psi) + \cos(\Phi) \cos(\Psi) & \sin(\Phi) \cos(\Theta) \\ \cos(\Phi) \sin(\Theta) \cos(\Psi) + \sin(\Phi) \sin(\Psi) & \cos(\Phi) \sin(\Theta) \sin(\Psi) - \sin(\Phi) \cos(\Psi) & \cos(\Phi) \cos(\Theta) \end{bmatrix}$$

Finally a rotor body-axis system r is defined whose origin is located at the center of mass of the main rotor and motor armature and with unit vectors aligned with the tilt body-axis system. Figure 2.5 shows the relationship between the rotor body-axis system and the inertial frame.

Consider a vector quantity v such as position or angular velocity. Let v_r be the vector quantity measured with respect to the rotor body-axis system and v_t be the vector quantity measured with respect to the tilt body-axis system.

$$\begin{aligned} v_r &= r_x \hat{r}_x + r_y \hat{r}_y + r_z \hat{r}_z \\ v_t &= t_x \hat{t}_x + t_y \hat{t}_y + t_z \hat{t}_z \end{aligned} \quad [2.6]$$

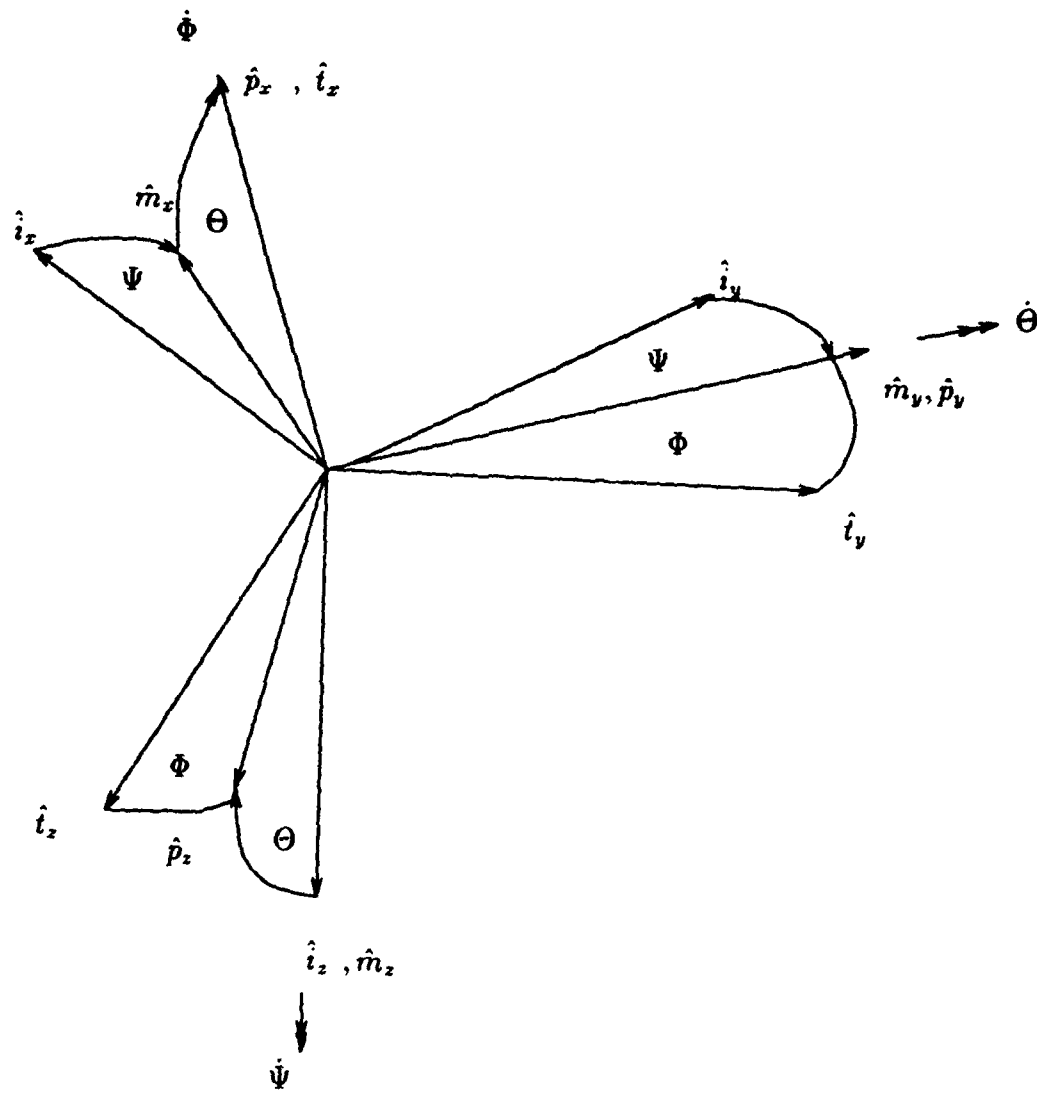


Figure 2.4 Orientation of the tilt body-axis system with respect to the inertial frame.

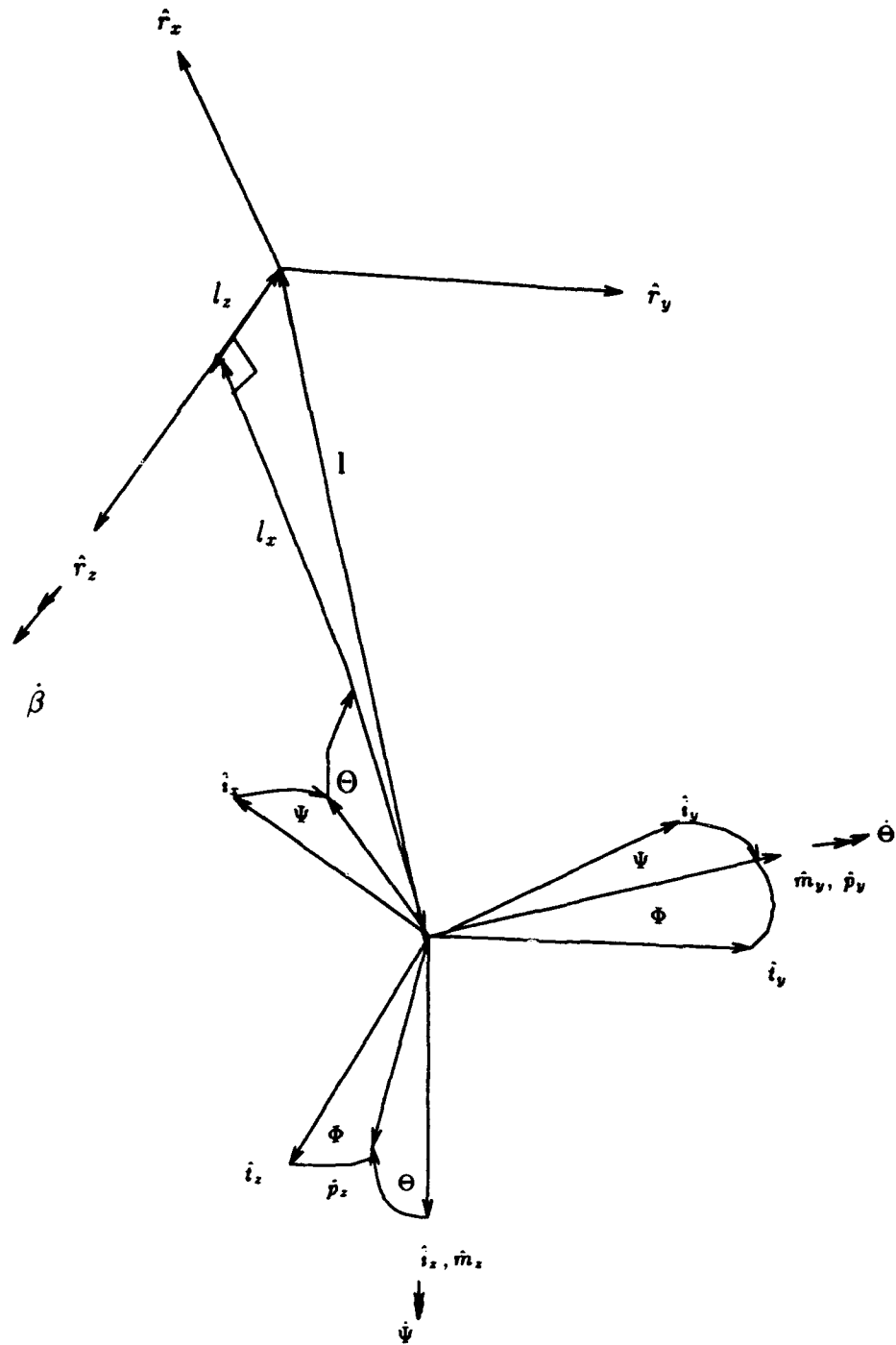


Figure 2.5 Relationship between the rotor body system and the inertial frame.

The vector \mathbf{v} as observed from an inertial frame is given by

$$\mathbf{v} = \mathbf{v}_r + \mathbf{v}_t \quad [2.7]$$

But since \mathbf{t} and \mathbf{r} are parallel,

$$\mathbf{v} = (r_x + t_x) \hat{t}_x + (r_y + t_y) \hat{t}_y + (r_z + t_z) \hat{t}_z \quad [2.8]$$

The relationship between the components of \mathbf{v} reckoned with respect to the tilt axis system and the components of \mathbf{v} reckoned with respect to the inertial frame are given by

$$\begin{bmatrix} r_x + t_x \\ r_y + t_y \\ r_z + t_z \end{bmatrix} = \mathbf{T}^{i \text{ to } t} \begin{bmatrix} i_x \\ i_y \\ i_z \end{bmatrix} \quad [2.9]$$

Consider the position of the origin of the rotor body-axis system relative to the tilt body-axis system. Note that this position is constant. Let l_x, l_y and l_z denote the x, y and z distances measured from the origin of the tilt body system to the origin of the rotor body system (Note $l_y = 0$). These constants are useful in formulating an inertia tensor for the rotor center of mass.

A relationship between the angular velocities of a rotating rigid body axis system and a set of generalized inertial angular velocities (i.e Euler angles) is also needed. Figures 2.2, 2.3, and 2.4 show the orientations of the Euler angular velocities with respect to the inertial frame. The Euler angles are considered inertial because they uniquely define the orientation of a body. Body fixed angular velocities are non-inertial since they do not uniquely define the orientation of the body. Consider a body which has three rotational degrees of freedom and no translational degrees of freedom (i.e. tilt body). Assume that the origin of the body-axis system and the origin of the inertial frame are coincident. The angular velocity of the body reckoned with respect to the inertial frame ${}^i\omega^b$ may be written as

$${}^i\omega^b = \omega_{b_x} \hat{b}_x + \omega_{b_y} \hat{b}_y + \omega_{b_z} \hat{b}_z \quad [2.10]$$

$$\begin{aligned}
&= \omega_{i_x} \hat{i}_x + \omega_{i_y} \hat{i}_y + \omega_{i_z} \hat{i}_z \\
&= \dot{\Psi} \hat{i}_z + \dot{\Theta} \hat{m}_y + \dot{\Phi} \hat{p}_x
\end{aligned} \tag{2.11}$$

The mathematical relationship between the body-axis angular velocities and the Euler angular velocities is given below [6].

$$\begin{bmatrix} \omega_{b_x} \\ \omega_{b_y} \\ \omega_{b_z} \end{bmatrix}_{\mathbf{b}} = \begin{bmatrix} 1 & 0 & -\sin(\Theta) \\ 0 & \cos(\Phi) & \cos(\Theta) \sin(\Phi) \\ 0 & -\sin(\Phi) & \cos(\Theta) \cos(\Phi) \end{bmatrix} \begin{bmatrix} \dot{\Phi} \\ \dot{\Theta} \\ \dot{\Psi} \end{bmatrix}_{\hat{p}_x, \hat{m}_y, \hat{i}_z} \tag{2.12}$$

Note that the tilt, pipe and mast body angular velocities can be transformed to Euler angular velocities by direct application of Equation 2.12.

2.2 Kinetic Energy

In general the total kinetic energy of a system of n rigid bodies is given by

$$T = \frac{1}{2} \sum_{i=1}^n m_i v_i^2 + \frac{1}{2} \sum_{i=1}^n \{\omega_i\}^T [I]_i \{\omega_i\} \tag{2.13}$$

where v_i is the velocity of the center of mass of the i th body, $[I]_i$ is the inertia tensor of the i th body, and $\{\omega_i\}$ is the angular velocity of the i th body. The total kinetic energy of the TROFM is equal to the sum of its four components.

$$T = T_m + T_p + T_T + T_R \tag{2.14}$$

In order to apply Lagrange's equation, the kinetic energy of the system must be expressed in inertial coordinates.

Consider the kinetic energy of the mast T_m . The inertia tensor of the mast is constant when observed from the mast coordinate system and the \mathbf{m}_{xy} and \mathbf{m}_{xz} planes are planes of symmetry.

$$\mathbf{I}_m = \begin{bmatrix} I_{xxm} & 0 & 0 \\ 0 & I_{yy m} & I_{yzm} \\ 0 & I_{yzm} & I_{zzm} \end{bmatrix} \tag{2.15}$$

Since the m frame does not translate, the kinetic energy of the mast is

$$T_m = \frac{1}{2} \{i_{\omega^m}\}^T [I]_m \{i_{\omega^m}\} \quad [2.16]$$

where $[I]_m$ is the inertia tensor of the mast in \hat{m} coordinates. Since \hat{m}_z and \hat{i}_z are coincident and the rotation is about \hat{i}_z only, Equation 2.12 reduces to

$$i_{\omega^m} = \dot{\Psi} \hat{i}_z \quad [2.17]$$

Substituting Equation 2.17 into the Equation 2.13 one obtains an expression for the kinetic energy of the mast in generalized inertial coordinates.

$$T_m = I_{zzm} \dot{\Psi}^2 \quad [2.18]$$

Consider the kinetic energy of the pipe body T_p . Since the pipe is fixed at the origin of the pipe body axis system, the kinetic energy of the pipe body is given by:

$$T_p = \frac{1}{2} \{i_{\omega^p}\}^T [I]_p \{i_{\omega^p}\} \quad [2.19]$$

where $[I]_p$ is the inertia tensor of the pipe body as observed from the p coordinate axis system. The inertia tensor is constant when observed from the p coordinate axis system. Since the p_{xy} and p_{yz} planes are planes of symmetry, the inertia tensor becomes

$$I_p = \begin{bmatrix} I_{xzp} & 0 & I_{xzp} \\ 0 & I_{yyp} & 0 \\ I_{xzp} & 0 & I_{xzp} \end{bmatrix} \quad [2.20]$$

The angular velocities are transformed to inertial coordinates. Recall that the pipe body has two degrees of freedom, Θ and Ψ ; thus, from Equation 2.12 one obtains

$$\{i_{\omega^p}\} = \begin{bmatrix} -\sin(\Theta)\dot{\Psi} \\ \dot{\Theta} \\ \cos(\Theta)\dot{\Psi} \end{bmatrix}_{\hat{p}_x, \hat{m}_y, \hat{i}_z} \quad [2.21]$$

Substituting Equation 2.21 into Equation 2.19, one obtains an expression for the kinetic energy of the pipe in inertial coordinates.

$$T_p = \frac{1}{2} I_{xxp} \sin^2(\Theta) \dot{\Psi}^2 - I_{xyp} \sin(\Theta) \dot{\Psi}^2 \cos(\Theta) + \frac{1}{2} I_{yyp} \dot{\Theta}^2 + \frac{1}{2} I_{zyp} \cos^2(\Theta) \dot{\Psi}^2 \quad [2.22]$$

The kinetic energy of the tilt body system is given by

$$T_t = \frac{1}{2} \{i\omega^t\}^T [I]_t \{i\omega^t\} + \frac{1}{2} m_t l_{tcmcr}^2 \dot{\Phi}^2 \quad [2.23]$$

where l_{tcmcr} is the perpendicular distance between the center of mass of the tilt body and the shaft of the tilt servo. The inertia tensor is given by

$$I_t = \begin{bmatrix} I_{xxt} & 0 & I_{xzt} \\ 0 & I_{yyt} & 0 \\ I_{xzt} & 0 & I_{zzt} \end{bmatrix} \quad [2.24]$$

The angular velocity vector $\{i\omega^t\}$ is expressed in terms of its Euler angle components. Recall that the tilt body has three degrees of freedom, Ψ , Θ , and Φ ; thus, Equation 2.12 may be substituted directly into Equation 2.23.

$$\begin{aligned} T_t = & \frac{1}{2} I_{xxt} \dot{\Phi}^2 - I_{xxt} \sin(\Theta) \dot{\Psi} \dot{\Phi} + \frac{1}{2} I_{xxt} \sin^2(\Theta) \dot{\Psi}^2 - I_{xzt} \sin(\Phi) \dot{\Theta} \dot{\Phi} + \quad [2.25] \\ & I_{xzt} \sin(\Phi) \sin(\Theta) \dot{\Psi} \dot{\Theta} + I_{xzt} \cos(\Theta) \cos(\Phi) \dot{\Psi} \dot{\Phi} - I_{xzt} \cos(\Theta) \cos(\Phi) \dot{\Psi}^2 \sin(\Theta) + \\ & \frac{1}{2} I_{yyt} \cos^2(\Phi) \dot{\Theta}^2 + I_{yyt} \cos(\Phi) \cos(\Theta) \sin(\Phi) \dot{\Psi} \dot{\Theta} + \frac{1}{2} I_{yyt} \cos^2(\Theta) \sin^2(\Phi) \dot{\Psi}^2 + \\ & \frac{1}{2} I_{zzt} \sin^2(\Phi) \dot{\Theta}^2 - I_{zzt} \sin(\Phi) \dot{\Theta} \cos(\Theta) \cos(\Phi) \dot{\Psi} + \frac{1}{2} I_{zzt} \cos^2(\Theta) \cos^2(\Phi) \dot{\Psi}^2 \\ & + \frac{1}{2} m l_{tcmcr}^2 \dot{\Psi}^2 \end{aligned}$$

Finally the kinetic energy of the rotor is found. Recall that the rotor coordinate axis system is fixed to the center of mass of the rotor body and oriented parallel to the tilt body axis system. This means that the rotor body axis system translates as well as rotates when observed from the inertial frame. The rotor body is assumed to

be axisymmetric about the \hat{r}_z axis since the rotor is spinning at high speed relative to the other rigid bodies in the system. This assumption is based on actuator disk theory as it applies to propellers. The kinetic energy of the rotor is the sum of its rotational and translational components.

$$T_r = \frac{1}{2} \{^i\omega^r\}^T [I]_r \{^i\omega^r\} + \frac{1}{2} m_r \left\{ \left\{ ^i v^r \right\} \right\}^2 \quad [2.26]$$

The rotor has four degrees of freedom, Ψ , Θ , Φ , and β . The angle β is the angular position of the rotor blade with respect to the r coordinate system. Since the rotor is assumed axisymmetric, the inertia tensor as observed from the r coordinate system is constant and diagonal.

$$I_r = \begin{bmatrix} I_{xxr} & 0 & 0 \\ 0 & I_{xxr} & 0 \\ 0 & 0 & I_{zzr} \end{bmatrix} \quad [2.27]$$

The rotor spins about the \hat{r}_z axis with an angular velocity of $\dot{\beta}$. The rotor axis system also rotates with respect to the inertial frame. The total angular velocity of the rotor is the vector sum of the angular velocity of the tilt body components and the rotor body components (see page 12)

$$\{^i\omega^r\} = \begin{bmatrix} 1 & 0 & -\sin(\Theta) \\ 0 & \cos(\Phi) & \cos(\Theta)\sin(\Phi) \\ 0 & -\sin(\Phi) & \cos(\Theta)\cos(\Phi) \end{bmatrix} \begin{bmatrix} \dot{\Phi} \\ \dot{\Theta} \\ \dot{\Psi} \end{bmatrix}_{\hat{p}_x, \hat{m}_y, \hat{i}_z} + \begin{bmatrix} 0 \\ 0 \\ \dot{\beta} \end{bmatrix}_r \quad [2.28]$$

Substituting Equation 2.28 into the first term of Equation 2.26 one obtains an expression for the rotational kinetic energy of the rotor body in inertial coordinates.

$$\begin{aligned} T_{rot} = & \frac{1}{2} I_{xxr} \dot{\Phi}^2 - I_{xxr} \sin(\Theta) \dot{\Psi} \dot{\Phi} + \frac{1}{2} I_{xxr} \sin^2(\Theta) \dot{\Psi}^2 + \frac{1}{2} I_{xxr} \cos^2(\Phi) \dot{\Theta}^2 + \\ & I_{xxr} \cos(\Phi) \cos(\Theta) \sin(\Phi) \dot{\Psi} \dot{\Theta} + \frac{1}{2} I_{xxr} \cos^2(\Theta) \sin^2(\Phi) \dot{\Psi}^2 + \frac{1}{2} I_{zzr} \sin^2(\Phi) \dot{\Theta}^2 - \\ & I_{zzr} \cos(\Phi) \cos(\Theta) \sin(\Phi) \dot{\Psi} \dot{\Theta} - I_{zzr} \sin(\Phi) \dot{\Theta} \dot{\beta} + \frac{1}{2} I_{zzr} \cos^2(\Theta) \cos^2(\Phi) \dot{\Psi}^2 + \\ & I_{zzr} \cos(\Theta) \cos(\Phi) \dot{\Psi} \dot{\beta} + \frac{1}{2} I_{zzr} \dot{\beta}^2 \end{aligned} \quad [2.29]$$

The translational kinetic energy of the rotor body is given by

$$T_{r_{tran}} = \frac{1}{2} \{i\omega^t\}^T \begin{bmatrix} m_r (l_z)^2 & 0 & m_r (l_x) (l_z) \\ 0 & m_r (l_x)^2 & 0 \\ m_r (l_x) (l_z) & 0 & m_r (l_x)^2 \end{bmatrix} \{i\omega^t\} + \frac{1}{2} m_r (l_x - l_{rcmcr})^2 \dot{\Phi}^2 \quad [2.30]$$

where l_{rcmcr} is the perpendicular distance between the center of mass of the rotor and the shaft of the tilt angle position servo. Substituting Equation 2.12 into Equation 2.30 one obtains an expression for the translational kinetic energy of the rotor body in inertial coordinates.

$$\begin{aligned} T_{r_{tran}} = & \frac{1}{2} m_r (l_z)^2 \dot{\Phi}^2 - m_r (l_x)^2 \sin(\Theta) \dot{\Psi} \dot{\Phi} + \frac{1}{2} m_r (l_x)^2 \sin^2(\Theta) \dot{\Psi}^2 + \quad [2.31] \\ & \frac{1}{2} m_r (l_x)^2 \cos^2(\Phi) \dot{\Theta}^2 + \frac{1}{2} m_r (l_x)^2 \cos^2(\Theta) \sin^2(\Phi) \dot{\Psi}^2 + \\ & \frac{1}{2} m_r (l_x)^2 \sin^2(\Phi) \dot{\Theta}^2 + \frac{1}{2} m_r (l_x)^2 \cos^2(\Theta) \cos^2(\Phi) \dot{\Psi}^2 + \frac{1}{2} m_r l_{rcmcr}^2 \dot{\Phi}^2 \\ & m_r (l_x) (l_z) \sin(\Phi) \sin(\Theta) \dot{\Theta} \dot{\Psi} + m_r (l_x) (l_z) \cos(\Theta) \cos(\Phi) \dot{\Psi} \dot{\Phi} - \\ & m_r (l_x) (l_z) \cos(\Theta) \cos(\Phi) \sin(\Theta) \dot{\Psi}^2 - m_r (l_x) (l_z) \sin(\Phi) \dot{\Theta} \dot{\Phi} \end{aligned}$$

The kinetic energy of each of the rigid bodies is now expressed in inertial coordinates. Substituting Equations 2.18, 2.22, 2.25, 2.29 and 2.31 into Equation 2.14 one obtains an expression for the kinetic energy of the entire system in inertial coordinates.

$$\begin{aligned} T = & I_{zz} m \dot{\Psi}^2 + \frac{1}{2} I_{xyp} \sin^2(\Theta) \dot{\Psi}^2 - I_{xyp} \sin(\Theta) \dot{\Psi}^2 \cos(\Theta) + \frac{1}{2} I_{yyp} \dot{\Theta}^2 + \\ & \frac{1}{2} I_{xxt} \dot{\Phi}^2 - I_{xxt} \sin(\Theta) \dot{\Psi} \dot{\Phi} + \frac{1}{2} I_{xxt} \sin^2(\Theta) \dot{\Psi}^2 - I_{xzt} \sin(\Phi) \dot{\Theta} \dot{\Phi} + \\ & I_{xzt} \cos(\Theta) \cos(\Phi) \dot{\Psi} \dot{\Phi} - I_{xzt} \cos(\Theta) \cos(\Phi) \dot{\Psi}^2 \sin(\Theta) + \frac{1}{2} I_{yyt} \cos^2(\Phi) \dot{\Theta}^2 + \\ & I_{yyt} \cos(\Phi) \cos(\Theta) \sin(\Phi) \dot{\Psi} \dot{\Theta} + \frac{1}{2} I_{yyt} \cos^2(\Theta) \sin^2(\Phi) \dot{\Psi}^2 + \frac{1}{2} I_{zzt} \sin^2(\Phi) \dot{\Theta}^2 - \\ & I_{zzt} \sin(\Phi) \dot{\Theta} \cos(\Theta) \cos(\Phi) \dot{\Psi} + \frac{1}{2} I_{zzt} \cos^2(\Theta) \cos^2(\Phi) \dot{\Psi}^2 + \frac{1}{2} m l_{rcmcr}^2 \dot{\Psi}^2 \\ & \frac{1}{2} I_{xxr} \dot{\Phi}^2 - I_{xxr} \sin(\Theta) \dot{\Psi} \dot{\Phi} + \frac{1}{2} I_{xxr} \sin^2(\Theta) \dot{\Psi}^2 + \frac{1}{2} I_{xxr} \cos^2(\Phi) \dot{\Theta}^2 + \quad [2.32] \\ & I_{xxr} \cos(\Phi) \cos(\Theta) \sin(\Phi) \dot{\Psi} \dot{\Theta} + \frac{1}{2} I_{xxr} \cos^2(\Theta) \sin^2(\Phi) \dot{\Psi}^2 + \frac{1}{2} I_{zzr} \sin^2(\Phi) \dot{\Theta}^2 - \\ & I_{zzr} \cos(\Phi) \cos(\Theta) \sin(\Phi) \dot{\Psi} \dot{\Theta} - I_{zzr} \sin(\Phi) \dot{\Theta} \dot{\Phi} + \frac{1}{2} I_{zzr} \cos^2(\Theta) \cos^2(\Phi) \dot{\Psi}^2 + \end{aligned}$$

$$\begin{aligned}
& I_{zzr} \cos(\Theta) \cos(\Phi) \dot{\Psi} \dot{\beta} + \frac{1}{2} I_{zzr} \dot{\beta}^2 + \frac{1}{2} m_r (l_x)^2 \dot{\Phi}^2 - m_r (l_x)^2 \sin(\Theta) \dot{\Psi} \dot{\Phi} + \\
& \frac{1}{2} m_r (l_x)^2 \cos^2(\Phi) \dot{\Theta}^2 + \frac{1}{2} m_r (l_x)^2 \cos^2(\Theta) \sin^2(\Phi) \dot{\Psi}^2 + \\
& \frac{1}{2} m_r (l_x)^2 \sin^2(\Phi) \dot{\Theta}^2 + \frac{1}{2} m_r (l_x)^2 \cos^2(\Theta) \cos^2(\Phi) \dot{\Psi}^2 + \frac{1}{2} m_r l_{rcmcr}^2 \dot{\Phi}^2 + \\
& m_r (l_x) (l_x) \sin(\Phi) \sin(\Theta) \dot{\Theta} \dot{\Psi} + m_r (l_x) (l_x) \cos(\Theta) \cos(\Phi) \dot{\Psi} \dot{\Phi} - \\
& m_r (l_x) (l_x) \cos(\Theta) \cos(\Phi) \sin(\Theta) \dot{\Psi}^2 - m_r (l_x) (l_x) \sin(\Phi) \dot{\Theta} \dot{\Phi} + \\
& \frac{1}{2} m_r (l_x)^2 \sin^2(\Theta) \dot{\Psi}^2 + I_{xzt} \sin(\Phi) \sin(\Theta) \dot{\Psi} \dot{\Theta} + \frac{1}{2} I_{zzp} \cos^2(\Theta) \dot{\Psi}^2
\end{aligned}$$

2.3 Lagrange's Equation

Lagrange's equation is used to determine the equations of motion from the kinetic energy expression of Equation 2.32.

$$\frac{d}{dt} \left(\frac{dT}{dq_i} \right) - \frac{dT}{dq_i} = Q_i \quad [2.33]$$

where q_i is the i th generalized coordinate and Q_i is a generalized force. In this case four generalized coordinates are used, Φ , Θ , Ψ and β . The application of Equation 2.33 results in four equations of motion.

$$\frac{d}{dt} \left(\frac{dT}{d\dot{\beta}} \right) - \frac{dT}{d\beta} = F_\beta \quad [2.34]$$

$$\frac{d}{dt} \left(\frac{dT}{d\dot{\Psi}} \right) - \frac{dT}{d\Psi} = F_\Psi \quad [2.35]$$

$$\frac{d}{dt} \left(\frac{dT}{d\dot{\Theta}} \right) - \frac{dT}{d\Theta} = F_\Theta \quad [2.36]$$

$$\frac{d}{dt} \left(\frac{dT}{d\dot{\Phi}} \right) - \frac{dT}{d\Phi} = F_\Phi \quad [2.37]$$

Evaluation of these equations yields the full nonlinear equations of motion of the system.

2.4 Linearization of Equations of Motion

The kinematic equations which result from the evaluation of the left hand side of Lagrange's equation are linearized in two steps. First the following assumptions are made:

- Perturbations about operating point are small, i.e. $\Delta\Theta, \Delta\Psi, \Delta\Phi \leq 15^\circ \Rightarrow \sin(x) = x; \cos(x) = 1$.
- Products of small angular velocities are negligible, i.e. $\dot{\Theta}\dot{\Psi} \approx 0, \dot{\Phi}\dot{\Psi} \approx 0$, etc..
- Products of Inertia such as I_{xy} and I_{yz} are negligible.

The resulting equations of motion are

$$F_\Phi = I_a \ddot{\Phi} + I_{zxr} \dot{\beta}(\dot{\Theta} + \Phi\dot{\Psi}) + I_c \Theta \ddot{\Psi} \quad [2.38]$$

$$F_\Theta = I_b \ddot{\Theta} + I_c \Phi \ddot{\Psi} - I_{zxr} \dot{\beta}(\dot{\Phi} - \Theta\dot{\Psi}) - I_{zxr} \Phi \ddot{\beta} \quad [2.39]$$

$$F_\Psi = I_c \Phi \ddot{\Theta} + I_d \ddot{\Psi} + I_{zxr} \ddot{\beta} - I_{zxr} \dot{\beta}(\Theta\dot{\Theta} - \Phi\dot{\Phi}) \quad [2.40]$$

$$F_\beta = I_{zxr}(\ddot{\beta} - \Phi\ddot{\Theta} + \ddot{\Psi}) \quad [2.41]$$

where

$$I_a = (I_{xxr} + I_{xxt} + m_t l_{icmcr}^2 + mr(l_{rcmcr} - l_z)^2 + m_r l_z^2) \quad [2.42]$$

$$I_b = (I_{yyr} + I_{yyt} + I_{xxr} + m_r l_x^2)$$

$$I_c = (-I_{zxt} + I_{xxr} + I_{yyt} - I_{zxr})$$

$$I_d = (2I_{zxm} + I_{zxt} + I_{zxp} + I_{zxr} + m_r l_x^2)$$

$$I_e = m_r l_z^2 - I_{xxt} - I_{xxr}$$

2.4.1 Generalized Forces

A generalized force is not always a true force. If q_i is a translational displacement, then Q_i is a true force; however, if q_i is an angular displacement then Q_i is a torque. In this case all generalized forces are torques. To evaluate each generalized force, one imagines that one of the coordinates, q_i is increased by a small amount δq_i while all other coordinates which appear in the kinetic energy expression remain fixed. Next, an expression for the work, δW_{q_i} , done by all driving and dissipative forces is formulated. In general the work may be expressed as

$$\delta W_{q_i} = F_{q_i} \delta q_i \quad [2.43]$$

Equation 2.43 is then solved for the generalized force F_{q_i} . Work is taken positive or negative depending on whether the forces tend to increase or decrease q_i . The method described above is used to derive expressions for F_{Ψ} , F_{Θ} , F_{Φ} and F_{β} . First consider the forces acting in the Ψ direction. There is a lateral force exerted by the tilted rotor and some frictional forces in the bearing at the base of the mast opposing the rotor force. Equation 2.43 is used to determine the generalized force F_{Ψ} . One may write an expression for the total work done by the driving and dissipative forces through an incremental displacement $\delta\Psi$ as

$$\delta W_{\Psi} = F_{\Psi} \delta\Psi \quad [2.44]$$

or

$$\delta W_{\Psi} = (F_{\Psi_{rotor}} + F_{\Psi_{fric}}) \delta\Psi \quad [2.45]$$

The torque produced by the lateral thrust of the tilted rotor is given by

$$F_{\Psi_{rotor}} = F_R \sin \Phi \cos \Theta l_x \quad [2.46]$$

The mast bearing exerts three types of frictional torques, static, coulomb and viscous. The viscous bearing torque is modeled by Equation 2.47.

$$F_{\Psi_{F_{viscous}}} = -\mu \dot{\Psi} \quad [2.47]$$

The goal of this development is to derive a linear model of the system; therefore, static and coulomb friction are not considered since these phenomenon are highly nonlinear. The effects of such nonlinear phenomena are assessed in Chapter 3. The generalized force F_{Ψ} immediately follows from Equations 2.45, 2.46 and 2.47.

$$F_{\Psi} = F_R \sin \Phi \cos \Theta l_x - \mu \dot{\Psi} \quad [2.48]$$

where μ is the viscous friction coefficient of the yaw bearing.

Now consider the generalized force F_{Θ} . From Equation 2.43 one obtains

$$\delta W_{\Theta} = F_{\Theta} \delta\Theta \quad [2.49]$$

Note that F_{Θ} will be similar to F_{ψ} since similar driving and dissipative forces are at work. There exists a driving force exerted by the rotor which tends to increase Θ . This force is described by the following expression.

$$F_{\Theta} = F_R l_x \cos \Phi \quad [2.50]$$

There also exists static, coulomb and viscous frictional torques in the pipe bearing similar to those in the mast bearing. The viscous frictional torques are modeled by Equation 2.51.

$$F_{\Theta_{viscous}} = -\nu \dot{\Theta} \quad [2.51]$$

At the nominal flight condition the main rotor generates thrust to overcome gravitational effects. There is also a platform located approximately 1.5 rotor diameters below the main rotor level flight condition. The platform is perpendicular to the downwash of the main rotor. This configuration results in a ground effect phenomenon which causes the fuselage to behave as though there is a torsional spring located at the pivot point. In other words, for a given main rotor angular velocity, the thrust decreases with an increase in altitude (pitch angle) and increases with a decrease in altitude. A ground effect spring constant is defined such that

$$F_{\Theta_{GE}} = -k_{GE} \Theta. \quad [2.52]$$

The gravitational force on the center of mass of the entire system acting over a length $l_{cg} \hat{p}_x$ exerts a torque which tends to decrease Θ .

$$F_{\Theta_g} = -m g l_{cg} \cos \Theta \quad [2.53]$$

Equation 2.43 can now be written as

$$\delta W_{\Theta} = (F_R l_x \cos \Phi - \nu \dot{\Theta} - m g l_{cg} \cos \Theta - k_{GE} \Theta) \delta \Theta \quad [2.54]$$

It follows that

$$F_{\Theta} = F_R l_x \cos \Phi - \nu \dot{\Theta} - m g l_{cg} \cos \Theta - k_{GE} \Theta \quad [2.55]$$

The generalized forces F_{Φ} and F_{β} are evaluated using the results of the system identification experiments of Chapter 3. The identification experiments have shown that

the main rotor can be modeled by a second order differential equation in angular velocity when the pitch and yaw axes are restrained in their nominal positions.

$$\ddot{\beta} = -\tau_2 \dot{\beta} - \tau_1 \beta + \tau_1 \dot{\beta}_{com} \quad [2.56]$$

Identification experiments have also shown that a second order differential equation adequately describes the tilt servo or roll axis dynamics.

$$\ddot{\Phi} = -k_6 \dot{\Phi} - k_5 \Phi + k_5 \Phi_{com} \quad [2.57]$$

Substituting these relations into Equations 2.38 and 2.41 for the test conditions, one may obtain differential equations for the generalized forces (torques) F_β and F_Φ .

$$F_\beta = I_{zzr} \ddot{\beta} = I_{zzr} \frac{\tau_1 (\dot{\beta}_{com} - \dot{\beta}) - \ddot{\beta}}{\tau_2} \quad [2.58]$$

$$F_\Phi = I_a \ddot{\Phi} = I_a (-k_6 \dot{\Phi} - k_5 \Phi + k_5 \Phi_{com}) \quad [2.59]$$

The propeller force F_R and drag torque T_D are nonlinear functions of main rotor angular velocity which may be linearized about a nominal angular velocity to obtain

$$F_R \approx \frac{\partial F_R}{\partial \dot{\beta}} \dot{\beta} + k_2 \quad [2.60]$$

$$T_D \approx \frac{\partial T_D}{\partial \dot{\beta}} \dot{\beta} + k_4 \quad [2.61]$$

The experiments which determine the values of the gradients and constants of these equations are described in detail in Chapter 3.

Substituting the generalized force expressions into Equation 2.38, 2.39, 2.40 and 2.41 and applying the assumptions of Section 2.3 one obtains a set of nonlinear coupled differential equations

$$I_a (-k_6 \dot{\Phi} - k_5 \Phi + k_5 \Phi_{com}) = I_a \ddot{\Phi} + I_{zzr} \dot{\beta} (\dot{\Theta} + \Phi \dot{\Psi}) + I_c \Theta \ddot{\Psi} \quad [2.62]$$

$$\left[\frac{\partial F_R}{\partial \dot{\beta}} \dot{\beta} + k_2 \right] l_x - \nu \dot{\Theta} - mgl_{cg} - k_{GE} \Theta = I_b \ddot{\Theta} + I_c \Phi \ddot{\Psi} - I_{zzr} \dot{\beta} (\dot{\Phi} - \Theta \dot{\Psi}) - I_{zzr} \Phi \ddot{\beta} \quad [2.63]$$

$$\left[\frac{\partial F_R}{\partial \dot{\beta}} \dot{\beta} + k_2 \right] l_x \Phi - \mu \dot{\Psi} + \left[\frac{\partial T_D}{\partial \dot{\beta}} \dot{\beta} + k_4 \right] = I_c \Phi \ddot{\Theta} + I_d \ddot{\Psi} + I_{zzr} \dot{\beta} - I_{zzr} \dot{\beta} (\Theta \dot{\Theta} - \Phi \dot{\Phi}) \quad [2.64]$$

$$I_{zzr} \frac{\tau_1 (\dot{\beta}_{com} - \dot{\beta}) - \ddot{\beta}}{\tau_2} = I_{zzr} (\ddot{\beta} - \Phi \ddot{\Theta} + \ddot{\Psi}) \quad [2.65]$$

2.4.2 Linearization using Taylor Series

The second step of the linearization process is to solve Equations 2.62, 2.63, 2.64 and 2.65 for the highest order derivatives and approximate the resulting equations using the first two terms of a Taylor series expansion. Let $f(\mathbf{p}, t)$ be a column vector representing the highest order derivatives. The Taylor series expansion becomes

$$f(\mathbf{p}, t) = f(\bar{\mathbf{p}}, t) + \left(\frac{\partial f}{\partial \mathbf{p}} \right)_{\bar{\mathbf{p}}}^T (\mathbf{p} - \bar{\mathbf{p}}) + HOT \quad [2.66]$$

where $\mathbf{p} = [\mathbf{x}^T \mathbf{u}^T]$ is the augmented state and control vectors and $\bar{\mathbf{p}}$ contains the nominal values of \mathbf{p} . A state space realization follows directly from this step.

$$\dot{\mathbf{x}} = \mathbf{A}\mathbf{x} + \mathbf{B}\mathbf{u} \quad [2.67]$$

$$\mathbf{y} = \mathbf{C}\mathbf{x}$$

where

$$\mathbf{x} = [\dot{\Phi} \quad \dot{\Theta} \quad \dot{\Psi} \quad \ddot{\beta} \quad \dot{\beta} \quad \Phi \quad \Theta \quad \Psi]^T \quad [2.68]$$

$$\mathbf{u} = [\dot{\beta}_{com} \quad \Phi_{com}]^T \quad [2.69]$$

and

$$\bar{\mathbf{x}} = [0 \quad 0 \quad 0 \quad 0 \quad -300 \text{ rad/sec} \quad 0 \quad 0 \quad 0]^T \quad [2.70]$$

$$\bar{\mathbf{u}} = [-300 \text{ rad/sec} \quad 0]^T \quad [2.71]$$

$$\mathbf{A} = \begin{bmatrix} \frac{\partial \dot{\Phi}}{\partial \dot{\Phi}} & \frac{\partial \dot{\Phi}}{\partial \dot{\Theta}} & \frac{\partial \dot{\Phi}}{\partial \dot{\Psi}} & \frac{\partial \dot{\Phi}}{\partial \ddot{\beta}} & \frac{\partial \dot{\Phi}}{\partial \dot{\beta}} & \frac{\partial \dot{\Phi}}{\partial \Phi} & \frac{\partial \dot{\Phi}}{\partial \Theta} & \frac{\partial \dot{\Phi}}{\partial \Psi} \\ \frac{\partial \dot{\Theta}}{\partial \dot{\Phi}} & \frac{\partial \dot{\Theta}}{\partial \dot{\Theta}} & \frac{\partial \dot{\Theta}}{\partial \dot{\Psi}} & \frac{\partial \dot{\Theta}}{\partial \ddot{\beta}} & \frac{\partial \dot{\Theta}}{\partial \dot{\beta}} & \frac{\partial \dot{\Theta}}{\partial \Phi} & \frac{\partial \dot{\Theta}}{\partial \Theta} & \frac{\partial \dot{\Theta}}{\partial \Psi} \\ \frac{\partial \dot{\Psi}}{\partial \dot{\Phi}} & \frac{\partial \dot{\Psi}}{\partial \dot{\Theta}} & \frac{\partial \dot{\Psi}}{\partial \dot{\Psi}} & \frac{\partial \dot{\Psi}}{\partial \ddot{\beta}} & \frac{\partial \dot{\Psi}}{\partial \dot{\beta}} & \frac{\partial \dot{\Psi}}{\partial \Phi} & \frac{\partial \dot{\Psi}}{\partial \Theta} & \frac{\partial \dot{\Psi}}{\partial \Psi} \\ \frac{\partial \ddot{\beta}}{\partial \dot{\Phi}} & \frac{\partial \ddot{\beta}}{\partial \dot{\Theta}} & \frac{\partial \ddot{\beta}}{\partial \dot{\Psi}} & \frac{\partial \ddot{\beta}}{\partial \ddot{\beta}} & \frac{\partial \ddot{\beta}}{\partial \dot{\beta}} & \frac{\partial \ddot{\beta}}{\partial \Phi} & \frac{\partial \ddot{\beta}}{\partial \Theta} & \frac{\partial \ddot{\beta}}{\partial \Psi} \\ 0 & 0 & 0 & 0 & 1 & 0 & 0 & 0 \\ 1 & 0 & 0 & 0 & 0 & 0 & 0 & 0 \\ 0 & 1 & 0 & 0 & 0 & 0 & 0 & 0 \\ 0 & 0 & 1 & 0 & 0 & 0 & 0 & 0 \end{bmatrix} \quad [2.72]$$

$$\mathbf{B}^T = \begin{bmatrix} \frac{\partial \bar{\Phi}}{\partial \beta_{com}} & \frac{\partial \bar{\Theta}}{\partial \beta_{com}} & \frac{\partial \bar{\Psi}}{\partial \beta_{com}} & \frac{\partial \beta}{\partial \beta_{com}} & 0 & 0 & 0 & 0 \\ \frac{\partial \bar{\Phi}}{\partial \Phi_{com}} & \frac{\partial \bar{\Theta}}{\partial \Phi_{com}} & \frac{\partial \bar{\Psi}}{\partial \Phi_{com}} & \frac{\partial \beta}{\partial \Phi_{com}} & 0 & 0 & 0 & 0 \end{bmatrix} \quad [2.73]$$

The non-zero elements of the state space model are given below:

$$\frac{\partial \bar{\Phi}}{\partial \Phi} = -k_6 \quad [2.74]$$

$$\frac{\partial \bar{\Phi}}{\partial \Theta} = \frac{-I_{zrz} \bar{\beta}}{I_a} \quad [2.75]$$

$$\frac{\partial \bar{\Phi}}{\partial \Phi} = -k_5 \quad [2.76]$$

$$\frac{\partial \bar{\Phi}}{\partial \Theta} = -\frac{I_c \left[\frac{\partial T_D}{\partial \beta} \bar{\beta} + k_4 \right]}{I_a I_d} \quad [2.77]$$

$$\frac{\partial \bar{\Phi}}{\partial \Phi_{com}} = k_5 \quad [2.78]$$

$$\frac{\partial \bar{\Theta}}{\partial \bar{\Phi}} = \frac{I_{zrz} \bar{\beta}}{I_b} \quad [2.79]$$

$$\frac{\partial \bar{\Theta}}{\partial \Theta} = \frac{-\nu}{I_b} \quad [2.80]$$

$$\frac{\partial \bar{\Theta}}{\partial \beta} = \frac{\frac{\partial F_R}{\partial \beta} I_z}{I_b} \quad [2.81]$$

$$\frac{\partial \bar{\Theta}}{\partial \Phi} = -\frac{\left[\frac{\partial T_D}{\partial \beta} \bar{\beta} + k_4 \right] (I_d + I_c)}{I_b I_d} \quad [2.82]$$

$$\frac{\partial \bar{\Theta}}{\partial \Theta} = -\frac{k_{GE}}{I_b} \quad [2.83]$$

$$\frac{\partial \bar{\Psi}}{\partial \bar{\Psi}} = -\frac{\mu}{I_d} \quad [2.84]$$

$$\frac{\partial \ddot{\Psi}}{\partial \dot{\beta}} = \frac{\partial T_D}{\partial \dot{\beta}} \quad [2.85]$$

$$\frac{\partial \ddot{\Psi}}{\partial \Phi} = \frac{-I_c \left[l_x \left(\frac{\partial F_B}{\partial \dot{\beta}} \ddot{\beta} + k_2 \right) - m g l_{cg} \right] + I_b l_x \left(\frac{\partial F_B}{\partial \dot{\beta}} \ddot{\beta} + k_2 \right)}{I_b I_d} \quad [2.86]$$

$$\frac{\partial \ddot{\Phi}}{\partial \dot{\beta}} = -\frac{I_{zsr}}{I_d} \quad [2.87]$$

$$\frac{\partial \ddot{\beta}}{\partial \dot{\Psi}} = \frac{\tau_2 \mu}{I_d} \quad [2.88]$$

$$\frac{\partial \ddot{\beta}}{\partial \dot{\beta}} = -\frac{\tau_2 \frac{\partial T_D}{\partial \dot{\beta}} + \tau_1 I_d}{I_d} \quad [2.89]$$

$$\frac{\partial \ddot{\beta}}{\partial \Phi} = -\tau_2 \frac{\left[\frac{\partial F_B}{\partial \dot{\beta}} \ddot{\beta} + k_2 \right] (I_b - I_c - I_d) l_x + (I_c + I_d) m g l_{cg}}{I_d I_b} \quad [2.90]$$

$$\frac{\partial \ddot{\beta}}{\partial \dot{\beta}} = \frac{\tau_2 (-I_d + I_{zsr})}{I_d} \quad [2.91]$$

$$\frac{\partial \ddot{\beta}}{\partial \dot{\beta}_{com}} = \tau_1 \quad [2.92]$$

2.5 Newtonian Equations of Motion

A simplified Newtonian approach is used to derive the TROFM equations of motion to verify the Lagrangian results. The analysis assumed that pitch and yaw axes are uncoupled. This assumption is valid for small deviations, $\Delta\Theta \leq 15^\circ$, $\Delta\Psi \leq 15^\circ$ about the operating point, $\bar{\Theta} = \bar{\Psi} = 0$.

The following torques and forces acted on the system: rotor thrust, rotor drag torque, viscous friction, ground effect, gyroscopic couples, and gravitational force. Nonlinear friction is not considered here.

Figure 2.6 shows a free body diagram of the pitch axis. Applying Newton's law

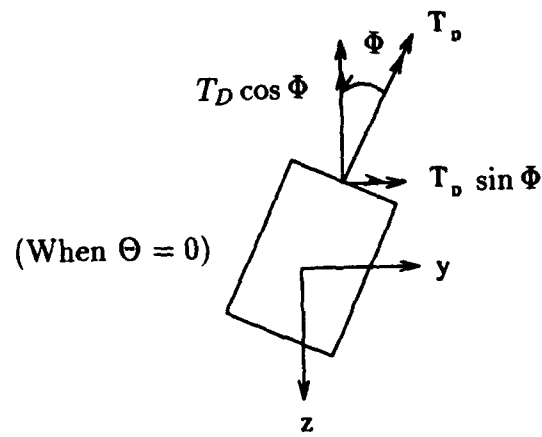
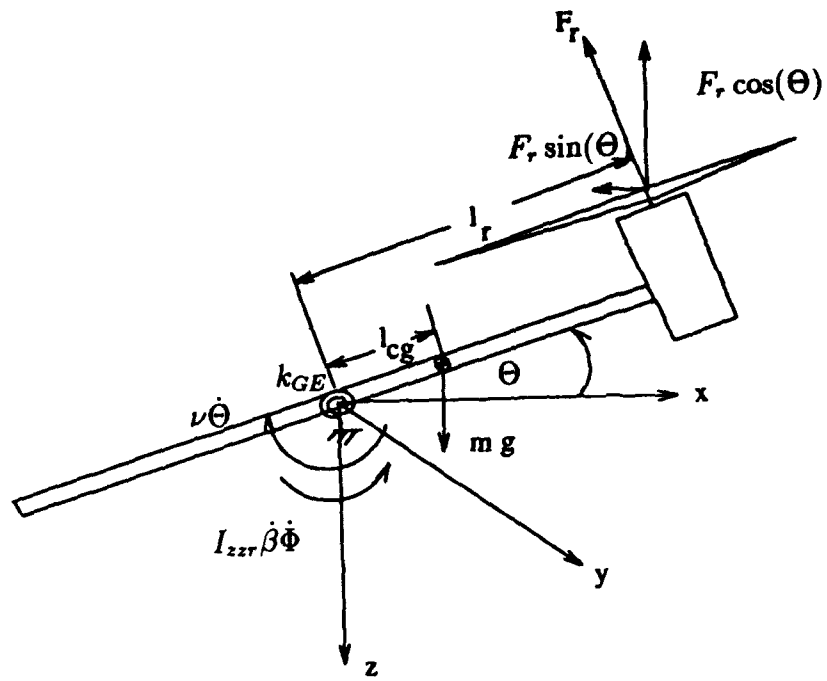


Figure 2.6 Free body diagram of the pitch axis.

to the pitch axis one obtains

$$I_{yy}\ddot{\Theta} = F_R l_r \cos \Phi - m g l_{cg} \cos \Theta - \nu \dot{\Theta} - k_{GE} \Theta - T_D \sin \Phi + I_{zzr} \dot{\beta} \dot{\Phi} \quad [2.93]$$

Where F_R and T_D are experimentally determined to be linear functions of the main rotor angular velocity about the operating point $\bar{\beta}$ in Section 3.3.3.

$$F_R = \left[\frac{\partial F_R}{\partial \beta} \dot{\beta} + k_2 \right] \quad [2.94]$$

$$T_D = \left[\frac{\partial T_D}{\partial \beta} \dot{\beta} + k_4 \right] \quad [2.95]$$

Substituting Equations 2.94 and 2.95 into 2.93 and solving for $\ddot{\Theta}$ one obtains

$$\ddot{\Theta} = -\frac{(\frac{\partial T_D}{\partial \beta} \dot{\beta} + k_4)}{I_{yy}} \sin \Phi + \frac{(\frac{\partial F_R}{\partial \beta} \dot{\beta} + k_2) l_r}{I_{yy}} \cos \Phi - \frac{m g l_{cg}}{I_{yy}} \cos \Theta - \frac{\nu \dot{\Theta}}{I_{yy}} - \frac{k_{GE} \Theta}{I_{yy}} + \frac{I_{zzr} \dot{\beta} \dot{\Phi}}{I_{yy}} \quad [2.96]$$

Since Φ and Θ are assumed to be small ($\leq 15^\circ$), one may write

$$\ddot{\Theta} \approx -\frac{\frac{\partial T_D}{\partial \beta} \dot{\beta} + k_4}{I_{yy}} \Phi + \frac{(\frac{\partial F_R}{\partial \beta} \dot{\beta} + k_2) l_r}{I_{yy}} - \frac{m g l_{cg}}{I_{yy}} - \frac{\nu \dot{\Theta}}{I_{yy}} - \frac{k_{GE} \Theta}{I_{yy}} + \frac{I_{zzr} \dot{\beta} \dot{\Phi}}{I_{yy}} \quad [2.97]$$

Figure 2.7 shows a free body diagram of the yaw axis. Applying Newton's laws, one may write

$$I_{zz} \ddot{\Psi} = F_R l_r \sin \Phi \cos \Theta + T_D \cos \Phi - \mu \dot{\Psi} - I_{zzr} \dot{\beta} \cos \Phi \quad [2.98]$$

Solving for $\ddot{\Psi}$ and assuming Φ , Θ and $\Psi \leq 15^\circ$ one obtains

$$\ddot{\Psi} \approx \frac{\frac{\partial F_R}{\partial \beta} \dot{\beta} + k_2}{I_{zz}} l_r \Phi + \frac{\frac{\partial T_D}{\partial \beta} \dot{\beta} + k_4}{I_{zz}} - \frac{I_{zzr} \dot{\beta}}{I_{zz}} - \frac{\mu \dot{\Psi}}{I_{zz}} \quad [2.99]$$

Figure 2.8 shows a free body diagram of the roll axis. Applying Newton's laws and the results of the tilt servo identification of Chapter 3 one may write

$$I_{xxt} \ddot{\Phi} = -I_{zzr} \dot{\beta} (\dot{\Theta} + \Phi \dot{\Psi}) + I_{xxt} \Theta \ddot{\Psi} + I_{xxt} (-k_6 \dot{\Phi} - k_5 \Phi + k_5 \Phi_{com}) \quad [2.100]$$

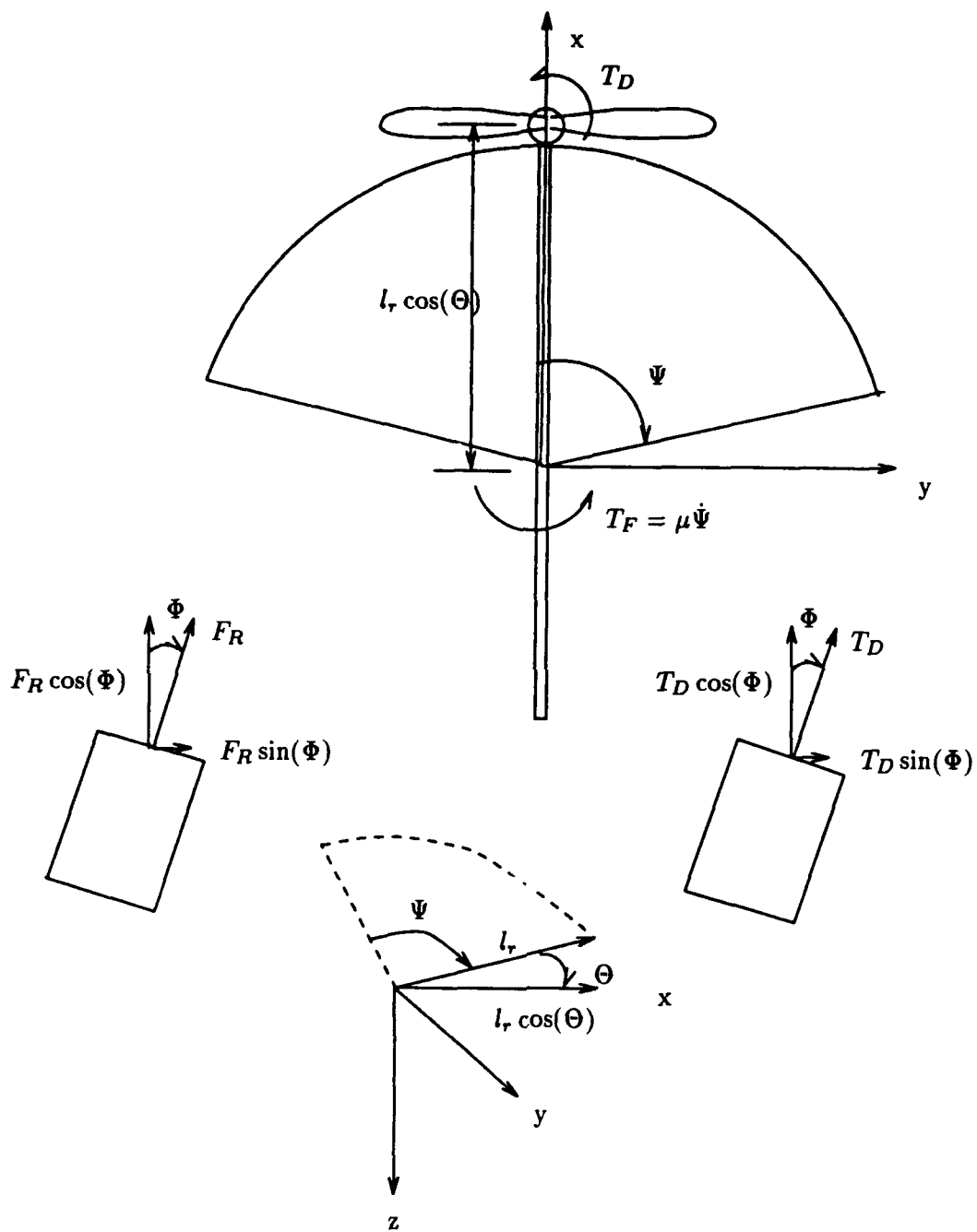


Figure 2.7 Free body diagram of the yaw axis.

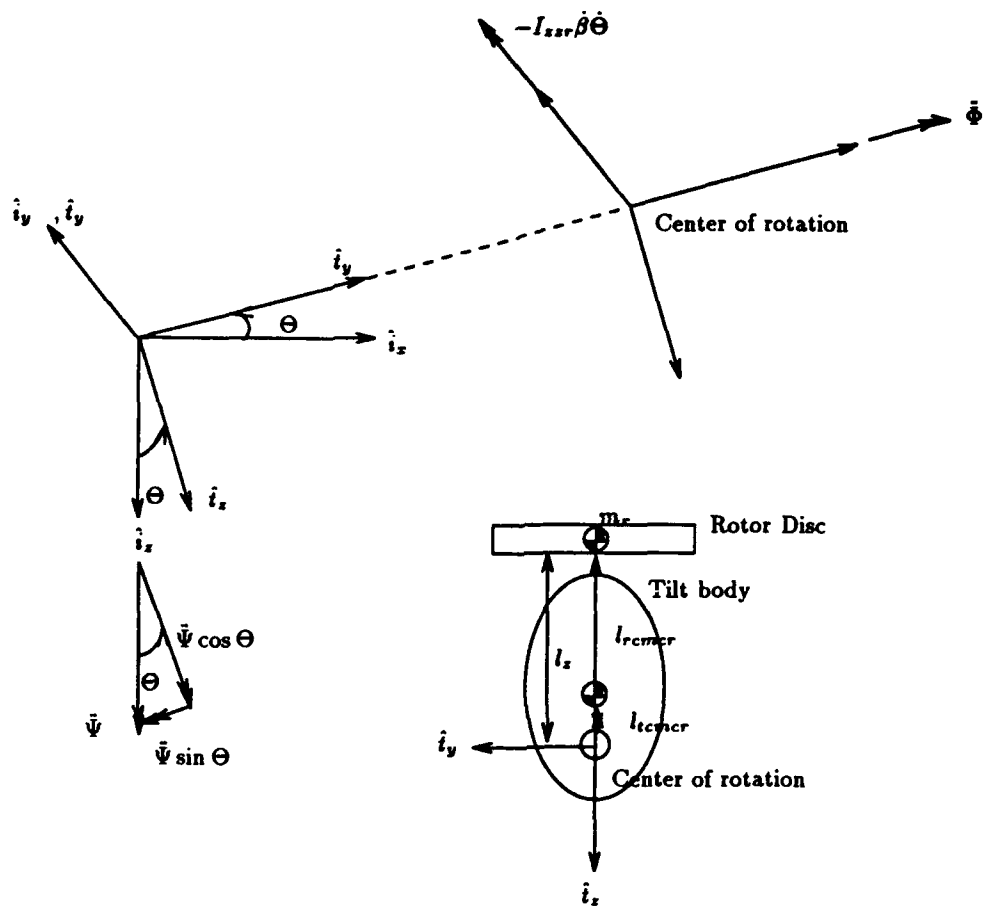


Figure 2.8 Free body diagram of the roll (tilt) axis.

Solving for $\ddot{\Phi}$ one obtains

$$\ddot{\Phi} = \Theta \ddot{\Psi} + (-k_6 \dot{\Phi} - k_5 \Phi + k_5 \Phi_{com}) - \frac{I_{zzr}}{I_{xxt}} \dot{\beta} (\dot{\Theta} + \Phi \dot{\Psi}) \quad [2.101]$$

Figure 2.9 shows a free body diagram of the main rotor and motor armature. Applying Newton's law and using the results of the main motor identification of Chapter 3 one may write

$$I_{zzr} (\ddot{\beta} + \ddot{\Psi} - \Phi \ddot{\Theta}) = \frac{I_{zzr}}{\tau_2} (\tau_1 (\dot{\beta}_{com} - \dot{\beta}) - \ddot{\beta}) \quad [2.102]$$

Equations 2.97, 2.99, 2.101 and 2.102 are solved simultaneously for the highest order derivatives. Substituting the expressions for the highest order derivatives into Equation 2.66 and evaluating the first two terms of the Taylor series, one obtains a linear approximation of the system which may be written in the state space form of Equation 2.67. The non-zero elements of the state space matrix are given below:

$$\frac{\partial \ddot{\Phi}}{\partial \Phi_{com}} = k_5 \quad [2.103]$$

$$\frac{\partial \ddot{\Phi}}{\partial \dot{\Phi}} = -k_6 \quad [2.104]$$

$$\frac{\partial \ddot{\Phi}}{\partial \Phi} = -k_5 \quad [2.105]$$

$$\frac{\partial \ddot{\Phi}}{\partial \dot{\Theta}} = \frac{-I_{zzr} \dot{\beta}}{I_{xxt}} \quad [2.106]$$

$$\frac{\partial \ddot{\Theta}}{\partial \dot{\Phi}} = \frac{I_{zzr} \dot{\beta}}{I_{yy}} \quad [2.107]$$

$$\frac{\partial \ddot{\Theta}}{\partial \Phi} = -\frac{\frac{\partial T_D}{\partial \beta} \dot{\beta} + k_4}{I_{yy}} \quad [2.108]$$

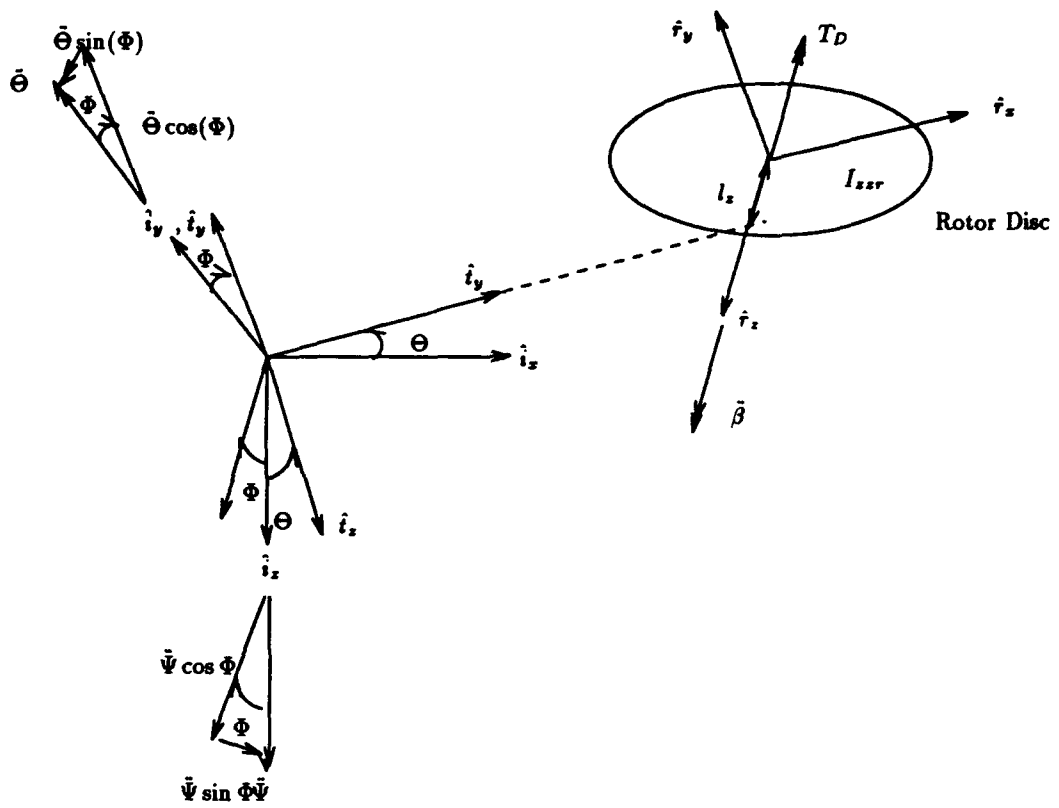


Figure 2.9 Free body diagram of the main rotor and motor armature.

$$\frac{\partial \ddot{\theta}}{\partial \dot{\beta}} = \frac{\frac{\partial F_R}{\partial \dot{\beta}} \dot{\beta} l_r}{I_{yy}} \quad [2.109]$$

$$\frac{\partial \ddot{\theta}}{\partial \dot{\theta}} = \frac{-\nu}{I_{yy}} \quad [2.110]$$

$$\frac{\partial \ddot{\theta}}{\partial \dot{\theta}} = \frac{-k_{GE}}{I_{yy}} \quad [2.111]$$

$$\frac{\partial \ddot{\psi}}{\partial \dot{\beta}} = \frac{\frac{\partial T_D}{\partial \dot{\beta}}}{I_{zz}} \quad [2.112]$$

$$\frac{\partial \ddot{\psi}}{\partial \dot{\Phi}} = \frac{\left[\frac{\partial F_R}{\partial \dot{\beta}} \dot{\beta} + k_2 \right] l_r}{I_{zz}} \quad [2.113]$$

$$\frac{\partial \ddot{\psi}}{\partial \dot{\psi}} = \frac{-\mu}{I_{zz}} \quad [2.114]$$

$$\frac{\partial \ddot{\psi}}{\partial \dot{\beta}} = \frac{-I_{zzr}}{I_{zz}} \quad [2.115]$$

$$\frac{\partial \ddot{\beta}}{\partial \dot{\psi}} = \frac{\tau_2 \mu}{I_{zz}} \quad [2.116]$$

$$\frac{\partial \ddot{\beta}}{\partial \dot{\beta}} = -\frac{\tau_2 \frac{\partial T_D}{\partial \dot{\beta}} + \tau_1}{I_{zz}} \quad [2.117]$$

$$\frac{\partial \ddot{\beta}}{\partial \dot{\Phi}} = \frac{(I_{yy} - I_{zz}) l_r \left[\frac{\partial F_R}{\partial \dot{\beta}} \dot{\beta} + k_2 \right] + I_{zz} m g l_{cg}}{I_{zz} I_{yy}} \quad [2.118]$$

$$\frac{\partial \ddot{\beta}}{\partial \dot{\beta}} = \frac{\tau_2 (I_{zzr} - I_{zz})}{I_{zz}} \quad [2.119]$$

$$\frac{\partial \ddot{\beta}}{\partial \dot{\beta}_{com}} = \tau_1 \quad [2.120]$$

2.6 Comparison of Linear Lagrangian and Newtonian Models

Table 3.1 contains the numerical values of the physical parameters needed to compute the elements of the state space matrices. Substituting these values into the results obtained in Sections 2.4 and 2.5 one obtains the theoretical A and B state space matrices.

$$A_{Lagrange} = \begin{bmatrix} -14.18 & 52.63 & 0 & 0 & 0 & -153.42 & 1.5136 & 0 \\ -0.6383 & -1.062 & 0 & 0 & -0.07066 & -2.138 & -2.722 & 0 \\ 0 & 0 & -0.7153 & -0.00202 & -0.01465 & 7.162 & 0 & 0 \\ 0 & 0 & 160.627 & -17.63 & -654.94 & -168.54 & 0 & 0 \\ 0 & 0 & 0 & 1 & 0 & 0 & 0 & 0 \\ 1 & 0 & 0 & 0 & 0 & 0 & 0 & 0 \\ 0 & 1 & 0 & 0 & 0 & 0 & 0 & 0 \\ 0 & 0 & 1 & 0 & 0 & 0 & 0 & 0 \end{bmatrix} \quad [2.121]$$

$$B_{Lagrange} = \begin{bmatrix} 0 & 0 & 0 & 655.2 & 0 & 0 & 0 & 0 \\ 153.2 & 0 & 0 & 0 & 0 & 0 & 0 & 0 \end{bmatrix}^T \quad [2.122]$$

$$A_{Newton} = \begin{bmatrix} -14.18 & 52.67 & 0 & 0 & 0 & -153.42 & 2.032 & 0 \\ -0.6383 & -1.062 & 0 & 0 & -0.07066 & -2.143 & -2.722 & 0 \\ 0 & 0 & -0.7153 & -0.00202 & -0.01465 & 7.168 & 0 & 0 \\ 0 & 0 & 160.627 & -17.63 & -654.94 & -168.64 & 0 & 0 \\ 0 & 0 & 0 & 1 & 0 & 0 & 0 & 0 \\ 1 & 0 & 0 & 0 & 0 & 0 & 0 & 0 \\ 0 & 1 & 0 & 0 & 0 & 0 & 0 & 0 \\ 0 & 0 & 1 & 0 & 0 & 0 & 0 & 0 \end{bmatrix} \quad [2.123]$$

$$B_{Newton} = \begin{bmatrix} 0 & 0 & 0 & 655.2 & 0 & 0 & 0 & 0 \\ 153.2 & 0 & 0 & 0 & 0 & 0 & 0 & 0 \end{bmatrix}^T \quad [2.124]$$

One can see that the two methods of analysis generate nearly identical linear models with the exception of the A_{17} term.

3. SYSTEM IDENTIFICATION

3.1 System Identification Methods

Accurate knowledge of the physical parameters which comprise the elements of the state space model of Chapter 2 is essential to the development of linear control systems. Numerical values of most physical parameters could not be obtained analytically; therefore, experimental procedures are used to obtain estimates of the parameters. Parametric (maximum likelihood) and non-parametric (frequency response) system identification methods are used to obtain those estimates.

3.1.1 Continuous Frequency Response

The frequency response of a system is defined as the steady state response of a system to a sinusoidal input signal. For BIBO (bounded input bounded output) stable linear systems, the output signal will be sinusoidal in steady state but different from the input in amplitude and phase. The frequency response function describing the sinusoidal steady state can be obtained by replacing s with $j\omega$ in the system transfer function $T(s)$.

$$T(s)|_{j\omega} = T(j\omega) \quad [3.1]$$

Recall the definition of the Laplace transform of a continuous signal $f(t)$, where $f(t)$ is defined for $t \geq 0$;

$$\mathcal{L}\{f(t)\} = F(s) = \int_0^{\infty} f(t)e^{-st} dt \quad [3.2]$$

thus;

$$F(s)|_{j\omega} = F(j\omega) = \mathcal{F}\{f(t)\} = \int_0^{\infty} f(t)e^{-j\omega t} dt \quad [3.3]$$

which is defined as the Fourier transform of $f(t)$. Consider an input signal whose Fourier transform is

$$I(j\omega) = \int_0^{\infty} i(t)e^{-j\omega T} dt \quad [3.4]$$

Applying the input signal to a linear system $T(j\omega)$, the output signal is given by

$$O(j\omega) = T(j\omega)I(j\omega). \quad [3.5]$$

it follows that

$$T(j\omega) = \frac{O(j\omega)}{I(j\omega)} \quad [3.6]$$

One may now deduce a method to experimentally determine the transfer function $T(s)$ of a linear system,

- Observe the input-output time histories;
- Evaluate the ratio of the output and input Fourier Transforms;
- Plot the magnitude and phase characteristics and determine the pole-zero locations of $T(s)$ using Bode analysis.

3.1.2 Method of One Frequency at a Time (Continuous)

One method of experimentally determining a transfer function is as follows: apply a sinusoidal input of amplitude A and frequency ω to the system of interest;

$$i(t) = A \sin \omega t \quad [3.7]$$

wait until the transients have died out and observe the steady state system response on an oscilloscope to determine the magnitude and phase of the output.

$$o(t) = B \sin(\omega t + \phi) \quad [3.8]$$

Evaluating the ratio of the output to input one can deduce the frequency response function of the system for the test frequency ω .

$$T(j\omega) = \frac{B}{A} e^{j\phi} \quad [3.9]$$

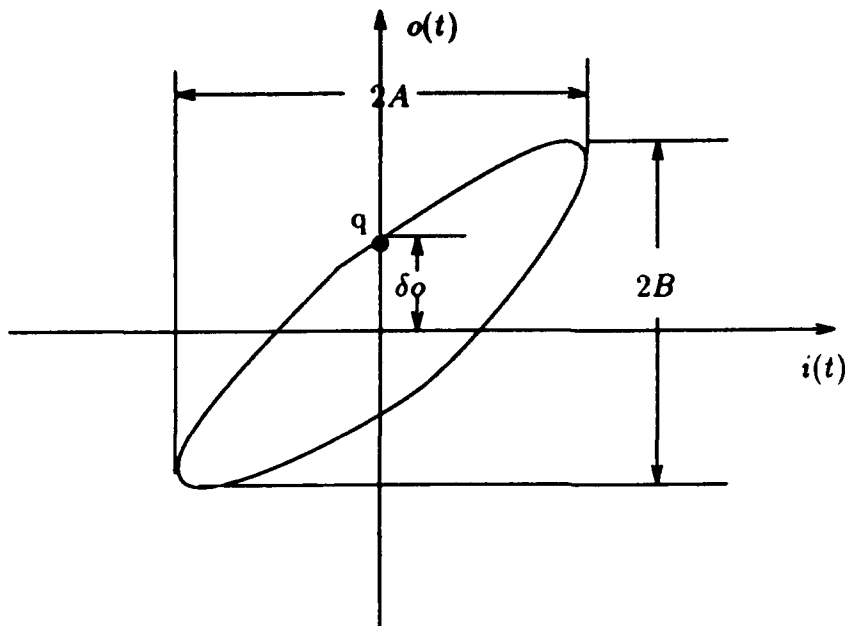


Figure 3.1 Determining amplitude ratio and phase angle from an X-Y plot of output sinusoid versus input sinusoid.

The amplitude ratio B/A and the phase angle ϕ may be determined by plotting $o(t)$ versus $i(t)$ using the X-Y mode of an oscilloscope. The equation of the output sinusoid may be written

$$o(t) = B \sin(\omega t) \cos(\phi) + B \cos(\omega t) \sin(\phi) \quad [3.10]$$

Note that when $i(t) = 0$, $\sin(\omega t) = 0$; thus, $\cos(\omega t) = \pm 1$ and $\delta o = o(t)|_{i(t)=0} = B \sin(\phi)$. The phase angle may then be computed from Equation 3.11.

$$\phi = \pm \arcsin \frac{\delta o}{B} \quad [3.11]$$

Figure 3.1 shows how these parameters are obtained from the oscilloscope display. The sign of ϕ may be determined by noting that when $i(t)$ goes through zero (point q) from negative to positive then $\cos(\omega t) = +1$ [17]. This means that if the curve advances clockwise in time, the sign of ϕ is positive (phase lead). Similarly if the curve advances counter-clockwise in time the sign of ϕ is negative (phase lag). The major disadvantage of this method of continuous time frequency response system identification lies its inability to evaluate the frequency response function for more

than one frequency at a time. This makes the continuous time method slow and tedious.

3.1.3 Discrete Frequency Response

Digital computers specially equipped for real time data acquisition are well suited to experimentally determine the frequency response function of a sampled data system. Since digital computers cannot evaluate a continuous time Fourier transform, one must define a Discrete Fourier Transform (DFT) which can be calculated from a finite record of sampled data.

Recall the definition of a z -transform of a discrete sequence of sampled data $f(kT)$ where $k \in 0, 1, 2 \dots \infty$ and T is the sampling period.

$$\mathcal{Z}\{f(k)\} \equiv F(z) \equiv \sum_{k=0}^{\infty} f_k z^{-k} \quad [3.12]$$

It can be shown that the relationship between the s and z domain is given by

$$z = e^{sT} \quad [3.13]$$

Thus, the frequency response of a discrete system with transfer function $T(z) = O(z)/I(z)$ can be obtained by

$$T(e^{j\omega T}) = \frac{O(e^{j\omega T})}{I(e^{j\omega T})} \quad [3.14]$$

If the sequence f_k is periodic, i.e. $f(kT) = f(kT + NT)$ then the Discrete Fourier Transform can be defined as the finite sum

$$\sum_{k=0}^{N-1} f_k e^{-\frac{j2\pi nkT}{NT}} \equiv DFT(f_k) \quad [3.15]$$

or

$$DFT(f_k) \equiv F_n \equiv \sum_{k=0}^{N-1} f_k e^{-\frac{j2\pi nk}{N}} \quad [3.16]$$

The DFT has the following properties:

- It is discrete in frequency since it is defined only at $\omega_n = (2\pi n)/(NT)$
- It is periodic in frequency since

$$e^{\frac{-j2\pi nk}{N}} = e^{\frac{-j2\pi nk}{N} + 2\pi l} \quad [3.17]$$

which follows from Euler's formula

$$e^{j\theta} = \cos(\theta) + j \sin(\theta) = \cos(\theta + 2\pi l) + j \sin(\theta + 2\pi l) \quad [3.18]$$

where l is an integer.

3.1.4 Method of One Frequency at a Time (Discrete)

One method of evaluating the frequency response of a sampled data system is analogous to the continuous time method of one frequency at a time. Apply a discrete time sinusoid with zero order hold to the system to be identified.

$$i(kT) = A \sin(\omega_n kT) \quad [3.19]$$

Record the steady state response of the system in discrete time using a data acquisition system.

$$o(kT) = B \sin(\omega_n kT + \phi) \quad [3.20]$$

Evaluate the discrete frequency response function $T(e^{j\omega_n T})$ of the test system using the following facts:

$$B/A = |T(e^{j\omega_n T})|, \quad [3.21]$$

$$\phi_n = \arg(T(e^{-j\omega_n T}))$$

The amplitude ratio and phase angle may be determined by plotting $o(kT)$ versus $i(kT)$ on the computer display and using the technique described in Section 3.1.2. The accuracy of the estimated transfer function is affected by: the number of samples (N), noise, transients and nonlinearities in the test system. The solution to these problems is to compute the best fit sinusoid to the output by estimating B and ϕ_n which best fit $o(kT)$ [4]. Define the estimate of the output:

$$\hat{o}(kT) = B \sin(\omega_n kT + \phi_n) \quad [3.22]$$

$$= B \sin(\phi_n) \cos(\omega_n kT) + \quad [3.23]$$

$$\begin{aligned}
& B \cos(\phi_n) \sin(\omega_n kT) \\
& = B_c \cos(\omega_n kT) + B_s \sin(\omega_n kT)
\end{aligned}$$

Form a quadratic cost function:

$$\mathcal{J} = \frac{1}{N} \sum_{k=0}^{N-1} (o(kT) - \hat{o}(kT))^2 \quad [3.24]$$

$$\begin{aligned}
& = \frac{1}{N} \sum_{k=0}^{N-1} (o(kT) - B_c \cos(\omega_n kT) - \\
& \quad B_s \sin(\omega_n kT))^2
\end{aligned} \quad [3.25]$$

Find B_c and B_s such that \mathcal{J} is minimized,

$$\begin{aligned}
\frac{\partial \mathcal{J}}{\partial B_c} & = \frac{1}{N} \sum_{k=0}^{N-1} 2(o(kT) - B_c \cos(\omega_n kT) - \\
& \quad B_s \sin(\omega_n kT))(-\cos(\omega_n kT)) = 0
\end{aligned} \quad [3.26]$$

$$\begin{aligned}
\frac{\partial \mathcal{J}}{\partial B_s} & = \frac{1}{N} \sum_{k=0}^{N-1} 2(o(kT) - B_c \cos(\omega_n kT) - \\
& \quad B_s \sin(\omega_n kT))(-\sin(\omega_n kT)) = 0
\end{aligned} \quad [3.27]$$

For $\omega_n = 2\pi n/N$

$$B_c = \frac{2}{N} \sum_{k=0}^{N-1} o(kT) \cos(2\pi nk/N) \quad [3.28]$$

$$B_s = \frac{2}{N} \sum_{k=0}^{N-1} o(kT) \sin(2\pi nk/N) \quad [3.29]$$

It follows that;

$$B_c - jB_s = \frac{2}{N} \sum_{k=0}^{N-1} o(kT) e^{-j2\pi kn/N} \quad [3.30]$$

$$= \frac{2}{N} DFT(o(kT)) \quad [3.31]$$

thus,

$$DFT(o(kT)) = \frac{N}{2} [B_c - jB_s] \quad [3.32]$$

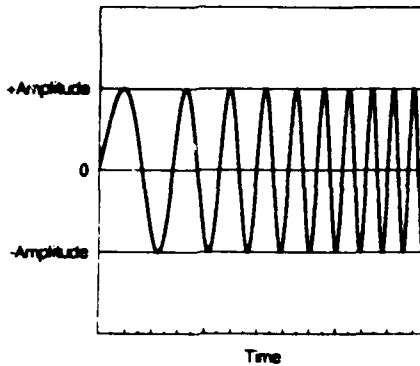


Figure 3.2 Typical chirp waveform

Therefore the transfer function is given by

$$T(e^{j\omega_n T}) = \frac{DFT(o(kT))}{DFT(i(kT))} \quad [3.33]$$

One may conclude that the DFT automatically computes the best fit sinusoid to the output in a least squares sense.

3.1.5 Frequency Sweep Method

An alternative to the method of one frequency at a time is to apply a sinusoidal input whose frequency varies from low to high over the range of interest. Such a signal is called a chirp. Figure 3.2 shows a typical chirp waveform. The equation of a discrete time chirp is given below:

$$i(kT) = A_o + A \sin(\omega_k kT) \quad [3.34]$$

where

$$\omega_k = \omega_{start} + \frac{k}{N}(\omega_{end} - \omega_{start}) \quad [3.35]$$

The frequency sweep system identification method is outlined below.

- Determine frequency range of interest.

- Select sampling rate such that $1/T \geq (10\omega_{end})/(2\pi)$. This follows from Shannon's sampling theorem.
- Choose nominal operating point A_o .
- Apply the chirp input to the system $T(z)$ and observe the output.
- Compute the DFT of the input and output sequences using Equation 3.16.
- Plot magnitude and phase of

$$T(e^{j\omega_n T}) = \frac{DFT(o(kT))}{DFT(i(kT))} \quad [3.36]$$

versus

$$\omega_n = \frac{2\pi n}{NT}. \quad [3.37]$$

- Estimate the pole-zero locations of the continuous time transfer function using Bode analysis.

3.1.6 Maximum Likelihood Parameter Estimation

Consider a system of linear dynamic equations:

$$\mathbf{x}(0) = \mathbf{x}_0 \quad [3.38]$$

$$\dot{\mathbf{x}}(t) = \mathbf{A}\mathbf{x}(t) + \mathbf{B}u(t) + \mathbf{n}(t) \quad [3.39]$$

$$\mathbf{z}(t_i) = \mathbf{C}\mathbf{x}(t_i) + \mathbf{D}u(t_i) + \eta(t_i) \quad [3.40]$$

Equation 3.39 is a continuous-time differential equation and Equation 3.40 is defined only at the instants t_i . This is representative of a dynamic system with data sampled by a digital computer. The measurement noise η is assumed to be a sequence of independent, zero mean, diagonal covariance Gaussian vectors. The $\mathbf{A}, \mathbf{B}, \mathbf{C}, \mathbf{D}$ matrices are functions of a vector of unknown parameters ξ . An estimate of the true value of ξ based on the measured response $\mathbf{z}(\cdot)$ to an input $u(\cdot)$ is computed using an implementation of a maximum likelihood estimation program MMLE described

in Reference [12]. The general form of a maximum likelihood estimator is given in Equation 3.41.

$$\hat{\xi}[\mathbf{z}(\cdot)] = \arg \max_{\xi} L[\mathbf{z}(\cdot), \xi] \quad [3.41]$$

where L is the likelihood function. For the system described above, the likelihood function takes the form of a multivariate probability distribution function [8].

$$L[\mathbf{z}(\cdot), \xi] = [(2\pi)^m \det[GG^*]]^{-N/2} \exp \left\{ \frac{1}{2} \sum_{i=1}^N [\tilde{\mathbf{z}}_{\xi}(t_i) - \mathbf{z}(t_i)]^* (GG^*)^{-1} [\tilde{\mathbf{z}}_{\xi}(t_i) - \mathbf{z}(t_i)] \right\} \quad [3.42]$$

where $\tilde{\mathbf{z}}_{\xi}(t_i)$ is the Kalman filter estimate of $\mathbf{z}(t_i)$ based on measurements up to t_{i-1} .

The discrete Kalman filter takes the form of a current state estimator.

$$\tilde{\mathbf{x}}(t_i) = \Phi \tilde{\mathbf{x}}_{\xi}(t_{i-1}) + \Gamma \frac{1}{2} [\mathbf{u}(t_i) + \mathbf{u}(t_{i-1})] \quad [3.43]$$

$$\tilde{\mathbf{z}}_{\xi}(t_i) = \mathbf{C} \tilde{\mathbf{x}}_{\xi}(t_i) + \mathbf{D} \mathbf{u}(t_i) \quad [3.44]$$

$$\hat{\mathbf{x}}_{\xi}(t_i) = \tilde{\mathbf{x}}_{\xi}(t_i) + \mathbf{K} [\mathbf{z}(t_i) - \tilde{\mathbf{z}}_{\xi}(t_i)] \quad [3.45]$$

where $\Phi = e^{\mathbf{A}T}$, $\Gamma = \int_0^T e^{\mathbf{A}\tau} \mathbf{B} d\tau$, \mathbf{K} is the Kalman gain matrix and GG^* is the covariance matrix of the residuals $\mathbf{z}(t_i) - \tilde{\mathbf{z}}_{\xi}(t_i)$. One can see that the estimate $\tilde{\mathbf{z}}_{\xi}(t_i)$ is a function of ξ because the Kalman filter depends on the system matrices.

Initial guesses for ξ are given to the MMLE program. An iterative optimization routine varies the values of ξ until the likelihood function is maximized. The program actually finds ξ which minimizes the less complex negative log likelihood function of Equation 3.46 which is equivalent to maximizing Equation 3.42 since $\ln L[\mathbf{z}(\cdot), \xi]$ is a monotonic.

$$J(\xi) = \frac{1}{2} \sum_{i=1}^N \left[[\tilde{\mathbf{z}}_{\xi}(t_i) - \mathbf{z}(t_i)]^* (GG^*)^{-1} [\tilde{\mathbf{z}}_{\xi}(t_i) - \mathbf{z}(t_i)] \right] + \frac{1}{2} N \ln(\det(GG^*)) \quad [3.46]$$

The MMLE program returns the maximum likelihood estimate of the parameter vector $\hat{\xi}$.

3.1.7 Pseudo Random Binary Sequences (PRBS)

Pseudo Random Binary Sequences (PRBS) or maximum length sequences (m-sequences) generated by feedback shift registers have properties of a good input test

signal for system identification work [3]. PRBS test signals are generated by a computer implementation of Figure 3.3. PRBS are periodic with period $P = (2^n - 1)T$, where n is the number of shift registers T is the sampling period. The implementation used in the TROFM identification test uses 13 shift registers with a sampling period of $T = 0.02245$ sec. The minimum time the signal remained in a positive or negative state is set to $5T = .1123$ sec and the initial state of each shift register is randomly set before each test.

3.2 Actuators

The main rotor and tilt servo are the two TROFM actuators. Their principals of operation are discussed below.

3.2.1 Main Rotor

The the thrust produced by the main rotor F_R is a function of the angular velocity of the rotor $\dot{\beta}$. The angular velocity of the rotor is described by a differential equation. The main rotor is driven by a DC motor and its angular velocity is measured by a DC tachometer. The commanded rotor angular velocity calculated by the control computer is converted to a analog reference voltage by a D/A converter . This reference voltage is sent to a pulse width modulated amplifier (PWM) which controlled the motor speed. The amplifier compared the reference voltage generated by the computer to the feedback voltage generated by the tachometer and adjusted the current supplied to the motor to decrease the angular velocity difference. Figure 3.4 shows a block diagram of the velocity tracking control system implemented by the PWM.

3.2.2 Tilt Servo

The actuator which tilted the main rotor is a rotary position servo commonly found in remote control model airplanes. The actual servo is a Futaba 9102 which produces 69.5 oz-in of torque and slews at $273^\circ/\text{sec}$. The servo position is controlled

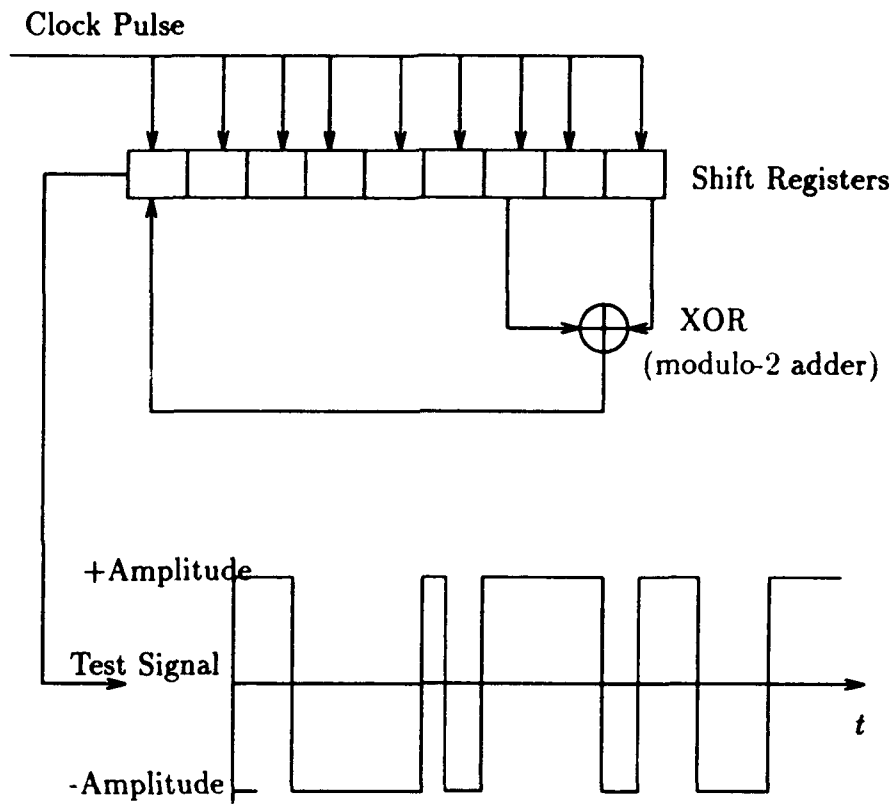


Figure 3.3 Typical PRBS and PRBS signal generator consisting of digital components.

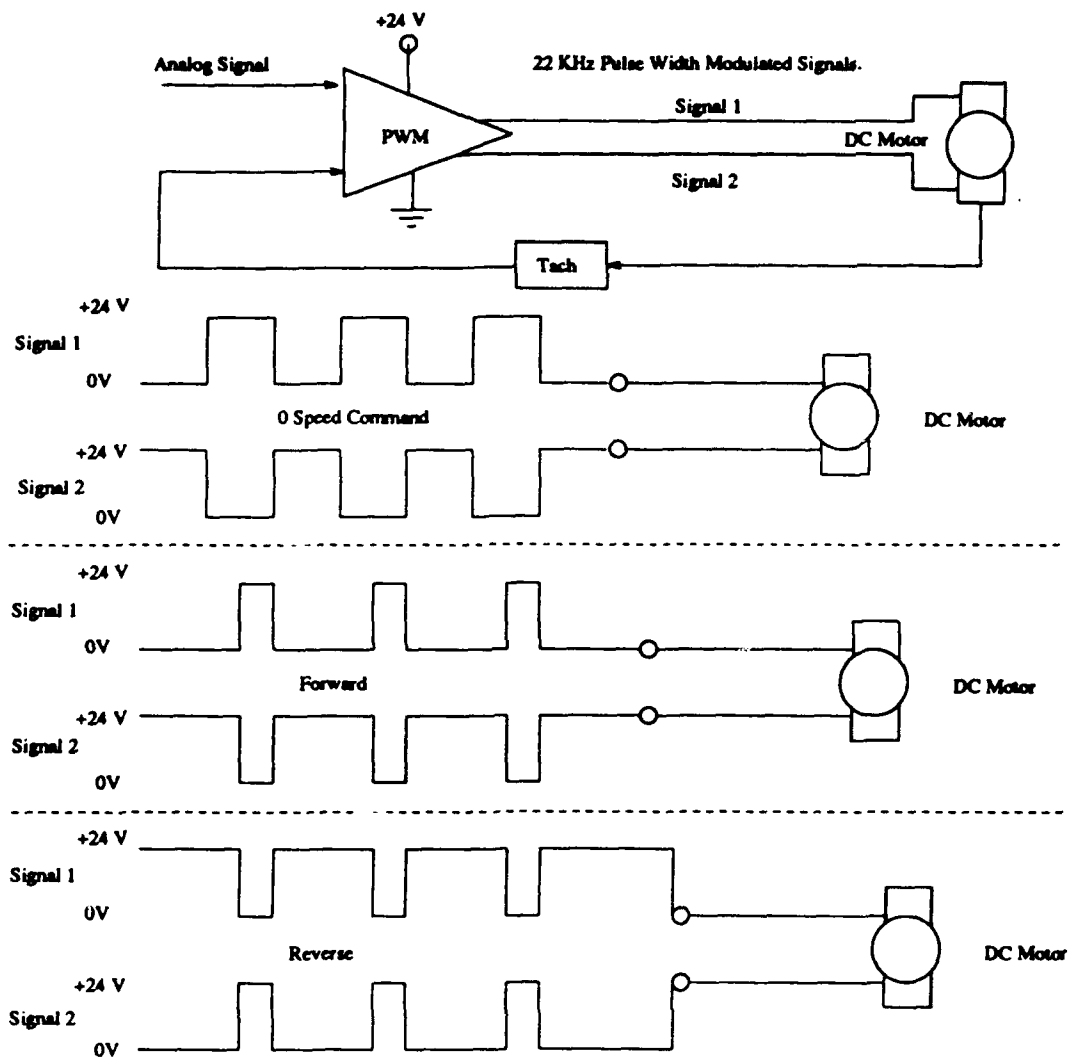


Figure 3.4 Main rotor angular velocity control system.

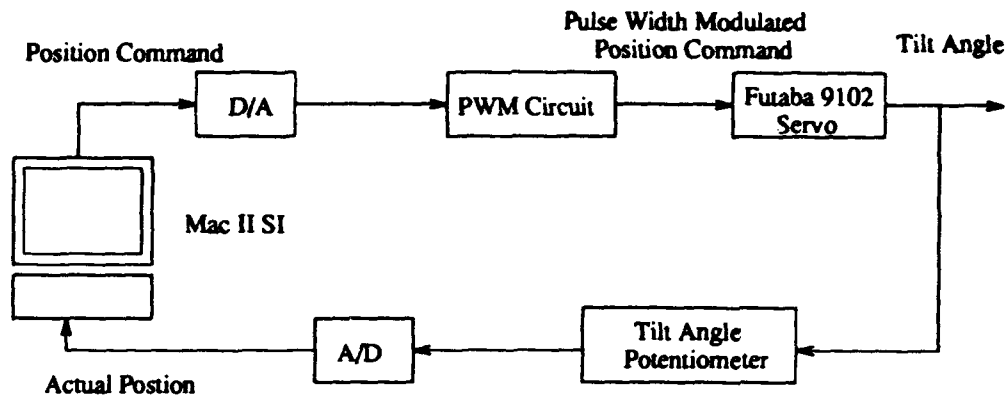


Figure 3.5 Block diagram of tilt servo angular position control system.

by the width of a pulse applied to the servo's control terminal. A proportional control system is built into the servo by the manufacturer for the purpose of tracking position commands. An external potentiometer configured as a voltage divider is used to determine the actual angular position of the output shaft. The control computer produces analog outputs for actuator control, but the servo requires that position commands be in the form of pulses of varying widths. A pulse width modulator is built to convert the analog output of the computer to a periodic signal of square waves whose duty cycle is proportional to the voltage produced by the analog output. A schematic of this circuit is included in Appendix A. Figure 3.5 shows a block diagram of the servo control system and the apparatus used to measure and command the angular position of the output shaft.

3.3 Identification of State Space Model

The form of the state space model is determined analytically in Chapter 2. Several important parameters could not be determined analytically; therefore, experiments are conducted to estimate these unknowns as well as correct deficiencies in the analytical model. Figure 3.6 shows the system identification process used to determine the state space model of the TROFM.

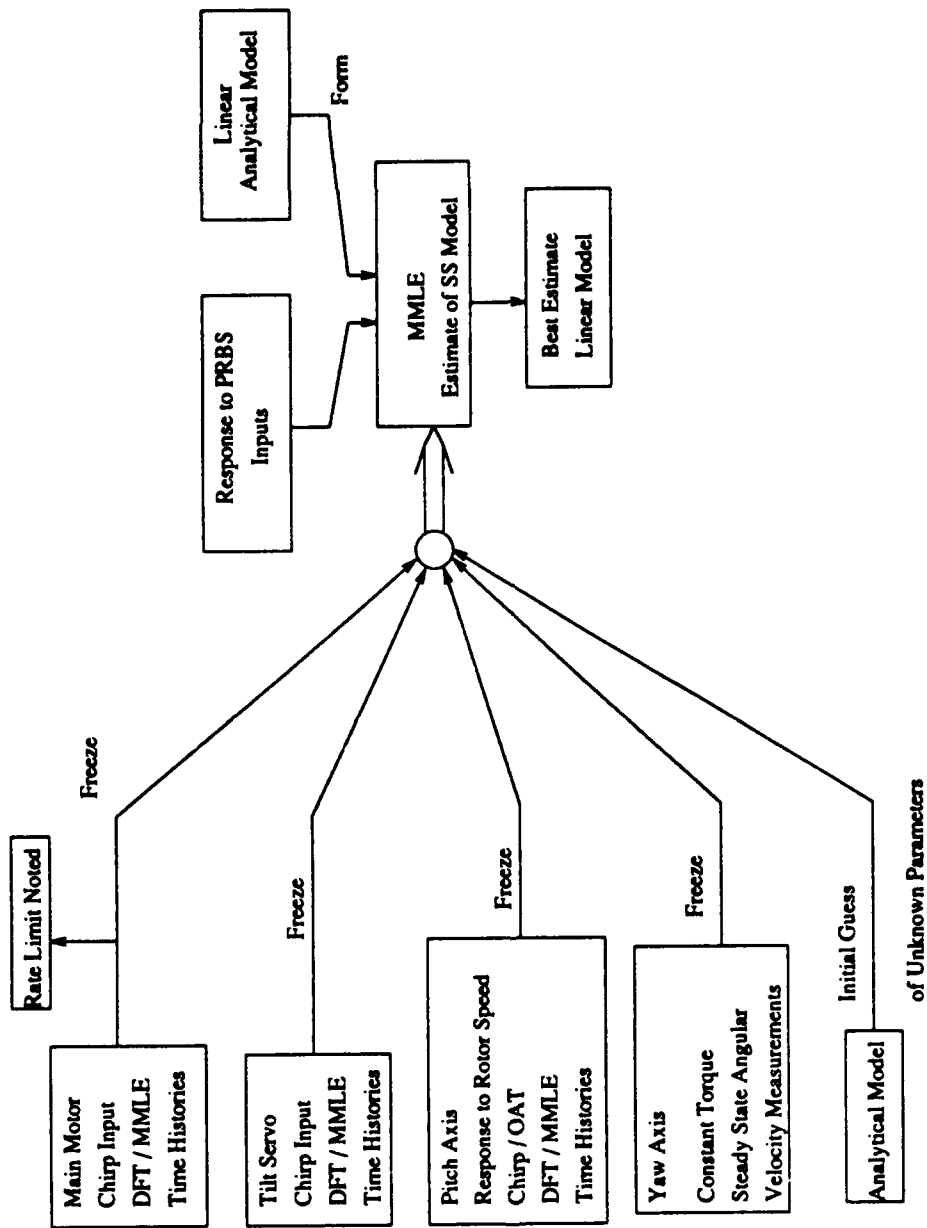


Figure 3.6 Flow chart of the system identification process used to determine the state space model of the TROFM.

3.3.1 Main Motor (Rotor) Identification

Both frequency response (non-parametric) and maximum likelihood (parametric) methods are used to identify the characteristics of the main motor. A chirp input signal is used to excite the main motor. The chirp consists of 2048 data points and sweeps a frequency range of 6.5 rad/sec to 46 rad/sec. The nominal rotor speed is 300 rad/sec and the chirp amplitude is 10.47 rad/sec. The roll (tilt), pitch and yaw axes are restrained at $\Phi = 0, \Psi = 0$ and $\Theta = 0$ rad during this test to insure that coupling between the axes do not affect the results. The Bode plot generated from the DFT suggests that the system was second order because of the -40 dB/dec magnitude slope starting at $\omega_{n \text{ main}} \approx 24$ rad/sec and the characteristics of the phase curve (going from 0° at low frequencies to -90° at 24 rad/sec and to -180° at 40 rad/sec). The 2 dB resonant peak indicates that the system has a damping ratio of $\zeta_{\text{main}} \approx 0.35$. The transfer function $\dot{\beta}(s)/\dot{\beta}_{\text{com}}(s)$ is assumed to be of the form:

$$\frac{\dot{\beta}(s)}{\dot{\beta}_{\text{com}}(s)} = \frac{\omega_{n \text{ main}}^2}{s^2 + 2\zeta_{\text{main}}\omega_{n \text{ main}}s + \omega_{n \text{ main}}^2} \quad [3.47]$$

A maximum likelihood analysis is then performed to determine the best estimates of $\omega_{n \text{ main}}$ and ζ_{main} . The estimates from the DFT results are used as initial guesses to start the numerical search. The zero order hold on the input signal introduces approximately a half sampling period delay [12]. This was corrected in the analysis by replacing the input with Equation 3.48.

$$\dot{\beta}_{\text{com new}}(k) = \frac{1}{2}(\dot{\beta}_{\text{com}}(k+1) + \dot{\beta}_{\text{com}}(k)) \quad [3.48]$$

The maximum likelihood estimate of the main motor transfer function is given in Equation 3.49.

$$\frac{\dot{\beta}(s)}{\dot{\beta}_{\text{com}}(s)} = \frac{655.2}{s^2 + 17.62s + 655.2} \quad [3.49]$$

It follows that $\omega_{n \text{ main}} = 25.597$ rad/sec and $\zeta_{\text{main}} = 0.3442$. This compares favorably to the initial estimate obtained from the DFT results. Figure 3.7 shows the simulated and actual (rate limit induced DC offset removed) responses of the output $\dot{\beta}$ to the

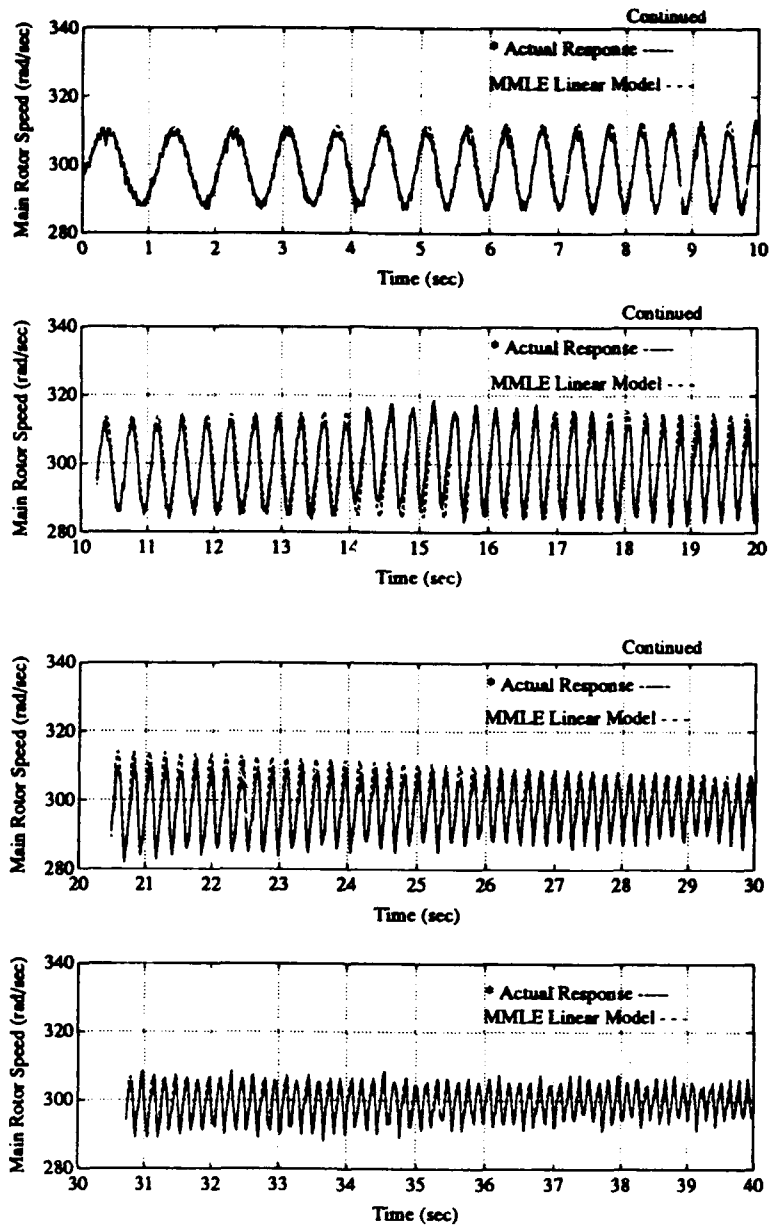


Figure 3.7 Main motor (rotor) response* to a chirp input. (* DC offsets caused by rate limit subtracted out.)

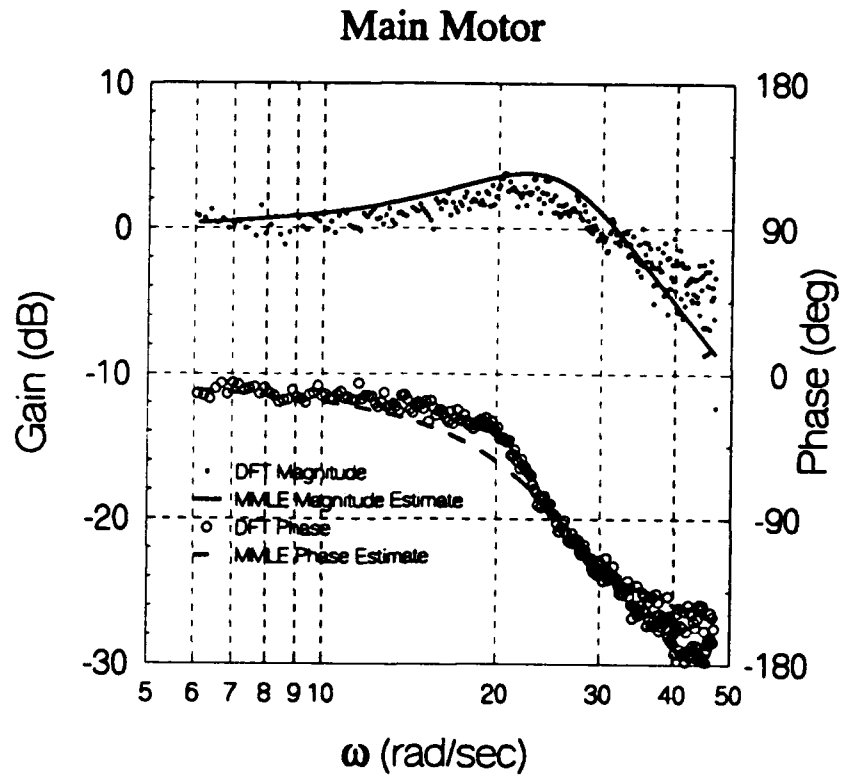


Figure 3.8 Main motor frequency response.

chirp $\dot{\beta}_{com}$ input signal. Figure 3.8 shows the Bode plots of the maximum likelihood and DFT transfer function estimates.

An unusual trend is observed in the actual output time history. At frequencies greater than 25 rad/sec, the positive peak values of $\dot{\beta}(t)$ decrease as the frequency of $\dot{\beta}_{com}(t)$ increases. The negative peaks of the output increase to about $2\dot{\beta}_{com}(t)$ at the resonant frequency and slowly decrease at frequencies higher than the resonant frequency. This non-linear phenomenon has the effect of lowering the nominal value of $\dot{\beta}(t)$ at frequencies greater than 25 rad/sec by 6 to 7 rad/sec. The time histories used to identify the linear model are based on this nonlinear data with the effective high frequency DC offset removed. The linear model follows the nonlinear time history up to the resonant peak at 25 rad/sec and follows amplitude well throughout the test frequency range with a DC offset of 6 to 7 rad/sec for test frequencies greater than 25 rad/sec.

Close examination of the time history allows one to ascertain the type of nonlinear phenomenon at work. The slope of $\dot{\beta}(t)$ going up is less than the slope of $\dot{\beta}(t)$ going down which indicates that a rate limit is present. The $\dot{\beta}(t)$ time history is differentiated according to Equation 3.50.

$$\ddot{\beta}(k) = \frac{\dot{\beta}(k+1) - \dot{\beta}(k)}{T} \quad [3.50]$$

It was found that $\ddot{\beta}(t)$ is limited to about 180 rad/sec² in the positive direction (acceleration). Rate limiting is not factor in the negative direction (deceleration). In order to simulate the nonlinear main motor, the structure shown in Figure 3.9 is assumed. The structure of the linear model is shown for comparison in Figure 3.10. The linear model values $a = 17.67$ and $K = 30.08$ are used to start an iterative search for a and K which best fit the nonlinear time history data in a visual sense. Values of a and K which fit the nonlinear time history well are found to be $a = 23$ and $K = 100$. Figure 3.11 shows the actual and nonlinear simulated response of the main rotor speed to a chirp input. One can see that the nonlinear simulation models the actual response quite well. Chapter 3 will show that the linear model is suitable for pitch and yaw axis control design since the closed loop bandwidths of the command

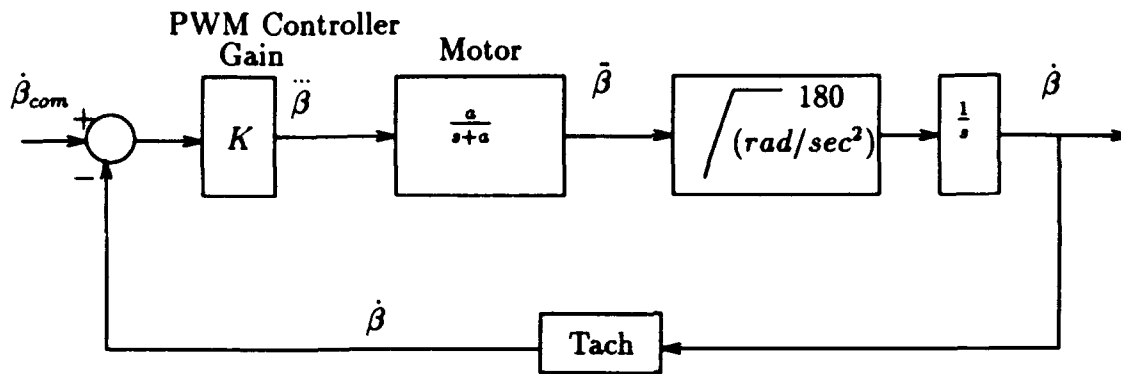


Figure 3.9 Block diagram of rate limited main motor model.

systems are at least a factor of 2 below the frequency where the nonlinear rate limit effects appear.

The rate limit described above is actually an acceleration limit because main motor speed is rate limited. The motor is acceleration limited in the positive direction for two reasons: drag torque and limited power. At the nominal $\dot{\beta}$, the motor is drawing power from the amplifier to overcome drag torque. To accelerate in the opposite direction of the nominal drag torque vector the motor requires more power from the amplifier to overcome an increase in drag torque as well as inertial torques. Since the amplifier is already using significant power to maintain the nominal $\dot{\beta}$, it is unable to increase the rotor speed as quickly in the direction of the nominal drag torque vector. Decreasing rotor speed from the nominal $\dot{\beta}$ can be accomplished by simply removing the power, since drag torque and friction passively cause the rotor to decelerate. The amplifier is also capable of driving the rotor in reverse which means that at the nominal $\dot{\beta}$, it has much more power available to decelerate than accelerate. Figure 3.12 graphically illustrates these principles. The limited power also introduces another important nonlinear effect, $\dot{\beta}$ saturation. The amplifier eventually runs out of power to accelerate the rotor since all of the power is used to overcome drag torque. This critical speed was experimentally determined to be $\dot{\beta}_{max} = 362$ rad/sec. The saturation nonlinearity is considered in the control system design.

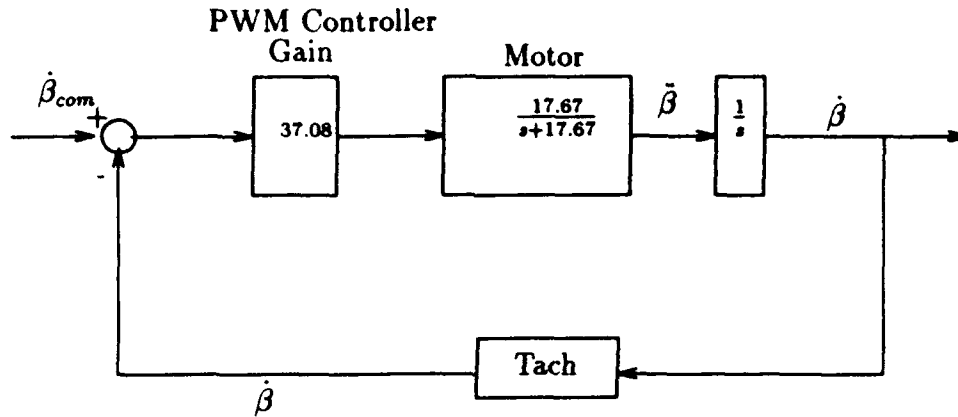


Figure 3.10 Block diagram of linear main motor model.

3.3.2 Tilt Servo

Frequency response and maximum likelihood methods are used to identify the characteristics of the tilt servo. A chirp input signal is applied to the control terminal of the servo. The chirp consists of 2048 data points with a frequency range of 2.75 to 30.5 rad/sec. The output shaft position is sampled at 50.84 Hz or 319.28 rad/sec. The pitch and yaw axes are restrained at $\Theta = 0$ and $\Psi = 0$ rad while the main rotor maintains its nominal speed of 300 rad/sec. The Bode plot generated from the DFT suggests that the system was second order because of the -40 dB/dec slope at frequencies greater than $\omega_{n \text{ tilt}} \approx 12$ rad/sec and the characteristics of the phase curve (going from 0° at steady state to -90° at $\omega = 12$ rad/sec to 180° at 25 rad/sec). The shape of the Bode magnitude curve in the region of $\omega_{n \text{ tilt}} \approx 12$ rad/sec indicates that $\zeta_{\text{tilt}} \approx 0.6$. The transfer function $\Phi(s)/\Phi_{com}(s)$ is assumed to be of the form

$$\frac{\Phi(s)}{\Phi_{com}(s)} = \frac{\omega_n^2 \text{ tilt}}{s^2 + 2\zeta_{\text{tilt}}\omega_n \text{ tilt} + \omega_n^2 \text{ tilt}} \quad [3.51]$$

A maximum likelihood analysis is performed to determine the best estimates of $\omega_n \text{ tilt}$ and ζ_{tilt} . The estimates from the DFT results are used as initial guesses to start the numerical search. A zero order hold is used on the input signal; therefore, in an approximate sense, a half sampling period delay was introduced. To compensate for

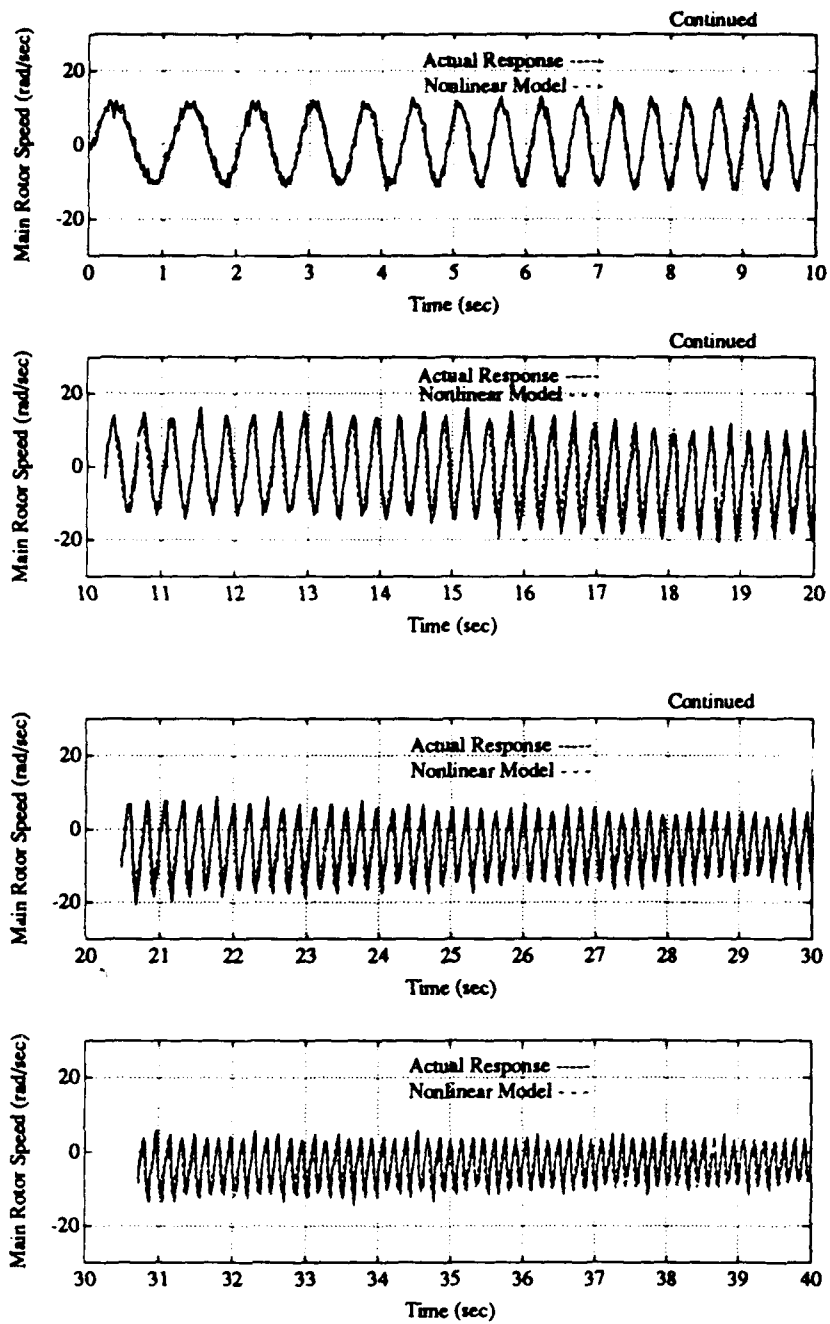


Figure 3.11 Actual and nonlinear simulated response of main rotor speed to a chirp input.

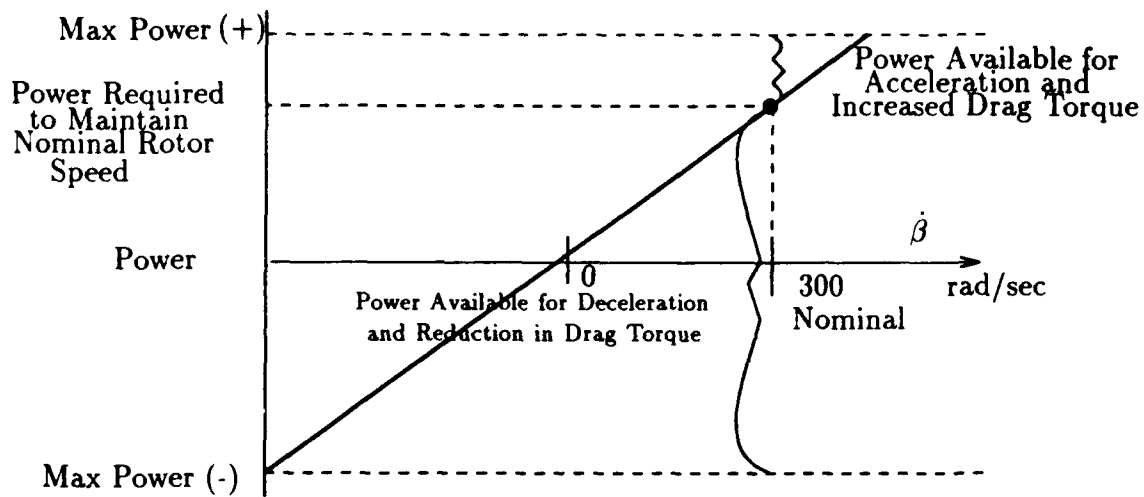


Figure 3.12 Cause of main rotor speed rate limit.

this time delay, the input is replaced by Equation 3.52.

$$\Phi_{com}(k) = \frac{\Phi_{com}(k+1) - \Phi_{com}(k)}{2} \quad [3.52]$$

The maximum likelihood estimate of the tilt servo transfer function is given by Equation 3.53.

$$\frac{\Phi(s)}{\Phi_{com}(s)} = \frac{153.42}{s^2 + 14.18s + 153.42} \quad [3.53]$$

It follows that $\omega_n \text{ tilt} = 12.39 \text{ rad/sec}$ and $\zeta_{\text{tilt}} = 0.5724$. This compares favorably to the initial estimate obtained from the DFT results. Figure 3.13 shows the simulated and actual time history responses of the output Φ to the chirp Φ_{com} input signal. Figure 3.14 shows the Bode plots of the maximum likelihood and DFT transfer function estimates.

3.3.3 Drag Torque, Thrust and Rotor Speed

The relationship between rotor thrust and rotor velocity is determined experimentally. The apparatus shown in Figure 3.16 is used to measure the rotor force as the rotor speed is slowly varied from 0 to 362 rad/sec. The rotor speed was measured by a DC tachometer mounted on the motor. A second order polynomial is fitted to the experimental measurement using a least squares procedure. The curve is linearized about the nominal rotor speed $\dot{\beta} = 300 \text{ rad/sec}$. This linearized relation is given in Equation 3.54 and shown in Figure 3.15.

$$F_R \approx \frac{\partial F_R}{\partial \dot{\beta}} \dot{\beta} + k_2 = -0.003057 \frac{\text{lb}f}{\text{rad/sec}} \dot{\beta} - 0.59 \text{lb}f \quad [3.54]$$

An experiment was designed for the purpose of determining the rotor drag torque as a function of main rotor angular velocity ($\dot{\beta}$). The pitch axis is restrained at $\Theta = 0$ during these experiments. Figure 3.17 shows a free body diagram of the system. Summing torques about the \hat{i}_z axis one obtains:

$$\sum M \hat{i}_z = F_R l_1 \sin \Phi - F_{SG} l_2 - T_{SF} - T_D = 0 \quad [3.55]$$

where F_R , F_{SG} , T_{SF} , and T_D denote the force generated by the main rotor, the force measured by the strain gage force transducer, yaw bearing static friction and the rotor drag torque respectively.

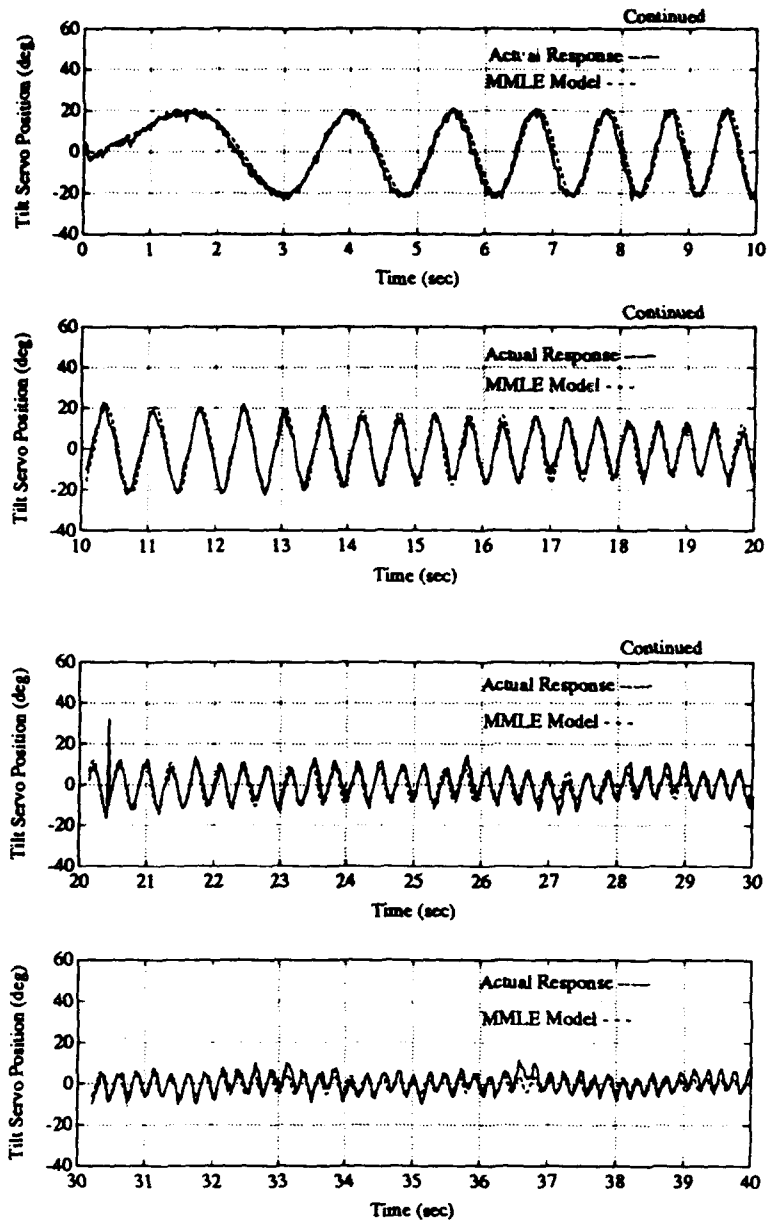


Figure 3.13 Response of tilt servo to chirp input.

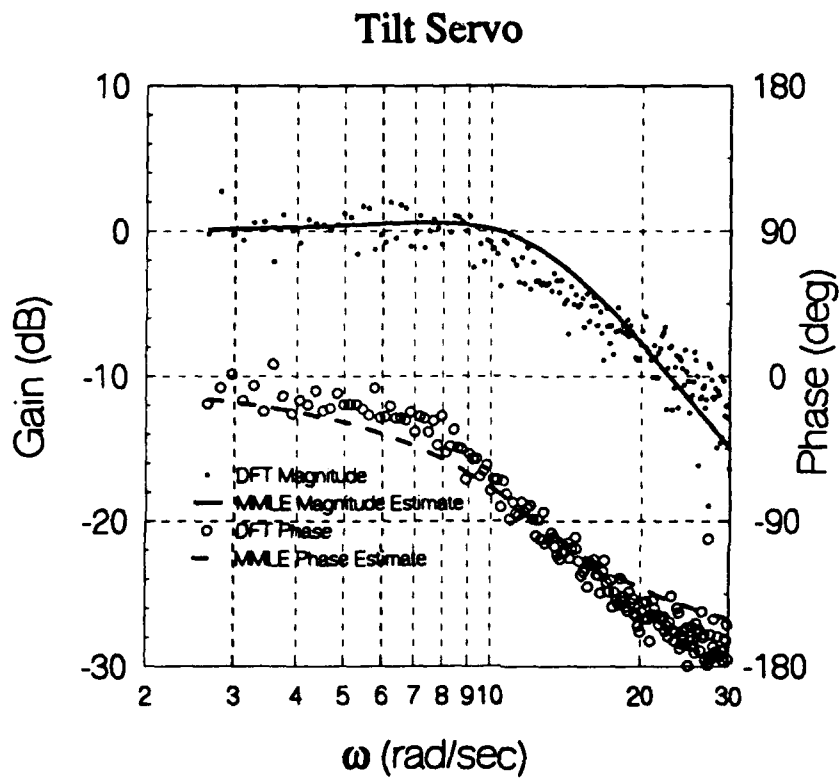


Figure 3.14 Tilt servo frequency response.

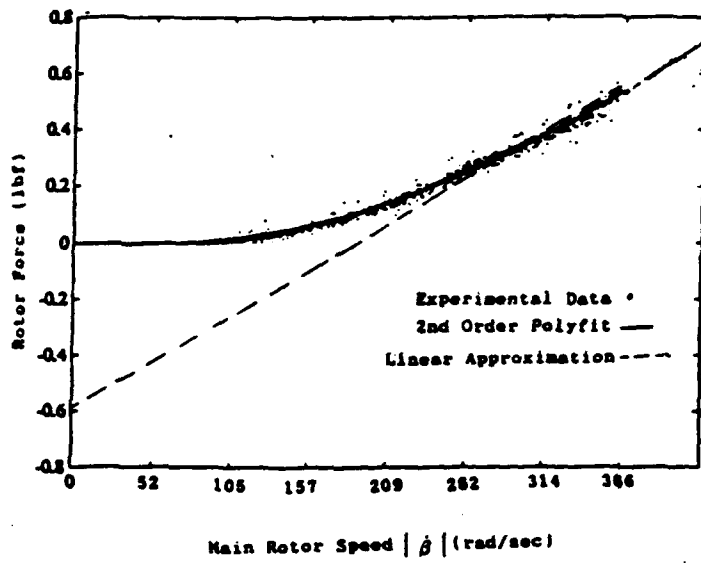


Figure 3.15 Rotor force F_R as a function of main rotor speed $|\dot{\beta}|$.

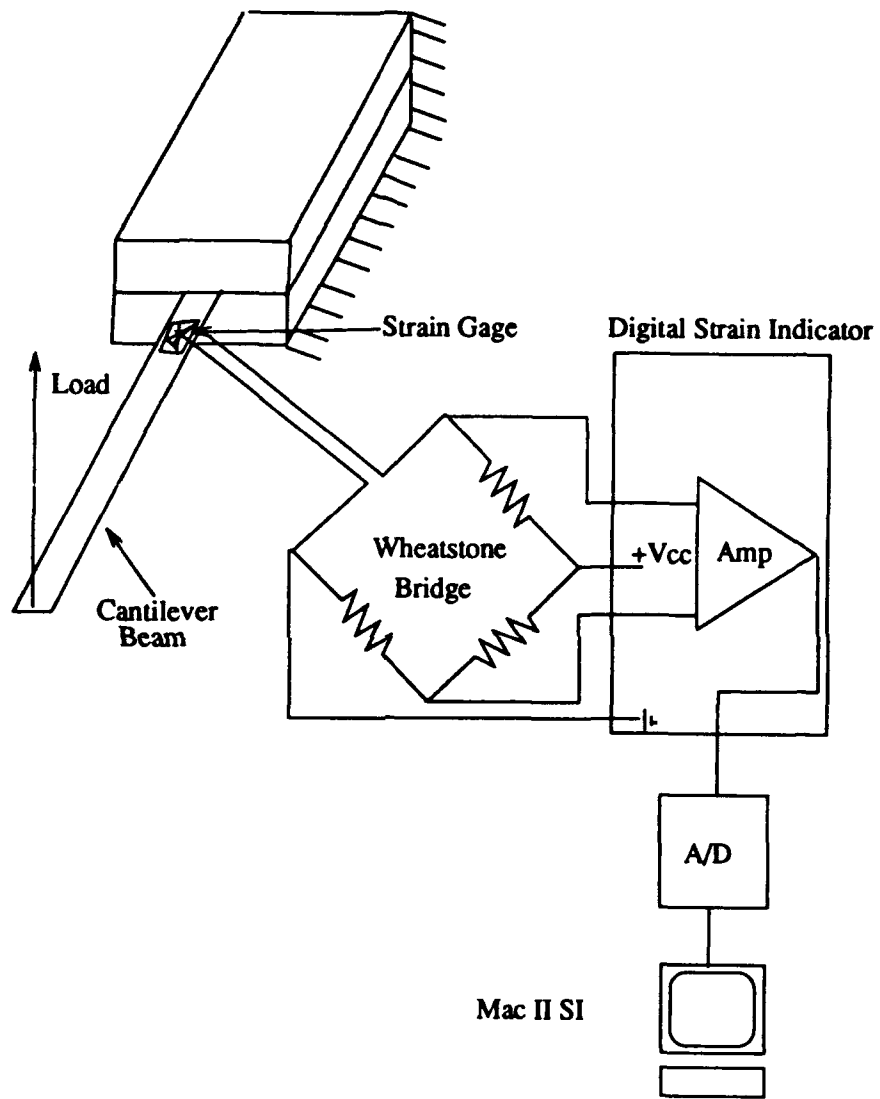


Figure 3.16 Sketch of apparatus used to measure forces.

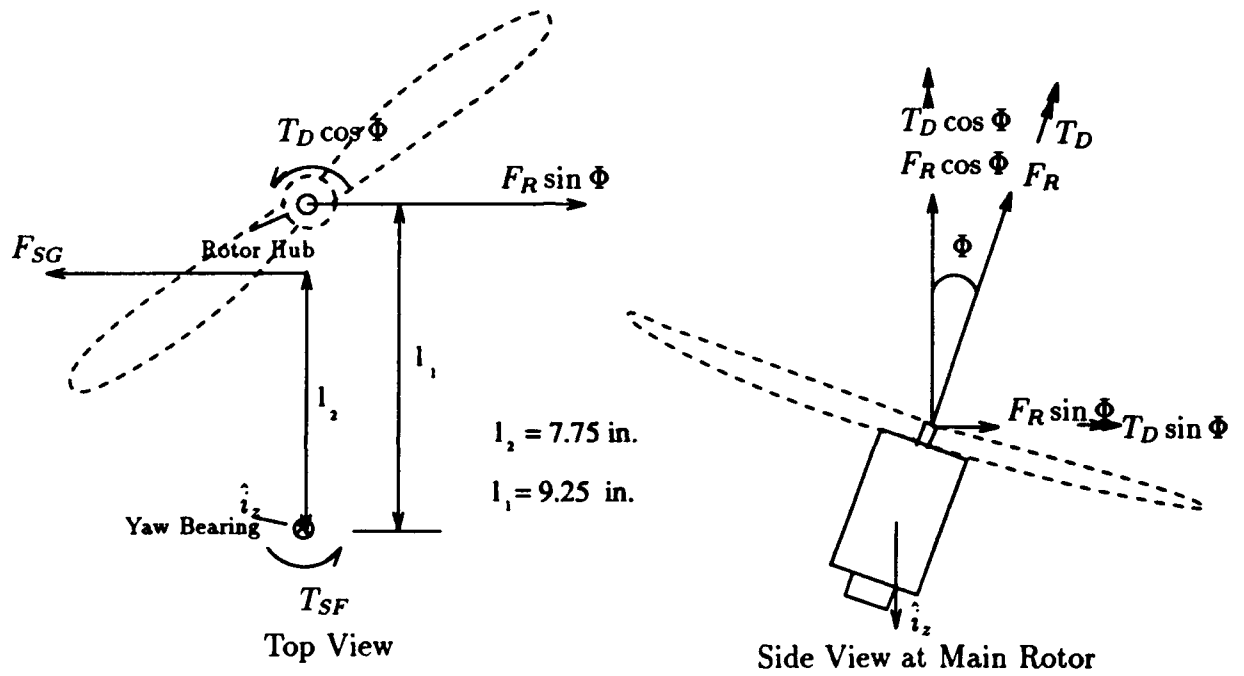


Figure 3.17 Free body diagram of system

The main rotor is tilted to $\Phi_1 = 20^\circ$ and $\dot{\beta}$ is varied from 0 to 362 rad/sec. The force is measured by the computer and plotted as a function of rotor angular velocity. The main rotor is then tilted to $\Phi_2 = -20^\circ$ and the process repeated. If the magnitude of T_{SF} is the same for positive and negative Φ and there is no drag torque generated by the rotor then the force versus velocity curves would be identical; however, drag torque exists and the static friction of the yaw bearing is direction dependent. Two moment equilibrium equations may now be written.

$$\sum M_{1\hat{i}_z} = F_R l_1 \sin \Phi_1 - F_{SG_1} l_2 - T_{SF_1} - T_D \cos(\Phi) = 0 \quad [3.56]$$

$$\sum M_{2\hat{i}_z} = F_R l_1 \sin \Phi_2 - F_{SG_2} l_2 - T_{SF_2} - T_D \cos(\Phi) = 0 \quad [3.57]$$

Since $\Phi_1 = -\Phi_2$, one may add these equations and solve for the drag torque.

$$T_D = \frac{(F_{SG_2} - F_{SG_1})l_2 + (T_{SF_2} - T_{SF_1})}{2 \cos \Phi} \quad [3.58]$$

The static friction torques are determined using the apparatus shown in Figure 3.16. A force is applied to the end of the pipe which causes the force transducer to deflect. The force is slowly removed until the spring force of the force transducer acting over l_2 and static friction torque balance.

$$T_{SF} = F_{SF} l_2 \quad [3.59]$$

The balancing force F_{SF} is measured in both the positive and negative Ψ directions. It has been determined that $F_{SF}(+\Psi) \approx 1.30\text{oz}$ and $F_{SF}(-\Psi) \approx 1.08\text{oz}$. Figure 3.18 shows F_{SG_1} as a function of $\dot{\beta}$ for $\Phi_1 = 20^\circ$ as measured by the computer. A second order polynomial least squares fit is applied to the data to facilitate the implementation of Equation 3.58. Figure 3.19 shows F_{SG_2} as a function of main rotor angular velocity for $\Phi_2 = -20^\circ$. By applying Equation 3.58 and using the least squares fits in Figures 3.18 and 3.19 one can obtain $T_D(\dot{\beta})$. Figure 3.20 shows the relationship between T_D and $\dot{\beta}$. The drag torque curve of Figure 3.20 is linearized about the nominal rotor speed of $\dot{\beta}=300$ rad/sec. This linear relationship is found to be

$$T_D \approx \frac{\partial T_D}{\partial \dot{\beta}} \dot{\beta} + k_4 = -0.000496 \dot{\beta} \frac{\text{ft.lbf.}}{\text{rad/sec}} - 0.08 \text{ft.lbf.} \quad [3.60]$$

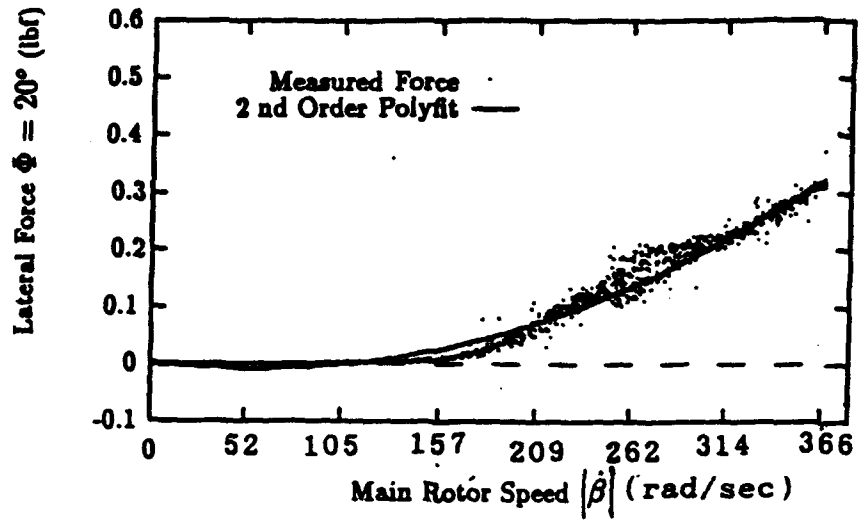


Figure 3.18 Lateral force F_{SG_1} for $\Phi_1 = 20^\circ$ as a function of $\dot{\beta}$.

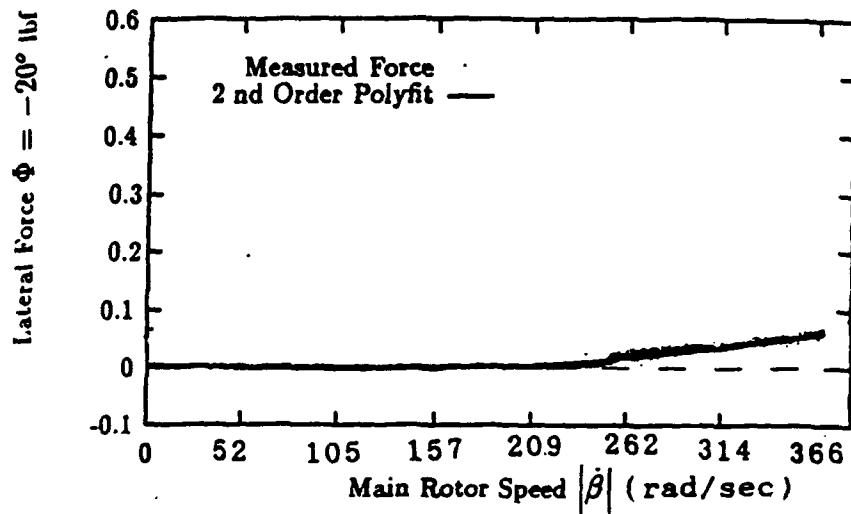


Figure 3.19 Lateral force F_{SG_2} for $\Phi_2 = -20^\circ$ as a function of $\dot{\beta}$.

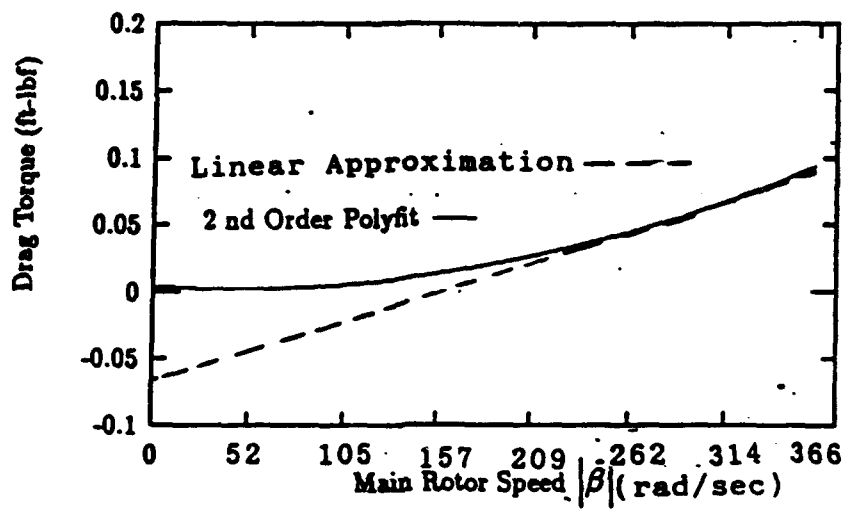


Figure 3.20 Main Rotor Drag torque as a function of $\dot{\beta}$.

3.3.4 Pitch to Rotor Speed Transfer Function

The pitch angle to rotor speed transfer function $\Theta(s)/\dot{\beta}(s)$ is to be determined. The roll and yaw axes are restrained at $\Phi = 0$ and $\Psi = 0$ during this test to insure inter-axis coupling does not affect the results. A chirp $\dot{\beta}_{com}$ is issued and the outputs $\dot{\beta}$ and Θ are measured. The input chirp consists of 4096 points sampled at 49.54 Hz and covers the frequency range between .05 and 3.2 rad/sec. Frequency response and MMLE methods are used to estimate the transfer function $\Theta(s)/\dot{\beta}(s)$. One At a Time (OAT) frequency response tests are also conducted to verify the chirp test results. The pitch axis is extremely difficult to identify because numerous nonlinear effects are present. The ground effect phenomenon introduces a nonlinear spring. For a fixed rotor speed and attitude Θ where the TROFM is in ground effect, a decrease in Θ results in a ground effect force which tends to restore Θ to its nominal value. Similarly an increase in Θ results in a loss of ground effect force which tends to restore Θ to its nominal value. These ground effect restoring forces F_{GE} are nonlinear because $\partial F_{GE}/\partial\Theta = f(\Theta)$ [7]. For large nominal values of Θ (large distances between platform and rotor), the gradient $\partial F_{GE}/\partial\Theta = 0$. In other words the TROFM is out of the ground effect. Other sources of nonlinearity include static and coulomb friction which are the probable cause of the hysteresis and beat phenomena which are observed in some of the OAT frequency response tests.

Despite the nonlinearities, a linear model is found which adequately describes the system for linear control design purposes. The transfer function $\Theta(s)/\dot{\beta}(s)$ is assumed to be of the form of Equation 3.61 which follows from the analysis of Chapter 2.

$$\frac{\Theta(s)}{\dot{\beta}(s)} = \frac{\partial F_R/\partial\dot{\beta}}{s^2 + 2\zeta_{pitch}\omega_n\text{pitch} + \omega_n^2\text{pitch}} \quad [3.61]$$

The maximum likelihood estimate of this transfer function is given by Equation 3.62.

$$\frac{\Theta(s)}{\dot{\beta}(s)} = \frac{0.0359}{s^2 + 1.064s + 2.7225} \quad [3.62]$$

The MMLE estimate nicely matches the low frequency portion of the DFT generated Bode plot but underestimates the resonant peak and break frequency. Based on the

results of the OAT frequency response tests, a modification to the MMLE estimate of $\partial F_R / \partial \dot{\beta}$ is made. The OAT tests indicate that the DFT chirp underestimates the low frequency magnitude curve by about 5 to 10 dB; therefore, the MMLE result is modified to Equation 3.63.

$$\frac{\Theta(s)}{\dot{\beta}(s)} = \frac{0.05}{s^2 + 1.064s + 2.7225} \quad [3.63]$$

OAT results indicate that the MMLE result made a good estimate of the pole locations. The OAT tests indicate a 2-4 dB droop in the magnitude curve between $\omega = 0.8$ and 1.2 rad/sec which suggests the existence of a third pole around $\omega = 0.7$ rad/sec. Assuming the pitch axis is a 3rd order system, the approximate -40 dB/dec slope at frequencies above 2 rad/sec suggests the existence of a first order zero around the 2 rad/sec region. No physical explanation as to why this would be a third order system was found.

The modified MMLE transfer function estimate was found to be an acceptable low order linear model of a higher order nonlinear system. DFT and OAT frequency responses as well as the modified MMLE frequency response are shown in Figure 3.21. The actual and simulated chirp response is shown in Figure 3.22. One can see that the simulated response is in phase with the actual response throughout the test. The amplitude follows well in the very low and high frequency ranges. In the middle of the response (mid frequency range) the MMLE response over-estimates the chirp amplitude. This is further evidence of a possible third pole around 0.7 rad/sec and a zero around 2 rad/sec.

3.3.5 Yaw Axis Friction Coefficient

In this test, the pitch axis is restrained at $\Theta = 0$ and the tilt angle is set such that it cancels the drag torque generated by the rotor spinning at 300 rad/sec. The tilt angle is increased (decreased) by 0.07 rad (-0.07 rad) and the steady state yaw angular velocity is determined from the slope of a yaw attitude versus time plot. The moment equilibrium equation below is used to compute the yaw axis viscous friction coefficient μ .

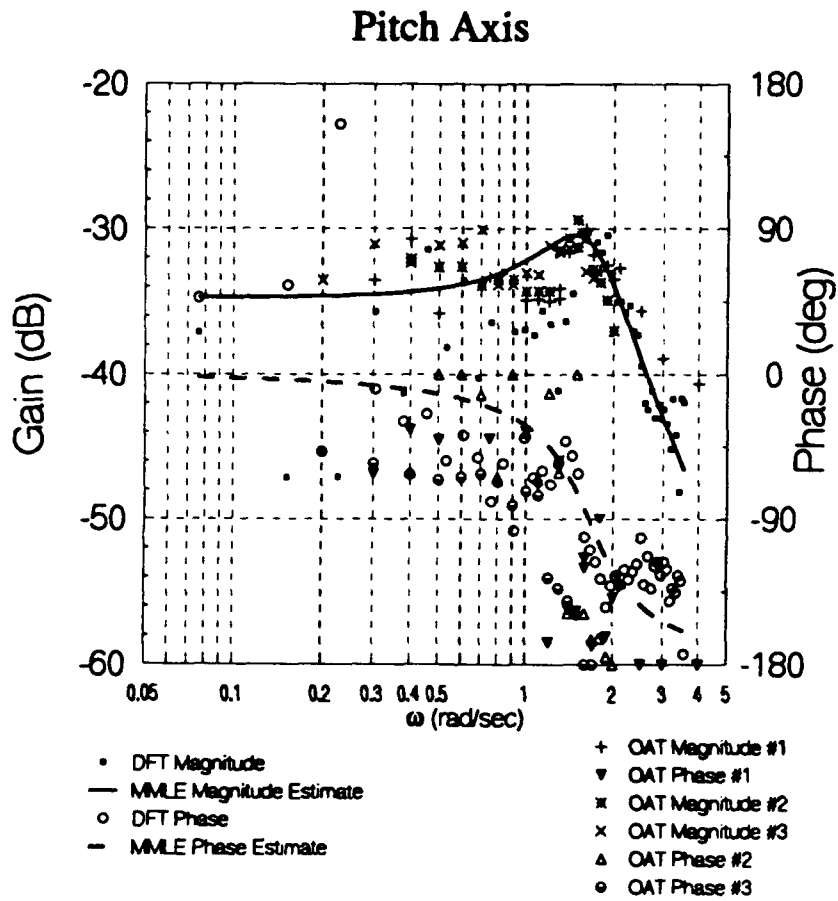


Figure 3.21 Frequency response of $\Theta(s)/\beta$ determined by OAT, DFT and maximum likelihood methods.

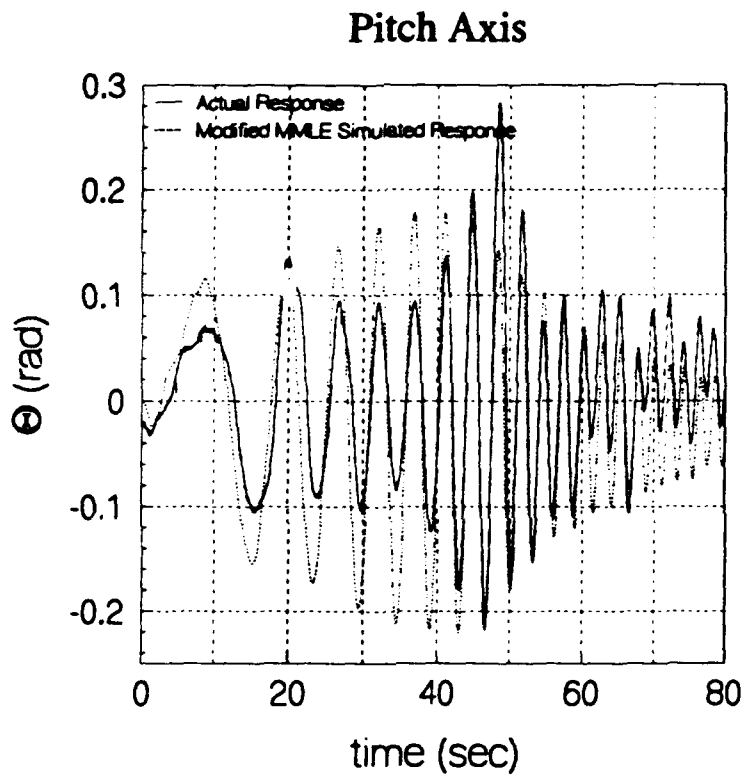


Figure 3.22 Pitch axis response to a chirp $\dot{\beta}_{com}$.

$$\sum M_o = T_R + \mu \dot{\Psi} = 0 \quad [3.64]$$

$$\left(\frac{\partial F_R}{\partial \beta} \dot{\beta} + k_2 \right) l_r \Phi - \mu \dot{\Psi} = 0 \quad [3.65]$$

The test is repeated several times in both directions. The average clockwise and counterclockwise yaw axis viscous friction coefficients are found to be $\mu_{cw} = 0.01983$ (ft-lbf) / (rad/sec) and $\mu_{ccw} = 0.02858$ (ft-lbf) / (rad/sec) respectively. This means that the yaw axis equation of motion is nonlinear since the viscous damping coefficient is direction dependant. For the purpose of linear control design, the CW and CCW viscous damping coefficients are averaged. An estimate of the $\Psi(s)/\Phi(s)$ transfer function based on the analysis of Chapter 1 and the results of this section is given in Equation 3.66.

$$\frac{\Psi(s)}{\Phi(s)} = \frac{\frac{\partial \dot{\Psi}}{\partial \Phi}}{s(s + \frac{\mu_{avg}}{I_d})} = \frac{7.1639}{s(s + 0.71526)} \quad [3.66]$$

3.3.6 Gyroscopic Couples

The elements of the state space model associated with gyroscopic couples were $\partial \ddot{\Theta} / \partial \dot{\Phi}$ and $\partial \ddot{\Phi} / \partial \dot{\Theta}$. In this experiment, two independently generated pseudo-random binary sequences with amplitudes of 15 rad/sec and 0.1 rad are simultaneously applied as inputs to the main rotor and tilt servo respectively. The input-output time histories are sampled at 44.54 Hz. The MMLE program is used to estimate the values of the gyroscopic stability derivatives. The results obtained from the MMLE program are given below.

$$\begin{aligned} \frac{\partial \ddot{\Theta}}{\partial \dot{\Phi}} &\approx -0.7030 \text{ sec} \\ \frac{\partial \ddot{\Phi}}{\partial \dot{\Theta}} &\approx 6.679 \text{ sec} \end{aligned} \quad [3.67]$$

Actual and simulated responses of the system to a set of PRBS inputs can be found in Section 3.4.

3.3.7 Back Substitution of Results into Analytical Model

The following stability derivatives are computed by back-substituting the results of the system identification into the analytical model developed in Chapter 1.

$$\frac{\partial \ddot{\beta}}{\partial \dot{\Psi}} = \frac{\tau_2 \mu}{I_d} = 160.6269 \text{ sec}^{-1} \quad [3.68]$$

$$\frac{\partial \ddot{\beta}}{\partial \Phi} = -168.5407 \text{ sec}^{-2} \quad [3.69]$$

$$\frac{\partial \ddot{\Psi}}{\partial \dot{\beta}} = \frac{\frac{\partial T_D}{\partial \beta}}{I_d} = -0.0146 \text{ sec}^{-1} \quad [3.70]$$

Maximum likelihood estimation of the stability derivatives $\partial \ddot{\Phi} / \partial \Theta$ and $\partial \ddot{\Theta} / \partial \Phi$ indicate that the model is insensitive to these parameters. Since the estimates were small, they were set to zero.

3.4 Results

Table 3.1 lists the measured and identified physical parameters necessary to obtain the state space model derived in Chapter 2. The moments of inertia are determined by measuring and weighing the components of the TROFM and performing weight and balance calculations.

The state space model used for control design is given below. Some parameter estimates in this model are based on earlier system identification results. A refined linear model was developed as time progressed.

$$A = \begin{bmatrix} -14.18 & 6.679 & 0 & 0 & 0 & -153.42 & 0 & 0 \\ -.638 & 1.064 & 0 & 0 & -.05 & 0 & -2.7225 & 0 \\ 0 & 0 & -0.715260 & -.002 & -.0146 & 7.16 & 0 & 0 \\ 0 & 0 & 160.63 & -17.63 & -655.2 & -168.54 & 0 & 0 \\ 0 & 0 & 0 & 1 & 0 & 0 & 0 & 0 \\ 1 & 0 & 0 & 0 & 0 & 0 & 0 & 0 \\ 0 & 1 & 0 & 0 & 0 & 0 & 0 & 0 \\ 0 & 0 & 0 & 1 & 0 & 0 & 0 & 0 \end{bmatrix} \quad [3.71]$$

Table 3.1 List of important physical parameters.

Parameter	Value	Units
$I_{xx} = I_a$	3.893×10^{-4}	slug - ft ²
$I_{yy} = I_b$	0.0321	slug - ft ²
I_c	-8.30×10^{-4}	slug - ft ²
$I_{zz} = I_d$	0.03386	slug - ft ²
I_{zzr}	7.64×10^{-4}	slug - ft ²
I_e	-2.892×10^{-4}	slug - ft ²
m_t	0.0139	slug
m_r	0.00314	slug
m	.1038	slug
g	32.2	ft/sec ²
l_{rcmer}	.09833	ft
l_{tcmer}	.043	ft
l_s	.09833	ft
$l_x = l_r$.742	ft
l_{cg}	0.0955	ft
ν	.03409	(ft - lbf)/(rad/sec)
μ	.02422	(ft - lbf)/(rad/sec)
$\frac{\partial F_R}{\partial \theta} = k_1$	-.03057	(lbf - sec)/rad
k_2	-.59	lbf
$\frac{\partial L_D}{\partial \theta} = k_3$	-.000496	(ft - lbf - sec)/rad
k_4	-.08	ft - lbf
β	-300	rad/sec
k_{GE}	.08737	(lbf - ft)/rad
τ_1	655.2	sec
τ_2	17.67	sec
k_5	153.42	sec ⁻²
k_6	14.18	sec ⁻¹

$$\mathbf{B} = \begin{bmatrix} 0 & 0 & 0 & 655.2 & 0 & 0 & 0 & 0 \\ 153.42 & 0 & 0 & 0 & 0 & 0 & 0 & 0 \end{bmatrix}^T$$

$$\mathbf{C} = \begin{bmatrix} 0 & 0 & 0 & 0 & 1 & 0 & 0 & 0 \\ 0 & 0 & 0 & 0 & 0 & 1 & 0 & 0 \\ 0 & 0 & 0 & 0 & 0 & 0 & 1 & 0 \\ 0 & 0 & 0 & 0 & 0 & 0 & 0 & 1 \end{bmatrix}$$

Figure 3.23 shows the actual and simulated response of this system to two independently generated PRBS $\dot{\beta}_{com}$ and Φ_{com} input signals where $T = 0.05$ sec and $\dot{\beta}_{com} = \pm 10$ rad/sec and $\Phi_{com} = \pm 0.1$ rad. One can see that the linear model follows the actual responses reasonably well except for the yaw axis response. The linear model describes the short term response of the yaw axis quite well but diverges from the actual response as time progresses. The linear yaw axis model has a pure integral term which explains the divergence of the simulated yaw response. In reality static friction is present; therefore, each time the pitch rate equals zero, the static friction must be overcome by a control input. This explains why the actual response does not diverge. Empirically, the effect of static friction in the yaw axis can be described by replacing the pure integral term with a low frequency lag with a pole location around $s \approx -0.7153$. A refined system model is given in Equation 3.72. This model is the result of further system identification work inspired by physical insights obtained during the implementation of the control designs of Chapter 4. Figure 3.24 shows the actual and simulated response of this system to two independently generated PRBS $\dot{\beta}_{com}$ and Φ_{com} input signals where $T = 0.05$ sec and $\dot{\beta}_{com} = \pm 10$ rad/sec and $\Phi_{com} = \pm 0.1$ rad. One can see that the refined linear model follows all of actual responses reasonably

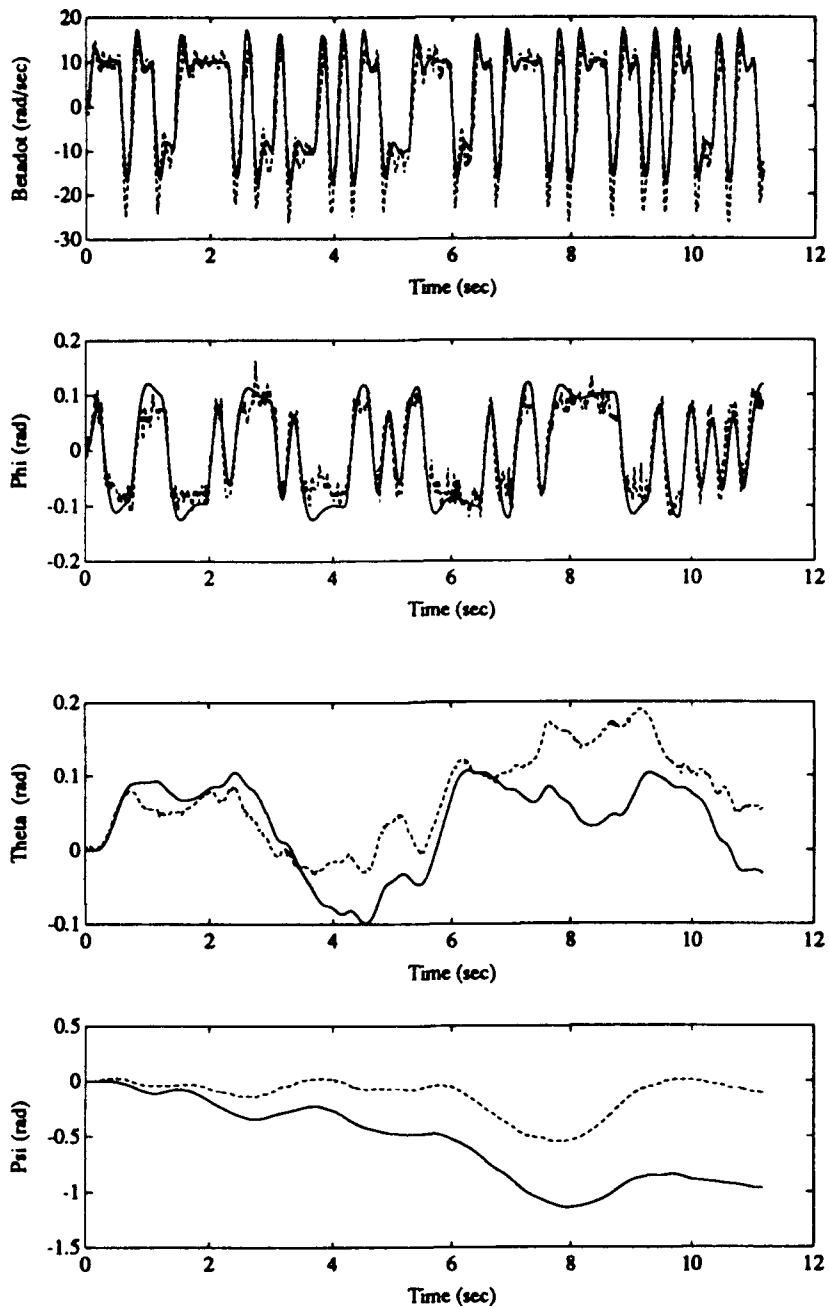


Figure 3.23 Response of control design model to PRBS inputs.

well. It is recommended that future researchers start their work using this model.

$$\mathbf{A} = \begin{bmatrix}
 -14.18 & 6.679 & 0 & 0 & 0 & -153.42 & 0 & 0 \\
 -.7030 & 1.064 & 0 & 0 & -.05 & 0 & -2.7225 & 0 \\
 0 & 0 & -1.429 & -.002 & -.0146 & 7.16 & 0 & 0.5105 \\
 0 & 0 & 160.63 & -17.63 & -655.2 & -168.54 & 0 & 0 \\
 0 & 0 & 0 & 1 & 0 & 0 & 0 & 0 \\
 1 & 0 & 0 & 0 & 0 & 0 & 0 & 0 \\
 0 & 1 & 0 & 0 & 0 & 0 & 0 & 0 \\
 0 & 0 & 0 & 1 & 0 & 0 & 0 & 0
 \end{bmatrix}$$

[3.72]

$$\mathbf{B} = \begin{bmatrix}
 0 & 0 & 0 & 655.2 & 0 & 0 & 0 & 0 \\
 153.42 & 0 & 0 & 0 & 0 & 0 & 0 & 0
 \end{bmatrix}^T$$

$$\mathbf{C} = \begin{bmatrix}
 0 & 0 & 0 & 0 & 1 & 0 & 0 & 0 \\
 0 & 0 & 0 & 0 & 0 & 1 & 0 & 0 \\
 0 & 0 & 0 & 0 & 0 & 0 & 1 & 0 \\
 0 & 0 & 0 & 0 & 0 & 0 & 0 & 1
 \end{bmatrix}$$

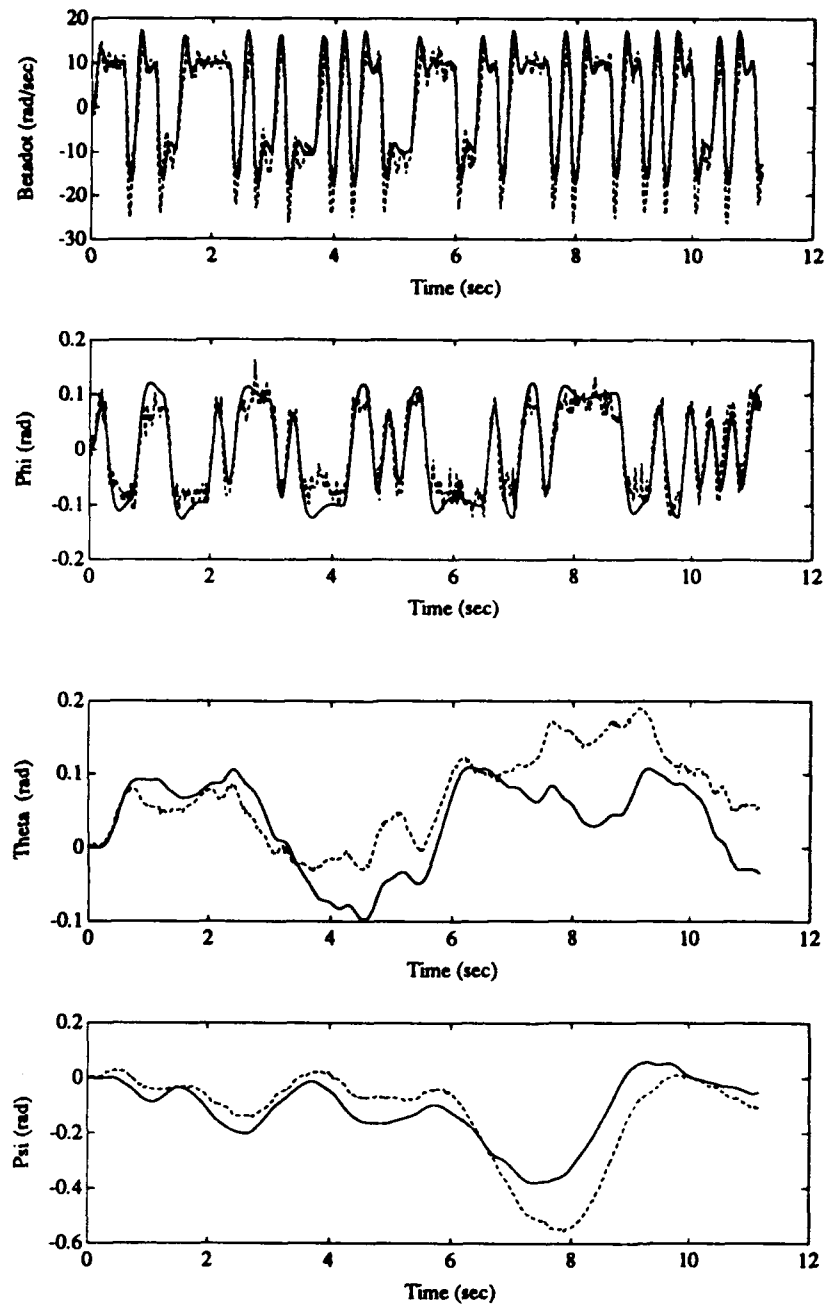


Figure 3.24 Response of refined model and actual system to PRBS inputs.

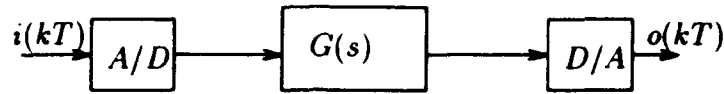
4. CONTROL SYSTEM DESIGN

Three types of control systems are designed for the purpose of determining their effects upon pilot performance. An open loop uncompensated system is designed such that a joystick commands main rotor speed for pitch axis control and rotor tilt angle for yaw axis control. A rate command system is designed where the joystick commands pitch and yaw rate. This is accomplished by using a feedback control system with lead-lag compensators. Pitch and yaw angle sensor signals can not be differentiated to obtain reliable rate feedback signals because of sensor noise. A Kalman filter is designed obtain reliable estimates of all unmeasurable states, particularly pitch and yaw rate ($\dot{\Theta}$ and $\dot{\Psi}$), in spite of noisy measurements, unknown disturbances and model uncertainty. Attitude command systems are designed such that the joystick commands pitch and yaw attitude. This is accomplished by feeding back attitude measurements from the pitch and yaw angle sensors to the main rotor and tilt servo respectively.

Compensators for the rate and attitude command systems are designed in continuous time assuming measurements are available for feedback. Discrete equivalents of the continuous compensators are then designed by emulation using a frequency prewarped bilinear transformation. The command systems are implemented digitally on a Mac II-si digital computer equipped with an A/D, D/A board.

4.1 Discrete Models of Sampled Data Systems

The systems developed in this chapter contain both continuous and discrete components. Compensators are designed assuming that continuous signals are available for feedback. Digital compensators (filters) are designed to emulate their continuous



is equivalent to :

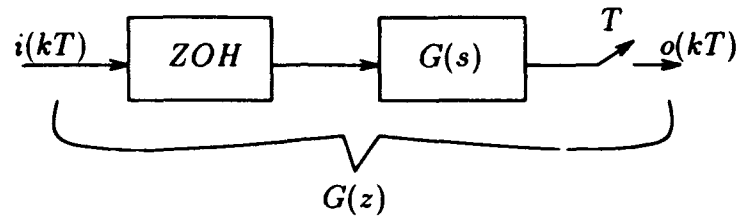


Figure 4.1 General sampled data system.

counterparts because a digital computer with A/D and D/A converters is used to implement control laws. The A/D converter samples continuous time signals at regular time intervals T . The computer then processes the samples through the control law (digital filter) and sends the command to a D/A converter which holds the command constant until the next sample is received. The D/A converter acts as a zero order hold (ZOH) which derives its name from the order of the polynomial function which describes the shape of the output between samples. Since the output is constant between samples, the polynomial is of order zero. Figure 4.1 shows the general A/D, D/A processes with a continuous time system. An exact discrete representation of Figure 4.1 is given by Equation 4.1 [4].

$$G(z) = (1 - z^{-1}) \mathcal{Z} \left\{ \frac{G(s)}{s} \right\} \quad [4.1]$$

where \mathcal{Z} denotes the z-transform of $G(s)/s$ which is given by

$$\mathcal{Z} \left\{ \frac{G(s)}{s} \right\} \equiv \mathcal{Z} \left\{ \mathcal{L}^{-1} \left\{ \frac{G(s)}{s} \right\} \right\} \quad [4.2]$$

where \mathcal{L}^{-1} denotes the inverse Laplace transform. Sampled data systems of this type may therefore be analyzed using z-transform techniques.

4.2 Digital Compensator Design by Emulation

Continuous compensators are designed using classical continuous control techniques. It is assumed that continuous measurements are available for feedback. The pitch and roll axes are assumed to be uncoupled and the yaw axis is assumed to be unaffected by main rotor speed. Digital filters or discrete compensators are designed to emulate the continuous compensator designs which are based on the above assumptions. The bilinear transformation (Equation 4.3) maps the stable region of the s -plane ($\Re(s) < 0$) into the stable region of the z -plane ($|z| < 1$).

$$s = \frac{2}{T} \frac{z - 1}{z + 1} \quad [4.3]$$

A considerable amount of distortion takes place even though the stability regions are coincident. This causes the frequency response characteristics of the digital filter to differ from those of the continuous compensator. To make the frequency responses of the digital and continuous filters equal at a particular frequency ω_1 , a prewarping factor is used [4]. The prewarped discrete equivalent compensator may be realized by implementing Equation 4.4.

$$K(z) = K(s) \Big|_{s = \frac{1}{\tan(\omega_1 T/2)} \frac{z-1}{z+1}} \quad [4.4]$$

4.3 Digital Filter Programming

Consider a digital filter of the form given in Equation 4.5.

$$K(z) = \frac{O(z)}{I(z)} = \frac{b_0 + b_1 z^{-1} + \dots + b_m z^{-m}}{1 + a_1 z^{-1} + a_2 z^{-2} + \dots + a_n z^{-n}} \quad [4.5]$$

Since z^{-1} represents a unit delay, a difference equation for the filter output may be written.

$$o(k) = -a_1 o(k-1) - a_2 o(k-2) - \dots - a_n o(k-n) + b_0 i(k) + b_1 i(k-1) + \dots + b_m i(k-m) \quad [4.6]$$

It can be seen that $n + m$ delays or storage registers must be used to realize this difference equation. Implementation of Equation 4.6 is called the direct programming

approach [15]. The number of storage registers may be reduced from $n + m$ to n where $n \geq m$ by using the standard programming method [15]. The pulse transfer function $O(z)/I(z)$ may be written

$$K(z) = \frac{O(z)}{I(z)} = \frac{O(z)}{H(z)} \frac{H(z)}{I(z)} \quad [4.7]$$

where

$$\frac{O(z)}{H(z)} = b_0 + b_1 z^{-1} + \dots + b_m z^{-m}$$

and

$$\frac{H(z)}{I(z)} = \frac{1}{1 + a_1 z^{-1} + a_2 z^{-2} + \dots + a_n z^{-n}}$$

The following difference equations may now be written

$$o(k) = b_0 h(k) + b_1 h(k-1) + b_2 h(k-2) + \dots + b_m h(k-m) \quad [4.8]$$

$$h(k) = i(k) - a_1 h(k-1) - a_2 h(k-2) - \dots - a_n h(k-n) \quad [4.9]$$

Note that only n storage registers are required to obtain $o(k)$. This saves computer memory and processing time. The difference equations are implemented as dot products.

$$h(k) = [-a_0 \quad -a_1 \quad \dots \quad -a_n] \cdot [i(k) \quad h(k-1) \quad \dots \quad h(k-n)] \quad [4.10]$$

$$o(k) = [b_0 \quad b_1 \quad \dots \quad b_n] \cdot [h(k) \quad h(k-1) \quad \dots \quad h(k-m)] \quad [4.11]$$

4.4 Open Loop System

The joystick is used to control main rotor speed and rotor tilt angle for pitch and yaw control respectively. No stability augmentation systems are implemented in this case. Figure 4.2 shows a block diagram of the open loop systems. Joystick commands are sampled and sent to the actuator every 0.05 sec. For the purpose of analysis, the pitch Θ and roll Φ axes are assumed to be uncoupled since the primary pitch axis

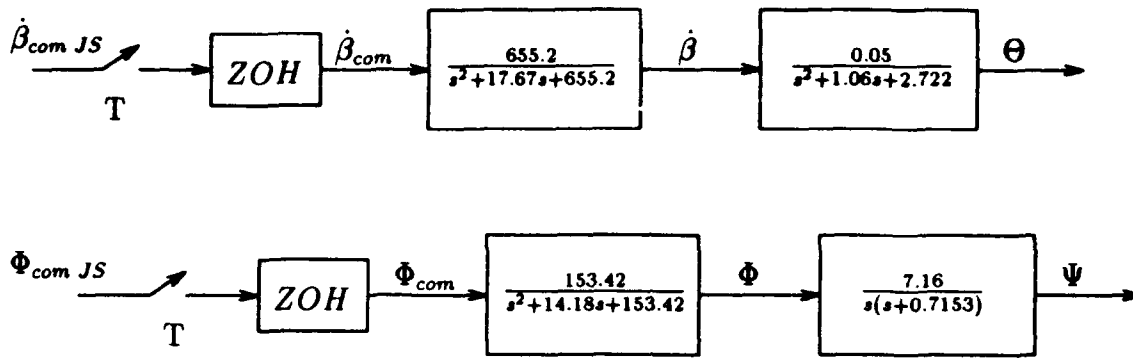


Figure 4.2 Open loop command system block diagram.

controller is main rotor speed $\dot{\beta}$. Figure 4.3 shows the Bode plot of the open loop pitch axis system of Figure 4.2. One can see that it has a flat frequency response out to about 1.65 rad/sec and very low gain (-35 dB). The Bode plot of the open loop yaw system is shown in Figure 4.4. One can see that the system crossover frequency is at 2.7 rad/sec and the phase margin is 15° . The low frequency -20 dB/dec slope is indicative of the presence of a pure integral or $1/s$ term in the system dynamics.

Actuators are saturated digitally before they hit their physical limits for safety reasons. The main rotor is limited to speeds between 240 and 360 rad/sec while the travel of the tilt servo is limited to the region $-0.3 \leq \Phi \leq 0.3$ rad. The rate limit on the main rotor discussed in Chapter 3 is not considered since its effects are not significant in the frequency range of interest (see Chapter 5).

4.5 Attitude Command Systems

4.5.1 Yaw Axis

The following specifications are set for the yaw attitude command system

- Closed loop stability.
- Gain Margin ≥ 6 dB
- Phase Margin $\varphi_m \geq 40^\circ$.

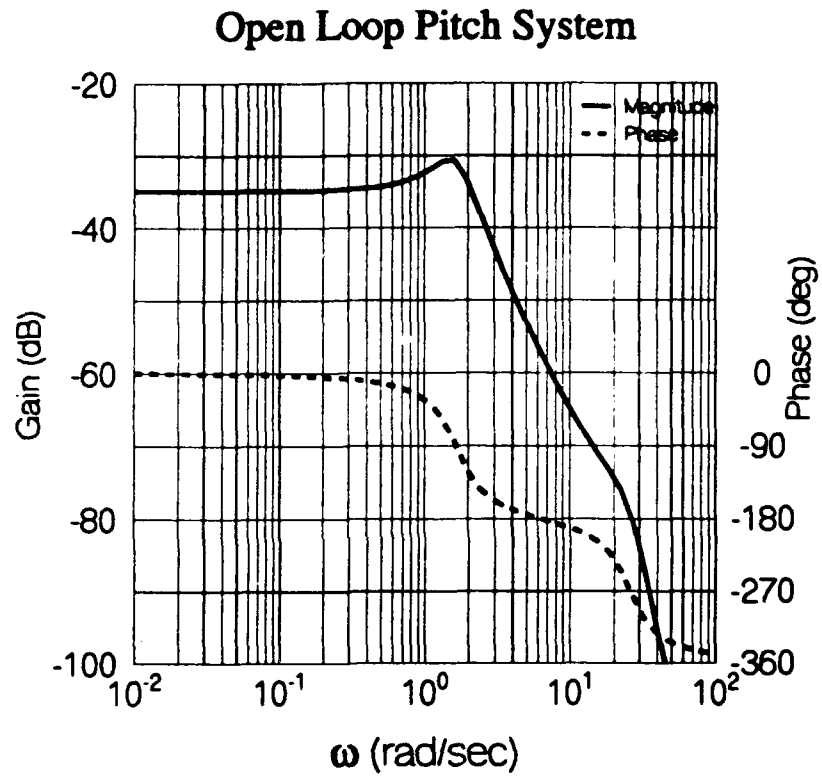


Figure 4.3 Bode plot of open loop pitch system $\Theta(j\omega)/\dot{\beta}_{com}(j\omega)$.

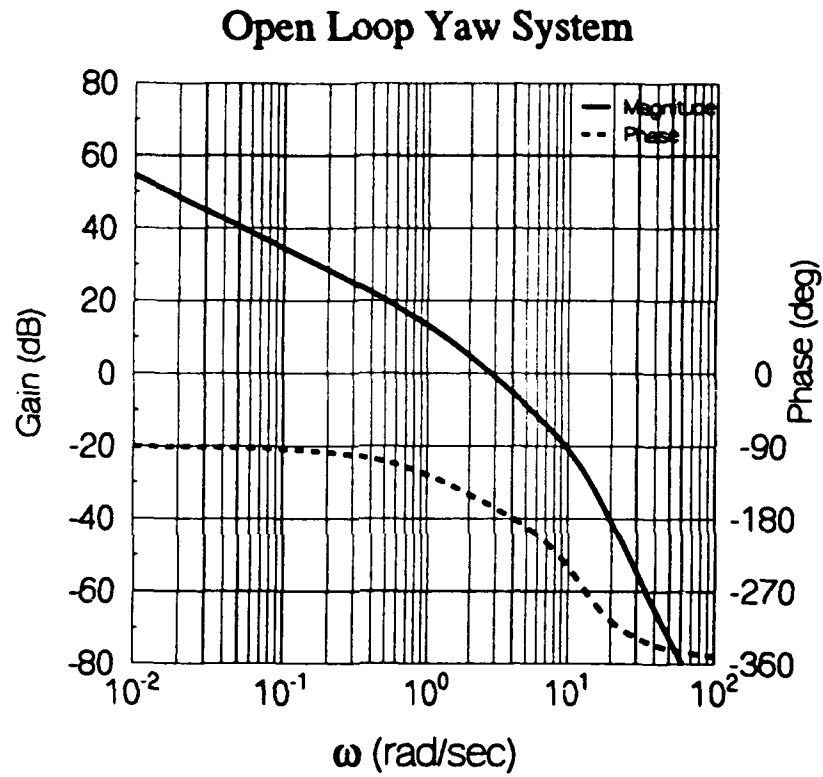


Figure 4.4 Bode plot of open loop yaw system $\Psi(j\omega)/\Phi_{com}(j\omega)$.

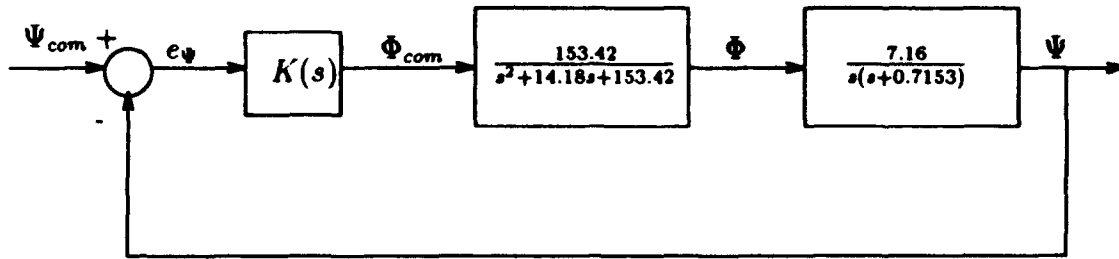


Figure 4.5 Closed loop continuous yaw attitude command system.

- Closed Loop -3 dB cutoff frequency $\omega_{-3dB} > 3$ rad/sec.
- Steady state error to a step $\leq 5\%$ ($K_p \geq 19$) where K_p is the position error constant [16].

Figure 4.5 shows a block diagram of the closed loop yaw axis, tilt servo dynamics and cascade compensator. The steady state requirement is met without compensation because of the pure integral term in the yaw axis dynamics.

$$K_p = \lim_{s \rightarrow 0} \frac{153.42}{s^2 + 14.18s + 153.42} \frac{7.16}{s(s + .7153)} = \frac{7.16}{0} = \infty \quad [4.12]$$

From Figure 4.6, one can see that the uncompensated system has the following properties:

- Gain crossover frequency $\omega_{gc} = 2.7$ rad/sec
- Phase margin $\varphi_m = 15^\circ$
- Gain margin = 5.33 dB

The target crossover frequency is selected to be $\omega_t = 3$ rad/sec. The phase deficiency at $\omega_t = 3$ rad/sec is 43° . A lead compensator is designed to contribute 60° of phase lead at 3 rad/sec. The form of the lead compensator is given in Equation 4.13 .

$$K(s) = \frac{K(\tau s + 1)}{\alpha \tau s + 1} \quad [4.13]$$

where

$$\alpha = \frac{1 - \sin \phi_{max}}{1 + \sin \phi_{max}}$$

and

$$\tau = \frac{1}{\omega_t \sqrt{\alpha}}$$

where ϕ_{max} is the maximum phase lead contribution of the filter. In this case $\alpha = 0.0718$ and $\tau = 1.244$. The increase in gain due to the inclusion of the lead filter at 3 rad/sec is 11.43 dB; therefore, the filter gain is set to -11.43 dB or $K = 0.26795$. Theoretically this configuration meets the specifications; however, it is experimentally determined that this compensator did not satisfy the steady state error requirements. This is because the compensator is designed based on a linear model which includes only viscous friction. In practice, static and coulomb friction exist and these phenomena have significant effect upon steady state error. A lag compensator is cascaded with the lead compensator designed above to improve steady state tracking. The entire compensator is given by Equation 4.14.

$$K(s) = 0.26795 \overbrace{\frac{s + .5}{s + .001}}^{\text{Lag}} \overbrace{\frac{1.244s + 1}{0.0893s + 1}}^{\text{Lead}} \quad [4.14]$$

Figures 4.6 and 4.7 show the continuous open and closed loop Bode plots for the yaw attitude command system. One can see that the compensated system meets the specifications.

- Closed loop stability.
- Gain Margin = 10.43 dB
- Phase Margin $\varphi_m = 66.93^\circ$.
- Closed Loop -3 dB cutoff frequency $\omega_{-3dB} = 6.154$ rad/sec.
- Zero steady state error to a step input ($K_p = \infty$)

Figure 4.8 shows a block diagram of the yaw attitude sampled data system. The digital compensator $K(z)$ is designed to emulate the continuous compensator designed above. The bilinear transformation with prewarping is used to design the discrete

Open Loop Continuous Yaw Attitude Command System

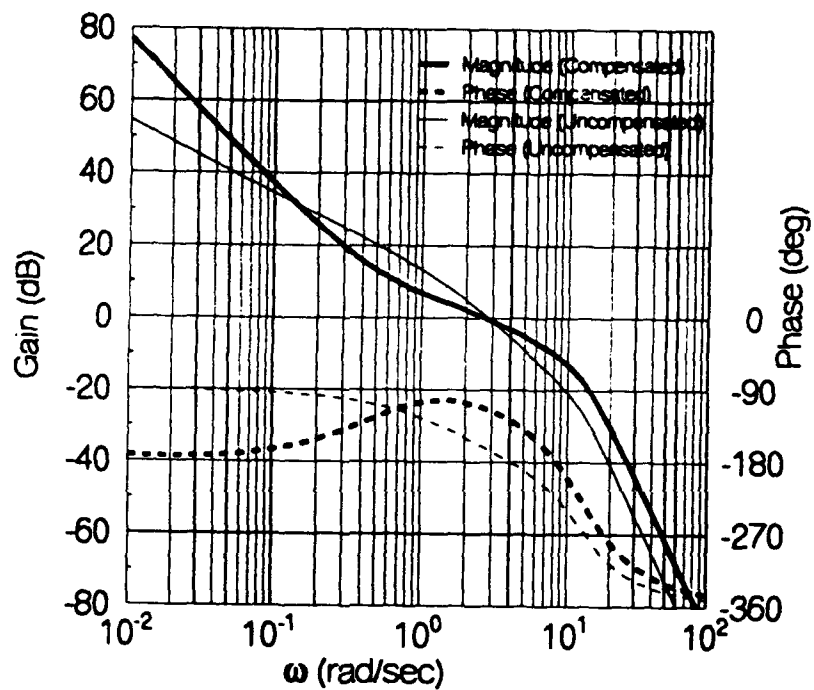


Figure 4.6 Bode plot of open loop continuous uncompensated and compensated yaw attitude command system $\Psi(j\omega)/e_{\psi}(j\omega)$.

Closed Loop Continuous Yaw Attitude Command System

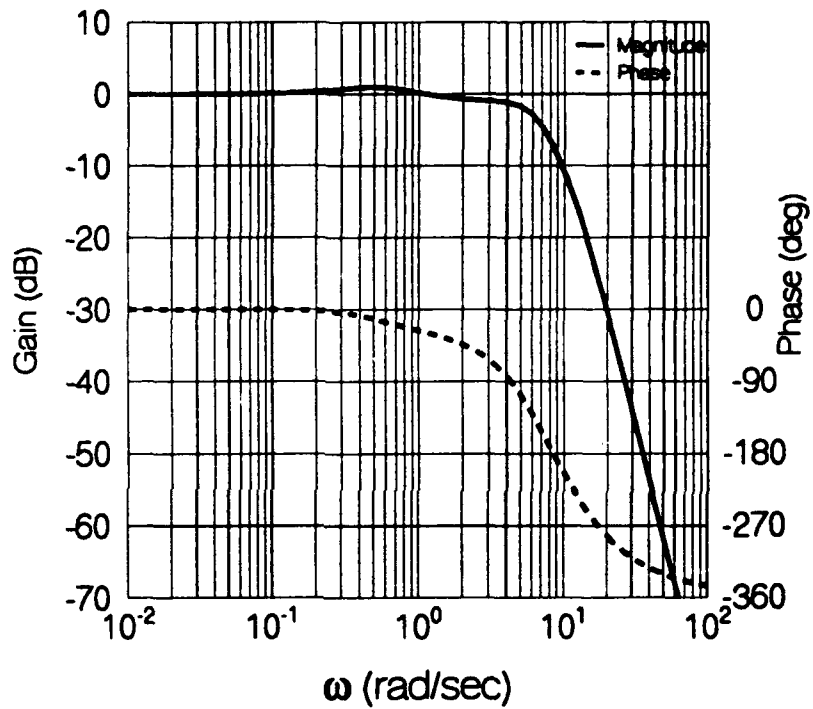
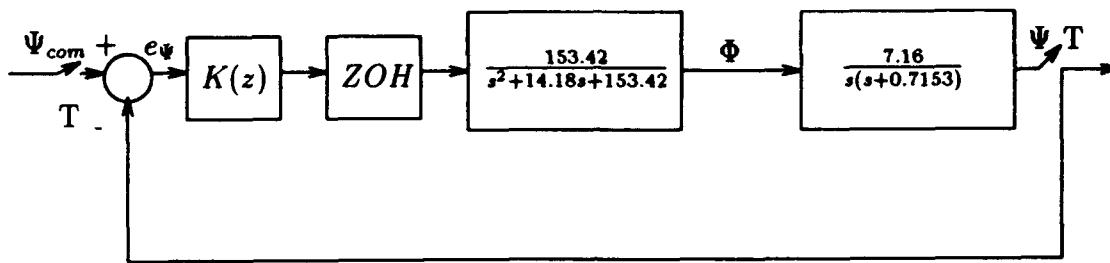


Figure 4.7 Bode plot of closed loop continuous compensated yaw attitude command system $\Psi(j\omega)/\Psi_{com}(j\omega)$.



OR EQUIVALENTLY:

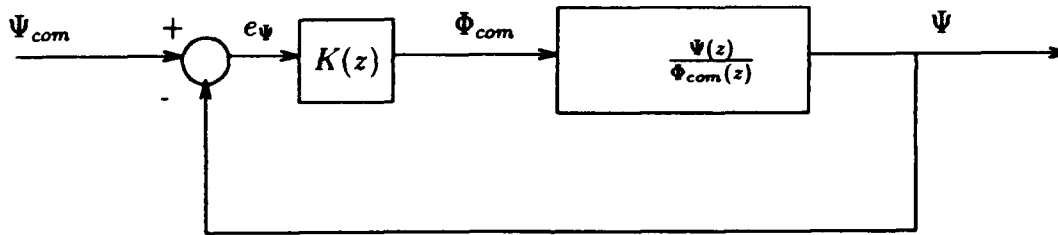


Figure 4.8 Closed loop sampled data yaw attitude command system.

equivalent. The sampling period is $T=0.05$ sec ($\omega_s = 125.6$ rad/sec) which exceeds the sampling theorem requirement since the closed loop bandwidth is $\omega_{-3dB} = 6.1504$ rad/sec. The warping frequency is selected to preserve the frequency response of the continuous filter at $\omega = 3$ rad/sec. The discrete equivalent filter is given below

$$K(z) = \frac{3.0104z^2 - 5.8276z + 2.8201}{z^2 - 1.5619z + 0.5620} \quad [4.15]$$

Figures 4.9 and 4.10 show the open and closed loop Bode plots of the discrete system of Figure 4.8. The properties of the discrete yaw attitude command system are:

- Closed loop stability.
- Gain Margin = 9.074 dB
- Phase Margin $\varphi_m = 63^\circ$.
- Open loop gain crossover frequency $\omega_{gc} = 2.7037$ rad/sec
- Closed Loop -3 dB cutoff frequency $\omega_{-3dB} = 6.16$ rad/sec.
- Zero steady state error to a step input ($K_p = \infty$)

which meet the specifications.

The digital filter $K(z)$ is implemented using the standard programming technique discussed in Section 4.3. Figure 4.11 shows the actual and simulated step responses of the yaw attitude command system. It can be seen that the desired control action is achieved. The short (< 0.5 sec) time delay at the beginning of the actual step responses is likely caused by static friction. The actual positive step response does not rise or attain steady state as quickly as the actual negative step response. Recall that the viscous yaw axis damping coefficients are direction dependent and the linear model used an average of the two coefficients. This explains why the motion of the yaw axis is more damped in the positive direction than the negative. Both positive and negative experimental step responses indicate that there is more damping present than predicted by the linear model. This is most likely the result of unmodeled nonlinear

Open Loop Discrete Yaw Attitude Command System

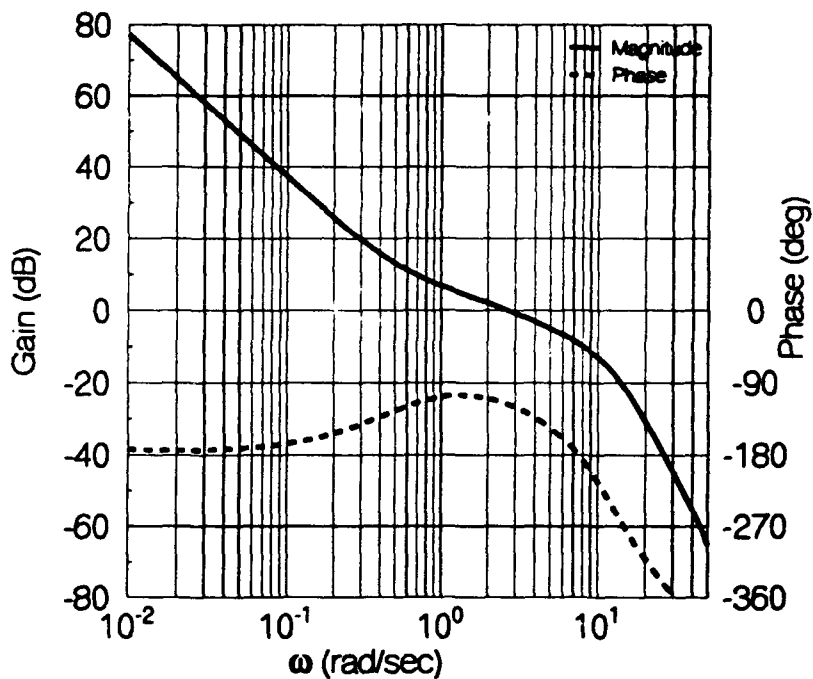


Figure 4.9 Bode plot of open loop discrete compensated yaw attitude command system $\Psi(e^{j\omega T})/e_{\Psi}(e^{j\omega T})$.

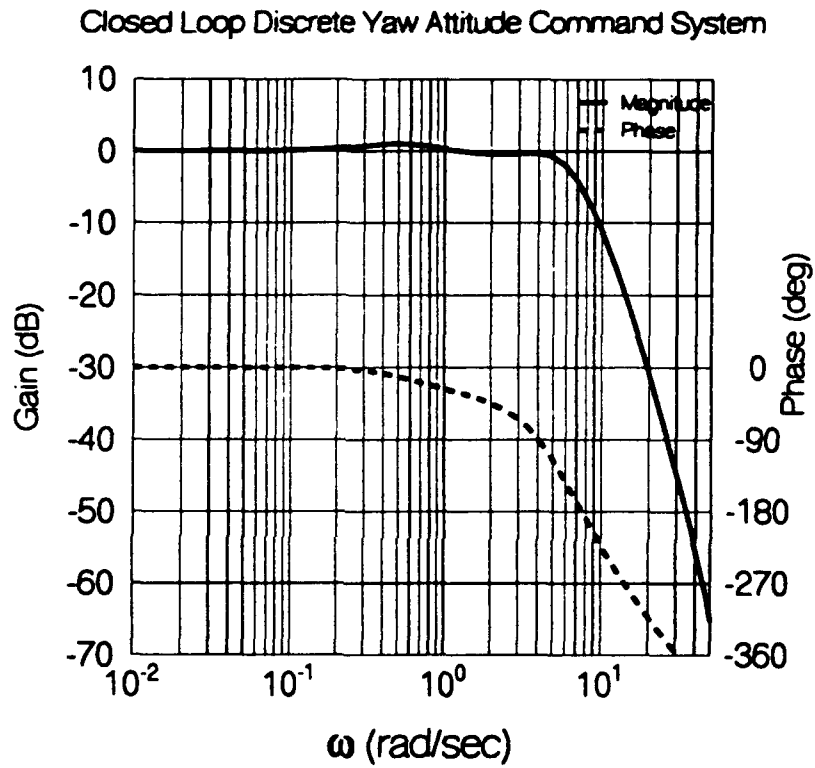


Figure 4.10 Bode plot of closed loop discrete compensated yaw attitude command system $\Psi(e^{j\omega T})/\Psi_{com}(e^{j\omega T})$.

coulomb friction. Despite the nonlinearities, one can see that this system does track attitude commands reasonably well. The refined model of Chapter 3 empirically models the effects of the static and coulomb friction by replacing the free $1/s$ in the denominator of the yaw transfer function with a lag term $1/(s + .7153)$. Figure 4.12 show the actual and simulated results using the refined yaw axis model. One can see that the refined yaw axis model predicts the behavior rather well.

4.5.2 Pitch Axis

The following specifications are set for the pitch attitude command systems:

- Closed loop stability.
- Gain Margin ≥ 6 dB
- Phase Margin $\varphi_m \geq 40^\circ$.
- Closed Loop -3 dB cutoff frequency $\omega_{-3dB} > 3$ rad/sec.
- Steady state error to a step $\leq 5\%$ ($K_p \geq 19$) where K_p is the position error constant [16].

Figure 4.13 shows a block diagram of the closed loop pitch axis dynamics, main rotor actuator and cascade compensator. First $K(s)$ is found to satisfy the steady state error requirement.

$$K_p = \lim_{s \rightarrow 0} \frac{K \cdot 655.2}{s^2 + 17.67s + 655.2} \frac{0.05}{s^2 + 1.064s + 2.722} = 0.0184 K \quad [4.16]$$

therefore $K = 1034.5$. The open loop system is unstable for the value of K chosen as indicated by the negative phase margin $\varphi_m = -4.0288^\circ$. A lag-lead compensator is designed to improve low frequency tracking and increase the phase margin at the target crossover frequency $\omega_t = 4$ rad/sec. The continuous compensator which met the specification is given in Equation 4.17.

$$K(s) = 1034.5 \frac{\overbrace{s+2}^{\text{Lag}}}{s+0.01} \frac{\overbrace{s+0.5}^{\text{Lead}}}{s+15} \quad [4.17]$$

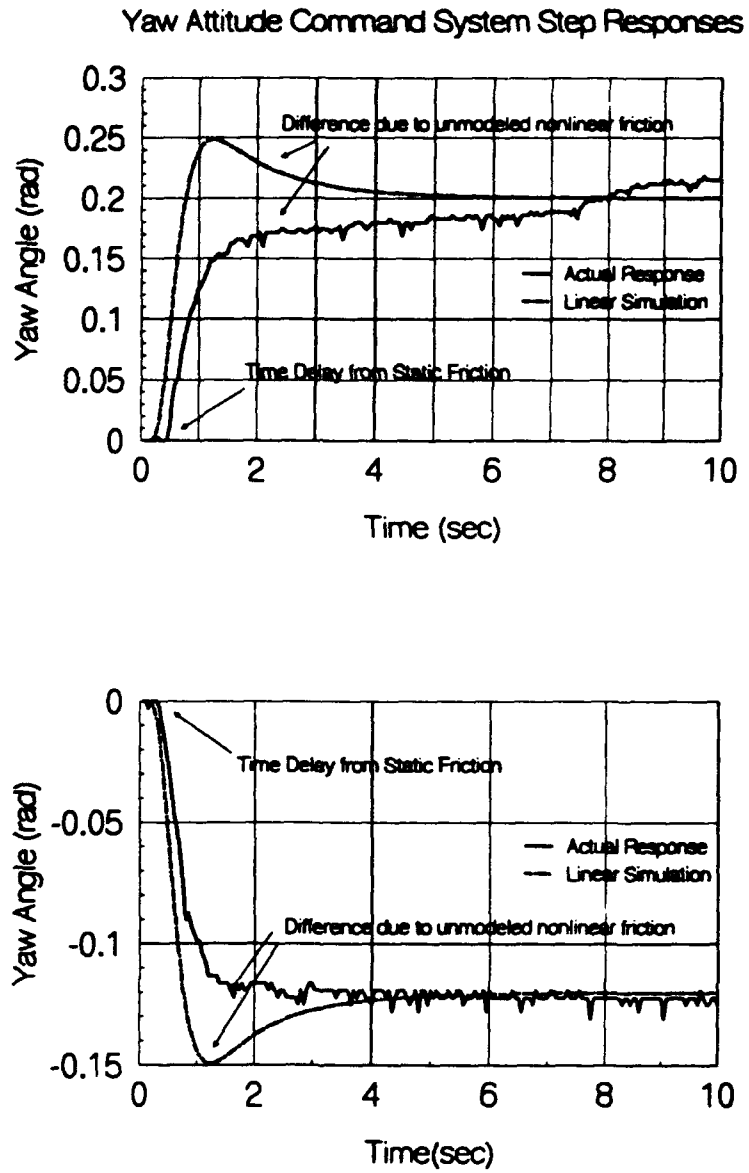


Figure 4.11 Simulated and actual yaw attitude command system step responses.

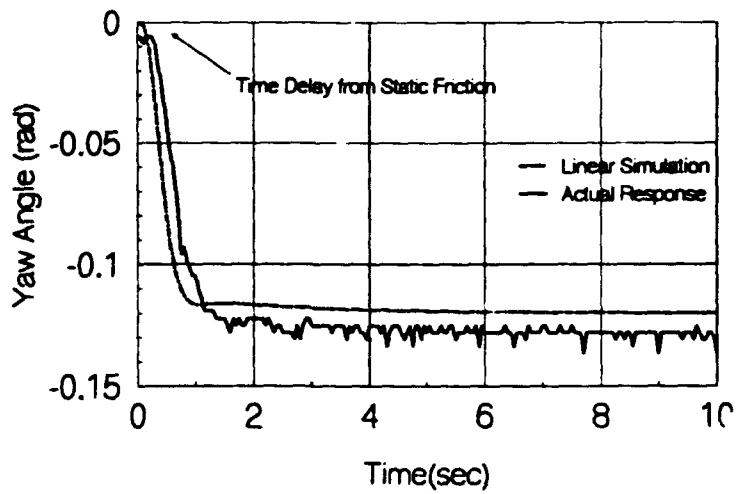
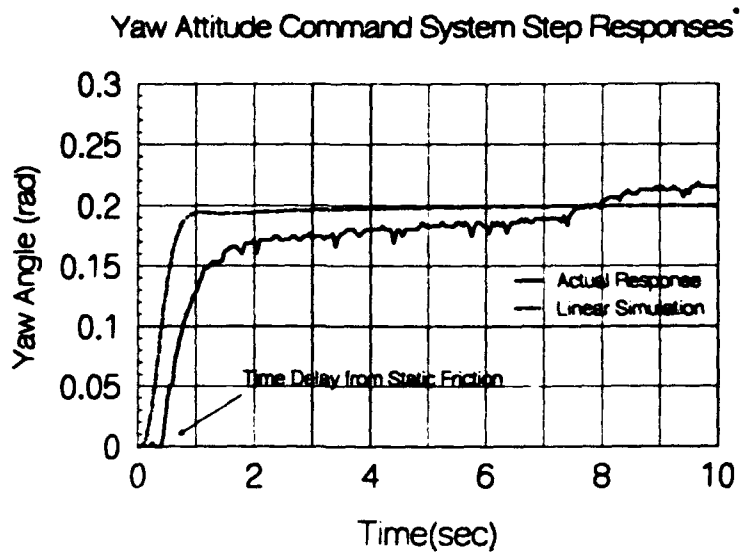


Figure 4.12 Simulated* and actual yaw attitude command system step responses. (* Refined yaw axis model.)

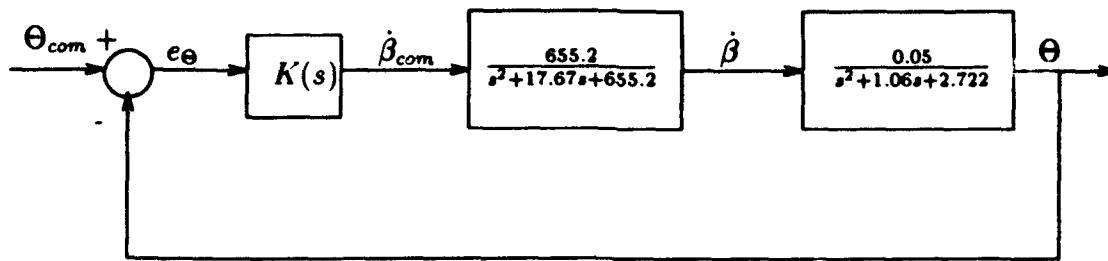


Figure 4.13 Sampled data pitch attitude command system.

Figures 4.14 and 4.15 show the open and closed loop Bode plots for the continuous pitch attitude command system. The continuous compensated system has the following characteristics:

- Gain margin = 13.98 dB
- Phase margin $\varphi_m = 52.15^\circ$
- Open loop gain crossover frequency $\omega_{gc} = 4.27$ rad/sec
- Closed loop -3 dB cutoff frequency $\omega_{-3dB} = 7.127$ rad/sec
- Steady state error to a step 0.8% or $K_p = 124$

One can see that the design meets the specifications.

Figure 4.16 shows a block diagram of the closed loop sampled data pitch axis command system. The digital compensator (filter) $K(z)$ is designed to emulate the continuous compensator $K(s)$. The bilinear transformation with frequency prewarping is used to accomplish this task. The warping frequency is selected to be $\omega_1 = 4$ rad/sec and the sampling period is chosen to be $T = 0.05$ sec ($\omega_s = 125.6$ rad/sec). The sampling frequency exceeds the closed loop -3 dB cutoff frequency by a factor of 17.64. The discrete equivalent compensator $K(z)$ is given by Equation 4.18.

$$K(z) = \frac{798.37z^2 - 1500.30z + 703.83}{z^2 - 1.45z + 0.45} \quad [4.18]$$

Figures 4.17 and 4.18 show the open and closed loop Bode plots of the discrete system of Figure 4.16. The properties of the discrete pitch attitude command system are:

Open Loop Continuous Pitch Attitude Command System

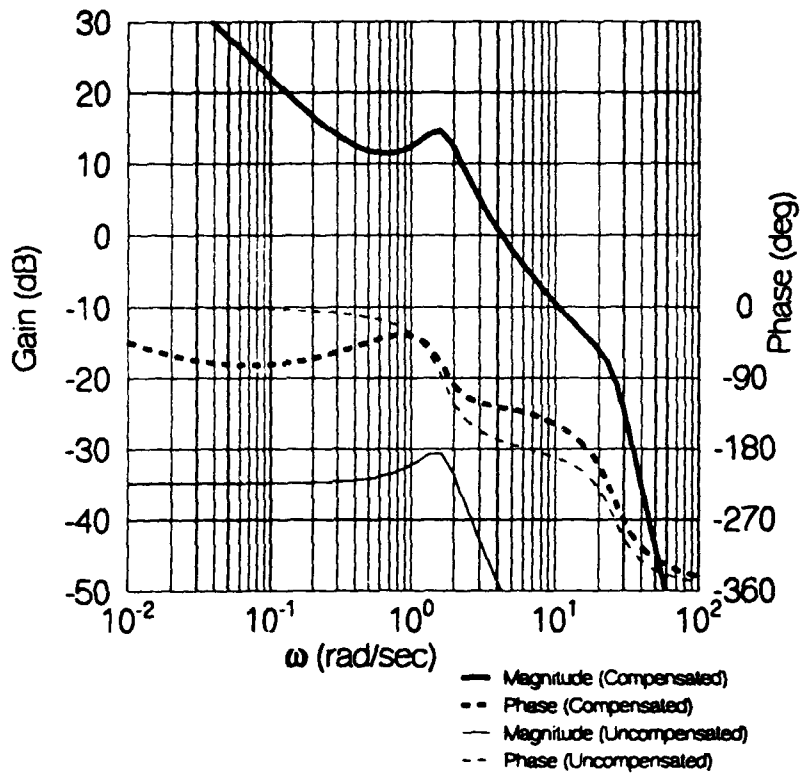


Figure 4.14 Bode plot of open loop continuous compensated and uncompensated pitch attitude command system $\Theta(j\omega)/e_{\Theta}(j\omega)$.

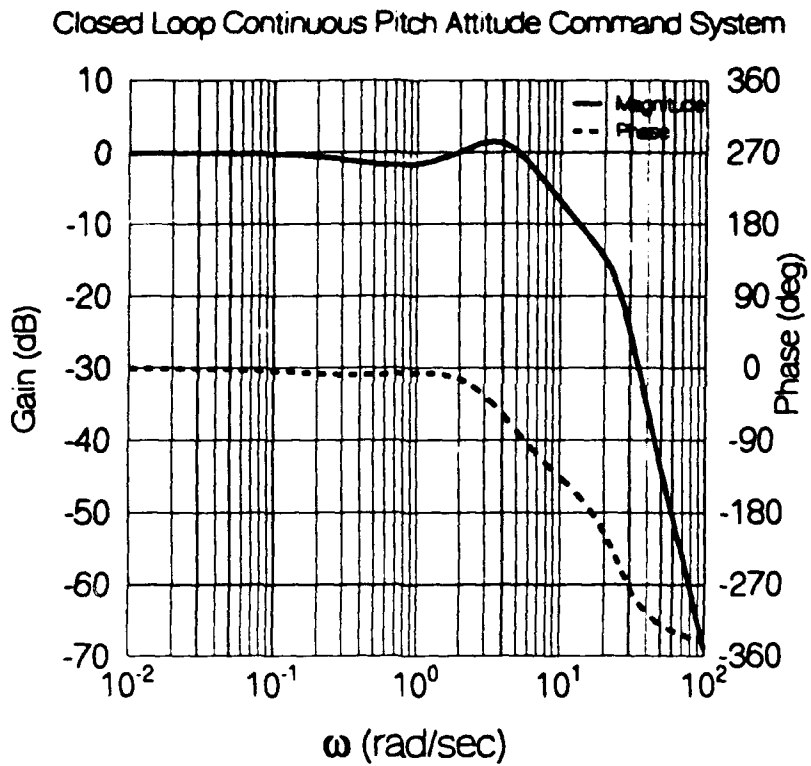


Figure 4.15 Bode plot of closed loop continuous compensated pitch attitude command system $\Theta(j\omega)/\Theta_{com}(j\omega)$.

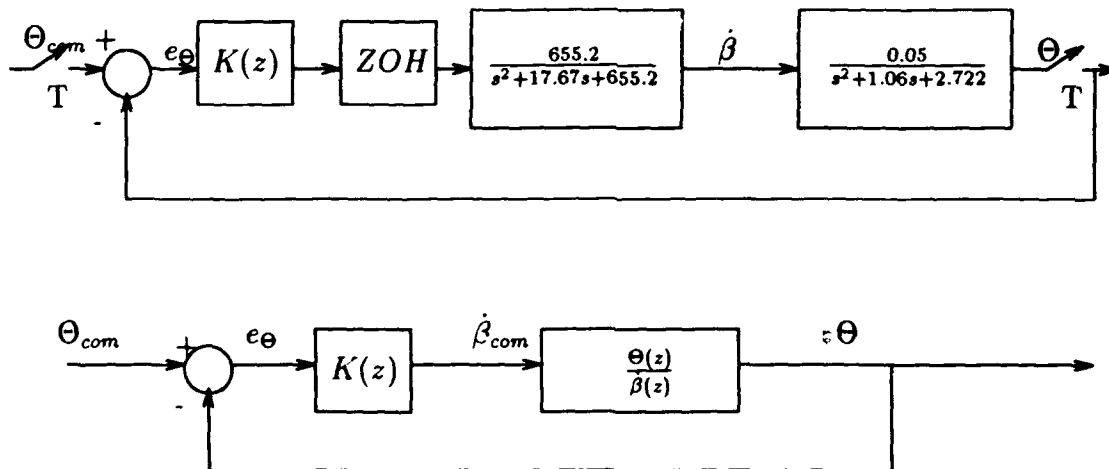


Figure 4.16 Sampled data pitch attitude command system.

- Gain margin = 11.87 dB
- Phase margin $\varphi_m = 46.03^\circ$
- Open loop gain crossover frequency $\omega_{gc} = 4.26$ rad/sec
- Closed loop -3 dB cutoff frequency $\omega_{-3dB} = 7.78$ rad/sec
- Steady state error to a step 0.8% or $K_p = 124$

which meet the specifications. The digital compensator is implemented using the standard programming technique described in Section 4.3. Figure 4.19 shows actual and simulated step responses of the pitch attitude command system. One can see that the desired control action is present. The actual response to a positive step Θ_{com} is lower than predicted for the first four seconds but approaches the simulated steady state value. The actual response to a negative step Θ_{com} overshoots the simulated response during the first second and reaches steady state faster than the simulated response. This is likely caused by the unmodeled main rotor speed rate limit. Recall that the linear model of the main rotor accurately described the actual frequency response out to 25 rad/sec. The step inputs consist of an infinite sum of sines of different amplitudes and frequencies; therefore, one can expect the unmodeled high frequency nonlinearity to have some effect on the step response. The forcing functions in the human pilot tests consist of a sum of 5 low frequency (<4 rad/sec) sine waves; therefore, the linear model adequately describes the main rotor dynamics in the frequency range of interest.

4.6 Rate Command Systems

In order to design rate command systems, rate measurements or estimates must be available for feedback. In this case, estimates of the angular rates are used because only attitude measurements are available. The simplest estimate of pitch and yaw rate given sampled attitude measurements is given by Equation 4.19.

$$\dot{\Theta}(k) = \frac{\Theta(k) - \Theta(k-1)}{T} ; \dot{\Psi}(k) = \frac{\Psi(k) - \Psi(k-1)}{T} \quad [4.19]$$

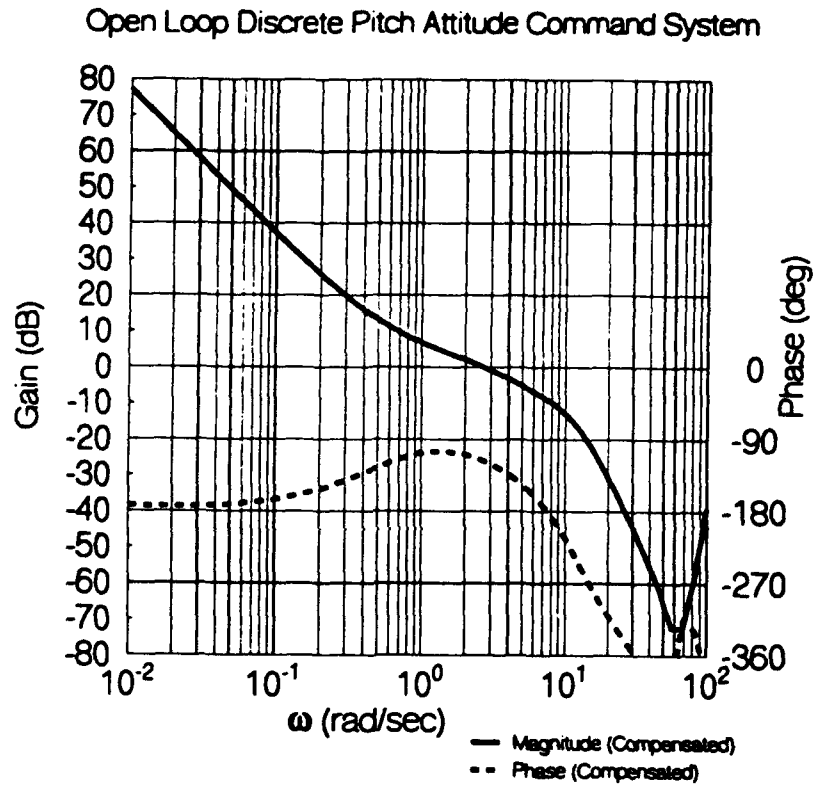


Figure 4.17 Bode plot of open loop discrete compensated pitch attitude command system $\Theta(e^{j\omega T})/e_{\Theta}(e^{j\omega T})$.

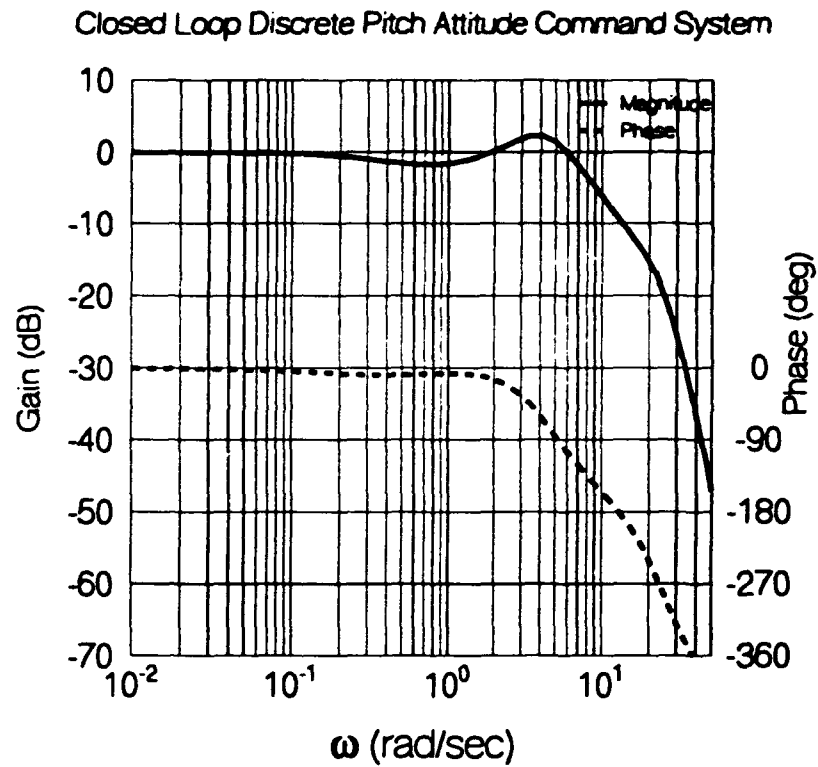


Figure 4.18 Bode plot of closed loop discrete compensated pitch attitude command system $\Theta(e^{j\omega T})/\Theta_{com}(e^{j\omega T})$.

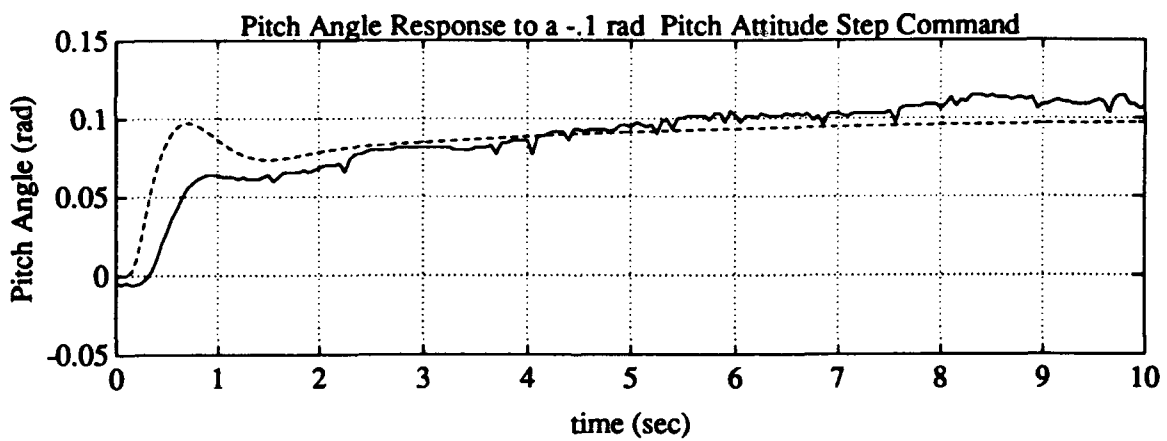
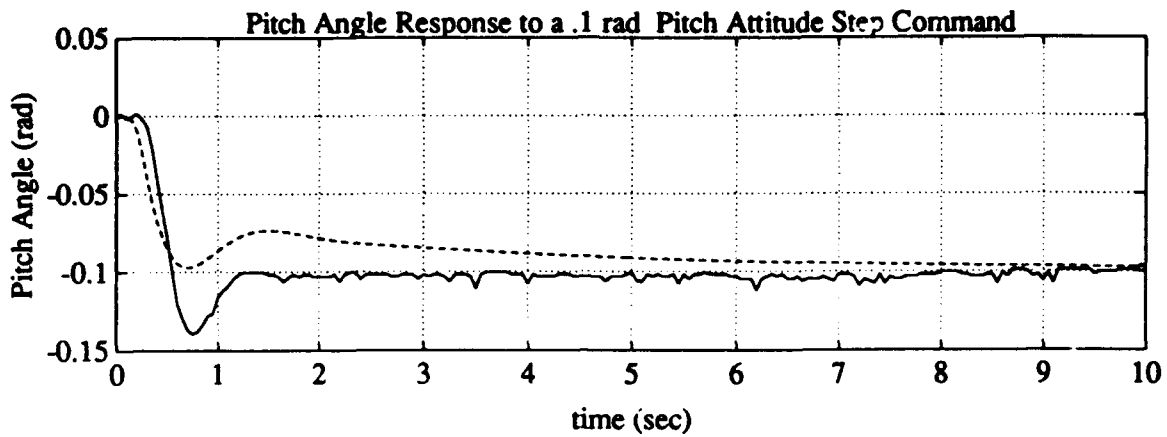


Figure 4.19 Simulated and actual step responses for pitch attitude command system.

Unfortunately the attitude measurements are contaminated with sensor noise and Equation 4.19 is very sensitive to noise. Sensor noise in the attitude measurements can make rate estimates calculated from Equation 4.19 have a large noise-to-signal ratio, especially for small T . Smoothed rate estimates are needed and obtained from an optimal state estimator or Kalman filter.

4.6.1 Kalman Filter

A digital steady state Kalman filter is designed to obtain reliable rate estimates in the presence of sensor and process noise. The process noise crudely accounts for unknown disturbances and model imperfections.

The continuous state space model of the TROFM is discretized for $T = 0.05$ sec.

$$\mathbf{x}(k+1) = \Phi \mathbf{x}(k) + \Gamma \mathbf{u}(k) + \mathbf{G} \mathbf{w}(k) \quad [4.20]$$

$$\mathbf{y}(k) = \mathbf{C} \mathbf{x}(k) + \mathbf{v}(k) \quad [4.21]$$

$$\mathbf{x}(k) = \left[\dot{\Phi}(k) \quad \dot{\Theta}(k) \quad \dot{\Psi}(k) \quad \ddot{\beta}(k) \quad \dot{\beta}(k) \quad \Phi(k) \quad \Theta(k) \quad \Psi(k) \right]^T$$

$$\mathbf{u}(k) = \left[\dot{\beta}_{com}(k) \quad \Phi_{com}(k) \right]^T$$

where $\Phi = e^{\mathbf{A}T}$, $\Gamma = \int_0^T e^{\mathbf{A}\tau} d\tau B$, $\mathbf{w}(k)$ is the process noise and $\mathbf{v}(k)$ is the sensor noise which are assumed to be zero mean, Gaussian "white" random sequences with covariances \mathbf{Q} and \mathbf{R} respectively. The discrete sensor noise covariance is assumed to be diagonal in form and the elements of the covariance matrix are computed from experimental data using Equation 4.22.

$$\sigma_i^2 = \frac{1}{N} \sum_{k=0}^N (v_i(k) - \mu_i)^2 \quad [4.22]$$

where $v_i(k)$ is a sequence of N actual measurements taken with the TROFM in its nominal configuration ($\Theta = 0$ rad, $\Psi = 0$ rad, $\Phi_{com} = 0$ rad, $\dot{\beta} = 300$ rad/sec). The

experimentally determined discrete sensor noise covariance matrix \mathbf{R} is given by

$$\mathbf{R} = \begin{bmatrix} 1.7596 & 0 & 0 & 0 \\ 0 & 5.060 \times 10^{-4} & 0 & 0 \\ 0 & 0 & 1.825 \times 10^{-6} & 0 \\ 0 & 0 & 0 & 1.480 \times 10^{-4} \end{bmatrix} \quad [4.23]$$

The Kalman filter takes the form of the prediction estimator of Equation 4.24.

$$\bar{\mathbf{x}}(k+1) = \Phi \bar{\mathbf{x}}(k) + \Gamma \mathbf{u}(k) + \mathbf{L}_p [\mathbf{y}(k) - \mathbf{C} \bar{\mathbf{x}}(k)] \quad [4.24]$$

where \mathbf{L}_p is the Kalman gain matrix and the over-bar denotes prediction estimates. A prediction estimator is used instead of a current estimator to compensate for the time delay between the measurement and D/A conversion caused by the computer processing time required to generate estimates and compute control outputs. In other words, by the time the control action is taken, time has advanced about one sample time. If a current estimator is used the estimates are about one sampling period old by the time the control signal is sent to the actuator.

The software used to compute the feedback matrix solves for the matrix \mathbf{L}_c associated with the current estimator of Equation 4.25 [5].

$$\hat{\mathbf{x}}(k) = \bar{\mathbf{x}}(k) + \mathbf{L}_c (\mathbf{y}(k) - \mathbf{C} \bar{\mathbf{x}}(k)) \quad [4.25]$$

where $\bar{\mathbf{x}}(k)$ is the predicted estimate based on a model prediction from the previous estimate.

$$\bar{\mathbf{x}}(k) = \Phi \hat{\mathbf{x}}(k-1) + \Gamma \mathbf{u}(k-1) \quad [4.26]$$

The relationship between \mathbf{L}_p and \mathbf{L}_c may be deduced as follows:

- substitute Equation 4.25 into 4.26 to obtain

$$\bar{\mathbf{x}}(k) = \Phi [\bar{\mathbf{x}}(k-1) + \mathbf{L}_c [\mathbf{y}(k-1) - \mathbf{C} \bar{\mathbf{x}}(k-1)]] + \Gamma \mathbf{u}(k-1) \quad [4.27]$$

- shifting the index by +1 one obtains

$$\bar{\mathbf{x}}(k+1) = \Phi \bar{\mathbf{x}}(k) + \Phi \mathbf{L}_c [\mathbf{y}(k) - \mathbf{C} \bar{\mathbf{x}}(k)] + \Gamma \mathbf{u}(k) \quad [4.28]$$

Comparing the structure of Equation 4.28 to that of Equation 4.24, one may deduce that the prediction estimator feedback gain matrix L_p is related to L_c by Equation 4.29.

$$L_p = \Phi L_c \quad [4.29]$$

The design software determines the gain matrix L_c such that the discrete current estimator of Equation 4.25 produces an optimal estimate of the state vector x [5]. The steady state Kalman gain matrix is computed from Equation 4.30.

$$L_c = PC^T(CPC^T + R)^{-1} \quad [4.30]$$

where P is the unique positive definite solution to the algebraic Riccati equation

$$P = \Phi [P - PC^T(CPC^T + R)^{-1}CP] \Phi^T + GQG^T \quad [4.31]$$

The matrix P is the a priori (before the measurement update) estimation error covariance.

A pragmatic design rule states that L_p should be adjusted such that the residuals $\hat{y} = (y(k) - C\bar{x}(k))$ lie within plus or minus two standard deviations of the variance of the residuals. The residual covariance is given by Equation 4.32.

$$P_{\hat{y}} = CPC^T + R \quad [4.32]$$

The free design parameter Q allows one to adjust the process noise and thereby adjust the feedback matrix L_p . Since the Kalman filter is based on a linear model of the system which assumes that the process noise has the same power at all frequencies ("white") and it is known that the actual plant has several low frequency nonlinear characteristics, the final adjustment of Q is performed by analyzing time history data. The PRBS time history responses of Chapter 3 are used to determine how the filter performs on-line. The process noise is first adjusted to meet the design requirements. Next the Kalman filtered rate estimates are compared to the differentiated attitude measurements and Q is further adjusted to produce acceptably

smooth rate estimates. The process noise covariance which yielded acceptable results is given in Equation 4.33

$$Q = \begin{bmatrix} 10 & 0 & 0 & 0 & 0 & 0 & 0 & 0 \\ 0 & 10^{-5} & 0 & 0 & 0 & 0 & 0 & 0 \\ 0 & 0 & 10^{-2} & 0 & 0 & 0 & 0 & 0 \\ 0 & 0 & 0 & 10^4 & 0 & 0 & 0 & 0 \\ 0 & 0 & 0 & 0 & 0 & 0 & 0 & 0 \\ 0 & 0 & 0 & 0 & 0 & 0 & 0 & 0 \\ 0 & 0 & 0 & 0 & 0 & 0 & 0 & 0 \\ 0 & 0 & 0 & 0 & 0 & 0 & 0 & 0 \end{bmatrix} \quad [4.33]$$

Figure 4.20 shows the Kalman filtered state estimates and the residuals with $\pm 2\sigma(\tilde{y})$ lines where applicable.

The TROFM is occasionally required to operate outside of the range where the linear model is valid (i.e. during start-up or when the pilot finds it necessary in order to complete a task (see Chapter 5)). The pitch axis is linearized about $\Theta = 0$ and the linear model is only valid for small deviations about $\Theta = 0$. Recall that ground effect is modeled as a linear spring. In reality, it is nonlinear since the effective spring "constant" is a function of Θ . For large positive pitch attitudes $K_{GE}(\Theta) = 0$ and for large negative pitch attitudes $K_{GE}(\Theta) \gg K_{GE}(0)$. This means that the rotor speed $\bar{\beta}$ required to trim the TROFM is a function of pitch angle. The relationship between $\bar{\beta}$ and Θ is experimentally determined and is modeled by the third order polynomial fit of Equation 4.34.

$$\bar{\beta}(\Theta) = 301.2 + 22.83 \Theta - 113.8 \Theta^2 + 120.57 \Theta^3 \quad [4.34]$$

This equation modeled the trim behavior over the range $-0.6 \leq \Theta \leq 0.6$ rad/sec. The estimated trim rotor speed is subtracted from the measured absolute $\dot{\beta}$ to eliminate biased Θ and $\dot{\Theta}$ estimates. Without accounting for the biased $\dot{\beta}$, the Kalman filter overestimates Θ and $\dot{\Theta}$ for high values of Θ since the estimate of the perturbation

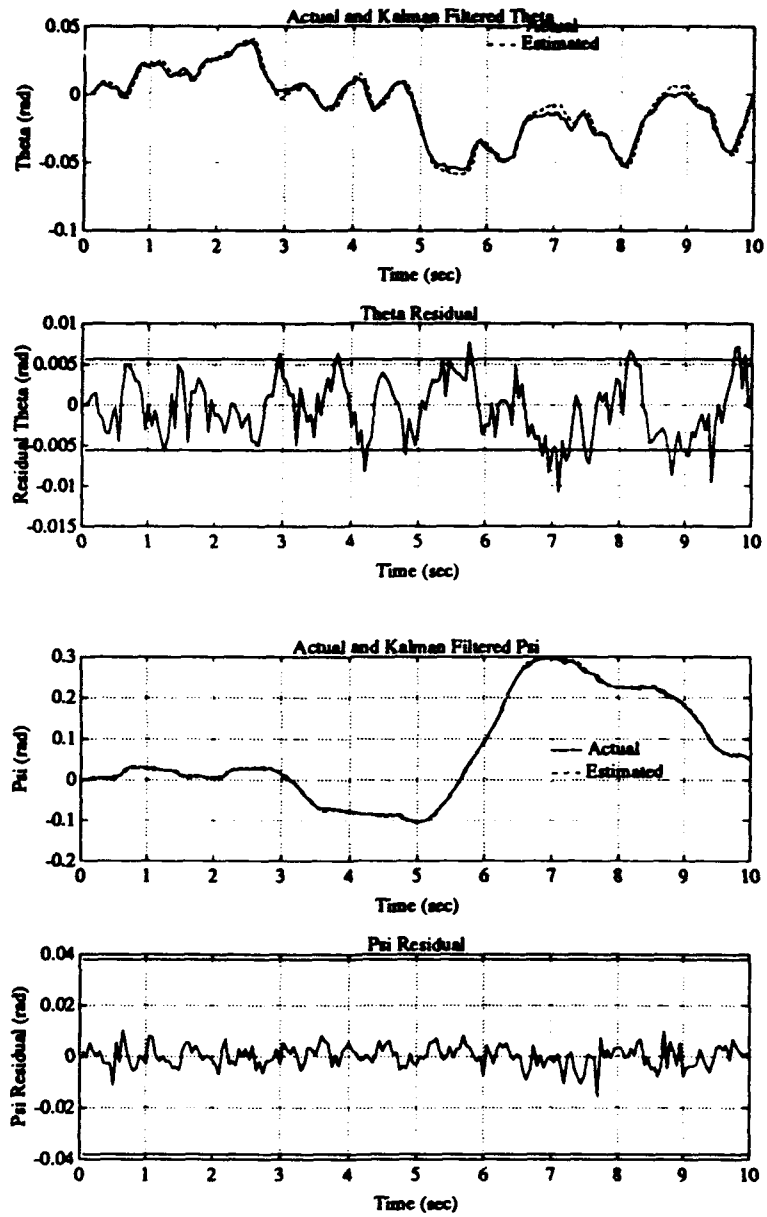


Figure 4.20 Kalman filtered state estimates, actual measurements and residuals with $\pm 2\sigma(\hat{y})$ lines from a PRBS test.

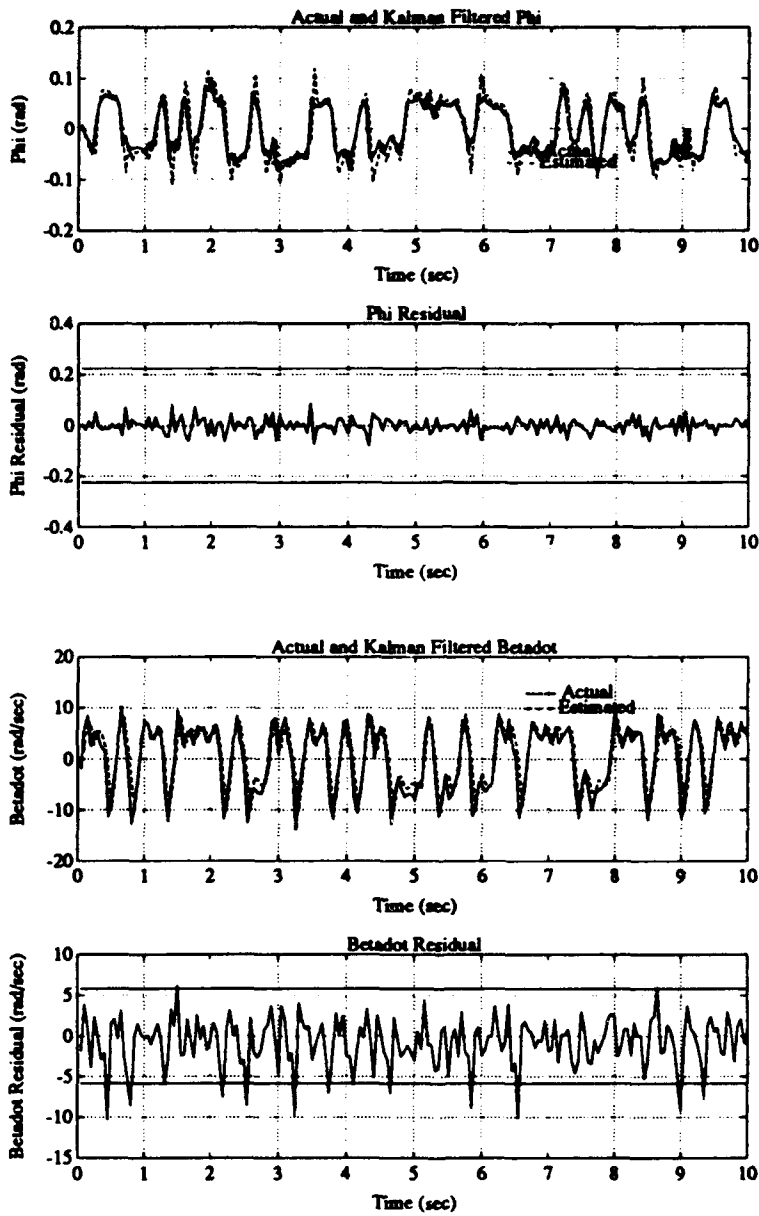


Figure 4.20, continued.

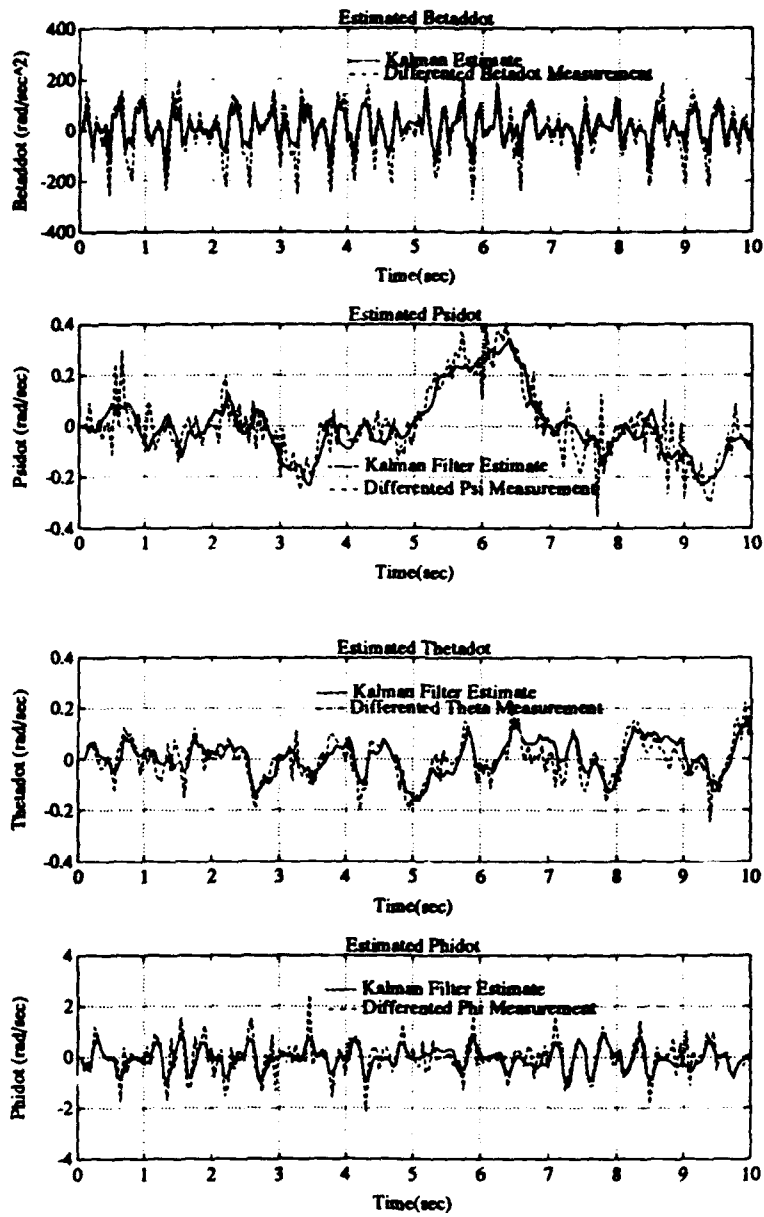


Figure 4.20, continued.

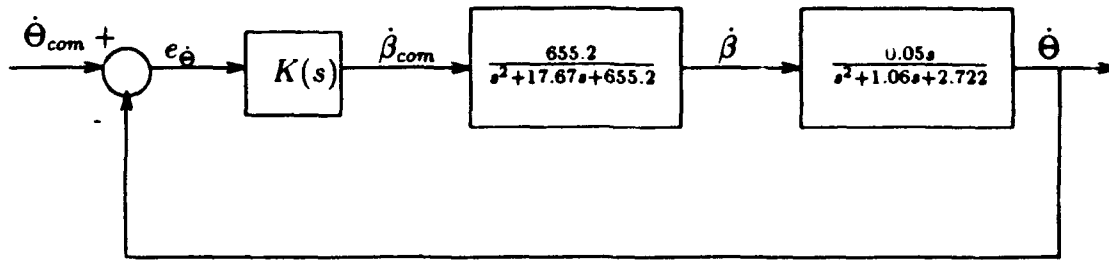


Figure 4.21 Block diagram of hypothetical continuous pitch rate command system

$\Delta\dot{\beta}$ is significantly higher than the true rotor speed perturbation.

$$\Delta\dot{\beta} = \dot{\beta} - 300 \text{ rad/sec} > \Delta\dot{\beta} = \dot{\beta} - \bar{\beta}(\Theta \gg 0) \quad [4.35]$$

Similarly at low values of Θ the Kalman filter underestimates Θ and $\dot{\Theta}$ because the perturbation $\Delta\dot{\beta}$ is significantly lower than the true rotor speed perturbation.

$$\Delta\dot{\beta} = \dot{\beta} - 300 \text{ rad/sec} < \Delta\dot{\beta} = \dot{\beta} - \bar{\beta}(\Theta \ll 0) \quad [4.36]$$

Equation 4.34 is used to preprocess absolute $\dot{\beta}$ measurements to yield accurate perturbation $\Delta\dot{\beta}$ estimates which are required for proper Kalman filter operation.

4.6.2 Pitch Rate Command System

The following specifications are set for the pitch rate command system

- Closed Loop Stability
- Gain margin ≥ 6 dB
- Phase margin $\varphi_m > 40^\circ$
- Closed loop -3 dB cutoff frequency $\omega_{-3dB} \geq 6$ rad/sec
- Steady state error to a step ≤ 25

Figure 4.21 shows a block diagram of the hypothetical continuous pitch rate command system. Figure 4.22 shows a Bode plot of the uncompensated open loop system. One can see that the uncompensated system has the characteristics of a differentiator at

low frequencies which results in very poor steady state tracking behavior. In order to meet the steady state requirement, an integral compensator of the form $K(s) = K/s$ is designed.

$$K_p = \lim_{s \rightarrow 0} \frac{655.2}{s^2 + 17.67s + 655.2} \frac{0.05s}{s^2 + 1.064s + 2.722} \frac{K}{s} = 0.0184K \quad [4.37]$$

The minimum gain K required to meet the steady state requirement is $K = 163.32$. The gain is increased to $K = 170$ to insure that the requirement is met. With this compensation, the system has an open loop crossover frequency of $\omega_{gc} = 3.2663$ with a gain margin of 12.66 dB and 0° of phase margin at 6.366 rad/sec. The phase deficiency is 43° at 7.25 rad/sec; therefore, a lead compensator is designed to contribute 65° of phase lead at this target crossover frequency. The total compensation is given by

$$K(s) = \frac{\overbrace{170}^{\text{Integral}}}{s} \frac{\overbrace{0.306s + 1}^{\text{Lead}}}{0.0306s + 1} \quad [4.38]$$

Figures 4.22 and 4.23 show the open and closed loop Bode plots of the compensated system. The compensated system has the following characteristics:

- Gain margin = 9.38 dB
- Phase margin $\varphi_m = 66^\circ$
- Open loop gain crossover frequency $\omega_{cg} = 5.98$ rad/sec
- Closed loop -3 dB cutoff frequency $\omega_{-3dB} = 11.11$ rad/sec
- Steady state error to a step = 24.5

which meet the specifications.

A digital filter is designed to emulate the continuous compensator of Equation 4.38. It is assumed that continuous pitch rate measurements are available for sampling. Figure 4.24 shows a block diagram of the hypothetical sampled data pitch rate command system. The digital compensator is computed using the bilinear transformation with

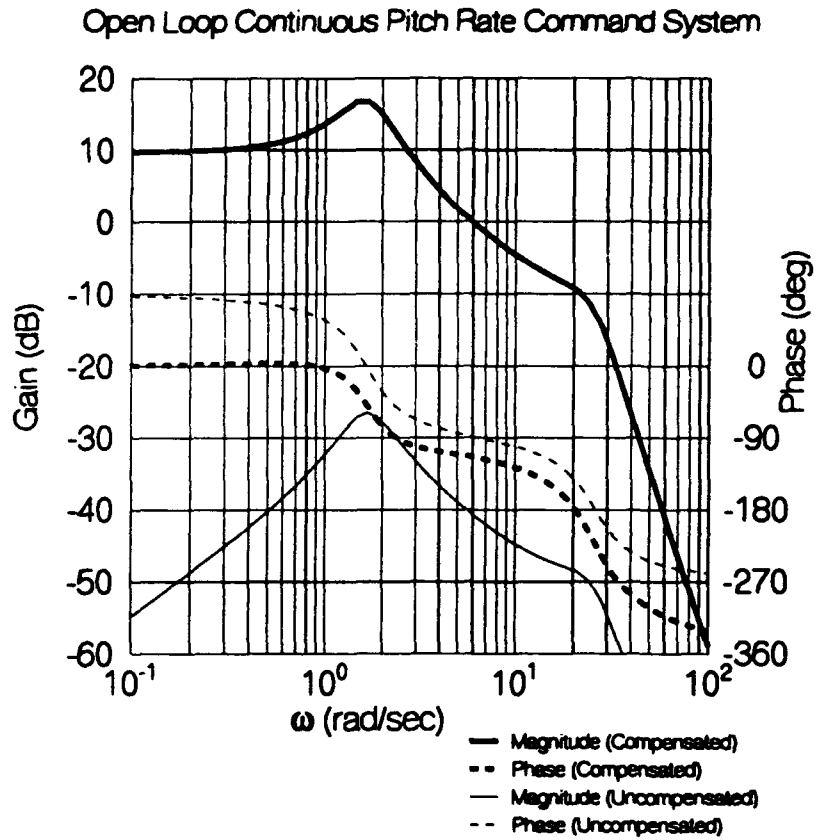


Figure 4.22 Bode plot of hypothetical open loop continuous compensated and uncompensated pitch rate command system $\dot{\Theta}(j\omega)/e_{\dot{\Theta}}(j\omega)$.

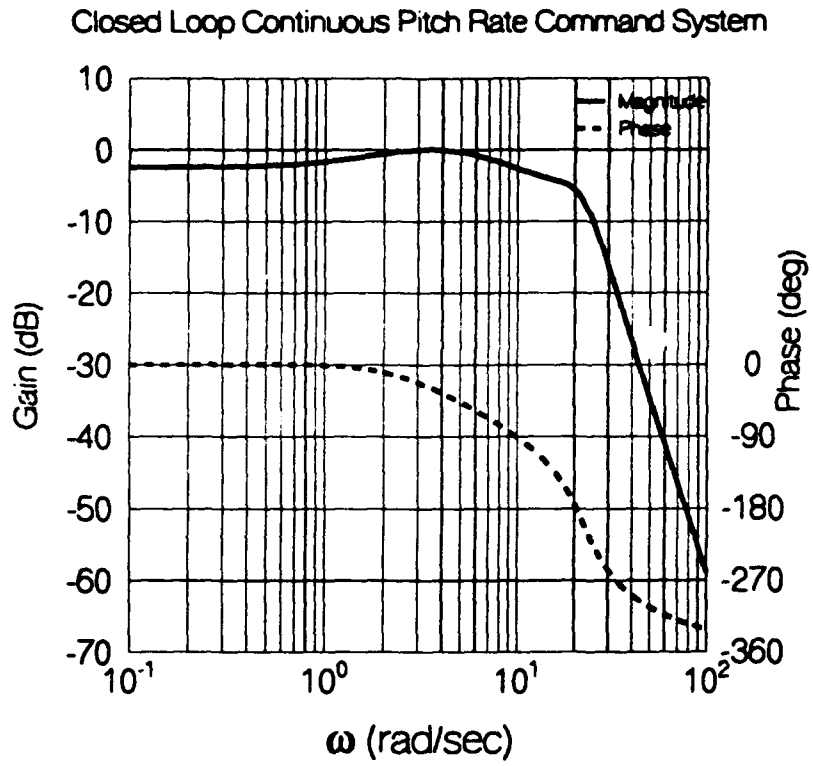


Figure 4.23 Bode plot of hypothetical closed loop continuous compensated pitch rate command system $\dot{\Theta}(j\omega)/\dot{\Theta}_{com}(j\omega)$.

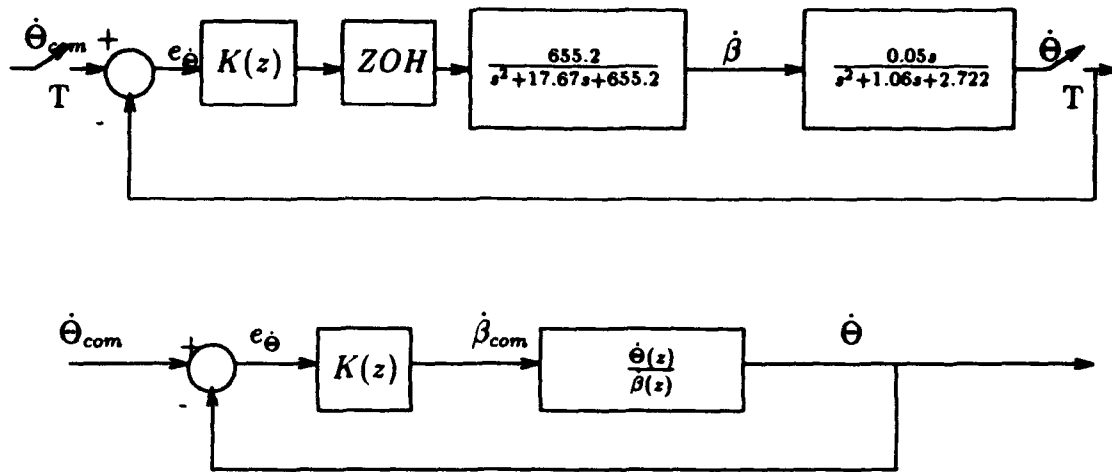


Figure 4.24 Block diagram of hypothetical sampled data pitch rate command system

prewarping for a sampling period of $T = 0.05$ sec and warping frequency $\omega_1 = 6$ rad/sec.

$$K(z) = \frac{49.71z^2 + 3.868z - 45.839}{z^2 - 1.096z + 0.967} \quad [4.39]$$

Figures 4.25 and 4.26 show the open and closed loop Bode plots for the discrete system of Figure 4.24. The characteristics of the discrete compensated system are:

- Gain margin = 8.33 dB
- Phase margin $\varphi_m = 57.52^\circ$
- Open loop gain crossover frequency $\omega_{cg} = 5.96$ rad/sec
- Closed loop -3 dB cutoff frequency $\omega_{-3dB} = 14.49$ rad/sec
- Steady state error to a step = 24.45

which meet the specifications. In reality continuous pitch rate measurements are not available for sampling but are estimated by the Kalman filter. Discussion of the effect of using rate estimates instead of sampling continuous rate measurements is deferred until Section 4.6.4.

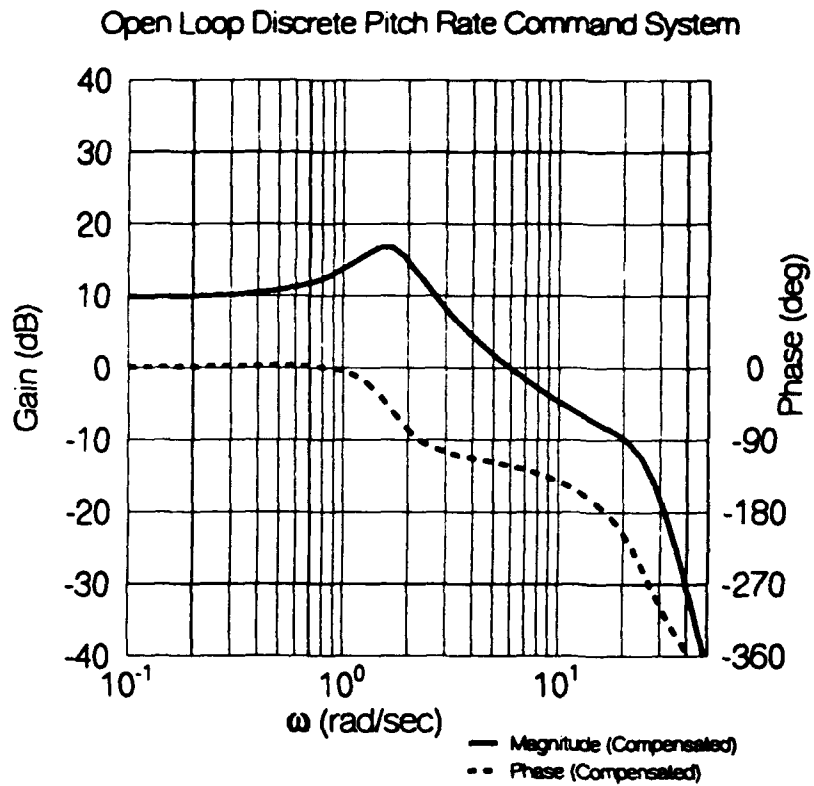


Figure 4.25 Bode plot of hypothetical open loop discrete compensated pitch rate command system $\hat{\Theta}(e^{j\omega T})/e_{\dot{\Theta}}(e^{j\omega T})$.

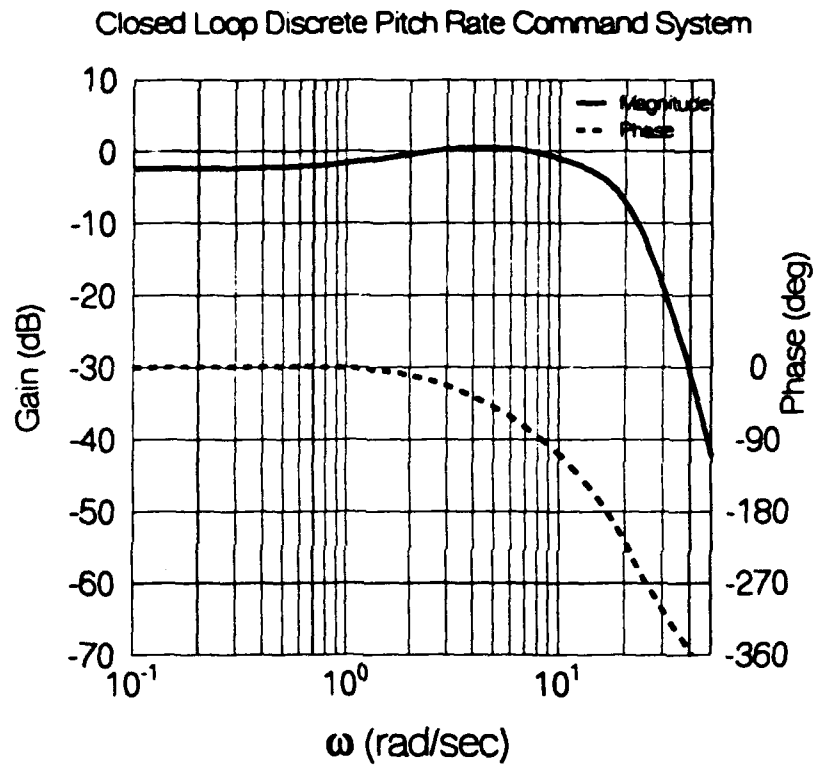


Figure 4.26 Bode plot of hypothetical closed loop discrete compensated pitch rate command system $\dot{\Theta}(e^{j\omega T})/\dot{\Theta}_{com}(e^{j\omega T})$.

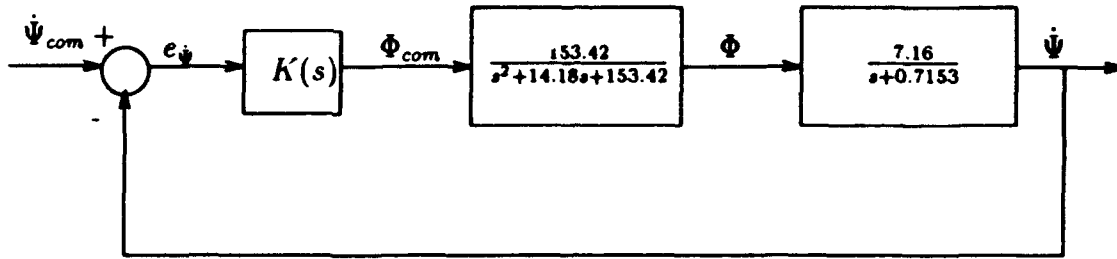


Figure 4.27 Block diagram of hypothetical continuous yaw rate command system

4.6.3 Yaw Rate Command System

The following specifications are set for the yaw rate command system:

- Closed Loop Stability
- Gain margin ≥ 6 dB
- Phase margin $\varphi_m > 40^\circ$
- Closed loop -3 dB cutoff frequency $\omega_{-3dB} \geq 6$ rad/sec
- Zero steady state error to a step; $K_p = \infty$.

Figure 4.27 shows a block diagram of the hypothetical continuous yaw rate command system. A Bode plot of the uncompensated system is shown in Figure 4.28. In order to meet the steady state error requirement an integral controller is implemented $K(s) = 1/s$.

$$K_p = \frac{7.16}{s + 0.7153} \frac{153.42}{s^2 + 14.18s + 153.42} \frac{1}{s} = \infty \quad [4.40]$$

This compensated system has an open loop gain crossover frequency of $\omega_{gc} = 2.509$ rad/sec with a 1.312 dB gain margin and 2.35° of phase margin. A lead compensator is designed to increase the open loop crossover frequency to $\omega_{gc} = 4$ rad/sec with a phase margin of 47.33° . The total compensation is given in Equation 4.41 .

$$K(s) = \frac{1}{s} \frac{0.5074s + 0.9}{0.0277s + 1} \quad [4.41]$$

Figures 4.28 and 4.29 show the Bode plots of the open and closed loop compensated system. The system properties are as follows:

- Gain margin = 8.80 dB
- Phase margin $\varphi_m = 47.34^\circ$
- Open loop gain crossover frequency $\omega_{cg} = 4.01$ rad/sec
- Closed loop -3 dB cutoff frequency $\omega_{-3dB} = 8.97$ rad/sec
- Steady state error to a step = 0

A digital filter is designed to emulate the continuous compensator. Emulation is accomplished using the bilinear transformation with prewarping for a sampling period of $T = 0.05$ sec and a warping frequency of 4 rad/sec. The discrete equivalent compensator is given by

$$K(z) = \frac{0.2518z^2 + 0.0215z - 0.2304}{z^2 - 1.0497z + 0.04978} \quad [4.42]$$

Figures 4.31 and 4.32 show the open and closed loop Bode plots of the hypothetical discrete system of Figure 4.30. The properties of the discrete yaw rate command system are as follows:

- Gain margin = 7.235 dB
- Phase margin $\varphi_m = 41.62^\circ$
- Open loop gain crossover frequency $\omega_{cg} = 4$ rad/sec
- Closed loop -3 dB cutoff frequency $\omega_{-3dB} = 8.97$ rad/sec
- Steady state error to a step = 0

which meet the specifications.

4.6.4 Effect of Kalman Filter in Feedback Loop

Figure 4.33 shows a block diagram of the actual rate command system implementation. Note the presence of the Kalman filter in the feedback loop. Obviously this is not the same as having rate measurements available for feedback. Figures 4.34

Open Loop Continuous Yaw Rate Command System

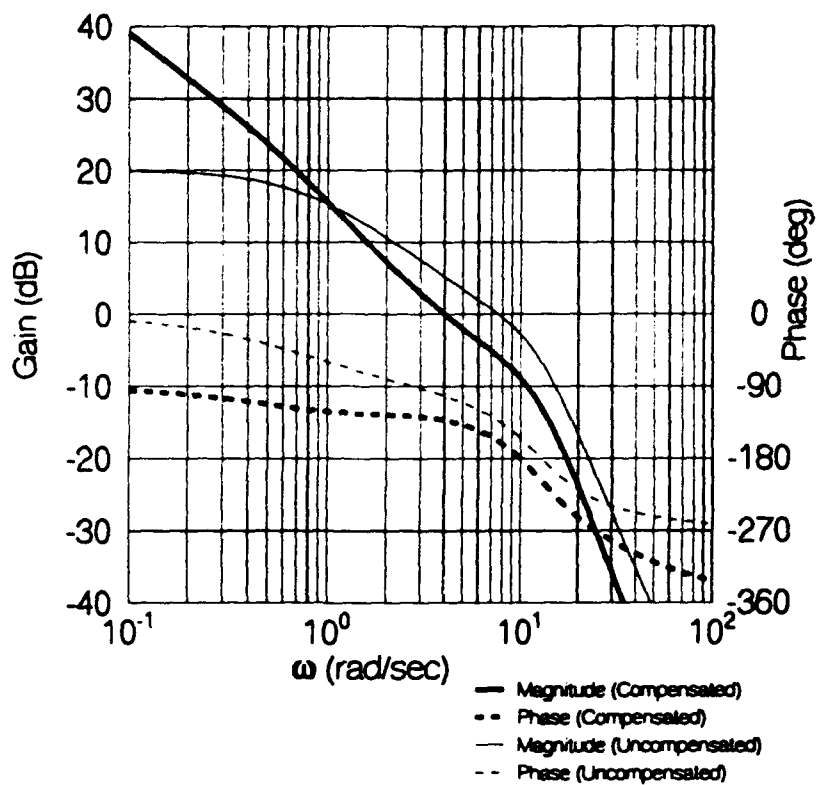


Figure 4.28 Bode plot of hypothetical open loop continuous compensated and uncompensated yaw rate command system $\Psi(j\omega)/e_{\Psi}(j\omega)$.

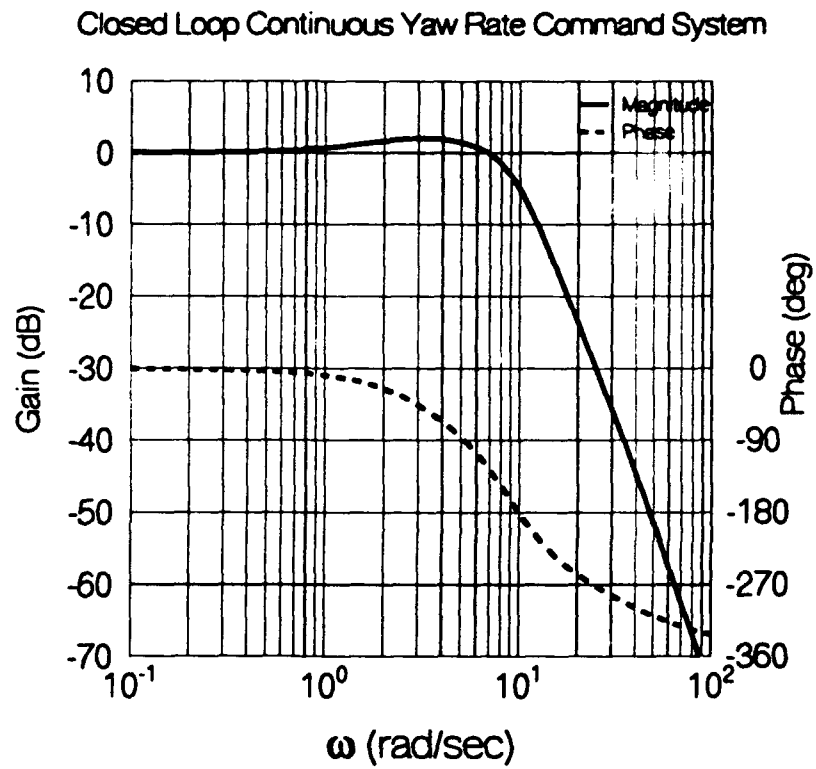


Figure 4.29 Bode plot of hypothetical closed loop continuous compensated yaw rate command system $\Psi(j\omega)/\Psi_{com}(j\omega)$.

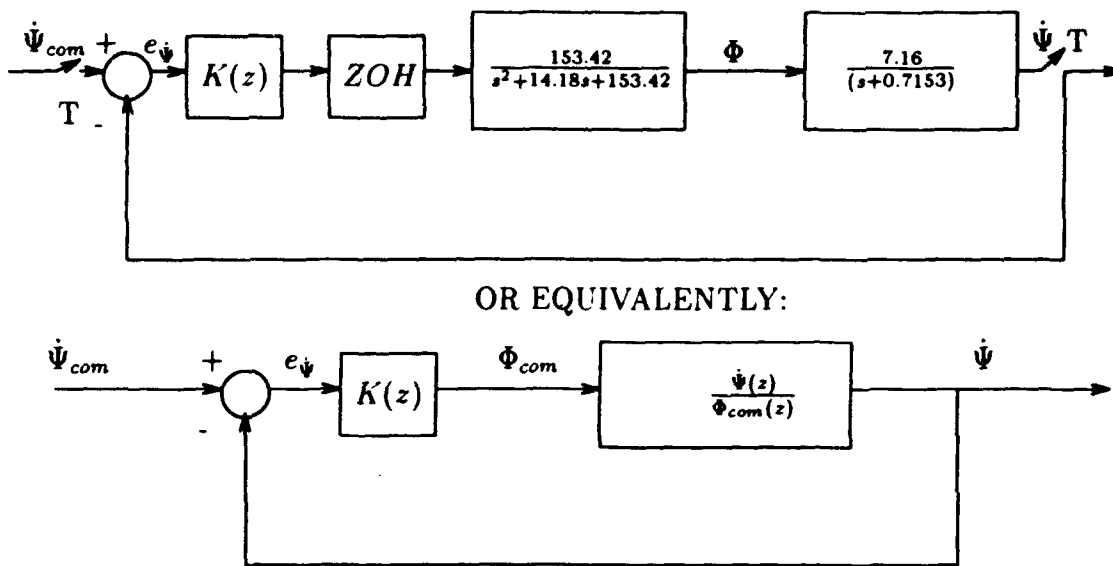


Figure 4.30 Block diagram of hypothetical sampled data yaw rate command system

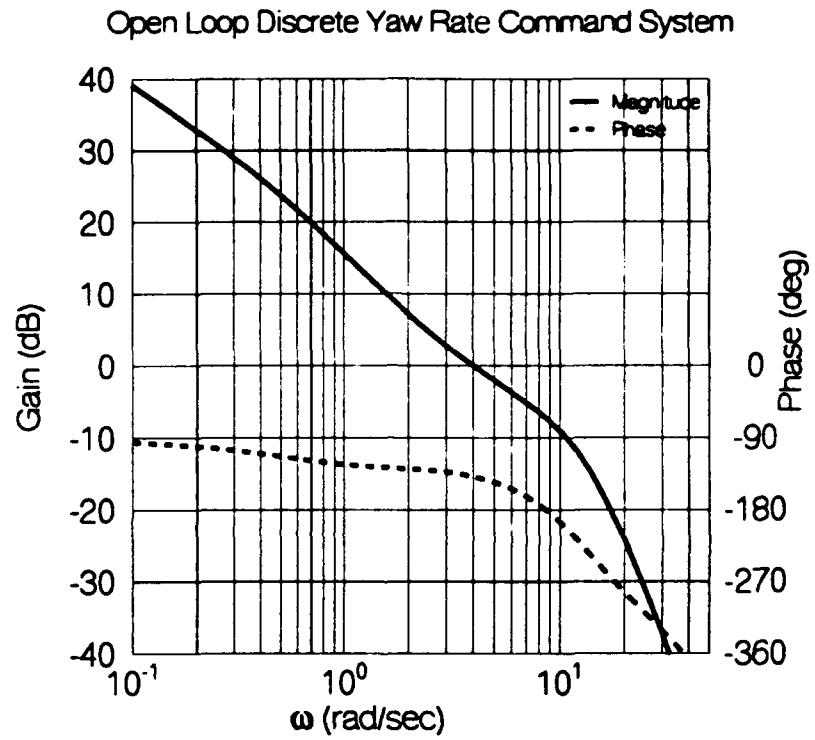


Figure 4.31 Bode plot of hypothetical open loop discrete compensated yaw rate command system $\dot{\Psi}(e^{j\omega T})/e_{\dot{\psi}}(e^{j\omega T})$.

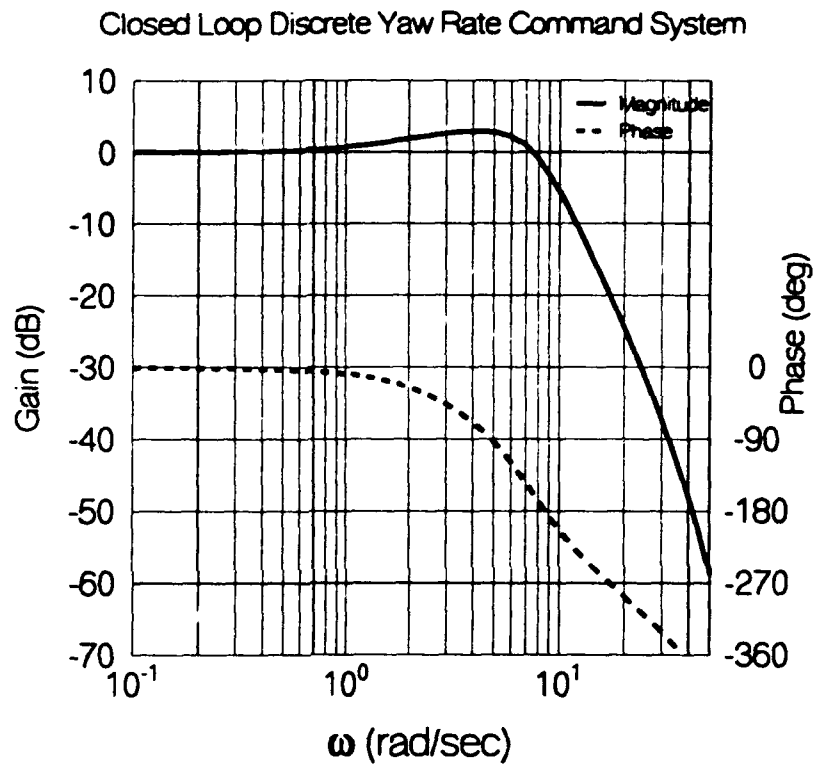


Figure 4.32 Bode plot of hypothetical closed loop discrete compensated yaw rate command system $\dot{\Psi}(e^{j\omega T})/\dot{\Psi}_{com}(e^{j\omega T})$.

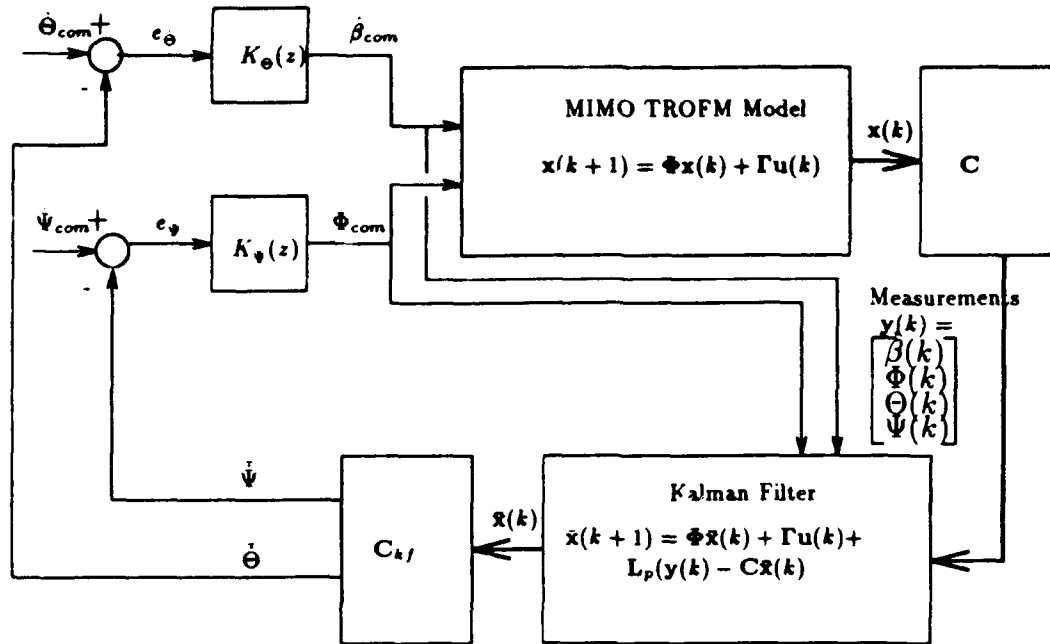


Figure 4.33 Block diagram of actual rate command system implementation.

and 4.35 compare the Bode plots of the single-input single-output (SISO) closed loop rate command systems developed above to the multi-input multi output (MIMO) model using Kalman filtered rate estimates for feedback. One can see that the low frequency behavior of the yaw rate command system is unchanged but the resonant peak is approximately 2.3 dB higher and the -3 dB cutoff frequency is reduced from 8.97 rad/sec to about 8 rad/sec. The low frequency behavior of the pitch rate command system is unchanged but the resonant peak is about 1 dB higher and the magnitude curve drops below -3 dB at 6.79 rad/sec to a minimum of -4.2 dB at 9.10 rad/sec. The magnitude curve crosses the -3dB line again at 13.64 rad/sec and finally drops below -3dB at 14.05 rad/sec. The high frequency behavior of the system is virtually unchanged. Figures 4.36 shows the step responses of the pitch and yaw rate command systems. The SISO simulated rate response, online Kalman filter rate estimate and differentiated attitude measurements are shown for comparison. One can see that the Kalman filter rate estimates are a compromise between the differentiated attitude measurement and the simulated response.

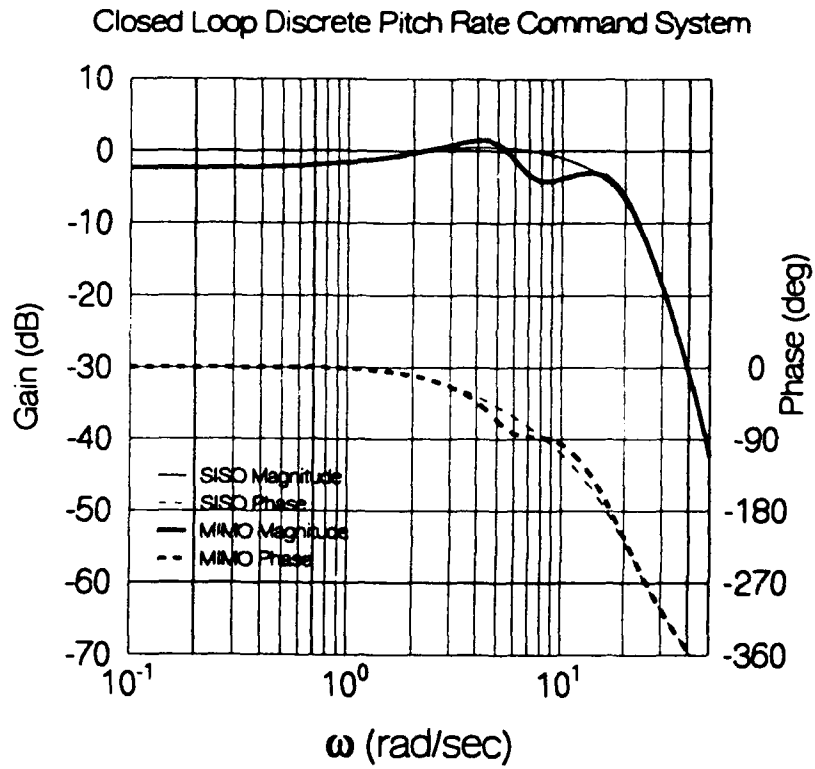


Figure 4.34 Bode plot of closed loop discrete pitch rate command system with and without Kalman filter. $\dot{\Theta}(e^{j\omega T})/\dot{\Theta}_{com}(e^{j\omega T})$.

6

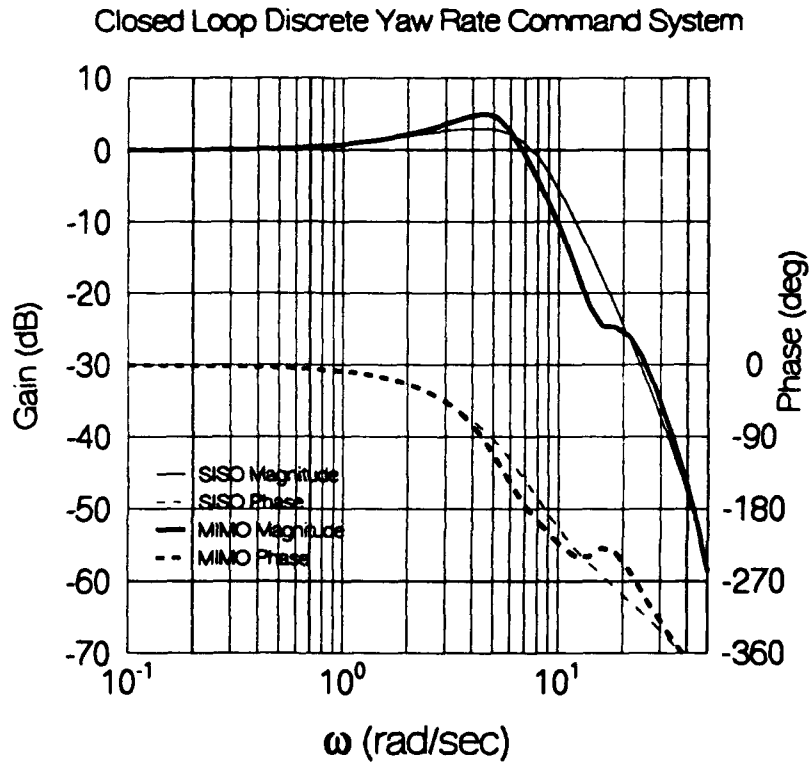


Figure 4.35 Bode plot of closed loop discrete yaw rate command system with and without Kalman filter. $\dot{\Psi}(e^{j\omega T})/\dot{\Psi}_{com}(e^{j\omega T})$

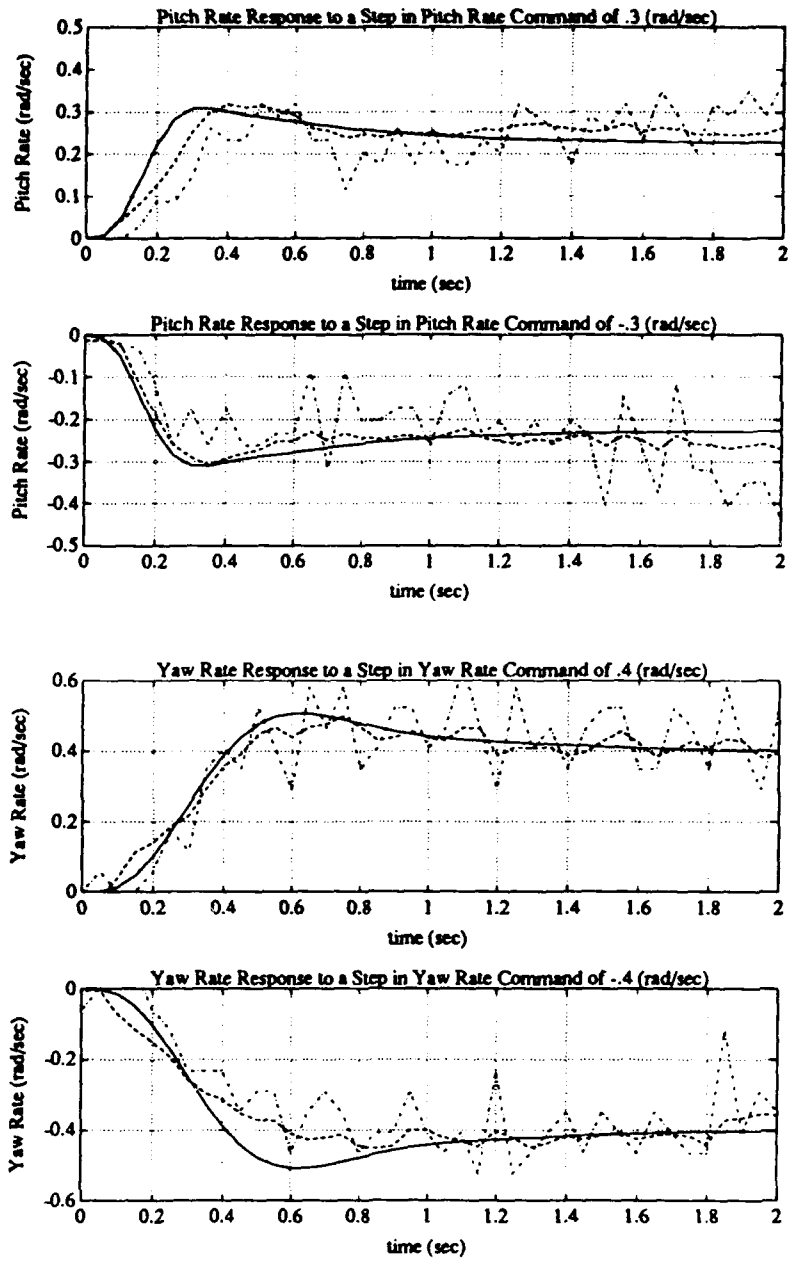


Figure 4.36 Step responses of SISO simulated, online Kalman filtered rate estimate, and differentiated attitude measurements for a) pitch rate b) yaw rate command systems.

5. MAN IN THE LOOP EXPERIMENTS

A study of the effects of command systems, displays and tasks on human pilot behavior is conducted. Loren P. Dean, a general aviation pilot uses the Cooper-Harper rating scale to evaluate the flying qualities of the TROFM using unaugmented, rate, and attitude command systems for two types of tasks and two different display types. Pilot and pilot-vehicle describing functions are obtained from time histories of dynamic tracking tasks where the pilot attempts to track a random appearing input. Compensatory instrument displays and a visual pursuit scene are used for the dynamic tracking tasks. The basic structure of a continuous time single loop pilot-vehicle system where the pilot attempts to track a random appearing input (forcing function) is given in Figure 5.1. Another task is devised which requires the pilot to move a stationary object from one platform to another in minimum time. The pilot evaluates the suitability of the three command systems for this task using the Cooper-Harper rating scale. Correlations between the Cooper-Harper ratings and quantitative descriptions of pilot behavior are made. The experimental results are

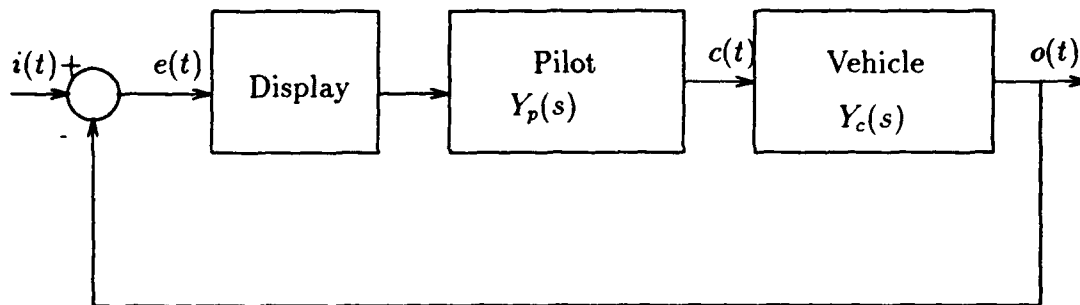


Figure 5.1 Basic structure of a continuous pilot in the loop tracking system.

compared to the classical theory of man-machine system dynamics which is based on McRuer's Crossover Model.

5.1 Apparatus and Procedure

The command systems, special equipment and experimental procedures used in the pilot in the loop tests are described below.

5.1.1 Control Systems

The TROFM is configured with the attitude command, rate command, and open loop systems designed in Chapter 4. Figure 5.2 shows simplified block diagrams of these command systems. The transfer function associated with the rate command systems $\dot{\Theta}/\dot{\Theta}_{com}$ and $\dot{\Psi}/\dot{\Psi}_{com}$ have nearly flat 0 dB frequency responses out to approximately 6.79 and 8 rad/sec respectively. Since the pilot is trying to control Θ and Ψ by manipulating $\dot{\Theta}$ and $\dot{\Psi}$, the effective controlled element is $Y_c \approx K/s$ at low frequencies. The attitude command systems Θ/Θ_{com} and Ψ/Ψ_{com} have nearly flat 0 dB frequency responses out to 7.78 and 6.16 rad/sec respectively. This makes the effective controlled element $Y_c \approx 1$ in the low frequency region.

5.1.2 Joystick

A position hold potentiometric joystick is used as the aircraft flight director. Position hold describes the characteristics of a joystick which maintains a fixed orientation (using friction) in the absence of an input. Longitudinal joystick deflection controls main rotor speed, pitch rate $\dot{\Theta}$ and pitch attitude Θ for the open loop, rate and attitude command systems respectively. The lateral portion of the joystick controls rotor tilt angle Φ , yaw rate $\dot{\Psi}$ and yaw attitude Ψ for the open loop, rate and attitude command systems respectively. The 1 K Ω joystick potentiometers are configured as voltage dividers powered by a 10 volt power supply. The wipers are connected to the A/D board on the control computer.

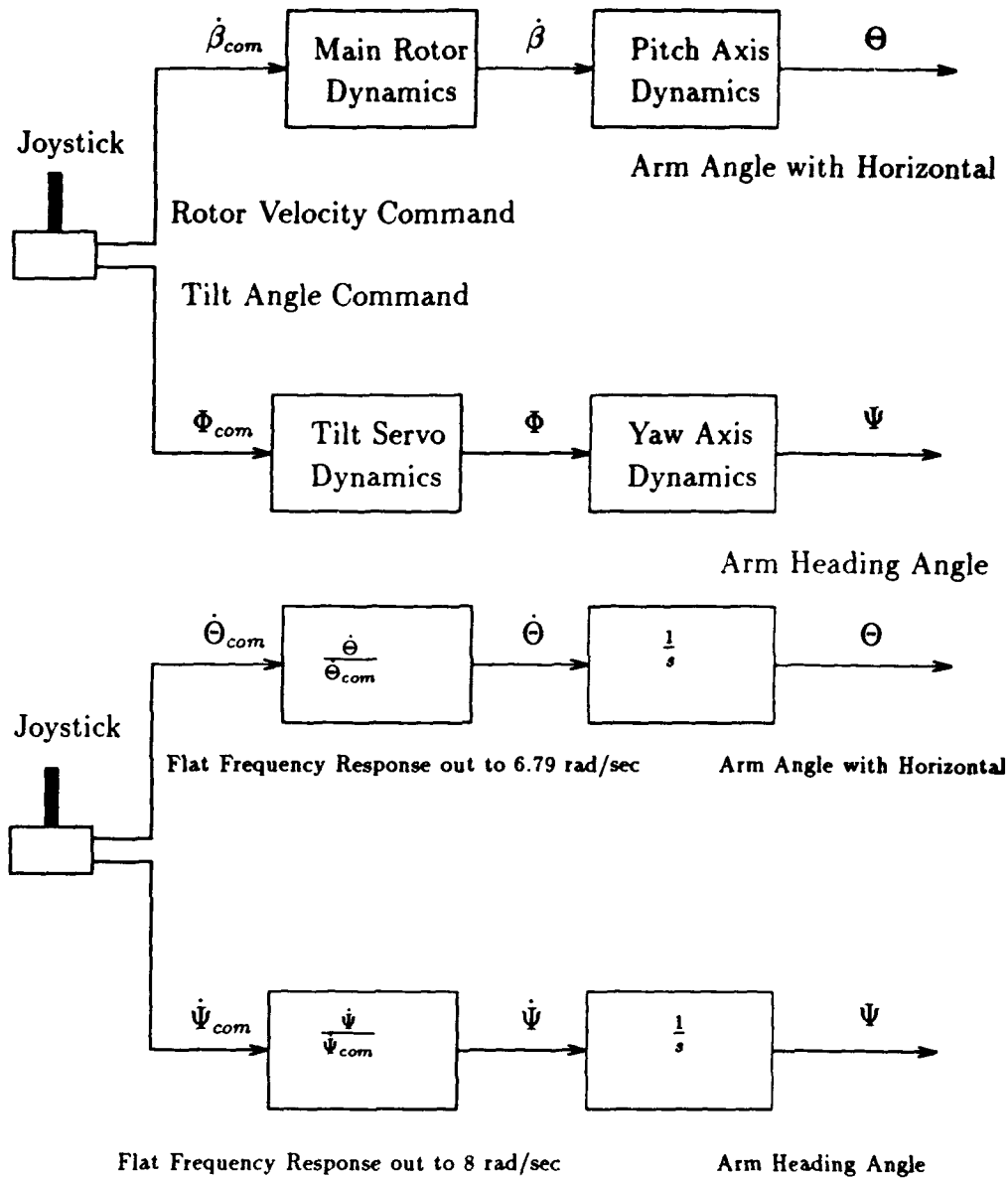


Figure 5.2 Simplified block diagrams of, open loop, rate and attitude command systems.

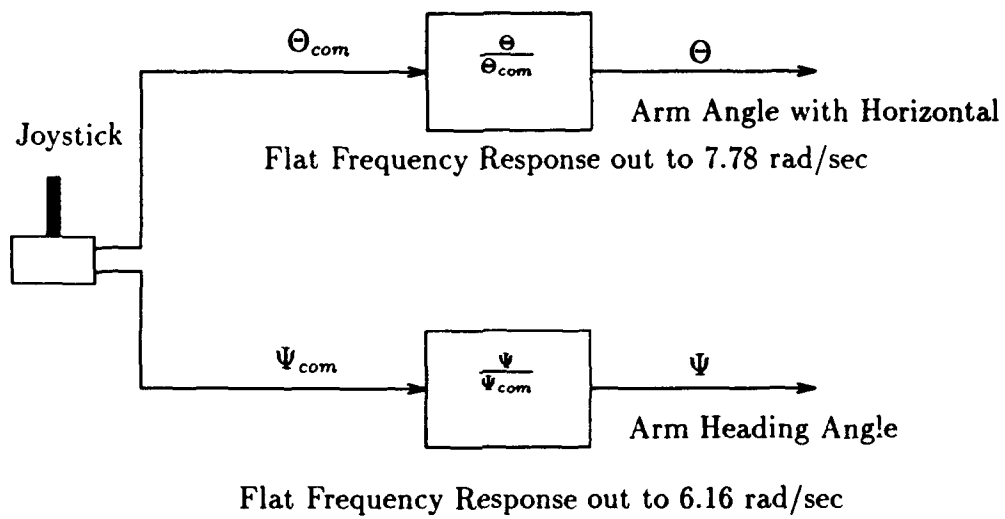


Figure 5.2, continued.

5.1.3 Pilot

Loren P. Dean, a general aviation pilot, evaluated the flying qualities of the TROFM. The pilot was a masters student in dynamics and control in the Purdue University School of Aeronautics and Astronautics. He had logged 230 hours in single engine land general aviation aircraft and maintained a current instrument rating. He had no prior experience evaluating aircraft handling qualities. The pilot was briefed on the Cooper-Harper rating scale and the scale flowchart (Figure 5.3) was used for all flying qualities evaluations. Pilot comments were recorded on audio tape for later transcription.

5.1.4 Experiment #1

The pilot is assigned the task of maneuvering the TROFM to a stationary object and moving the object to a specified position on an elevated platform in minimum time. Figure 5.4 shows a diagram of the apparatus used in this test. A tail hook is rigidly attached to the ballast of the TROFM for the purpose of picking up a small light weight spool. In each test the TROFM started from a position halfway between the spool and the target. A timer is started by flight test director and the pilot maneuvers the TROFM to the spool and picks it up using the tail hook. The pilot proceeds to move the spool to the elevated platform and attempts to bring the spool to rest in the desired performance region marked on the elevated platform. When the spool is at rest within the desired or adequate performance region and the tail hook removed, the timer is stopped and the pilot uses the Cooper-Harper rating scale to evaluate the TROFM command system being tested. The performance and suitability of each command system for the task is measured by the amount of time taken to complete the task and the Cooper-Harper handling qualities rating.

5.1.5 Experiments #2 and #3

The pilot is assigned the task of tracking random appearing inputs and keeping the tracking errors within desired performance bounds. The desired performance

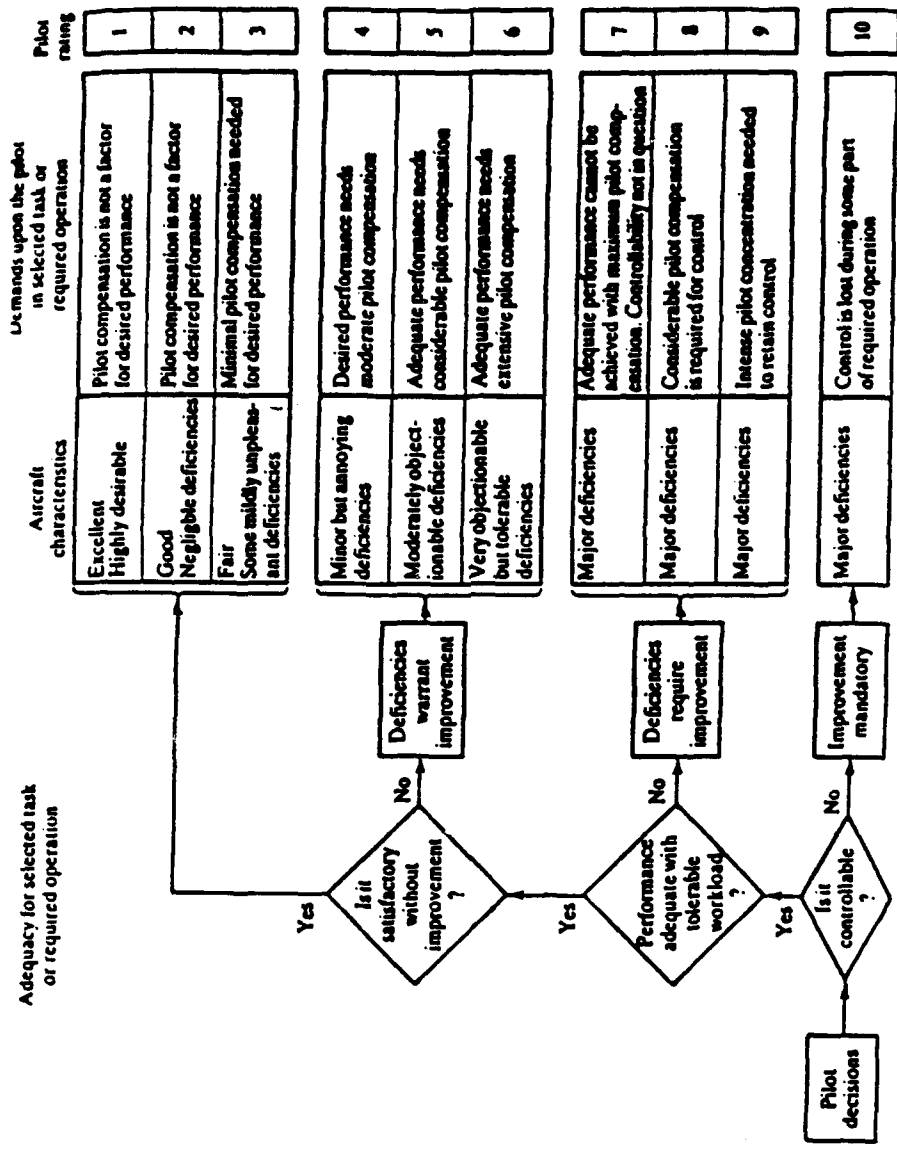


Figure 5.3 Cooper-Harper rating chart

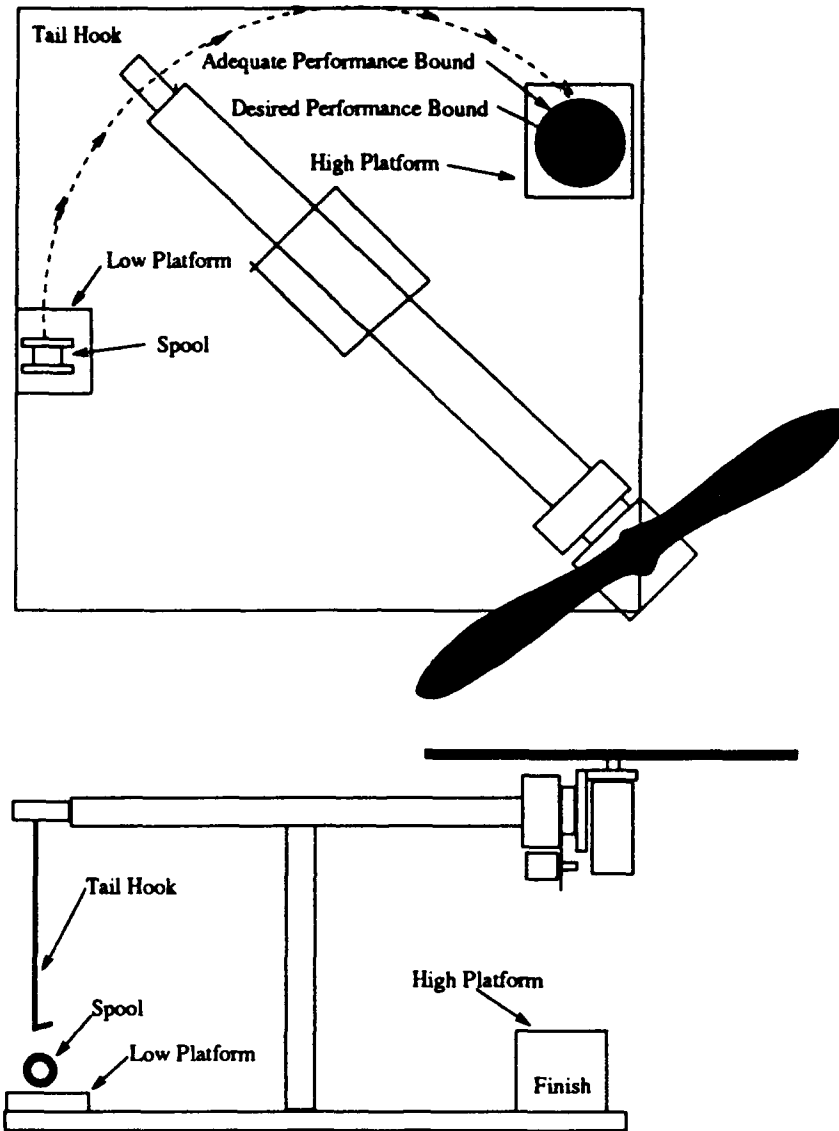


Figure 5.4 Diagram of the apparatus used in Experiment #1

region is defined as $\Theta_e \leq 0.07$ and $\Psi_e \leq 0.10$ rad. Minor excursions out of the desired performance region are allowed provided they are not excessive or prolonged and minimal pilot compensation is required to get back within the desired bounds.

Low (slow), medium and high (fast) bandwidth pseudo-random forcing functions are used in the dynamic tracking tests. Each forcing function consists of a sum of five sine waves.

$$i(kT) = \sum_{j=1}^5 A_j \sin(\omega_j kT + \phi_j) \quad [5.1]$$

Each forcing function contains $N = 1024$ discrete points which are sampled at $T \approx 0.05$ sec. The component sinusoids are carefully designed to have an integer number of cycles in 1024 samples and no frequency component is an integer multiple of another. The frequencies ω_j are roughly equidistant on a logarithmic scale. The phase angles ϕ_j are randomly selected for each run to maintain a random forcing function appearance while preserving RMS magnitudes and spectra. The forcing function signal composition for sampling frequency of $F_s = 20$ Hz is shown in Figure 5.5 and tabulated in Table 5.1.5. Typical forcing function time histories are shown in Figure 5.6. In multi-axis tasks there are no common frequencies in the pitch and yaw disturbance functions. In single axis tasks, the axis not in use is physically restrained and the joystick potentiometer controlling that axis is taken off line. The pilot takes no less than two practice runs on each command system before data is taken. During this practice time the pilot is able to adjust the sensitivity of the joystick to his liking so that the joystick does not degrade his performance or affect his ability to assign an appropriate HQR.

5.1.6 Instrument Display

In Experiment #2 the pilot uses a compensatory instrument display to determine the tracking error. A compensatory display is one in which the forcing function minus the modified control response is indicated. When using a compensatory display the pilot can determine the effects of the joystick deflection alone only under zero

Table 5.1 Signal composition of a) Low b) Medium s c) High bandwidth forcing functions.

a)

# of Cycles in 1024 samples	Frequency (rad/sec)	Amplitude (rad)
2	0.2453	0.045
3	0.3680	0.045
5	0.6133	0.045
11	1.3492	0.0225
17	2.0852	0.0225

b)

# of Cycles in 1024 samples	Frequency (rad/sec)	Amplitude (rad)
4	0.4906	0.045
6	0.7359	0.045
9	1.1039	0.045
14	1.7172	0.0225
12	2.5758	0.0225

c)

# of Cycles in 1024 samples	Frequency (rad/sec)	Amplitude (rad)
5	0.6138	0.045
8	0.9813	0.045
12	1.4719	0.045
18	2.2078	0.0225
26	3.1891	0.0225

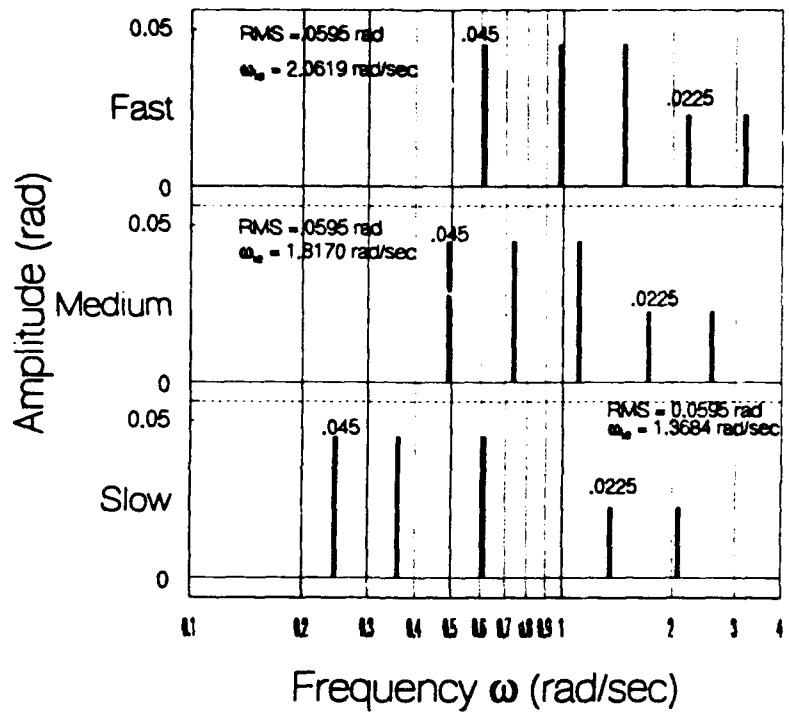


Figure 5.5 Forcing function signal composition

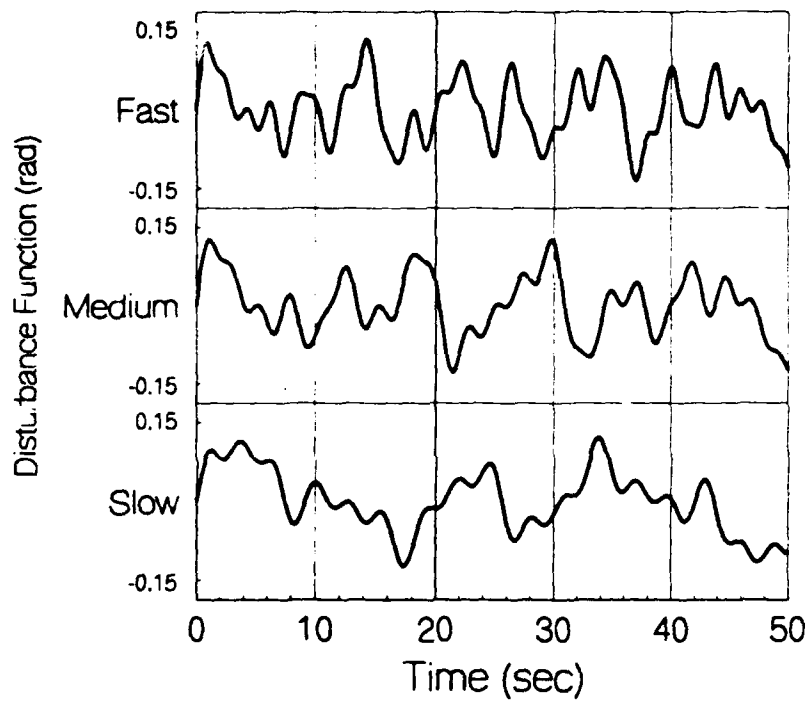


Figure 5.6 Typical forcing function time histories

input conditions. Figure 5.7 shows the instrument panel used in Experiment #2. This panel is displayed on the CRT of the control computer and is generated by National Instruments LabView program. The compensatory displays are made using LabView's virtual oscilloscope elements since these are the fastest displays available. The scope element indicates pitch error through the vertical position of a horizontal line. This error indication is aligned with the longitudinal joystick axis which controls the pitch axis. Unfortunately yaw error is indicated the same way as pitch error which is counter-intuitive. Yaw error would be better represented by the horizontal position of a vertical line. This would be aligned with the lateral joystick axis which is the primary yaw axis controller. Every combination of available elements was tried in an effort to obtain an intuitive yaw error display but each combination caused the sampling rate to drop to unacceptably low levels; therefore, two scope elements were the only choice in this case.

The pilot adjusted the joystick sensitivity to his liking during the practice runs using the sliders shown in Figure 5.7. After the practice runs the pilot is given 20 seconds to stabilize the aircraft and obtain near 0 error. The "Taking Data" light on the panel is then illuminated and the forcing function is sampled. The difference between the desired attitude and the actual aircraft attitude is displayed on the virtual oscilloscopes. Single axis tests are performed first to allow the pilot to get the feel of the individual axes before attempting to control both axes. Discrete time histories of the forcing function $i(kT)$, vehicle output $o(kT)$ and joystick deflection $c(kT)$ are recorded on diskette for analysis. The pilot uses the Cooper-Harper rating scale to evaluate the flying qualities of each configuration.

5.1.7 Visual Target

In Experiment #3 the pilot is assigned the task of tracking a moving target. The target is mounted on a custom built vertical x-y plotter shown in Figure 5.8. A high intensity LED is enclosed in an open ended tube which is mounted on the ballast of the TROFM. The pilot is asked to keep the light beam within the desired

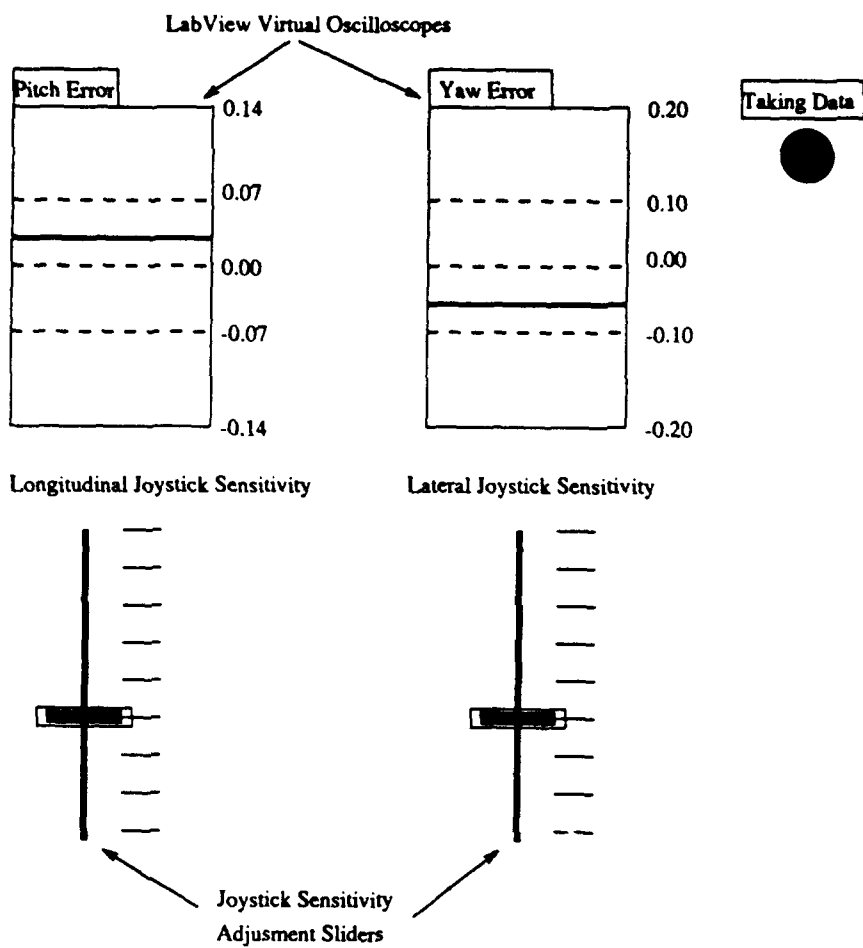


Figure 5.7 Diagram of the instrument panel

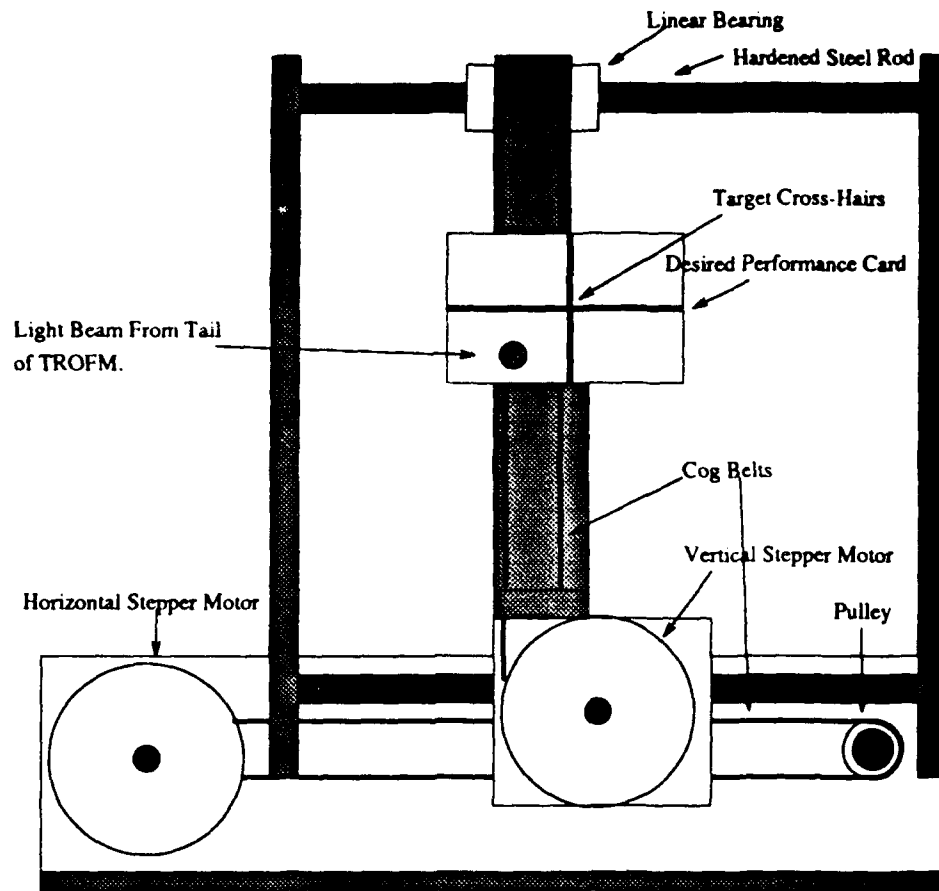


Figure 5.8 Diagram of the x-y plotter with target

performance bounds defined by a rectangular card with cross-hairs denoting ideal performance. The motion of the target is imparted by two independent computer controlled stepper motors which were salvaged from two Citizen 120D dot matrix printers. Stepper motors are chosen as motion drivers because of their ability to operate as open loop position controllers using only digital outputs from the control computer. Both analog outputs and 7 out of the 8 analog input channels are already in use by the TROFM; thus, open loop digital control is the only choice for additional motion driver mechanisms. The external circuitry required to drive the steppers is also custom built (refer to Appendix A for schematics). The target is able to move in 0.047" increments in both axes. The steppers are driven by the sum of sines forcing functions previously described, however in the multi-axis tests the component amplitudes are decreased by 10%, to compensate for a decrease in sample rate that is caused by excessive computer processing time required to drive the two steppers.

The target position in steps is correlated with the attitude of the TROFM by starting from a reference point and moving the target a specific number of steps and manually adjusting the TROFM attitude such that the light beam is centered on the target cross-hairs. The pitch and yaw axis calibration procedures yield the following relations:

$$\Theta_{com} = 0.00138 \frac{rad}{step} \#Pitch\ Steps + 0.1825\ rad \quad [5.2]$$

$$\Psi_{com} = 0.00129 \frac{rad}{step} \#Yaw\ Steps - 0.1571\ rad$$

The number of steps to move in each sampling period T is calculated using Equations 5.3 and 5.4.

$$\frac{\Delta\Theta_{step}}{\Delta T} = \text{int} [727.2 (\Theta_{com}(k+1) - \Theta_{com}(k) - 0.1825)] \quad [5.3]$$

$$\frac{\Delta\Psi_{step}}{\Delta T} = \text{int} [781.3 (\Psi_{com}(k+1) - \Psi_{com}(k) + 0.1571)] \quad [5.4]$$

The true forcing function time history is recorded in steps. When the test is over the true forcing function time history in radians is extracted from the step record by Equations 5.5 and 5.6.

$$\Theta_{com}(n) = 0.0138 \left[\sum_{k=0}^n \Delta\Theta_{step}(k) - 200steps \right] + 0.1825 \quad [5.5]$$

$$\Psi_{com}(n) = 0.0129 \left[\sum_{k=0}^n \Delta\Psi_{step}(k) + 200steps \right] - 0.1571 \quad [5.6]$$

The 200 step offsets are used to center the target between the stops that are used as reference positions.

5.2 Discussion

Analysis of Experiment #1 is straight forward. There are two measures of performance: handling qualities rating and time taken to complete the task. Experiments #2 and #3 are designed to contain much more information.

5.2.1 Experiments #2 and #3

Pilot describing functions and open loop pilot-vehicle describing functions are determined from the time histories recorded in Experiments #2 and #3. Describing functions are extracted from the discrete time histories using a Fast Fourier transform algorithm. The FFT yields results equivalent to the Discrete Fourier Transform (DFT) but the number of data points (N) in a set must be a power of two. The data sets collected in Experiments #2 and #3 contain $N = 2^{10} = 1024$ points to facilitate fast computation of frequency responses. Equation 5.7 gives the definition of the DFT of a general discrete time sequence.

$$X(n) = X(e^{j\omega n}) = DFT[x(kT)] = \sum_{k=0}^{N-1} x(kT)e^{-j2\pi kn/N} \quad [5.7]$$

It can be shown that the DFT is defined only at discrete frequencies $\omega_n = 2\pi F_s n/N$ where F_s is the sampling frequency in Hz. Consider the problem of determining

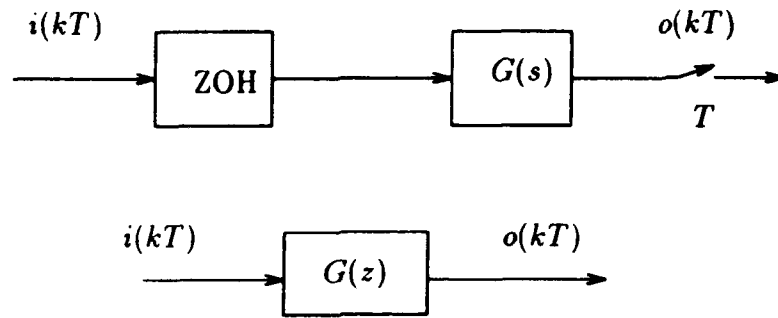


Figure 5.9 Block diagram of a sampled data system

the frequency response of the sampled data system in Figure 5.9 from experimental time history data, where the input is composed of a finite number of sinusoids and the sampling frequency is much greater (in this case 40x greater) than the highest frequency component of the input. Equation 5.8 mathematically expresses the relationship between the transfer function $G(z)$ and the input-output sequences.

$$G(z) = \frac{O(z)}{I(z)} \quad [5.8]$$

The frequency response of the the discrete transfer function $G(z)$ can be determined from Equation 5.9.

$$G(e^{j\omega_i T}) = \frac{O(e^{j\omega_i T})}{I(e^{j\omega_i T})} = \frac{DFT[o(kT)]}{DFT[i(kT)]} \quad [5.9]$$

where ω_i is a component frequency of the sum of sines input.

5.2.2 Open Loop Pilot-Vehicle Describing Functions

Figure 5.10 shows a block diagram of a single loop sampled data pilot-vehicle tracking system. The open loop pilot-vehicle describing functions are assumed to be of the form of the extended crossover model (Equation 5.10) described in References [9] and [13].

$$Y_p Y_c(j\omega) = \frac{K e^{-j(\tau\omega + \alpha/\omega)}}{j\omega} \quad [5.10]$$

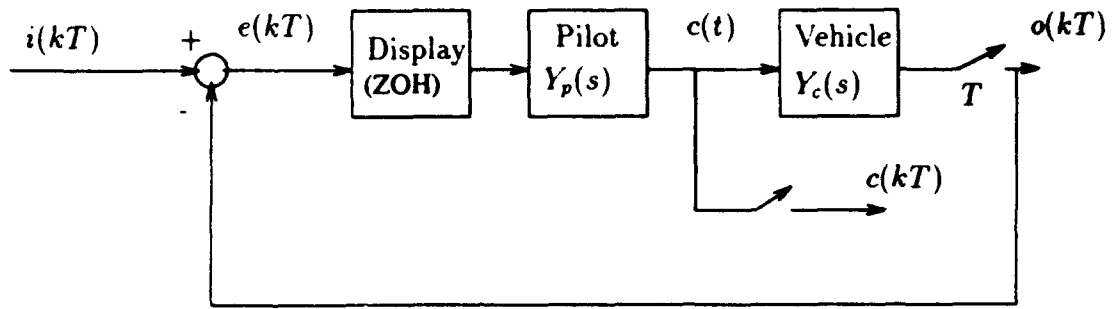


Figure 5.10 Block diagram of single loop sampled data pilot-vehicle tracking system.

where τ is the open loop time delay and α is the open loop phase droop parameter. The experimental open loop describing function $(Y_p Y_c)_{exp}$ is determined by computing the ratio of the DFT of the vehicle output $o(kT)$ and the DFT of the error $e(kT)$ perceived by the pilot from the display.

$$Y_p Y_{c_{exp}}(e^{j\omega_i T}) = \left. \frac{DFT[o(kT)]}{DFT[e(kT)]} \right|_{\omega_i} \quad [5.11]$$

where ω_i are the n component frequencies of the forcing function $i(kT)$. The continuous time transfer function of Equation 5.10 is fitted to the experimentally determined open loop describing function function of Equation 5.11. The parameters K, τ , and α which best fit the experimental open loop describing functions in a least squares sense on a logarithmic scale are calculated by the procedure outlined below. Note that

$$\begin{aligned} |Y_p Y_c(j\omega)| &= \left| \frac{k}{j\omega} \right| \\ \arg(Y_p Y_c(j\omega)) &= -\frac{\pi}{2} - (\tau\omega + \alpha/\omega) \end{aligned} \quad [5.12]$$

First find K which best fits the experimental magnitude data (measured in dB). Since the magnitude of $K/j\omega$ system has a 20dB/dec slope on a logarithmic frequency scale, one may write

$$Y_i = |Y_p Y_c(e^{j\omega_i T})|_{exp} = -20 \log_{10}(\omega_i) + b \quad [5.13]$$

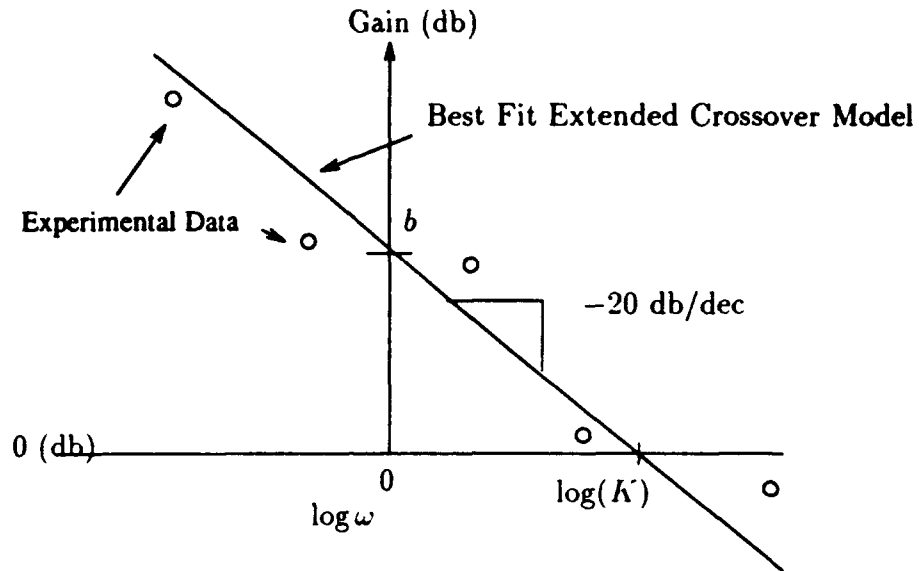


Figure 5.11 Diagram of the magnitude fitting procedure.

where b is the point where the magnitude line intersects the $\log_{10}(1 \text{ rad/sec}) = 0$ axis (Figure 5.11) .

Compute the value of b which best fits the experimental magnitude data in a least squares sense by solving the linear algebra problem of the form $\mathbf{A}b = \mathbf{Y}$ given below.

$$\begin{bmatrix} 1 \\ \vdots \\ 1 \end{bmatrix} b = \begin{bmatrix} Y_1 + 20 \log_{10} \omega_1 \\ \vdots \\ Y_n + 20 \log_{10} \omega_n \end{bmatrix} \quad [5.14]$$

The least squares estimate of b is given by

$$\hat{b} = (\mathbf{A}^T \mathbf{A})^{-1} \mathbf{A}^T \mathbf{Y} = \frac{1}{n} \sum_{i=1}^n (Y_i + 20 \log_{10} \omega_i) \quad [5.15]$$

The least squares estimate of K may now be computed from Equation 5.16.

$$\hat{K} = 10^{\frac{\hat{b}}{20}} \quad [5.16]$$

Recall that a $K/j\omega$ system has 90° or $\pi/2$ (rad) of phase lag at all frequencies. To obtain least squares estimate of τ and α the residual phase ϕ_{res} or the difference

between the experimentally determined phase and the $K/j\omega$ phase must be computed.

$$\phi_{res_i} = \arg[Y_p Y_c(e^{j\omega_i T})]_{exp} - \left(-\frac{\pi}{2}\right) \quad [5.17]$$

The parameters τ and α which best fit the residual phase data are computed by solving the linear algebra problem

$$\begin{bmatrix} j\omega_1 & \frac{1}{j\omega_1} \\ \vdots & \vdots \\ j\omega_n & \frac{1}{j\omega_n} \end{bmatrix} \begin{bmatrix} \tau \\ \alpha \end{bmatrix} = \begin{bmatrix} \phi_{res_1} \\ \vdots \\ \phi_{res_n} \end{bmatrix} \quad [5.18]$$

$\mathbf{A} \quad \mathbf{x} \quad = \quad \phi_{res}$

The least squares estimate of the parameter vector \mathbf{x} is given by

$$\hat{\mathbf{x}} = [\tau \ \alpha]^T = (\mathbf{A}^T \mathbf{A})^{-1} \mathbf{A}^T \phi_{res}. \quad [5.19]$$

Thus, least squares estimates of the extended crossover model can be obtained analytically.

5.2.3 One Third Law

The "one third law" has been developed from the crossover model to describe the performance of a human operator in a closed loop compensatory task [9]. This rule assumes that the input bandwidth is much less than the pilot-vehicle crossover frequency, relatively small remnant or noise is present in the control loop and the input spectrum is rectangular and the open loop pilot-vehicle describing function is of the form $K e^{-\tau s}/s$. The one third law is given in Equation 5.20.

$$\frac{\epsilon_\sigma^2}{\sigma_i^2} \approx \frac{1}{3} \left(\frac{\omega_{ei}}{\omega_c} \right)^2 \quad [5.20]$$

where σ_i^2 is the variance of the input, ϵ_σ^2 is the variance of the error, ω_{ei} is the effective input bandwidth and ω_c is the pilot-vehicle crossover frequency. The effective bandwidth of the forcing function is estimated from Equation 5.21 found in Reference [9].

$$\omega_{ei} = \frac{[\int_0^\infty \Phi_{ii}(\omega) d(\omega)]^2}{\int_0^\infty [\Phi_{ii}(\omega)]^2 d(\omega)} \quad [5.21]$$

where Φ_{ii} is the power spectral density of the input. The effective bandwidths of the low, medium and fast bandwidth forcing functions are calculated using a discretized Equation 5.21. The low, medium and fast effective bandwidths are 1.3684, 1.8170 and 2.0619 rad/sec respectively. The variance of each forcing function used in Experiment #2 and the single axis tests of Experiment #3 is $\sigma_i^2 = 0.595$ rad. The variance of the multi-axis forcing functions used in Experiment #3 is $\sigma = 0.536$ rad. One third laws for the slow, medium and fast bandwidth forcing functions are given below for input variances of 0.595 rad.

$$\left(\frac{e_\sigma}{\sigma_i}\right)_{low} \approx \frac{0.790}{\omega_c} \quad [5.22]$$

$$\left(\frac{e_\sigma}{\sigma_i}\right)_{med} \approx \frac{1.049}{\omega_c} \quad [5.23]$$

$$\left(\frac{e_\sigma}{\sigma_i}\right)_{fast} \approx \frac{1.190}{\omega_c}$$

The crossover frequency ω_c is taken to be equal to the least squares estimate of K computed by the method outlined in the previous section.

In practice the one third law must be modified to include a non-zero intercept. The existence of an intercept implies that zero RMS error is unattainable. This is because the pilot is not a linear element since he produces a remnant or pilot induced noise at frequencies other than those which compose the forcing functions.

5.2.4 Pilot Describing Functions

Reference [9] gives the general form of a precision pilot model for single loop systems, and the form for simplification of two of the dynamic elements,

$$Y_p = \underbrace{\widehat{K}_p}_{\text{Gain}} \underbrace{e^{-j\omega\tau}}_{\text{Pure Time Delay}} \underbrace{\left(\frac{T_{lead}j\omega + 1}{T_{lag}j\omega + 1}\right)}_{\text{Series Equalization}} \underbrace{\left[\frac{T_kj\omega + 1}{T_{k'}j\omega + 1}\right]}_{\substack{\text{Very-Low-Frequency} \\ \text{Lag-Lead}} \atop e^{-j\sigma/\omega}} \underbrace{\frac{1}{(T_{N_1}j\omega + 1) \left[\left(\frac{j\omega}{\omega_N}\right)^2 + \frac{2\xi_{NS}j\omega}{\omega_N} + 1\right]}}_{\substack{\text{Neuromuscular} \\ \text{Actuation System}} \atop e^{-j\omega T_N}}$$

where

$$\alpha \cong \frac{1}{T_K} - \frac{1}{T_{K'}} \quad [5.24]$$

and

$$T_N \cong T_{N_1} + \frac{2\xi_N}{\omega_N} \quad [5.25]$$

The major mid-frequency elements are the gain K_p , time delay τ and the lead-lag or lag-lead series equalization. The pilot model (Equation 5.26) in this study took advantage of the very low and high frequency approximations shown in Equation 5.24.

$$Y_p \cong K_p \left(\frac{T_{Lead}j\omega + 1}{T_{Lag}j\omega + 1} \right) e^{-j(\tau_e\omega + \alpha/\omega)} \quad [5.26]$$

The effective time delay parameter τ_e is defined by $\tau_e = (\tau + T_N)$. Reference [10] suggests that the series equalization parameters are limited to the following ranges:

$$0 \leq T_{Lead} \leq 5sec \quad [5.27]$$

$$0 \leq T_{Lag} \leq 20sec$$

The gain K_p is adjusted for overall system stability and good low frequency response. The pilot adjusts T_{Lead} and T_{Lag} such that the system can be stabilized by proper gain selection over a broad frequency range and $Y_p Y_c$ has the characteristics of a K/s plant over a considerable frequency range centered on the crossover frequency.

To determine appropriate values of $K_p, T_{Lead}, T_{Lag}, \tau_e$ and α from experimentally determined frequency response data, an iterative constrained optimization routine is used to minimize the cost function defined in Equation 5.28.

$$V = \sum_{\omega_i=\omega_1}^{\omega_n} \left[\left[\text{gain} \left(\frac{[DFT(c(kT))]}{[DFT(e(kT))]} \right) \Big|_{\omega_i} - \text{gain}(Y_{p \text{ est}}) \right]^2 + 0.02 \left[\text{arg} \left(\frac{[DFT(c(kT))]}{[DFT(e(kT))]} \right) \Big|_{\omega_i} - \text{arg}(Y_{p \text{ est}}) \right]^2 \right] \quad [5.28]$$

Where the gain is in decibels and the phase is in degrees.

Minimizing the weighted sum of squares cost function has been shown to be effective in matching frequency responses of low order equivalent systems to frequency responses extracted from flight time histories using FFTs [14]. A constrained optimization routine from the Matlab Optimization Toolbox is used to solve the optimization problem.

$$\min_{(K_p, T_{Lead}, T_{Lag}, \tau_e, \alpha)} V(K_p, T_{Lead}, T_{Lag}, \tau_e, \alpha) \text{ Subject to } 0 \leq T_{Lead} \leq 5sec \quad [5.29]$$

$$0 \leq T_{Lag} \leq 10sec$$

The 10 second constraint on T_{Lag} is chosen because the lag pole $1/T_{Lag}$ can not be accurately determined in all cases since the lowest frequency component sinusoid is approximately 0.21 rad/sec which is greater than the minimum lag pole location $1/10$ rad/sec; thus, estimates of $T_{Lag} > 10$ sec can only be interpreted as significant lag generation in the region where experimental frequency response data is available.

5.2.5 Product Rule

The product rule is an empirical formula which combines single axis HQRs to form an estimate of the overall multi-axis HQR. A pilot can control one axis better than he can control multiple axes; therefore, one can expect multi-axis HQRs to be worse than any single-axis HQR. The classical product rule [9] for a two axis system takes the form of a general hyperbola.

$$R_m = aR_1R_2 + bR_2 + cR_1 + d \quad [5.30]$$

The regression coefficients (a , b , c , d) are computed from a least squares fit of Equation 5.31 to experimental data.

$$R_m = aR_\Theta R_\Psi + bR_\Psi + cR_\Theta + d \quad [5.31]$$

where R_Θ and R_Ψ are single axis pitch and yaw HQRs respectively.

The regression coefficients are computed by solving the linear algebra problem of Equation 5.32

$$\begin{array}{ccc}
 \begin{bmatrix} R_{\Theta_1} R_{\Psi_1} & R_{\Psi_1} & R_{\Theta_1} & 1 \\ \vdots & \vdots & \vdots & \vdots \\ R_{\Theta_n} R_{\Psi_n} & R_{\Psi_n} & R_{\Theta_n} & 1 \end{bmatrix} & \begin{bmatrix} a \\ b \\ c \\ d \end{bmatrix} & = \begin{bmatrix} R_{m_1} \\ \vdots \\ R_{m_n} \end{bmatrix} \\
 \mathbf{A} & \mathbf{x} & = \mathbf{R}_m
 \end{array} \tag{5.32}$$

The least squares solution to Equation 5.32 is given by

$$\hat{\mathbf{x}} = [a \ b \ c \ d]^T = (\mathbf{A}^T \mathbf{A})^{-1} \mathbf{A}^T \mathbf{R}_M \tag{5.33}$$

It should be noted that hyperbolic product rules have some serious shortcomings. In most cases if a rating in one axis is extremely good, the product rule will predict the two axis rating to be better than the single axis ratings. These counter-intuitive predictions arise from the product rule's lack of recognition of the HQR scale. The HQR scale is limited to values between 1 and 10 while the general hyperbolic equation is not limited. One must therefore use judgement when interpreting the results of any product rule regression.

5.3 Results

5.3.1 Experiment #1

The amount of time taken to move a stationary object between the two platforms and the handling qualities rating assigned to a configuration by the pilot are the two measures of performance used in this test. Table 5.2 shows the results of Experiment #1.

The single letters (A,B,C) denote the first runs performed at the beginning of this study. The double letter runs are performed after all of the experiments have been run to see how experience affects both HQR and time performance. One can see that experience significantly reduces the amount of time taken to complete the task in all categories but has little effect on the HQR. The HQR margin of error is found to be

Table 5.2 Results of Experiment #1.

Run	Command System	HQR	Time(sec)
A	Open Loop	5.5→6	50.67
AA	Open Loop	5.5	36.15
B	Attitude	2.5→3	36.70
BB	Attitude	3.5→	19.70
C	Rate	3.5	37.00
CC	Rate	4	27.00

+/- .79 (HQR) for all experiments. This shows that the pilot HQR is a reliable and consistent measure of performance. Table 5.2 shows that the pilot achieved the best performance using the attitude command system. The attitude command system also receives the best HQRs . The pilot assigns better HQRs to the rate than the open loop command system. He also achieves better performance using rate rather than the open loop command system.

5.3.2 Experiments #2 and #3

5.3.2.1 Comparison of Displays

The visual scene is clearly preferred to the instrument display as can be deduced from Figure 5.12 and Table 5.3.

It is assumed that if a configuration receives a HQR of 1 in the instrument task, then the visual task will also receive a HQR of 1. The best fit lines computed from least squares fits are therefore constrained to pass through the point (1,1). A line with a slope of 1 indicates that the pilot's HQR is unaffected by display type. Lines with slopes less than 1 indicate that it is easier for the pilot to perform dynamic tracking tasks using the visual scene. The slopes of the best fit lines for single axis pitch and yaw cases are 0.4793 and 0.6932 respectively. A plot for the multi-axis case is not shown because Table 5.3 clearly shows that the visual scene is preferred. Many of the multi-axis instrument tasks receive HQRs of 10 indicating that control is lost during some part of the operation.

It is not surprising that the pilot prefers the visual scene to the instrument display because the pilot can perceive more information from the visual scene. When using the visual scene, the pilot can see and hear what the individual components of the TROFM are doing at any given time. This generates the possibility of the pilot opening more feedback channels and allows the pilot to act as a multi-variable feedback control system to obtain desired performance. The pilot is also able to determine whether an error increase is caused by joystick deflection or forcing function which is not possible with the compensatory instrument display. Pilot comments suggest

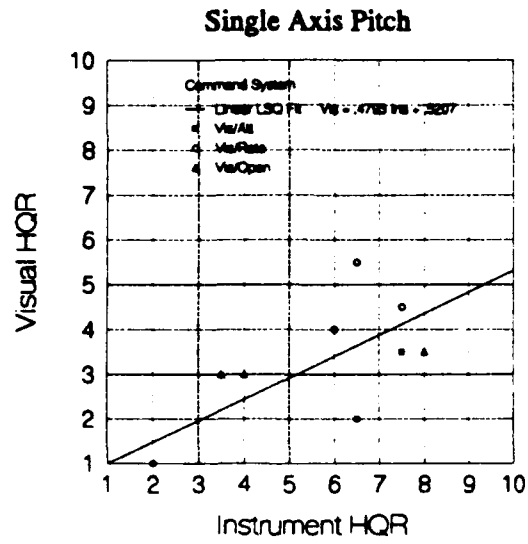
Table 5.3 Handling qualities ratings for instrument display and visual scene with identical tasks.

Axis/Command System	Instrument HQR	Visual HQR
Pitch/Attitude	2	1
Pitch/Attitude	6.5	2
Pitch/Attitude	7.5	3.5
Pitch/Rate	6	4
Pitch/Rate	7.5	4.5
Pitch/Rate	6.5	5.5
Pitch/Open Loop	3.5→4	3
Pitch/Open Loop	4	3
Pitch/Open Loop	8	3.5
Yaw/Attitude	4	3
Yaw/Attitude	3.5	3→3.5
Yaw/Attitude	3.5	3.5→4
Yaw/Rate	3.5	3
Yaw/Rate	5.5	3.5
Yaw/Rate	6.5	3.5
Yaw/Open Loop	4.5	4
Yaw/Open Loop	8	5.5
Yaw/Open Loop	9	8
Multi/Attitude	8	3
Multi/Attitude	8	5.5

Table 5.3, continued.

Axis/Command System	Instrument HQR	Visual HQR
Multi/Attitude	9.5	4.5
Multi/Rate	9	6.5
Multi/Rate	10	7
Multi/Rate	10	9
Multi/Open Loop	10	9
Multi/Open Loop	10	8
Multi/Open Loop	10	7

a)



b)

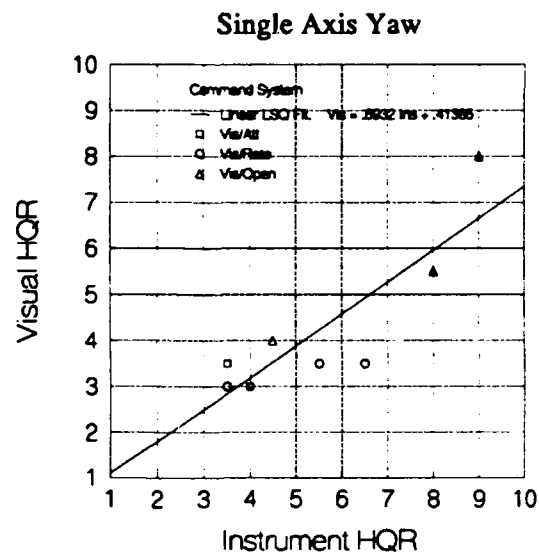


Figure 5.12 Visual versus instrument HQRs for a) pitch axis b) yaw axis tasks.

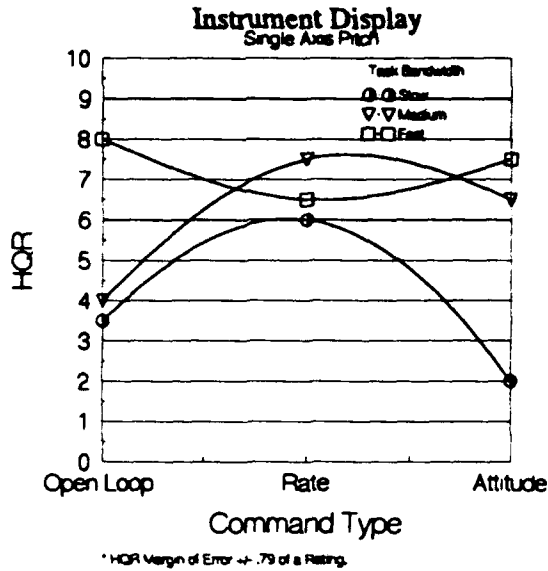


Figure 5.13 HQR as a function of command system and forcing function bandwidth using instrument display for single axis pitch task.

that the multi-axis instrument tasks would have been much easier if the yaw error indicator was aligned with the lateral joystick axis.

5.3.2.2 Instrument Display

Figures 5.13, 5.14, 5.15 and Table B.1 show the handling qualities ratings for the instrument test as a function of command system and forcing function bandwidth.

From Figure 5.13 one can see that for the single axis pitch task, HQRs increase as task bandwidth increases for all command systems except rate, where the order goes slow, fast, medium. The attitude command system receives the best rating (2) for the slow task while the open loop receives the best rating for the medium task (4) and the rate command system receives the best rating (6.5) for the fast task.

From Figure 5.14 one can see that the yaw attitude command system receives good HQRs for all forcing function bandwidths. The open loop command system receives better ratings than the rate command system for all bandwidth forcing functions

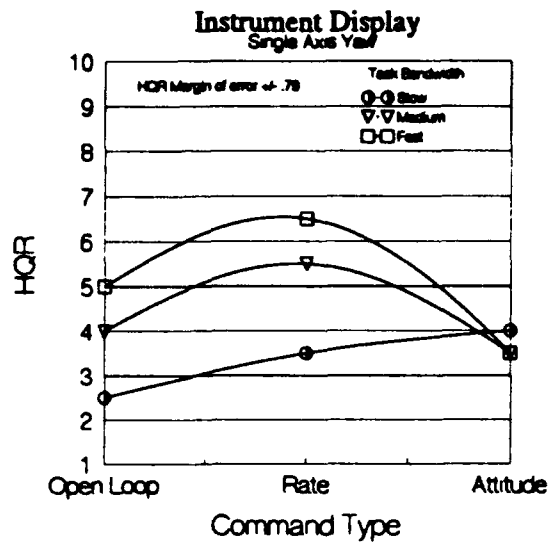


Figure 5.14 HQR as a function of command system and forcing function bandwidth using instrument display for single axis yaw task.

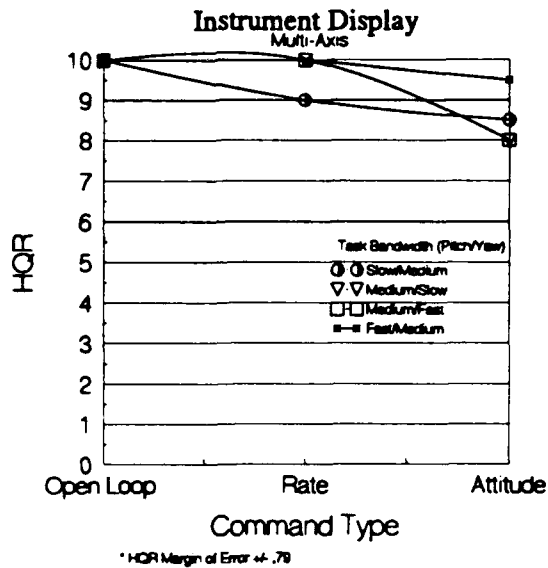


Figure 5.15 HQR as a function of command system and forcing function bandwidth using instrument display for multi-axis tasks.

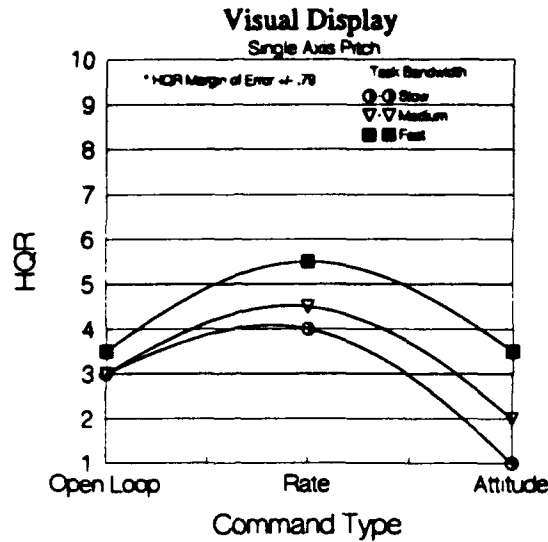


Figure 5.16 HQR as a function of command system and forcing function bandwidth using visual scene for single axis pitch task.

and is rated better than the attitude command system for tracking the slow forcing function.

Figure 5.15 shows that the open loop command system is uncontrollable in the multi-axis task. The rate command system is uncontrollable in all cases except for the combination of low bandwidth pitch and medium bandwidth yaw forcing functions. The attitude command system is controllable in all cases but receives very poor ratings. The pilot stated that the confusing yaw axis instrument display made the multi-axis tasks more difficult than they should have been.

5.3.2.3 Visual Scene

Figures 5.16, 5.17 and 5.18 show HQR as a function of command system and forcing function bandwidth for Experiment #3.

Figure 5.16 shows that for the single axis pitch cases, high bandwidth tasks receive higher (worse) HQRs than low bandwidth tasks in all cases. The attitude command

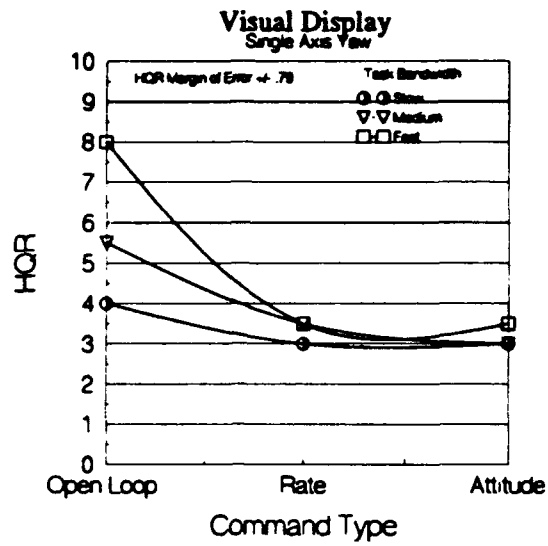


Figure 5.17 HQR as a function of command system and forcing function bandwidth using visual scene for single axis yaw task.

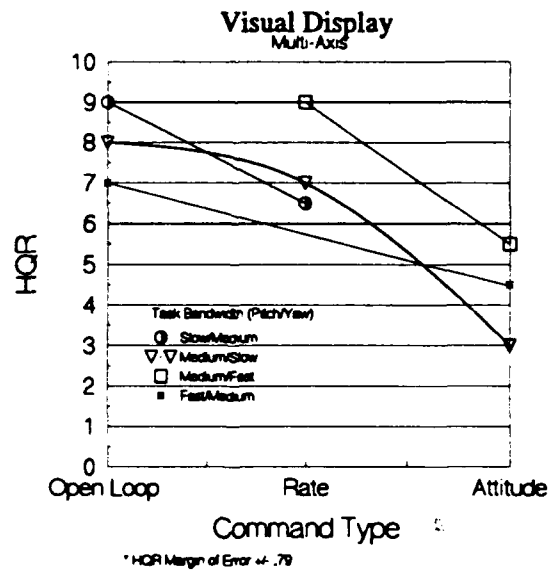


Figure 5.18 HQR as a function of command system and forcing function bandwidth using visual scene for multi-axis tasks.

system receive the best overall HQRs followed by the open loop and rate command systems.

Figure 5.17 indicates that the rate and attitude command systems essentially tie (i.e. within the ± 0.79 HQR margin of error) for the best HQRs while the open loop command system is clearly not the command system of choice.

Figure 5.18 illustrates that the open loop command system receives poor ratings, but the ratings improve as the bandwidth of the tasks increase. The rate and attitude command system HQRs improve as the bandwidth of the tasks decrease. The attitude command system receives the best overall HQRs.

5.3.2.4 Product Rule

A product rule regression is performed on the HQR data (Table 5.4) from the visual dynamic tracking test (Experiment #3). An estimate of the multi-axis HQR given the two single axis HQRs can be obtained from Equation 5.34.

$$R_m = -0.6779R_\theta R_\psi + 5.8322R_\psi + 3.5767R_\theta - 17.71 \quad [5.34]$$

One can see that the product rule estimates predict the actual multi-axis HQR to within ± 1.02 rating for 7 out of the 9 cases. It should be noted that only the 7 "good" points in Table 5.4 are used in the calculation of the regression coefficients.

The iso-rating curves in Figure 5.19 indicate that the multi-axis rating degrades as either single axis rating degrades. Upon close examination one can also deduce that a small degradation in the single axis yaw HQR will result in large multi-axis HQR degradation. One may also see that HQR degradations in the pitch axis have a less pronounced effect upon the multi-axis HQR. This indicates that the yaw axis is the most difficult to control in multi-axis tasks and one can expect the the pilot to concentrate more on the yaw axis than on pitch axis. Note that the product rule computes ratings which are beyond the bounds of the Cooper-Harper scale since it does not recognize these bounds. As stated previously product rules do not work if either or both single axis ratings are extremely good. In this case experimental data is available for a limited number of cases so the product rule should not be considered

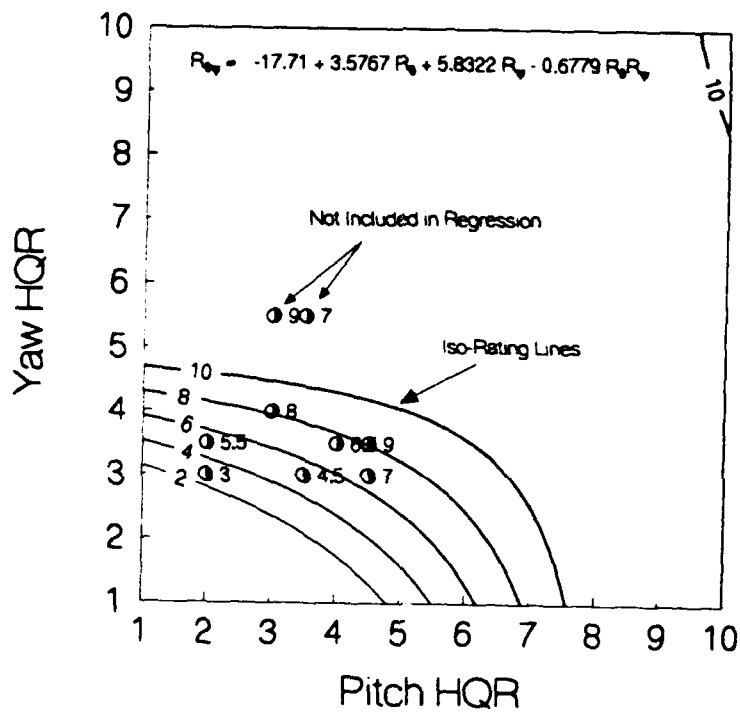


Figure 5.19 Product rule for visual scene.

Table 5.4 Actual single and multi-axis HQRs with product rule estimates of multi-axis HQR (* Not used in regression).

Pitch HQR	Yaw HQR	Multi-axis HQR	Est. Multi HQR	Error
2	3	3	2.87	0.13
3.5	3	4.5	5.19	-0.69
2	3.5	5.5	5.11	0.39
4.5	3	7	6.73	0.27
4	3.5	6.5	7.51	-1.02
4.5	3.5	9	8.12	0.88
3	5.5	9*	13.9	4.91
3	4	8	8.21	-0.21
3.5	5.5	7*	13.83	6.84

accurate far outside of the range covered by the experimental data ($2 \leq R_{\theta} \leq 4$ and $3 \leq R_{\psi} \leq 4.5$).

5.3.2.5 Assessment of adherence to crossover law

Recall that the crossover law states that in a closed loop compensatory task, the pilot will compensate so that the combined pilot-vehicle open loop dynamics is similar in appearance to a K/s plant with a pure time delay in the region of crossover. The Bode plots of the experimentally determined describing functions, as well as best fit extended crossover models to the experimental data are shown in Appendix B. The extended crossover model fits the experimental data well in cases where the pilot assigns HQRs ≤ 7 . This is as expected because HQRs > 7 indicate that controllability is in question.

The one third law condenses the information shown in the open loop Bode plots. Figures 5.20, 5.21 and 5.22 show the one third laws for the slow, medium and fast runs for the visual scene test. Figures 5.23, 5.24 and 5.25 shows the one third laws for the slow, medium and fast runs for the instrument test. One can see that the modified one third laws describe the trends in the all of the visual data well and most data scatter can be described by adjusting the intercept of the one third law line. The modified one third laws describe the medium and high bandwidth instrument cases fairly well with the exception of the cases affected by the crossover regression phenomenon [13]. Crossover regression occurs when the pilot reduces his gain to reduce the pilot-vehicle crossover frequency to maintain a reasonable tracking error. This can also occur when the pilot focuses his attention on one axis in a multi-axis task which opens the loop on the ignored axis. One can see that most instances of crossover regression occur when the pilot is involved in a medium or fast multi-axis tracking task. These plots also indicate how effective the pilot is in following the forcing function. The ratio e_o/σ_i can be thought of as normalized performance. A ratio of one indicates that no reduction of error is taking place. Ratios less than one indicate that the pilot is successfully tracking the forcing function and is effectively

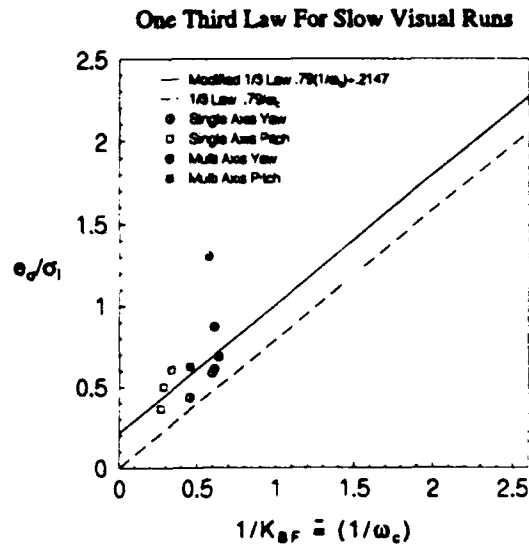


Figure 5.20 One third law for the visual scene with low bandwidth forcing functions.

reducing tracking errors. Figures 5.26 and 5.27 show the open loop describing functions and best fit crossover models for the pilot-vehicle using the instrument display and pitch and yaw attitude command systems respectively. Recall that the pitch and yaw attitude command systems had nearly flat 0 dB frequency responses out to 7.78 and 6.61 rad/sec respectively. The fact that the crossover model fits the experimental data well indicates that the pilot is generating lag compensation in the region of crossover. Upon examination of the pilot describing functions for these cases (Figures 5.28 and 5.29) one can see that the pilot is indeed generating lag compensation which is indicated by the negative slopes of the magnitude curves. The best fit pilot describing functions associated with Figures 5.28 and 5.29 are found to be

Pitch:

$$Y_p = 3.6668 \frac{(0.1361s + 1)}{2.045s + 1} e^{-j(0.0385\omega + 0.3696/\omega)} \quad [5.35]$$

Yaw:

$$Y_p = 7.6828 \frac{(1.1772s + 1)}{10s + 1} e^{-j(0.3507\omega + 0.1769/\omega)} \quad [5.36]$$

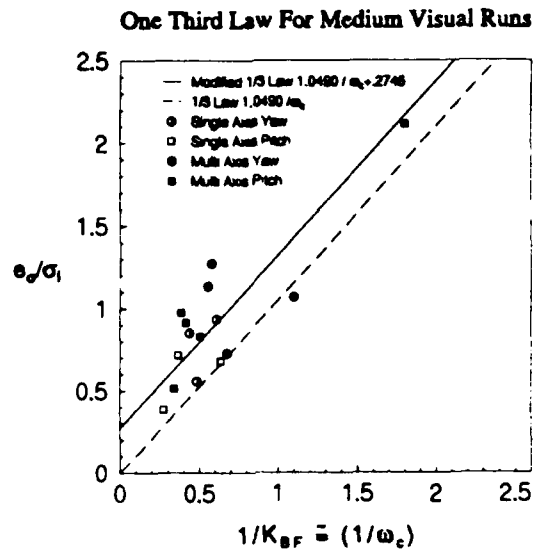


Figure 5.21 One third law for visual scene with medium bandwidth forcing functions.

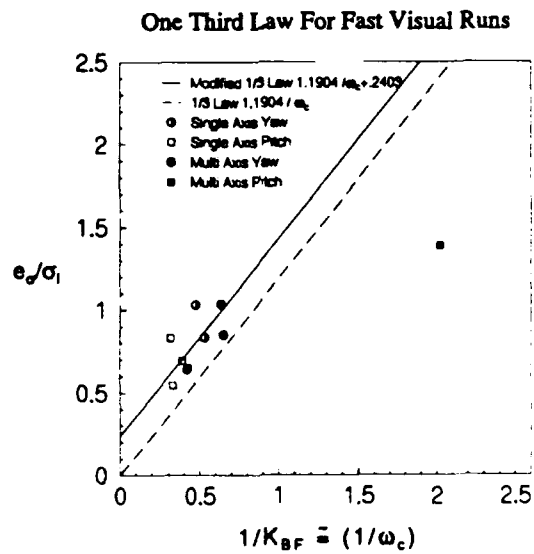


Figure 5.22 One third laws for the visual scene with fast bandwidth forcing functions.

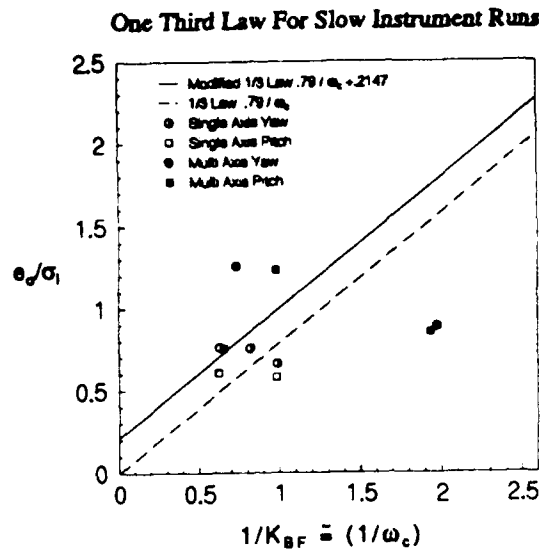


Figure 5.23 One third laws for the instrument display with low bandwidth forcing functions.

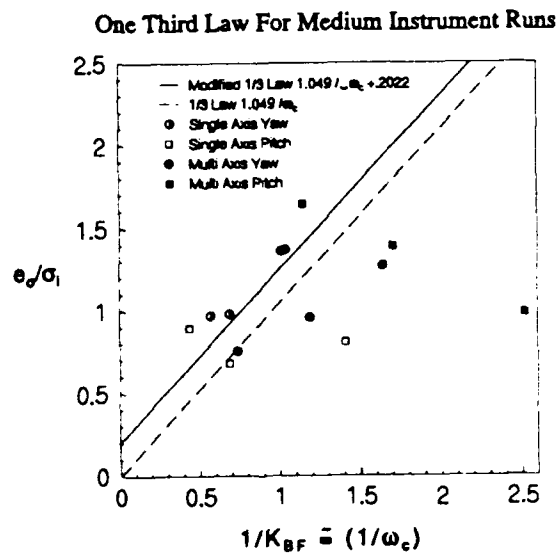


Figure 5.24 One third laws for the instrument display with medium bandwidth forcing functions.

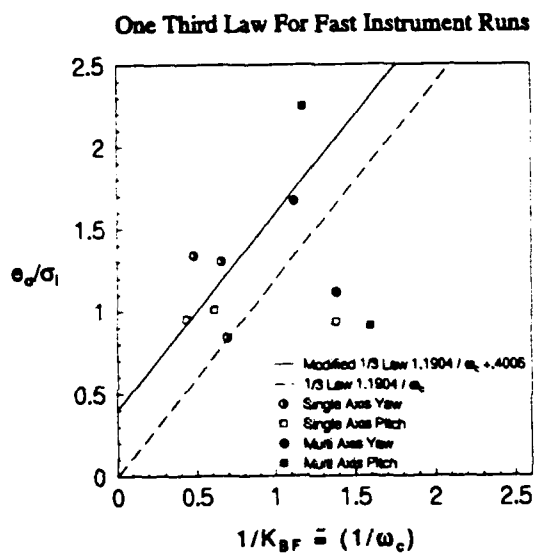


Figure 5.25 One third laws for the instrument display with fast bandwidth forcing functions.

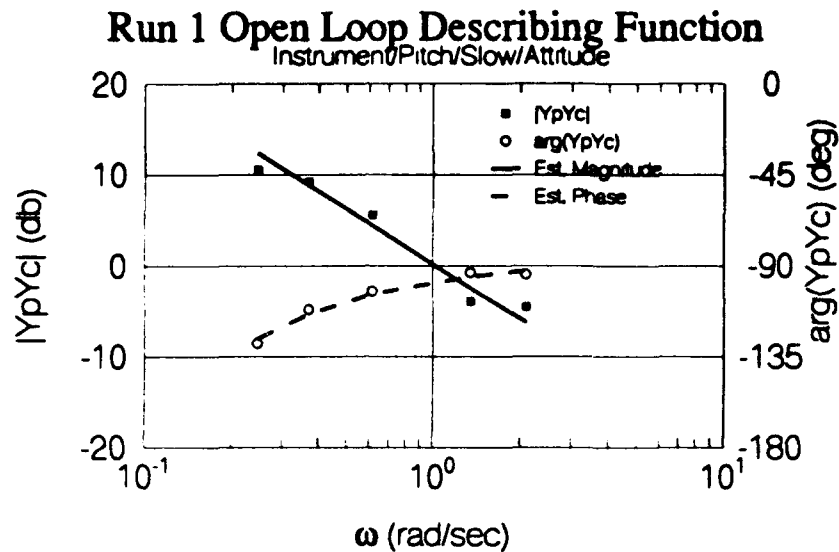


Figure 5.26 Open loop pilot-vehicle describing function for a low bandwidth single axis pitch forcing function with instrument display and attitude command system.

[b] Figures 5.30 and 5.31 show open loop pilot-vehicle describing functions and best fit extended crossover models for pitch and yaw rate command systems used with instrument displays. One can see that the crossover model describes the trends quite well.

Recall that the pitch and yaw rate command systems have nearly flat 0 dB frequency responses out to approximately 6.79 rad/sec and 8 rad/sec. Since the controlled elements Y_c are simple integrators in the forcing function frequency range, one can expect that the pilot will act as a pure gain element to make the open loop pilot-vehicle describing function appear as a k/s plant. Figures 5.32 and 5.33 show pilot describing functions associated with the open loop describing functions of Figures 5.30 and 5.31. One can see that the pilot is primarily acting as a pure gain compensator with time delay as indicated by the relatively flat magnitude and slightly negative phase curves. Estimates of the pitch and yaw describing functions are given in Equations 5.37 and 5.38.

$$Y_p = 7.3164 \frac{(3.6829s + 1)}{10s + 1} e^{-j(0.1554\omega - 0.0339/\omega)} \quad [5.37]$$

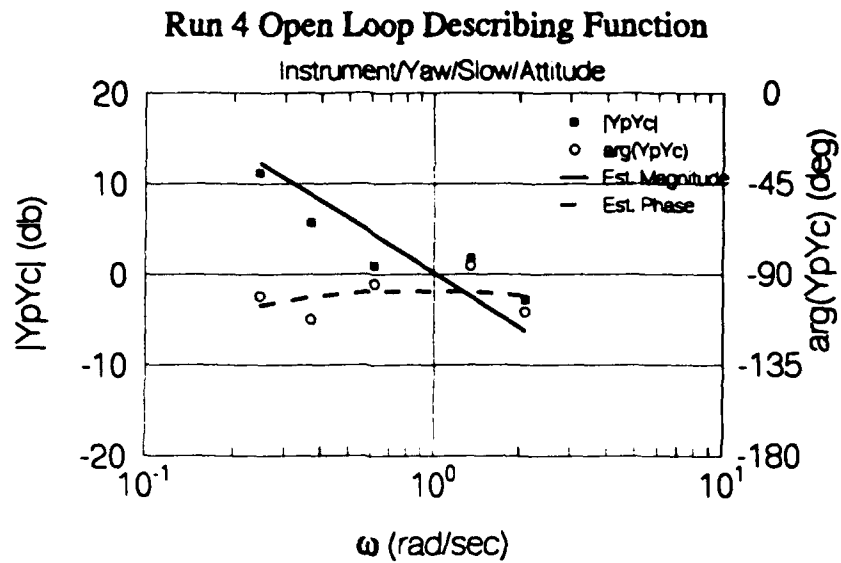


Figure 5.27 Open loop pilot-vehicle describing function for a low bandwidth single axis yaw forcing function with instrument display and attitude command system.

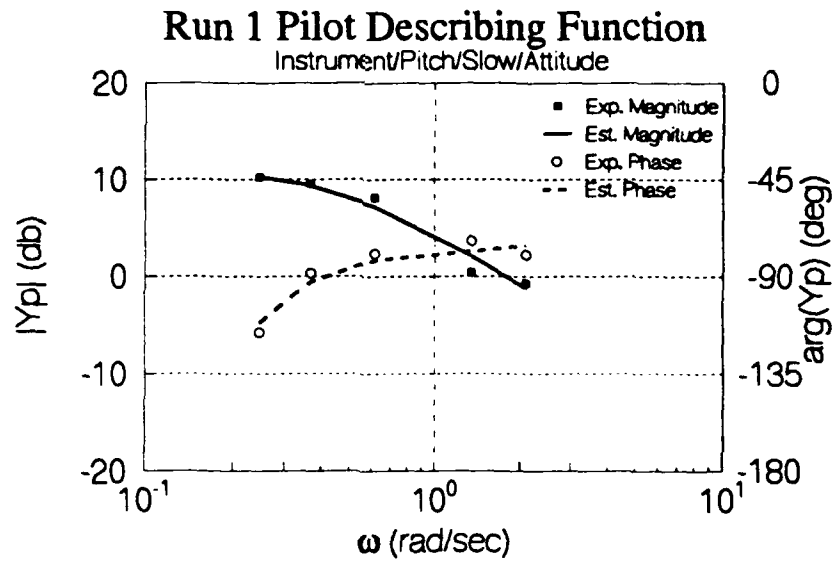


Figure 5.28 Pilot describing function for a low bandwidth single axis pitch forcing function with instrument display and attitude command system.

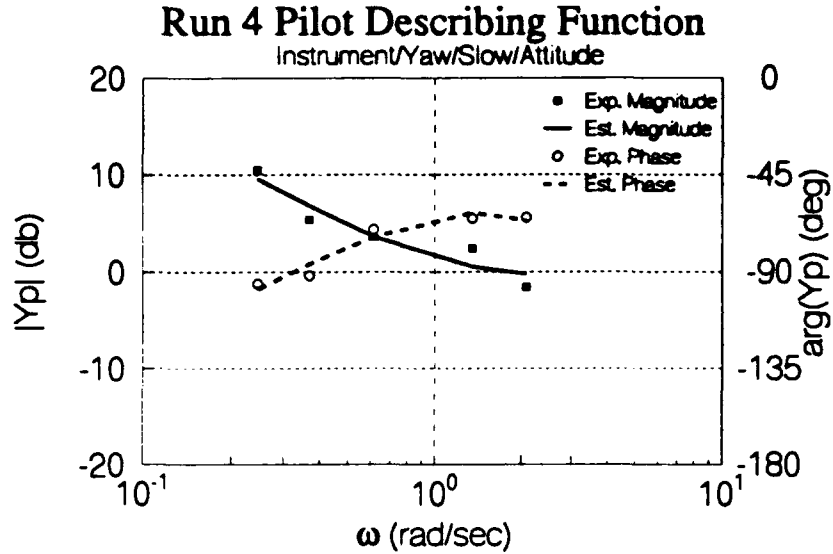


Figure 5.29 Pilot describing function for a low bandwidth single axis yaw forcing function with instrument display and attitude command system.

$$Y_p = 1.4513 \frac{(0.2688s + 1)}{4 \times 10^{-6}s + 1} e^{-j(0.4915\omega + 0.1769/\omega)} \quad [5.38]$$

The open loop yaw command system shown in Figure 4.2 has the frequency response characteristics shown in Figure 4.4. One can see that it is primarily a rate command system with a crossover frequency at 2.43 rad/sec and has very little phase margin. This suggests that the pilot will have to generate lead compensation to increase the phase margin when the forcing function bandwidth approaches the yaw axis crossover frequency. Figure 5.34 shows the open loop pilot-vehicle describing functions for a high bandwidth ($\omega_{ei} = 2.06$ rad/sec) forcing function. One can see that the crossover model fits the magnitude and phase data well. Figure 5.35 shows the pilot describing function for this case. Note the positive slope of the magnitude curve around 2 rad/sec indicates the pilot is generating lead compensation. The phase curve is slightly above 0° between 1 and 2 rad/sec and then sinks below 0° above 2 rad/sec which indicates that the pilots phase lead is counteracted by his reaction time delay. The best fit pilot describing function for this case is given in Equation 5.39.

$$Y_p = 0.2914 \frac{(0.9032s + 1)}{0.1157s + 1} e^{-j(0.1275\omega + 1.2351/\omega)} \quad [5.39]$$

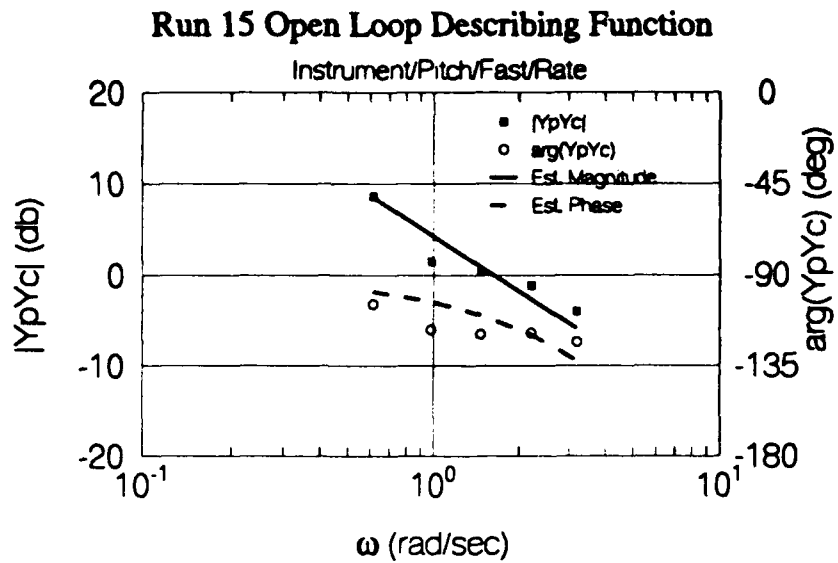


Figure 5.30 Open loop pilot-vehicle describing function for a high bandwidth single axis pitch forcing function with instrument display and rate command system.

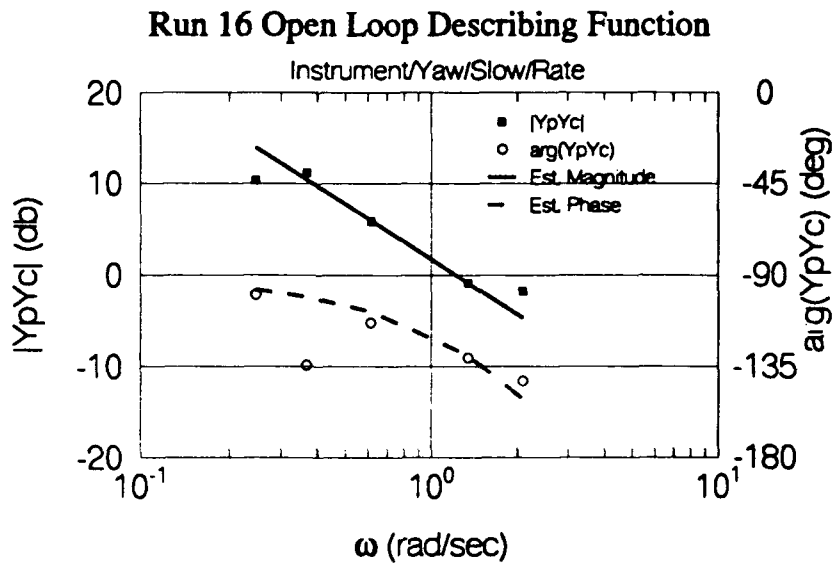


Figure 5.31 Open loop pilot-vehicle describing function for a low bandwidth single axis yaw forcing function with instrument display and rate command system.

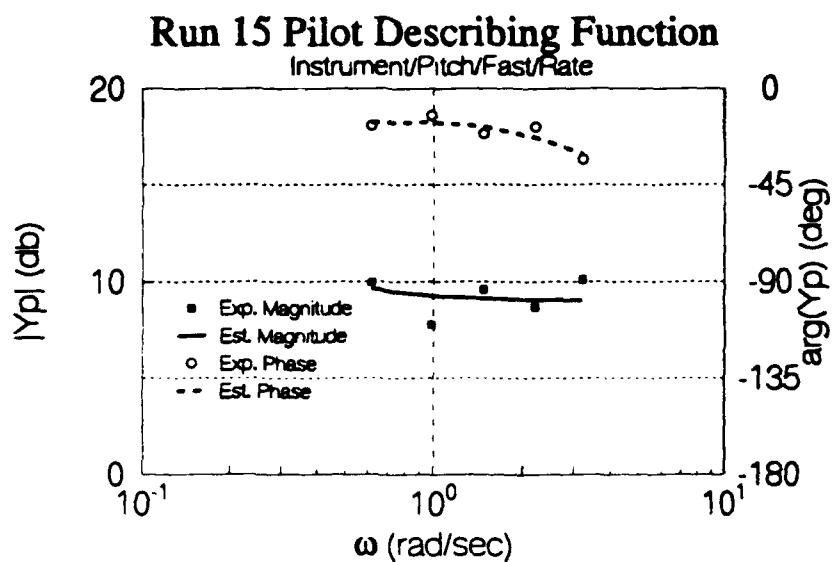


Figure 5.32 Pilot describing function for a high bandwidth single axis pitch forcing function with instrument display and rate command system.

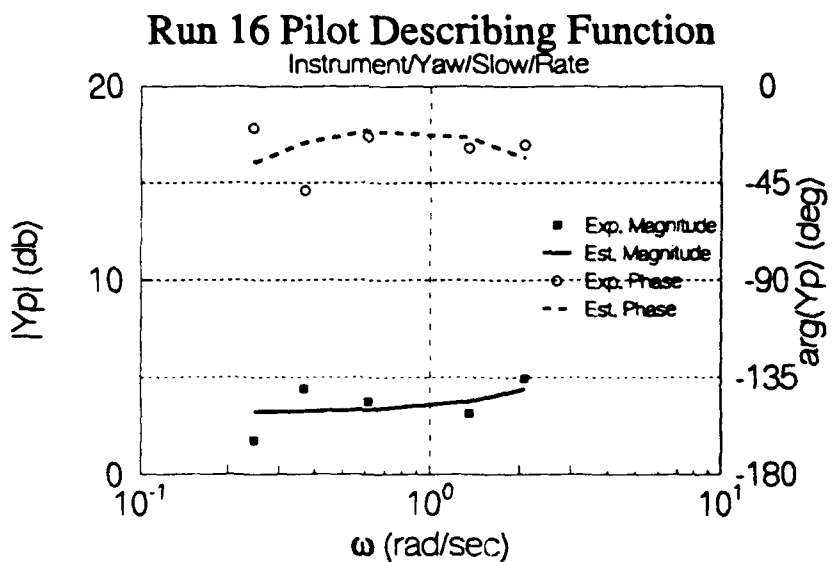


Figure 5.33 Pilot describing function for a low bandwidth single axis yaw forcing function with instrument display and rate command system.

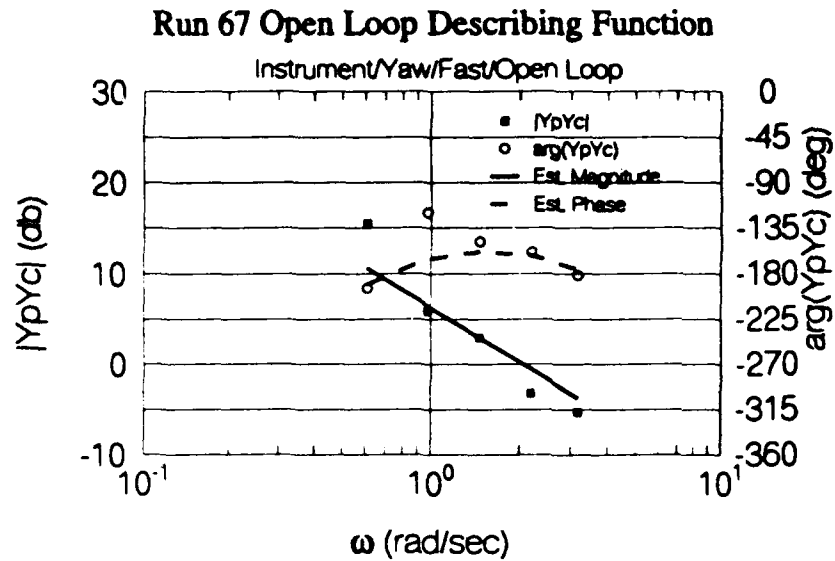


Figure 5.34 Open loop pilot-vehicle describing function for a high bandwidth single axis yaw forcing function with instrument display and open loop command system.

5.3.3 Pilot Compensation and Handling Qualities

The slope of the pilot magnitude curve at the best fit open loop pilot-vehicle crossover frequency is used as a measure of pilot compensation. This is chosen because it unambiguously indicates the type of compensation generated by the pilot and is not affected by time delay.

Figures 5.36 and 5.37 show how HQRs are affected by the amount of lead compensation for the single and multi-axis visual cases respectively. Second and first order polynomials are fitted to the experimental data and are given in Equations 5.40 and 5.41 for the single and multi-axis visual cases respectively.

$$HQR_{est} = 0.0017 \left[\left. \frac{d|Y_p|_{dB}}{d \log(\omega)} \right|_{\omega_c} \right]^2 + 0.122 \left. \frac{d|Y_p|_{dB}}{d \log(\omega)} \right|_{\omega_c} + 3.7925 \quad [5.40]$$

$$HQR_{est} = 0.1201 \left. \frac{d|Y_p|_{dB}}{d \log(\omega)} \right|_{\omega_c} + 6.7776 \quad [5.41]$$

One can see that lead compensation degrades HQRs while lag compensation improves them. This confirms the trends observed in References [11] and [9]. No conclusions as to how compensation affects HQRs can be made for the instrument cases because of data scatter.

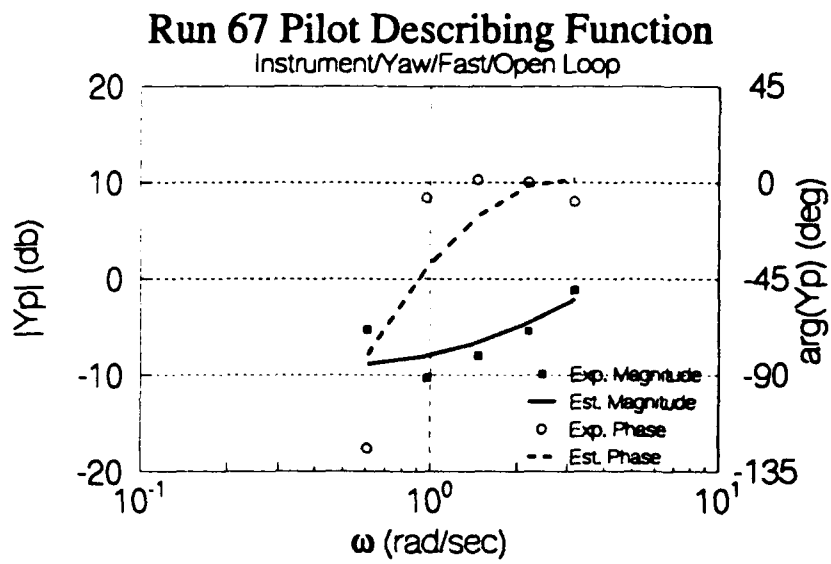


Figure 5.35 Pilot describing function for a high bandwidth single axis yaw forcing function with instrument display and open loop command system.

Normalized performance (e_o/σ_i) as a function of slope of the pilot magnitude curve at the open loop pilot-vehicle crossover frequency is shown for the single axis instrument, single axis visual and multi-axis visual tasks in Figures 5.38, 5.39 and 5.40 respectively. One can see that pilot performance improves as lag generation increases and degrades as lead compensation increases. Figures 5.38 and 5.39 indicate that the pilot achieves the best performance when generating significant amounts of lag ($Slope \leq -15dB/dec$). The experimental data shown in Figure 5.40 suggest that there is a lower limit to how much lag the pilot may generate and still improve performance. The pilot achieves the best performance when generating about -10 dB/dec of lag compensation and performance degrades as lag compensation increases. Figures 5.38, 5.39 and 5.40 all indicate that pilot lead compensation degrades overall performance.

From the above analysis one may conclude that the preferred pilot model is of the form

$$Y_p \doteq \frac{K e^{-\tau s}}{T_{Lag} s + 1} \quad [5.42]$$

This means that pilots prefer to generate lag compensation which implies that attitude command systems are desirable. More generally a desirable controlled element Y_c in a man-machine system should have the characteristics of a simple tracker (unity gain element). This modifies the assumption of Reference [1] that "human control behavior reaches optimum when the man becomes the analogue of a simple amplifier" and tasks of integration (lag) and differentiation (lead) degrade overall performance. The results of Experiments #2 and #3 validate the modification to the assumptions of Reference [1] made by Reference [11] which states controlled elements which require the pilot to generate low frequency lag compensation to achieve $Y_p Y_c \approx K e^{-\tau s}/s$ are desirable.

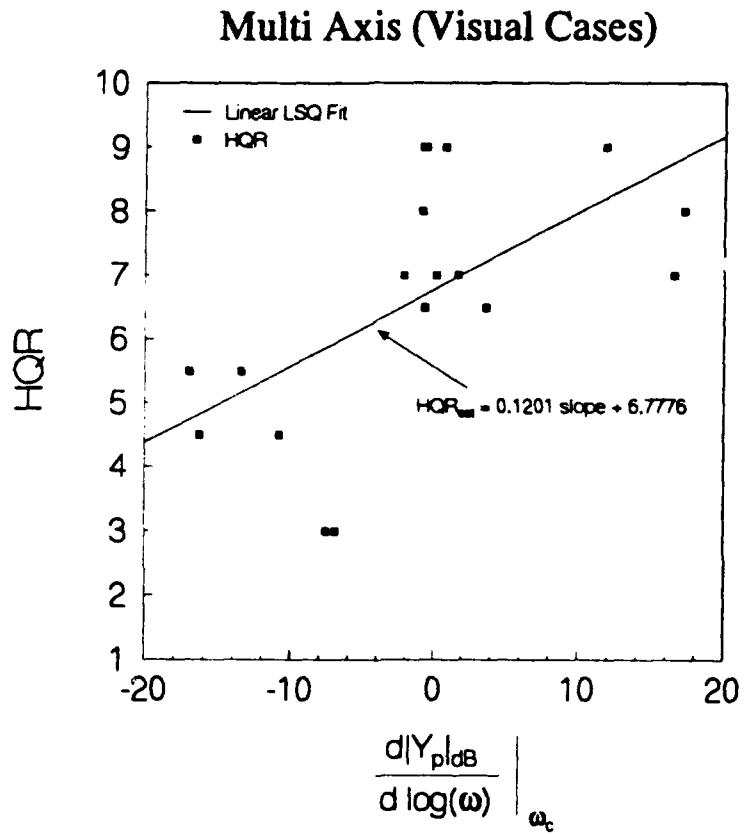


Figure 5.36 HQR as a function of slope of pilot Bode magnitude curve at the open loop pilot-vehicle crossover frequency for the multi-axis visual cases

Single Axis (Visual Cases)

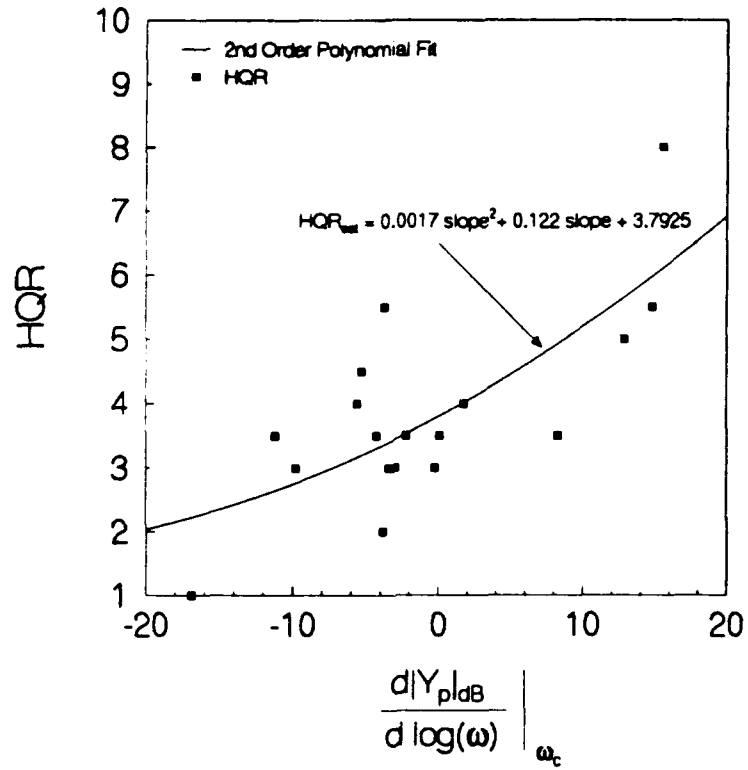


Figure 5.37 HQR as a function of slope of pilot Bode magnitude curve at the open loop pilot-vehicle crossover frequency for the single axis visual cases.

Single Axis Instrument Tasks

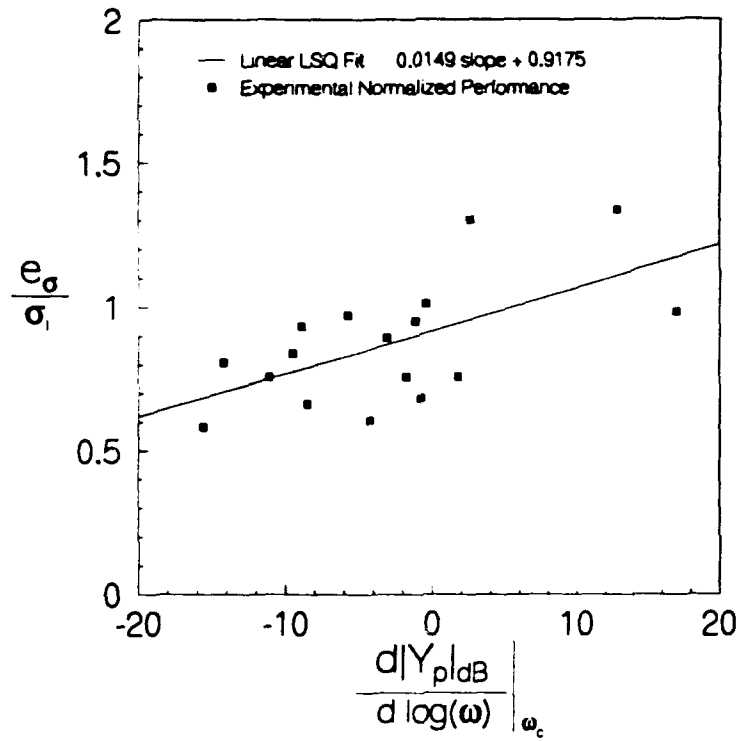


Figure 5.38 Normalized performance as a function of slope of pilot Bode magnitude curve at the open loop pilot-vehicle crossover frequency for the single axis instrument cases.

Single Axis Visual Tasks

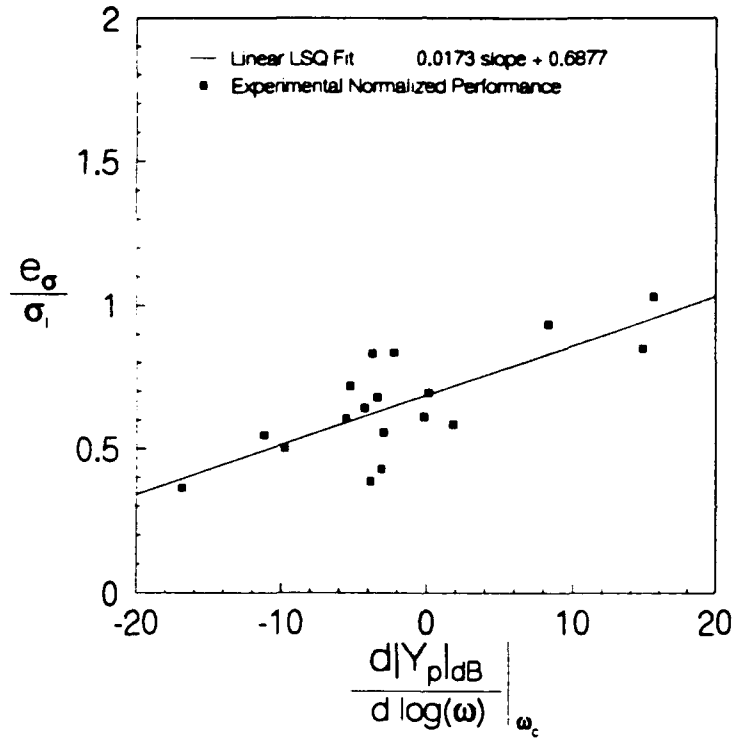


Figure 5.39 Normalized performance as a function of slope of pilot Bode magnitude curve at the open loop pilot-vehicle crossover frequency for the single axis visual cases.

Multi Axis Visual Tasks

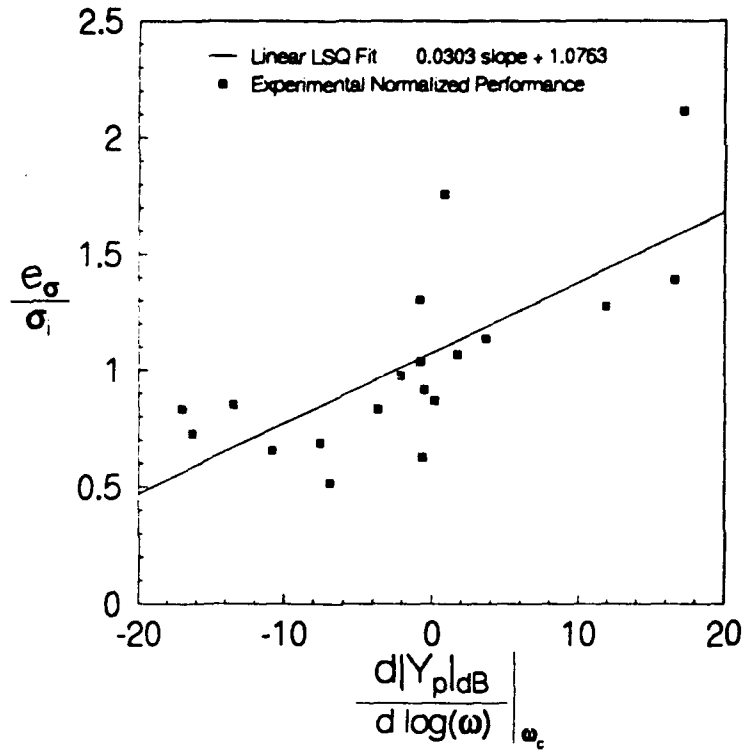


Figure 5.40 Normalized performance as a function of slope of pilot Bode magnitude curve at the open loop pilot-vehicle crossover frequency for the multi-axis visual cases.

6. CONCLUSIONS

A study of the effects of command systems, displays and tasks on human pilot behavior is conducted. A general aviation pilot uses the Cooper-Harper rating scale to evaluate the flying qualities of the TROFM using unaugmented, rate, and attitude command systems for two types of tasks and two different display types. Pilot and pilot-vehicle describing functions are obtained from time histories of dynamic tracking tasks where the pilot attempts to track a random appearing input. Compensatory instrument displays and a visual pursuit scene are used for the dynamic tracking tasks. Correlations between the Cooper-Harper ratings and quantitative descriptions of pilot behavior are made. The experimental results are compared to the classical theory of man-machine system dynamics which is based on McRuer's Crossover Model.

The pilot prefers attitude command systems when maneuvering to stationary objects and when tracking moving targets. This preference is independent of the display type and in most cases the forcing function bandwidth. It is found that lag compensation is easier for a pilot to generate than either lead or pure gain compensation. Handling qualities ratings and over-all performance degrade as the pilot is required to produce more lead compensation. This result implies that attitude command systems have desirable dynamic characteristics for controlled elements in pilot-vehicle systems where the pilot is attempting to track an attitude forcing function. More generally, this implies that desirable controlled elements in man-machine systems have unity gain (flat 0 dB frequency responses) over the frequency range of interest.

The pilot achieves the best performance in dynamic tracking tasks when using a visual pursuit scene as opposed to a compensatory instrument display. It is found that a product rule describes the handling qualities degradation associated with a multi-axis visual task within ± 1 HQR for 78 % of the cases.

The extended crossover model describes most of the experimentally determined open loop describing functions well in cases where the $HQR \leq 7$. It is also found that the type of pilot compensation can be predicted from knowledge of the machine dynamics, forcing function bandwidth and application of the theoretical crossover model. Pilot ratings are found to be repeatable since the HQRs for a given configuration are consistent (± 0.79 HQR).

7. RECOMMENDATIONS FOR FUTURE RESEARCH

Future researchers can use this equipment to conduct a study of how different types of manipulators (joysticks, etc.) effect performance and handling qualities ratings. It is recommended that a spring loaded center stick be one of the candidates because of its widespread use in other handling qualities studies. Improvements in the multi-axis compensatory instrument display are also in order. Studies similar to the one performed here can make use of command systems designed by modern multi-variable methods. The response and adaptation of the human operator to step changes in the TROFM dynamics can also be studied. This can simulate the in-flight failure of a stability augmentation system. Comparison of the pilot's response when maneuvering from one point to another to nonlinear time optimal "bang-bang" models can also be made.

In practice tilt rotor aircraft use constant speed rotors with variable pitch blades to govern the amount of lift produced. This configuration allows variations in lift to occur much faster since these variations are not limited by the bandwidth of the motor. A variable pitch rotor could enhance the TROFM discussed in this report.

REFERENCES

- [1] Birmingham, H.P. and F.V. Taylor, "A Human Engineering Approach to the Design of Man-Operated Continuous Control Systems," NRL Report 43333, April 7, 1954.
- [2] Cooper, G.E., and Harper, R.P., "The Use of Pilot Rating in the Evaluation of Aircraft Handling Qualities," NASA TN D-5153, 1969.
- [3] Eykhoff, Pieter, "System Identification Parameter and State Estimation," John Wiley & Sons, New York, 1974.
- [4] Franklin, G.F., Powell, J.D. and Workman, M.L., "Digital Control of Dynamic Systems," Addison-Wesley, New York, 1990.
- [5] Grace, A., Laub, A.J., Little, J.N., and Thompson, C., "Control System Toolbox for use with Matlab Users Guide," The Math Works Inc., South Natick, MA, October 1990.
- [6] Greenwood, D.T., "Principles of Dynamics," Prentice Hall, New Jersey, 1988.
- [7] Layton, D.M., "Helicopter Performance," Matrix Publishers, Inc., Beaverton, OR, 1984.
- [8] Maine, R.E. and Iliff, K.W. "Formulation and Implementation of a Practical Algorithm for Parameter Estimation with Process and Measurement Noise," SIAM Journal of Applied Mathematics, Vol 41, No. 3, Dec 1981, pp 558-579.
- [9] McRuer, D.T., and E.S. Krendel, "Mathematical Models of Human Pilot Behavior," AGARD-AG-188, Jan. 1974.
- [10] McRuer, D.T., and E.S. Krendel, "The Man-Machine System Concept," Proceedings of the IRE Vol. 50, No. 5, May, 1962.
- [11] McRuer, D.T., and E.S. Krendel, "The Human Operator as a Servo System Element," Journal of the Franklin Institute Vol. 267, No. 5 May and No.6, June, 1959.

- [12] Milne, Garth. "State Space Identification Tool *for use with Matlab Users Guide*," The Math Works Inc., South Natick, MA, March 1988.
- [13] Mitchell, D.G., Aponso, B.L., and R.H. Hoh, "Minimum Flying Qualities Volume I: Piloted Simulation Evaluation of Multiple Axis Flying Qualities," WRDC-TR-89-3125 Vol I, Jan. 1990.
- [14] Mitchell, D.G., Hoh, R.H., Ashkenas, I., Klein, R.H., Heffley, R.K., "Proposed Military Standard and Handbook - Flying Qualities of Air Vehicles," AFWAL-TR-82-3081 Vol. II, July 1982.
- [15] Ogata, K. "Discrete Time Control Systems," Prentice Hall, New Jersey, 1987.
- [16] Ogata, K. "Modern Control Engineering 2nd Edition," Prentice Hall, New Jersey, 1990.
- [17] Purdue University AAE 421L Laboratory Manual. 1990.
- [18] Skelton, R.E., "Dynamic Systems Control," Wiley and Sons, New York, 1988.
- [19] Wolfe, Dr. Gordon W., "Computer Peripherals That You Can Build," Tab Books Inc, Blue Ridge Summit, PA, 1982.

Appendix A: Schematics of Electronic Circuits

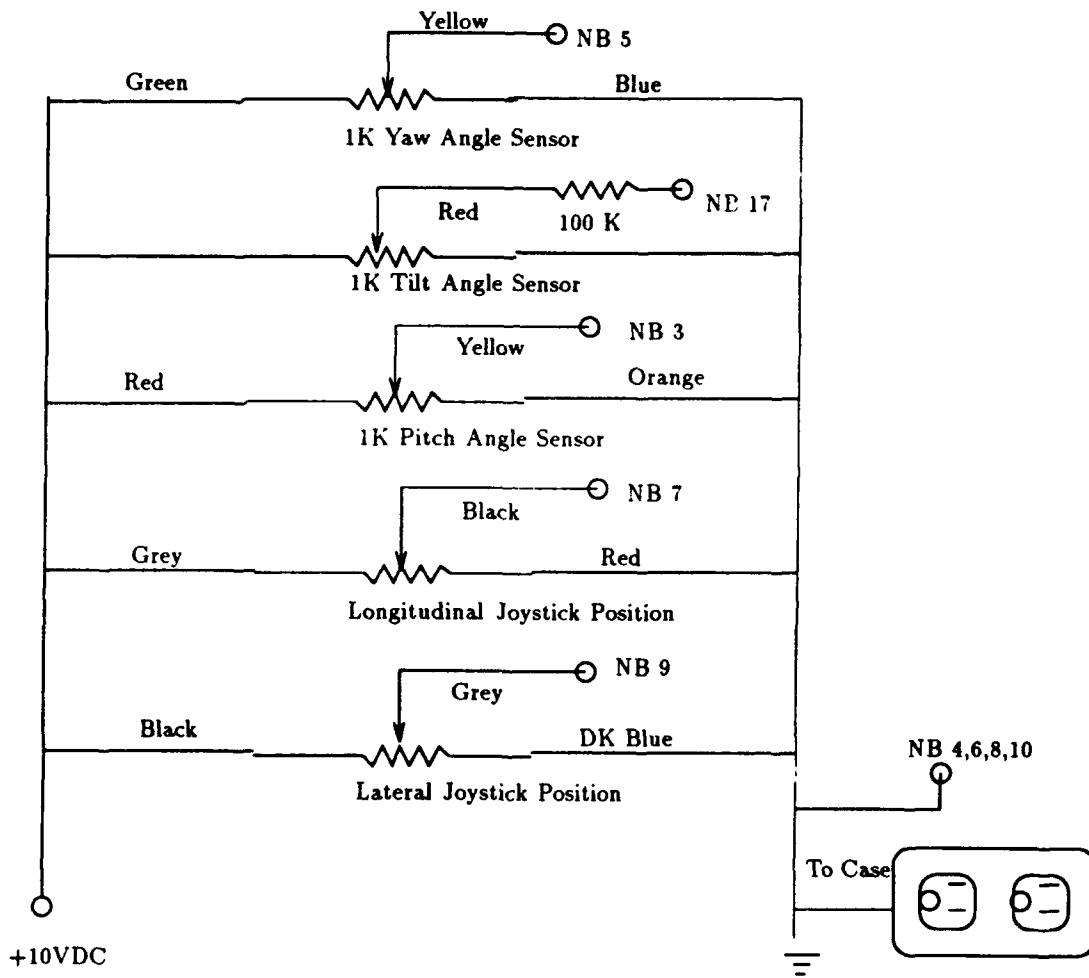


Figure A.1 Schematic of angular displacement sensors.

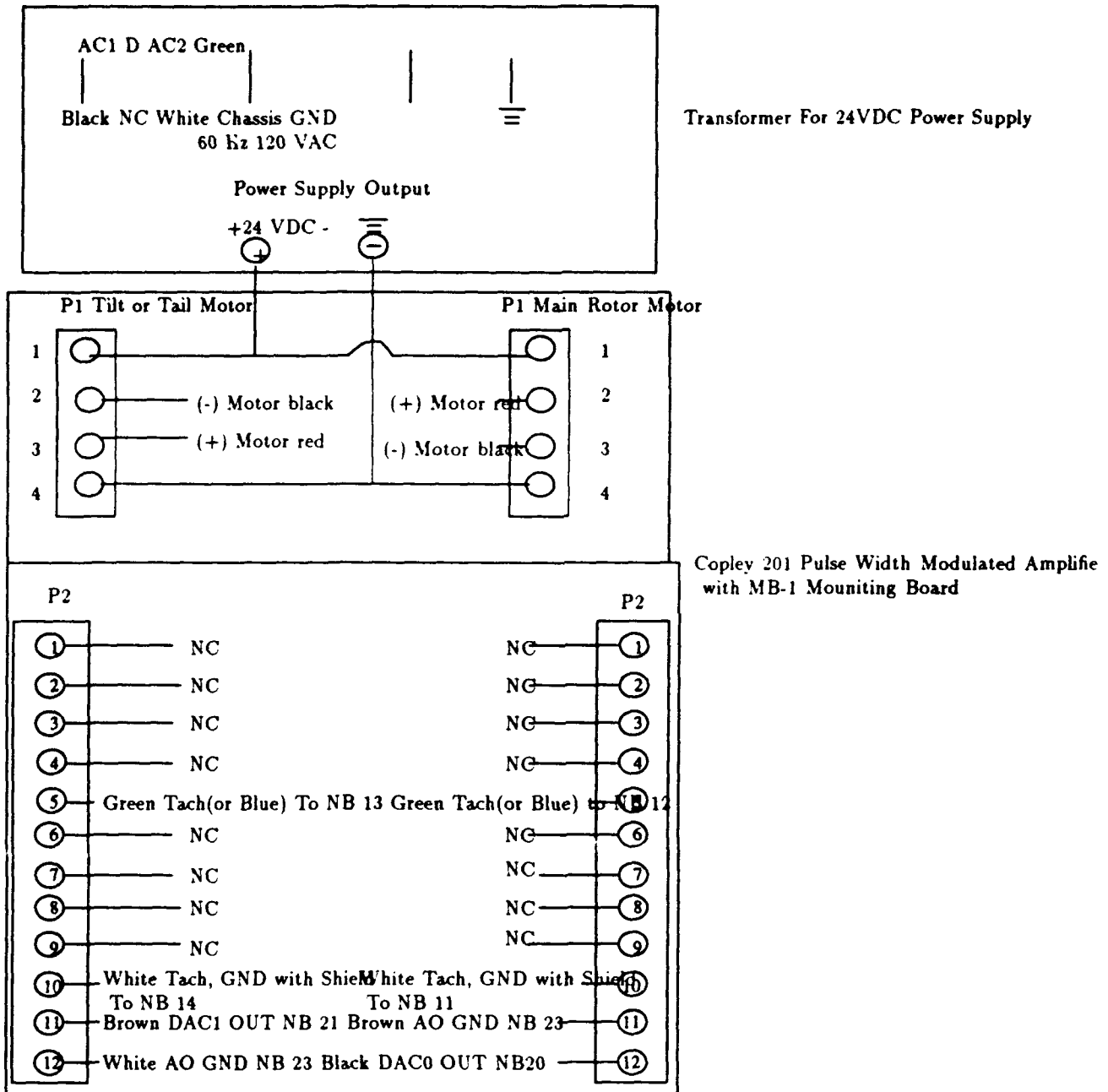


Figure A.2 Schematic of connections to Copley Model 201 Amplifier.

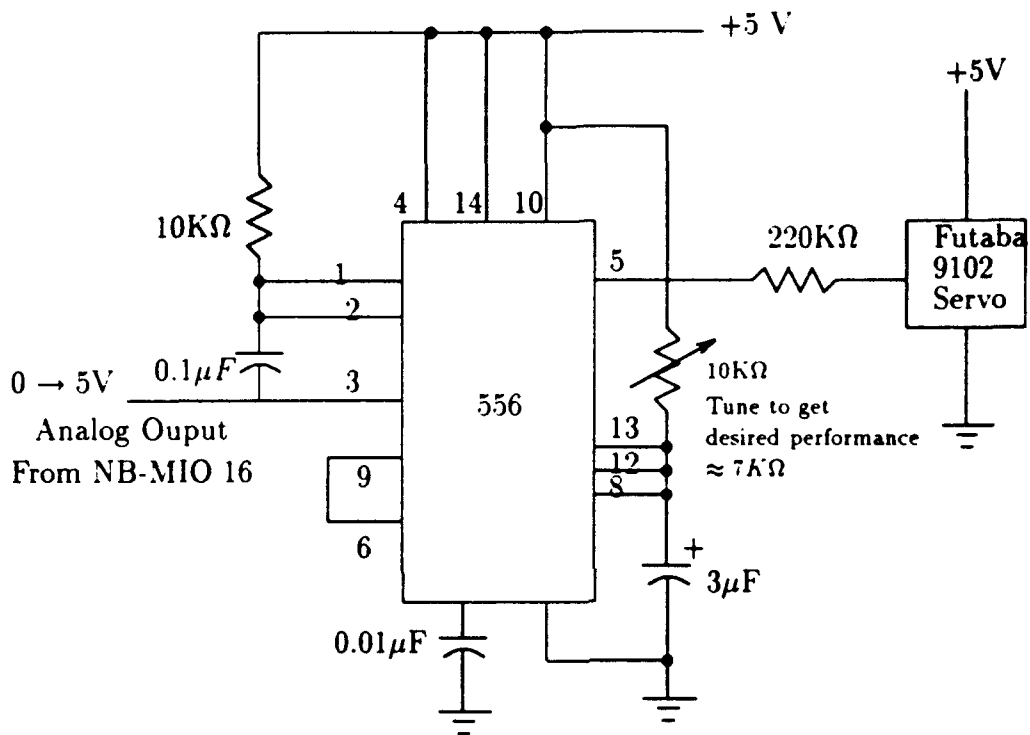
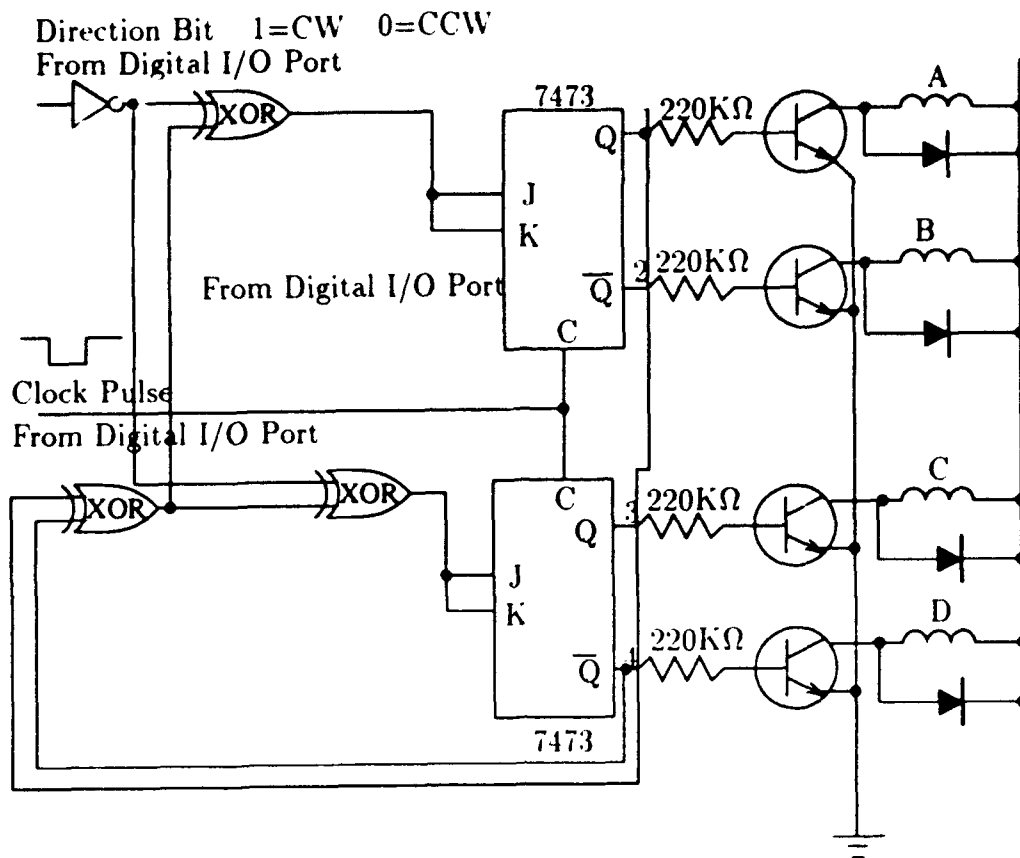


Figure A.3 PWM circuit for tilt servo.

See Reference [19] for details.



Instant	A	C	B	D
1	1	0	0	1
2	1	1	0	0
3	0	1	1	0
4	0	0	1	1

CW ↓ ↑ CCW

Figure A.4 Stepper motor logic circuit.

See Reference [19] for details.

Appendix B: Runlog for Piloted Experiments

This appendix contains the run log for the man in the loop experiments. The lists and tables use keys to indicate the configuration of the TROFM. The general form of the configuration key for the pilot comment list is "A/B; C/D C/D; /E". In single axis cases and individual table listings the form is "A/B/C/D/E". The following is a break down of the configuration key:

A. Display configuration

I. Instrument Display

V. Visual Scene

B. Number of axes to control

S. Single Axis

M. Multi Axis (2)

C. Axis to control

P. Pitch

Y. Yaw

D. Bandwidth of task

L. Low (Slow)

M. Medium

H. High (Fast)

E. Command System

A. Attitude (position)

R. Rate

O. Open loop (un-augmented)

B.1 Pilot Comments

The following are pilot comments transcribed from audio tape. The comments were recorded immediately after each run. Because of a recorder malfunction during the first twelve runs, no audio record was available for transcription. In those cases, key words or phrases recorded on paper by the flight test director were used.

Run-1 I/S/P/L/A: No comments recorded.

Run-2 I/S/P/M/A: Controllability in question. Jerking the stick makes it uncontrollable.

Run-3 I/S/P/H/A: If I jerk the stick at all it is uncontrollable. Smooth stick.

Run-4 I/S/Y/L/A: Jerking stick still a factor. Bad display (up-down yaw error display).

Run-5 I/S/Y/M/A: Low workload but same problems as above (4)

Run-6 I/S/Y/H/A: No comments recorded

Run-7 I/M; Y/M P/L; /A: Alot of concentration. More pilot compensation.

Run-8 I/M; Y/H P/L; /A: Alot of concentration. Learning curve.

Run-9 I/M; Y/L P/M; /A: Poor in pitch.

Run-10 I/M; Y/H P/M; /A: Uncontrollable, both (axes) bad. Let error slide.

Run-11 I/M; Y/L P/H; /A: Adequate.

Run-12 I/M; Y/M P/H; /A: Intense concentration. Very high workload.

Run-13 I/S/P/L/R: Controllable? Yes. Performance adequate with tolerable workload? I don't like the control characteristics of this. It is slow to react at first and too quick later. Aircraft characteristics were objectionable, but you could compensate for them. I'll give it a 6.

Run-14 I/S/P/M/R: Controllable? Yes. Performance not adequate but felt like I had more instantaneous control. very jerky and hard to keep between the bounds. Alot of compensation. I'll give it a 7 1/2.

Run-15 I/S/P/H/R: I'm going out of bounds alot but not because it is uncontrollable, but because it reacts so quickly to an input. You can't keep very narrow margins of error on this task. It was definitely controllable. I like this better than the other ones (13,14) but didn't do as well. I'd give it a 6 1/2.

Run-16 I/S/Y/L/R: Controllable? Yes. Performance adequate? Yes. Satisfactory without improvement? I don't like this type of system that well, but it was an easy test. Required a fair amount of compensation. The deficiencies were mildly unpleasant, but moderate compensation, so 3 1/2.

Run-17 I/S/Y/M/R: Controllable? Yes. Performance adequate with tolerable workload? Yes. Satisfactory without improvement? No. Workload was a little bit higher on this one. If the rate of change of an error was relatively fast, if I gave a large input, I almost got into a situation similar to a PIO (pilot induced oscillation). That is objectionable. Considerable compensation, I'd give it a 5 1/2.

Run-18 I/S/Y/H/R: Controllable? Yes. Performance adequate? marginal. Big problem with overshoot. I liked the fact that the responsiveness was better on this, but I kept going out of bounds on my control inputs. I would consider the overshoot very objectionable. Considerable pilot workload involved. I'd give it a 6 1/2.

Run-19 I/M;/Y/M;P/L; /R: Controllable? Almost no. Performance adequate? Definitely not. At best it's a 9. Two tasks at once, the pilot concentration is very intense. It's hard in the single axis case but almost impossible to do here. I'll give it a 9 but that's being generous.

Run-20 I/M/; Y/H P/L; /R: Controllable? I think it is controllable, actually I like it better than the last test we just did. The yaw is more responsive, almost too responsive. The same problems we had before, the overshoot. Pilot concentration is intense. Deficiencies: big problems with overshoot, problems with two things at once. It's a difficult task. I'll go down to a 9 1/2.

Run-21 I/M/; Y/L P/M; /R: Controllable? No. It's a 10. I had to let one axis go to correct for the other. Pitch was responsive when I needed it. Trying to control for yaw was tough to do.

Run-22 I/M; Y/H P/M; /R: It only gets worse, another 10. I can control one axis, but keeping the other one within bounds is next to impossible. I think the display has a lot to do with this. If the yaw was left-right and the pitch was up-down the way I think it should be, this would most likely be controllable.

Run-23 I/M; Y/L P/H; /R: I wouldn't say uncontrollable, but pretty close. The yaw error was kept within bounds pretty well, but the pitch error kept going out. I'd give it a 9 1/2.

Run-24 I/M; Y/M P/F; /R: No doubt about this rating, it's a 10.

Run-25 I/S/P/L/O: Controllable? Yes. Performance adequate with tolerable workload? Yes. Satisfactory without improvement? Not much required in the way of pilot compensation, a lot of control input needed in order to control this. I would say the deficiencies are minor but annoying. I'll give it a 3 1/2 to 4.

Run-26 I/S/P/M/O: Controllable? Yes. Performance adequate with tolerable workload? Yes. Satisfactory without improvement? A lot of control input is required for the task given. Have to have an input for every error shown on the display. It was a little bit harder to keep the medium bandwidth task in bounds than it was the slow bandwidth. Pilot compensations were a little bit more, but not overly burdensome. I'd give it a 4.

Run-27 I/S/P/H/O: Controllable? Yes. I originally said no because of the excessive overshoots involved with this. The major deficiency is the overshoot. It's extremely hard to control. The pilot compensation is not intense but there is a lot of pilot compensation involved. The biggest problem is the overshoot which would cause me to give it an 8.

Run-28 I/S/Y/L/O: Controllable? Yes. Performance adequate with tolerable workload? Yes. Satisfactory without improvement? If you give it a large input, you have to counteract that input for a short period of time and then center the joystick in order to keep from oscillation back and forth. Moderate pilot compensation, not a lot going on. Minor to moderately objectionable. 4 1/2.

Run-29 I/S/Y/M/O: Controllable? Yes. Performance adequate with tolerable workload? No. Overshoot a very big problem and again the problem of overcoming your previous inputs. Not a lot of pilot compensation involved. You have a lot of inputs going in but it doesn't take a lot of thinking, but the deficiency is major. I'd give this one an 8.

Run-30 I/S/Y/H/O: Same problems as last time, workload is a lot higher. I'll give it a 9.

Run-31 I/M; Y/M P/L; /O: Definitely a 10, it's uncontrollable.

Run-32 I/M; Y/H P/L; /O: Controllable? Barely. Performance adequate? No. I'll give it a 9.

Run-33 I/M; Y/L P/M; /O: Controllable? No. Response was too sluggish in the yaw axis. I was concentrating so much on yaw, I forgot about pitch. Definitely a 10.

Run-34 I/M; Y/H P/M; /O: Another 10. I had trouble with yaw again. Trouble with yaw seems to translate into pitch.

Run-35 I/M; Y/L P/H; /O: Another 10. Yaw control is very sluggish. Pitch seems OK but I have to concentrate on yaw too much.

- Run-36 I/M; Y/M P/H; /O: The worst of them all, a 10. I was pegged at the limits for most of the test.
- Run-37 V/S/Y/L/R: Controllable? Yes. Performance adequate with tolerable workload? Yes. Satisfactory without improvement? Yes. Deficiencies: a little hard to keep light centered on line during initialization phase. I think this is because it's a rate controller, at least I think it is. Deficiencies are not a big deal, easy to control, minimal compensation, I'll give it a 3.
- Run-38 V/S/Y/M/R: Controllable? Yes. Performance adequate with tolerable workload? Yes. Satisfactory without improvement? Yes. Little bit more overshoot, harder to control, I don't like it as much as the last one. Borderline satisfactory with out improvement so I'll give it a 3 1/2.
- Run-39 V/S/Y/H/R: Pretty much the same comments as the last one. I liked the slower bandwidth tasks better though. I'll go with a 3 1/2.
- Run-40 V/S/P/L/A: Controllable? Yes. Performance adequate with tolerable workload? Yes. Satisfactory without improvement? Yes. Pilot compensation is minimal, very easy to keep the light centered on the target at all times. I'll give it a 1.
- Run-41 V/S/P/M/A: Same results as last time but quick movements cause overshoot. Deficiencies are negligible though. I'll give it a 2.
- Run-42 V/S/P/H/A: Controllable? Yes. Performance adequate with tolerable workload? Yes. Satisfactory without improvement? No. Overshoot is much more pronounced. Large movements cause a large overshoot which is hard to correct for. Minor deficiencies, minimal compensation. I'll give it a 4.
- Run-43 V/S/P/L/O: Controllable? Yes. Performance adequate with tolerable workload? Yes. Satisfactory without improvement? Yes. Seems slow to react to commands but the tracking is relatively good. Not a whole lot of compensation

involved provided you don't get a large acceleration going where you have to recover from it. I'd give it a 3.

Run-44 V/S/P/M/O: Pretty much the same comments, overshoot becoming more pronounced, but the reaction time is better. I almost prefer this task more. I give it a 3.

Run-15 V/S/P/H/O: Controllable? Yes. Performance adequate with tolerable workload? Yes. Satisfactory without improvement? Borderline, overshoot is more pronounced. I'm catching myself trying to predict where the target will stop moving in order to prevent overshoot. Compensation is a little bit higher but not demanding at all, but the overshoot is an annoying deficiency. I'd give it a 3 1/2 to a 4.

Run-46 V/S/Y/L/O: Controllable? Yes. Performance adequate with tolerable workload? Yes. Satisfactory without improvement? There's a trade off between stick sensitivity and how quick you react. For a smaller stick sensitivity, the aircraft doesn't react as quickly to your inputs but you have less overshoot. For a large sensitivity, it reacts quickly but there's a lot more overshoot. It's not in the aircraft itself but it causes a problem. There is a little bit more compensation involved with this and this deficiency is a little annoying. I'd give it a 4.

Run-47 V/S/Y/M/O: Controllable? Yes. Performance adequate with tolerable workload? Yes. Satisfactory without improvement? Definitely not. It's extremely hard to keep the light centered on the target. A lot of overshoot involved the whole time. There's more pilot compensation involved but it's not extensive but would say it's considerable. The deficiencies are going from moderate to very objectionable. I'd give it a 5 1/2.

Run-48 V/S/Y/H/O: Controllable? Yes. Performance adequate with tolerable workload? Debatable. I had to drop the sensitivity on the stick to even attempt to stay on the card. Any input was either a full deflection to the left or right

in order to get the aircraft moving. A lot more compensation involved. Major deficiencies. I'd give it an 8.

Run-49 V/S/Y/L/A: Controllable? Yes. Performance adequate with tolerable workload? Yes. Satisfactory without improvement? Yes. In order to get maximum deflection to the left or right, the joystick sensitivity has to be set a little bit higher than I preferred. It seems a little bit jerky. Other than that it's a good controller. It works really well. I'd give it a 3.

Run-50 V/S/Y/M/A: Controllable? Yes. Performance adequate with tolerable workload? Yes. Satisfactory without improvement? Yes. As the bandwidth increases, overshoot is becoming more of a problem. A little bit harder to control, but it's not that big of a deal, not a lot of compensation involved. I'd give it a 3 to a 3 1/2.

Run-51 V/S/Y/H/A: Controllable? Yes. Performance adequate with tolerable workload? Yes. Satisfactory without improvement? Overshoot again is a problem. Not a lot of compensation involved. I'd give it a 3 1/2 to a 4.

Run-52 V/S/P/L/R: Controllable? Yes. Performance adequate with tolerable workload? Yes. Satisfactory without improvement? Tendency to overshoot a lot. It's a little bit annoying. I came off the card a little bit a few times. It's not too difficult of a task to track the card with this type of controller though. Compensation is moderate. But satisfactory without improvement no, because of minor but annoying deficiencies with moderate pilot compensation. I give it a 4.

Run-53 V/S/P/M/R: Pretty much the same comments as last time. Overshoot is getting to be more of a problem, can't use any jerky inputs. Jerky inputs give you a large amount of overshoot and you spend too much time correcting for them. Again the deficiencies are annoying to moderately objectionable. Pilot compensation is moderate. I'll give it a 4 1/2.

Run-54 V/S/P/H/R: Same problem as last time but overshoot is getting to be a much bigger problem. I'm having trouble keeping it on the card at some points. Pilot compensation is definitely higher, but not extensive. The overshoot is getting very objectionable. I'll give it a 5 1/2.

Run-55 V/M; Y/L P/M; A: Controllable? Yes. Performance adequate with tolerable workload? Yes. Satisfactory without improvement? Yes, I am having a little bit more problems with overshoot when we get into this multi-axis case. Not alot of compensation. Overshoot is mildly unpleasant so I'll give it a 3.

♦Run-56 V/M; Y/M P/H; A: Controllable? Yes. Performance adequate with tolerable workload? Yes, I only went off the card a couple of times. Satisfactory without improvement? Little bit more compensation required since the task is faster. Overshoot is a problem if you make large inputs. I don't have trouble doing the task but there is something about it I don't like. I'll give it a 4 1/2.

Run-57 V/M; Y/H P/M; A: Controllable? Yes. Performance adequate with tolerable workload? Debatable. Requires extensive pilot compensation. Deficiencies, overshoot is a problem. I'll give it a 5 1/2 to a 6.

Run-58 V/M; Y/M P/L; R: Controllable? Yes. Performance adequate with tolerable workload? Debatable. Having trouble with picking joystick gains. Each axis is very controllable but putting them together makes it alot more difficult. I'm having problems with overshoot. I'm having a hard time keeping centered on the card but I can keep it on the card pretty well, but my tendency is not to always be heading toward the center of the card, I may be heading away. I'll give it a 7.

Run-59 V/M; Y/M P/L; R: Controllable? Yes. Performance adequate with tolerable workload? I think my performance was adequate. It was definitely more difficult, alot of compensation involved. I think my performance was better on this one because my workload was higher, I went with what was natural to me in

the way of controlling an aircraft. I didn't think as much. I didn't get confused as much with the (joystick) sensitivities. I'd give it a 6 1/2.

Run-60 V/M; Y/H P/M; R: Controllable? Yes. Performance adequate with tolerable workload? No. Very hard to keep on the card with a tendency to be off the card for a very long time. Pilot compensation was maximum. I did not like this at all. I'd give it a 9.

Run-61 V/M; Y/M P/L; O: Controllable? Barely. Performance adequate? Definitely not. Almost impossible to keep on card. Very slow to react and extremely hard task to perform. Being generous, I'll give it a 9.

Run-62 V/M; Y/L P/M; O: Controllable? Yes. Performance adequate? No. It is a difficult controller to work with. a lot of pilot compensation, slow to react and once it finally does react, I need to counteract that input. I don't like this kind of controller. I felt more comfortable with this controller than the previous task (61). I'll give it an 8.

Run-63 V/M; Y/M P/H; O: Controllable? Yes. Performance adequate? I don't believe it was adequate but definitely better than the past (runs 61 and 62). I have no idea why but I felt more comfortable with this than I did the slower bandwidth tasks. I could keep it on the card pretty well and if I wasn't I was always heading back toward it. Deficiencies: a lot of overshoot and slow to react and a little slow to recover. I don't think adequate performance could be achieved with maximum pilot compensation. I'd give it a 7.

Run-65 I/S/Y/L/O: Controllable? Yes. Performance adequate? Yes. Satisfactory without improvement? Yes. Task is almost hands off, a "no brainer", no compensation. Keeping within the bounds is extremely easy to do. Again there is a problem with the overshoot but for this slow bandwidth it doesn't matter. I'd say a 2 1/2.

Run-66 I/S/Y/M/O: Controllable? Yes. Performance adequate? Yes. Satisfactory without improvement? Very little compensation involved at all. Minimal compensation. Very easy task to perform. Deficiencies were: slow to react and overshoot. I'd rate this around a 4.

Run-67 I/S/Y/H/O: Controllable? Yes. Performance adequate? Yes. Satisfactory without improvement? No. A lot of overshoot. It's real tough to keep it on zero so I just aimed to keep it within the bounds. For every input, I need a counter input. Moderately objectionable. I'd give it a 5.

B.2 Describing Functions and Performance Measures.

The graphs and tables of this section are the results of the man in the loop experiments. Describing function data and the corresponding best fit describing functions are plotted on the same graph. Key performance measures and best fit describing function parameters are tabulated. The following is a list of symbols for the tables of this appendix. (* Indicates definitions are taken from Reference [13].)

e_{σ} One standard deviation rms value for tracking error during the run (radians of pitch or yaw tracking error as appropriate).

e_{σ}/σ_i Normalized performance. If less than one, the pilot is effectively reducing errors. If greater than one the pilot is making matters worse.

c_{σ} One standard deviation rms value for joystick deflection during run (inches of longitudinal or lateral stick as appropriate).

ω_c Crossover frequency. Frequency at which the open-loop pilot-vehicle 0 dB line intersects the Bode amplitude asymptote calculated from a linear interpolation between the two describing function data points immediately above and below crossover (rad/sec). See Figure B.2.

* φ_m Bode open-loop phase margin at frequency of closed-loop gain crossover, ω_c ; computed from a straight line interpolation between the two describing function data points immediately above and below ω_c (deg). See Figure B.2.

*Slope_{ol} Slope of Bode open-loop amplitude asymptote between two data points immediately above and below gain crossover frequency (dB/dec).

$\tau_{e\ ol}$ Plant open loop high frequency time delay parameter from the exponential $\tau \omega$ (sec). Computed from a least squares fit of $\tau \omega + \alpha/\omega$ to the residual phase (experimental phase - (-90°)).

α_{ol} Plant open-loop low frequency phase droop parameter from the exponential α/ω . Computed from a least squares fit of $\tau \omega + \alpha/\omega$ to the residual phase (experimental phase - (-90°)).

$K_{ol} = \omega_{c\ est}$ Least squares estimate of open-loop pilot-vehicle gain or equivalently open loop crossover frequency.

HQR Cooper-Harper handling qualities rating

K_p Pilot gain computed from low order equivalent system fitting procedure.

T_{lead} Low order equivalent system estimate of pilot generated lead time constant (sec).

T_{lag} Low order equivalent system estimate of pilot generated lag time constant (sec).

τ_p Low order equivalent system estimate of high frequency pilot time delay parameter from the exponential $\tau_p \omega$ (sec).

α_p Low order equivalent system estimate of low frequency phase droop parameter from the exponential α_p/ω .

Slope_p Slope of low order equivalent pilot Bode amplitude curve at the least squares estimate of the open-loop pilot-vehicle crossover frequency.

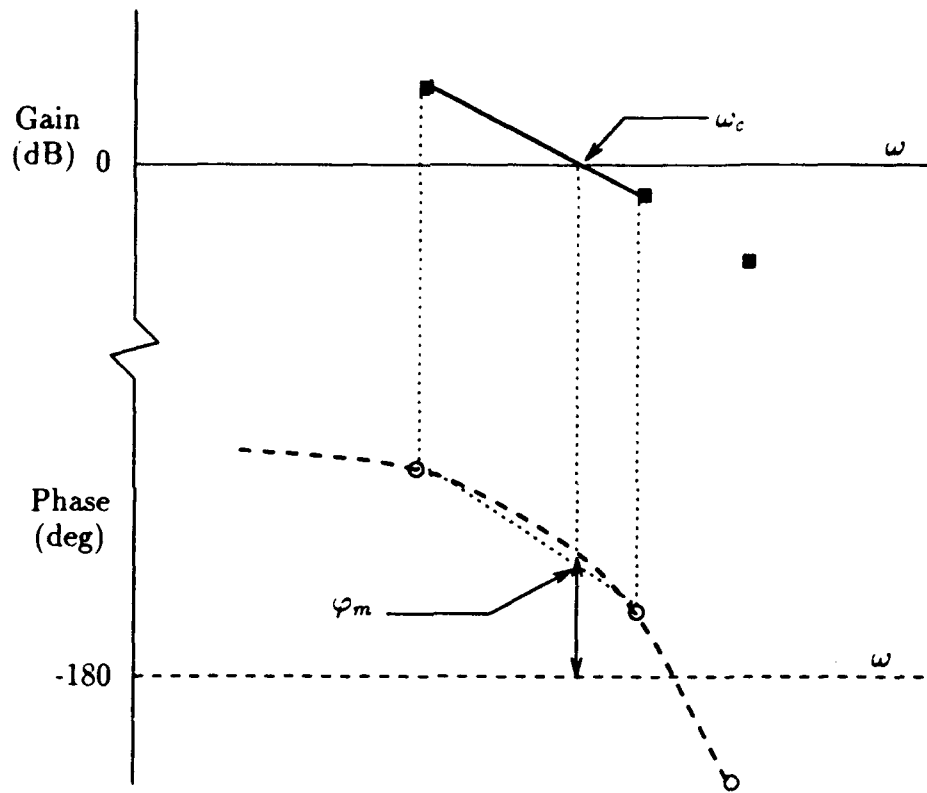


Figure B.1 Definition of linearly interpolated crossover frequency and phase margin.

Table B.1 Handling qualities ratings for instrument display and visual scene.

Pitch Bandwidth	Yaw Bandwidth	Command System	Instrument HQR	Visual HQR
Low		Attitude	2	1
Medium		Attitude	6.5	2
High		Attitude	7.5	3.5
Low		Rate	6	4
Medium		Rate	7.5	4.5
High		Rate	6.5	5.5
Low		Open Loop	3.5→4	3
Medium		Open Loop	4	3
High		Open Loop	8	3.5
	Low	Attitude	4	3
	Medium	Attitude	3.5	3→3.5
	High	Attitude	3.5	3.5→4
	Low	Rate	3.5	3
	Medium	Rate	5.5	3.5

Table B.1, continued.

Pitch Bandwidth	Yaw Bandwidth	Command System	Instrument HQR	Visual HQR
	High	Rate	6.5	3.5
	Low	Open Loop	4.5	4
	Medium	Open Loop	8	5.5
	High	Open Loop	9	8
Medium	Low	Attitude	8	3
Medium	High	Attitude	8	5.5
High	Medium	Attitude	9.5	4.5
Low	Medium	Rate	9	6.5
Medium	Low	Rate	10	7
Medium	Fast	Rate	10	9
Low	Medium	Open Loop	10	9
Medium	Low	Open Loop	10	8
High	Medium	Open Loop	10	7

Table B.2 Experimental results and least squares estimates of extended crossover model parameters.

Configuration	Run	e_σ (rad)	e_σ/σ_i	c_σ (in)	ω_c (rad/sec)	φ_M (deg)	Slope _{ol} (dB/dec)	$K_{ol} = \omega_c \text{ est}$	$T_{e\text{ ol}}$ (sec)	α_{ol} (1/sec)
I/S/P/L/A	1	0.0347	0.5832	0.0942	1.0492	82.5174	-12.6500	1.0197	0.0163	-0.1557
I/S/P/M/A	2	0.0481	0.8084	0.1306	0.5927	94.1075	-23.6990	0.7105	0.0243	0.0524
I/S/P/H/A	3	0.0556	0.9345	0.1510	NA	NA	NA	0.723	0.0912	-0.0534
I/S/Y/L/A	4	0.0395	0.6639	0.0429	1.6361	85.2860	-24.1200	1.016	-0.076	-0.0617
I/S/Y/M/A	5	0.0451	0.7580	0.0490	2.1642	61.4098	-13.4879	1.3539	-0.2817	0.2828
I/S/Y/H/A	6	0.0500	0.8403	0.0543	1.2751	92.7800	-19.9270	1.4382	-0.1521	0.0956
I/M/P/L/A	7	0.0510	0.8571	0.1385	0.4002	106.0100	-22.8500	0.5162	-0.2069	0.0609
I/M/Y/M/A	7	0.0758	1.2739	0.0823	0.7374	77.4400	-59.3200	0.6076	-0.5759	0.1519
I/M/P/M/A	9	0.0587	0.9866	0.1594	0.5032	96.2187	-44.9043	0.397	-0.0805	0.054
I/M/Y/L/A	9	0.0529	0.8891	0.0574	0.3607	110.8700	-15.0452	0.5063	-0.4016	0.311
I/M/P/M/A	10	0.0595	1.0000	0.1615	NA	NA	NA	0.2361	0.2445	-0.0473

Table B.2, continued.

Configuration	Run	e_{σ} (rad)	e_{σ}/σ_i	c_{σ} (in)	ω_c (rad/sec)	φ_M (deg)	Slope _{ol} (dB/dec)	$K_{ol} = \omega_{c_{est}}$	$T_{e_{ol}}$ (sec)	α_{ol} (1/sec)
I/M/Y/H/A	10	0.0663	1.1143	0.0720	0.8082	109.0300	-58.8600	0.7223	-0.3895	0.7633
I/M/P/H/A	12	0.0542	0.9109	0.1472	NA	NA	NA	0.627	-0.7024	0.2859
I/M/P/M/A	12	0.0572	0.9613	0.0621	0.8647	117.4120	-21.7977	0.8406	-0.5451	0.6058
I/S/P/L/R	13	0.0451	0.7580	0.0350	1.6180	47.0100	-2.9819	1.5271	-0.351	-0.2789
I/S/P/M/R	14	0.0533	0.8958	0.0413	2.0489	41.2470	-17.8835	2.277	-0.2719	-0.5123
I/S/P/H/R	15	0.0601	1.0191	0.0466	1.6469	61.0407	-8.5160	1.633	-0.2315	0
I/S/Y/L/R	16	0.0451	0.7580	0.0408	1.2561	51.5380	-19.5400	1.2199	-0.5085	0
I/S/Y/M/R	17	0.0579	0.9731	0.0524	1.5277	46.9307	-12.3765	1.7485	-0.4203	0
I/S/Y/H/R	18	0.0774	1.3008	0.0700	1.5610	55.9189	-24.0463	1.5163	-0.3971	0
I/M/P/L/R	19	0.0736	1.2370	0.0571	1.0518	44.4395	-23.7131	1.0256	-1.039	-1.0647
I/M/Y/M/R	19	0.0817	1.3731	0.0739	0.9596	60.0414	-17.1176	0.9633	-0.6142	0.3968

Table B.2, continued.

Configuration	Run	e_o (rad)	e_o/σ_i	c_o (in)	ω_c (rad/sec)	φ_M (deg)	Slope _{ol} (dB/dec)	$K_{ol} = \omega_c \text{ est}$	$T_{e_{ol}}$ (sec)	α_{ol} (1/sec)
I/M/P/M/R	21	0.0826	1.3882	0.0641	1.0814	49.9661	-59.3607	0.5857	-0.3162	-0.646
I/M/Y/L/R	21	0.0750	1.2605	0.0679	1.5588	43.3379	-28.4100	1.3717	-0.555	-0.0612
I/M/P/M/R	22	0.0978	1.6437	0.0759	0.7347	43.0251	-20.2483	0.871	-0.3964	-0.6321
I/M/Y/H/R	22	0.0994	1.6706	0.0900	1.1860	70.3883	-37.0731	0.8912	-0.6161	0.1079
I/M/P/H/R	24	0.1338	2.2487	0.1038	0.7819	29.1736	-16.8451	0.8519	-0.3219	-0.5483
I/M/Y/M/R	24	0.0811	1.3630	0.0734	0.9880	115.1800	-73.3482	0.9912	-0.4025	-0.2552
I/S/P/L/O	25	0.0361	0.6067	0.0010	NA	NA	NA	1.6065	0.0228	0
I/S/P/M/O	26	0.0406	0.6824	0.0011	1.9400	79.2500	-12.8000	1.4499	-0.0676	0
I/S/P/H/O	27	0.0566	0.9513	0.0015	2.7335	40.1680	-9.6700	2.3096	-0.3303	0
I/S/Y/L/O	28	0.0454	0.7630	Offline	NA	NA	NA	1.5873	-0.3882	-0.0367

Table B.2, continued.

Configuration	Run	e_{σ} (rad)	e_{σ}/σ_i	c_{σ} (in)	ω_c (rad/sec)	φ_M (deg)	Slope _{ol} (dB/dec)	$K_{ol} = \omega_c \tau_{ol}$	τ_{ol} (sec)	α_{ol} (1/sec)
I/S/Y/M/O	29	0.0760	1.2773	Offline	1.5915	41.2700	-40.2500	NA	NA	0
I/S/Y/H/O	30	0.0759	1.2756	Offline	1.5166	47.9100	-11.8718	NA	NA	0
I/M/Y/*/0	31→36	NA	0.0000	NA	NA	NA	NA	NA	NA	NA
V/S/Y/L/R	37	0.0364	0.6118	0.0329	1.3375	78.8200	-24.2100	1.64	-0.1827	-0.1819
V/S/Y/M/R	38	0.0557	0.9361	0.0504	1.7422	64.2692	-11.7200	1.6452	-0.2015	-0.3545
V/S/Y/H/R	39	0.0498	0.8370	0.0451	1.7220	58.2794	-63.6903	1.8807	-0.1807	-0.415
V/S/P/L/A	40	0.0217	0.3647	0.0029	NA	NA	NA	3.7255	-0.1958	0
V/S/P/M/A	41	0.0231	0.3882	0.0034	NA	NA	NA	3.6289	-0.1182	0
V/S/P/H/A	42	0.0326	0.5479	0.0048	NA	NA	NA	3.0314	-0.18	0.2174
V/S/P/L/O	43	0.0299	0.5025	0.0006	NA	NA	NA	3.5137	-0.763	0.5665
V/S/P/M/O	44	0.0404	0.6790	0.0009	1.6641	74.0700	-42.3823	1.5777	-0.3288	0.4222

Table B.2, continued.

Configuration	Run:	ϵ_σ (rad)	e_σ/σ_i	c_σ (in)	ω_c (rad/sec)	φ_M (deg)	Slope _{ol} (dB/dec)	$K_{ol} = \omega_{c\ est}$	$\tau_{e\ ol}$ (sec)	α_{ol} (1/sec)
V/S/P/H/O	45	0.0414	0.6958	0.0009	3.0860	38.9993	-17.4751	2.5678	-0.3199	0.5694
V/S/Y/L/O	46	0.0349	0.5866	0.1263	NA	NA	NA	1.679	-0.2267	0.0338
V/S/Y/M/O	47	0.0507	0.8521	0.1835	2.5031	31.9500	-58.8700	2.282	-0.3264	0.021
V/S/Y/H/O	48	0.0614	1.0319	0.5001	2.0545	39.3020	-38.2500	2.1119	-0.4512	0.1395
V/S/Y/L/A	49	0.0256	0.4303	0.0348	NA	NA	NA	2.1994	-0.154	-0.0629
V/S/Y/M/A	50	0.0332	0.5580	0.0451	NA	NA	NA	2.0671	-0.0971	0.085
V/S/Y/H/A	51	0.0382	0.6420	0.0519	NA	NA	NA	2.3636	-0.1935	0.66066
V/S/P/L/R	52	0.0361	0.6067	0.0327	1.9363	49.8662	-18.5720	2.9877	-0.4021	0
V/S/P/M/R	53	0.0428	0.7193	0.0387	2.2789	42.1900	-33.7228	2.7621	-0.3197	-0.4179
V/S/P/H/R	54	0.0496	0.8336	0.0449	2.4605	41.5800	-20.8558	3.1496	-0.1444	-0.8137

Table B.2, continued.

Configuration	Run	e_{σ} (rad)	e_{σ}/σ_i	c_{σ} (in)	ω_c (rad/sec)	φ_M (deg)	Slope _{ol} (dB/dec)	$K_{ol} = \omega_c \text{ est}$	τ_{eol} (sec)	α_{ol} (1/sec)
V/M/P/M/A	55	0.0277	0.5168	0.0376	NA	NA	NA	2.9392	-0.069	0.0107
V/M/Y/L/A	55	0.0369	0.6884	0.0501	2.0590	56.0935	-20.7704	1.5736	-0.254	0.0576
V/M/P/H/A	56	0.0351	0.6549	0.0476	2.9359	68.6484	-13.1989	2.3368	-0.1712	0.3838
V/M/Y/M/A	56	0.0390	0.7276	0.0529	1.3645	76.2821	-29.8521	1.4864	-0.1208	0.0395
V/M/P/M/A	57	0.0447	0.8340	0.0607	NA	NA	NA	1.9764	-0.2906	0.2217
V/M/Y/H/A	57	0.0457	0.8526	0.0620	1.7847	84.7780	-39.0399	1.53994	-0.2114	0.326
V/M/P/M/R	58	0.0524	0.9776	0.0474	NA	NA	NA	2.6173	-0.2272	-0.8837
V/M/Y/L/R	58	0.0467	0.8713	0.0362	NA	NA	NA	1.6388	-0.3196	-0.3601
V/M/P/L/R	59	0.0335	0.6250	0.0303	NA	NA	NA	2.206	-0.0726	-0.7157
V/M/Y/M/R	59	0.0609	1.1362	0.0472	2.1159	46.9849	-38.9850	1.8105	-0.2394	-0.4784

Table B.2, continued.

Configuration	Run	e_{σ} (rad)	e_{σ}/σ_i	c_{σ} (in)	ω_c (rad/sec)	φ_M (deg)	Slope _{ol} (dB/dec)	$K_{ol} = \omega_c \text{est}$	τ_{col} (sec)	α_{ol} (1/sec)
V/M/P/M/R	60	0.0492	0.9179	0.0445	1.7992	37.0088	-18.3064	2.4093	-0.0006	-1.1491
V/M/Y/F/R	60	0.0556	1.0373	0.0431	1.6936	69.8591	-28.4589	1.5806	-0.1652	-0.5179
V/M/P/L/O	61	0.0942	1.7575	0.0020	NA	NA	NA	0.2371	NA	NA
V/M/Y/M/O	61	0.0683	1.2743	0.2472	2.3440	23.2724	-38.2284	1.7414	-0.4437	-0.0891
V/M/P/M/O	62	0.1134	2.1157	0.0025	NA	NA	NA	0.554	-0.9164	-0.3613
V/M/Y/L/O	62	0.0698	1.3022	0.2527	2.0259	18.5429	-26.2918	1.7522	-0.8115	-0.6979
V/M/P/H/O	63	0.0745	1.3809	0.0016	NA	NA	NA	0.4945	-0.3585	-0.2335
V/M/Y/M/O	63	0.0573	1.0690	0.2074	1.3279	51.5126	-33.6949	0.9088	-0.4234	0.1989
I/S/Y/L/O	65	NA	0.0000	NA	NA	NA	NA	NA	NA	NA
I/S/Y/M/O	66	0.0585	0.9832	0.0327	2.0374	28.5337	-26.9763	1.4518	-0.5876	0.3995
I/S/Y/H/O	67	0.0795	1.3361	0.0445	1.8103	26.6210	-35.1629	2.0586	-0.3805	-0.9255

Table B.3 Best fit pilot describing function parameters and slope of pilot magnitude curve at the open loop pilot-vehicle crossover frequency.

Configuration	Run	K_p	T_{lead} (sec)	T_{lag} (sec)	τ_p (sec)	α_p (rad ² /sec)	HQR	$\omega_{c\ est}$ (rad/sec)	Slope _p (dB/dec)
I/S/P/L/A	1	3.668	.1361	2.0451	-.0385	-.3696	2	1.0197	-15.5914
I/S/P/M/A	2	7.3068	.9156	10	-.323	-.018	6.5	.7105	-14.2074
I/S/P/H/A	3	4.646	1.5904	10	-.2924	-.2409	7.5	.7230	-8.9142
I/S/Y/L/A	4	7.6828	1.1772	10	-.3230	-.1769	4	1.016	-8.5229
I/S/Y/M/A	5	11.978	.68	10	-.331	.1511	3.5	1.353	-11.0933
I/S/Y/H/A	6	6.4599	.7367	6.0613	-.1515	-.1812	3.5	1.4382	-9.5031
I/S/P/L/R	13	8.4067	2.0241	5.8196	-.2484	.0454	6	1.5271	-1.7479
I/S/P/M/R	14	5.8545	.7908	1.4397	-.159	-.0918	7.5	2.2770	-3.1044
I/S/P/H/R	15	1.4382	3.8629	10	-.1554	.0339	6.5	1.63040	-0.4421
I/S/Y/L/R	16	1.4513	.2688	4e-6	-.4915	-.1394	3.5	1.2199	1.7985
I/S/Y/M/R	17	7.8967	.9073	6.2136	-.1883	.5975	5.5	1.7485	-5.7526
I/S/Y/H/R	18	1.17	.3330	6e-6	-.3432	-.4053	6.5	1.2199	2.6333

Table B.3, continued.

Configuration	Run	K_p	T_{lead} (sec)	T_{lag} (sec)	T_p (sec)	α_p (rad ² /sec)	HQR	$\omega_{c\ est}$ (rad/sec)	Slope _p (dB/dec)
I/S/P/L/O	25	1349	1.2218	10	-.0423	-.0307	3.5	1.6065	-4.2547
I/S/P/M/O	26	522	3.3015	10	-.1303	-.2544	4	1.4499	-0.7944
I/S/P/H/O	27	793.15	1.7543	10	-.0517	-.1075	8	2.3096	-1.1584
I/S/Y/L/O	65	.4342	.35	0	-.1719	-.3003	2.5	1.7500	5.2269
I/S/Y/M/O	66	.0688	5	.2739	-.3135	-.5202	4	1.4515	17.0328
I/S/Y/H/O	67	.3346	.6704	0	-.2473	-1	5	2.0586	12.8874
V/S/Y/L/R	37	3.2013	5	9.0668	.0243	-.1455	3	1.6400	-0.2161
V/S/Y/M/R	38	1.4135	.5526	.0949	-.2902	-.4744	3.5	1.6452	8.2931
V/S/Y/H/R	39	13.1708	1.5159	10	-.0058	-.0502	3.5	1.8807	-2.2412
V/S/P/L/A	40	48.9543	.1171	10	-.1586	.0320	1	3.7255	-16.8596
V/S/P/M/A	41	39.7795	.5700	10	-.3376	-.0077	2	3.6289	-3.8601
V/S/P/H/A	42	5.6188	.2550	1.1896	-.2539	-.2317	3.5	3.0314	-11.2019
V/S/P/L/O	43	747.83	.2840	2.0788	-.3558	.3708	3	3.5137	-9.7869
V/S/P/M/O	44	269.37	.8144	1.2252	-.2652	-.0720	3	1.5777	-3.4092

Table B.3, continued.

Configuration	Run	K_p	T_{lead} (sec)	T_{lag} (sec)	τ_p (sec)	α_p (rad ² /sec)	HQR	$\omega_{c\ est}$ (rad/sec)	Slope _p (dB/dec)
V/S/P/H/O	45	161.72	4.9758	4.0538	.1935	-.0701	3.5	2.5678	0.0636
V/S/Y/L/O	46	0.5664	2.5328	1.4999	.1448	-.2522	4	1.6790	1.7617
V/S/Y/M/O	47	.1317	36.186	.2638	-.1038	-.9025	5.5	2.2820	14.8495
V/S/Y/H/O	48	.3126	.9107	0	-.2988	-.4743	8	2.1119	15.5783
V/S/Y/L/A	49	17.7259	1.0734	10	-.2071	-.403	3	2.1994	-3.1219
V/S/Y/M/A	50	14.7375	1.1787	10	-.2776	-.1013	3	2.0671	-2.9595
V/S/Y/H/A	51	19.9262	.8231	10	-.1732	-.0028	3.5	2.3636	-4.2878
V/S/P/L/R	52	50.8258	.5468	10	-.1636	.3920	4	2.9877	-5.5645
V/S/P/M/R	53	7.259	.4864	1.0985	-.1677	3.8e-4	4.5	2.7621	-5.2745
V/S/P/H/R	54	4.9566	.2184	.3227	-.1260	-.4893	5.5	3.1496	-3.7169
V/M/P/M/A	55	33.20	.4752	10	-.2927	.0196	3	2.9392	-6.9101
V/M/Y/L/A	55	12.302	.8344	10	-.2954	-.0373	3	1.5736	-7.5647
V/M/P/H/A	56	25.473	.4026	10	-.3639	.4864	4.5	2.3368	-10.7887
V/M/Y/M/A	56	15.2827	.3283	10	-.2784	-.0654	4.5	1.4864	-16.2670

Table B.3, continued.

Configuration	Run	K_p	T_{lead} (sec)	T_{lag} (sec)	T_p (sec)	α_p (rad ² /sec)	HQR	$\omega_{c\ est}$ (rad/sec)	Slope _p (dB/dec)
V/M/P/M/A	57	3.8834	9e-6	1.2322	-.2069	-.1908	5.5	1.9764	-16.9829
V/M/Y/H/A	57	2.4338	3e-6	.9615	.1248	-.3567	5.5	1.5399	-13.4412
V/M/P/M/R	58	7.456	.9567	2.0189	-.2661	-.2413	7	2.6173	-2.1271
V/M/Y/L/R	58	1.9015	5	4.0577	-.2015	-.3872	7	1.6388	0.1582
V/M/P/L/R	59	8.9677	2.27887	5.5518	-.2784	-.3031	6.5	2.206	-0.6575
V/M/Y/M/R	59	1.414	1.8919	.9464	-.1440	-.6482	6.5	1.8105	3.6450
V/M/P/M/R	60	17.2707	2.4259	10	-.0549	-.6667	9	2.4093	-0.5570
V/M/Y/F/R	60	3.2245	5	7.9468	-.0254	-.4123	9	.8	-0.7851
V/M/P/L/O	61	75.3987	5	4.6091	.4227	.0549	9	.2371	0.7787
V/M/Y/M/O	61	.1717	2.778	.4473	-.0779	-1	9	1.7414	11.8550
V/M/P/M/O	62	11.359	5	6.6e-5	.068	-.3701	8	.5540	17.2444
V/M/Y/L/O	62	1.4534	2.7127	10	.1982	-.8800	8	1.7522	-0.8283
V/M/P/H/O	63	15.3609	5	0	-.0733	-.6992	7	.4945	16.5811
V/M/Y/M/O	63	.3161	.3544	5e-5	-.3289	-.1979	7	.9088	1.6933

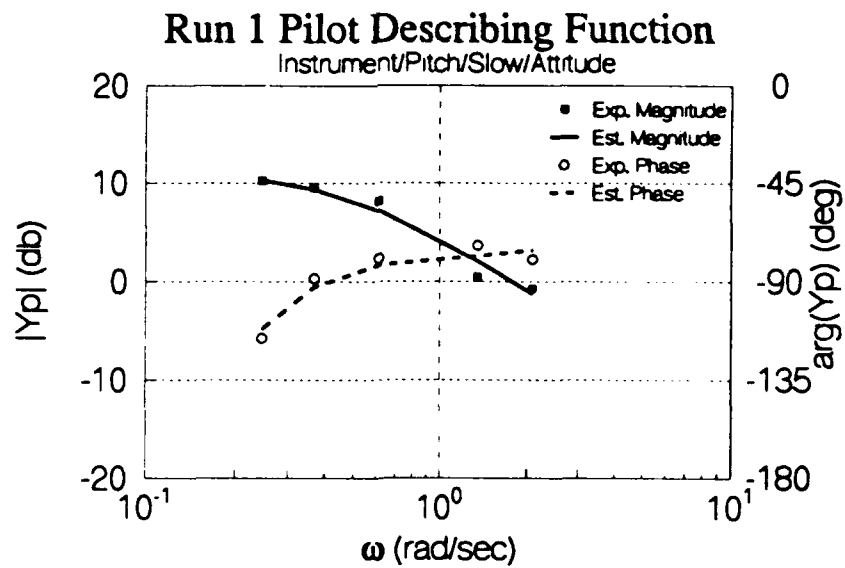
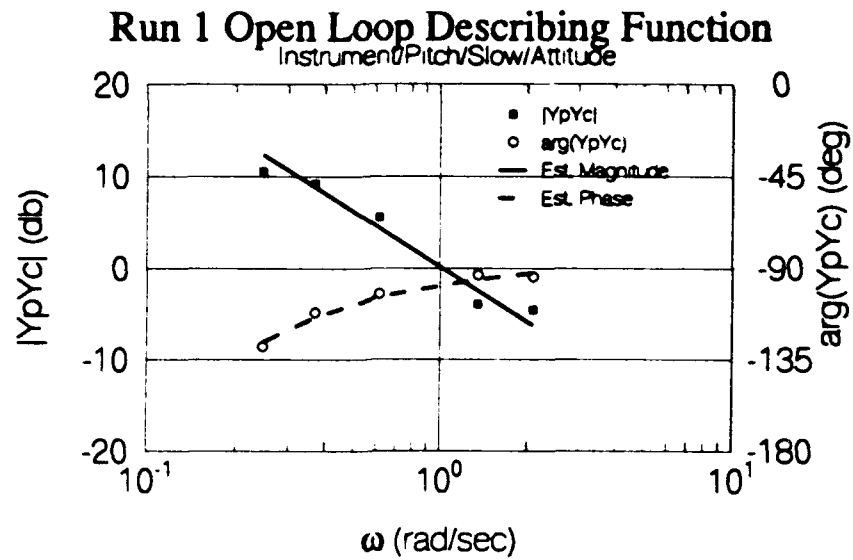


Figure B.2 Open loop pilot-vehicle and pilot describing functions.

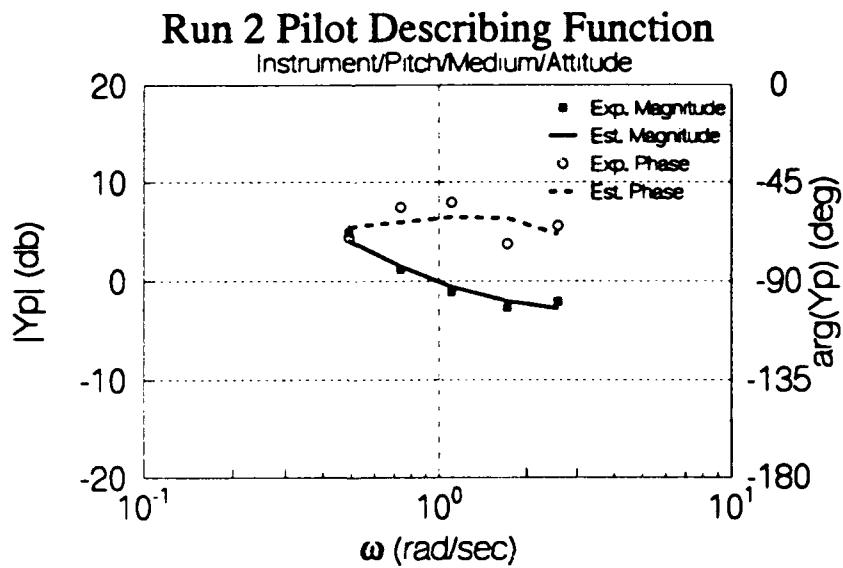
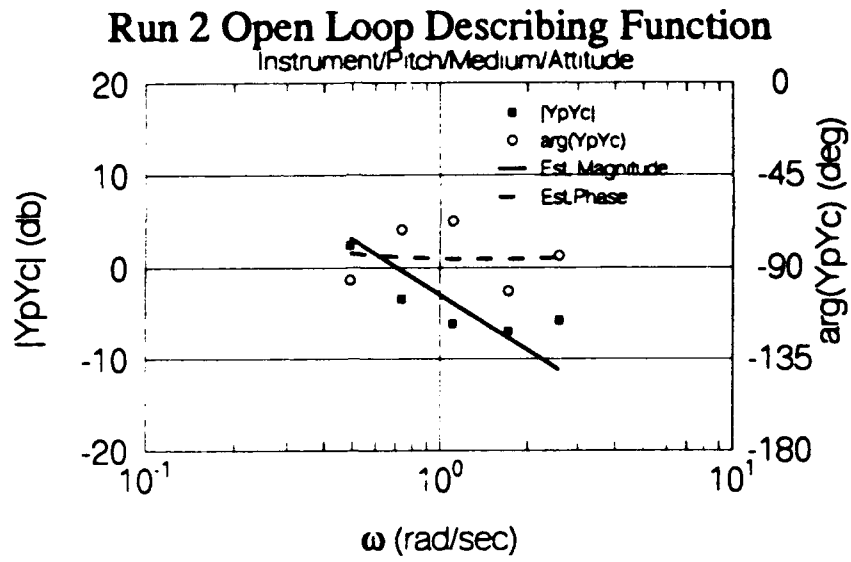


Figure B.2, continued.

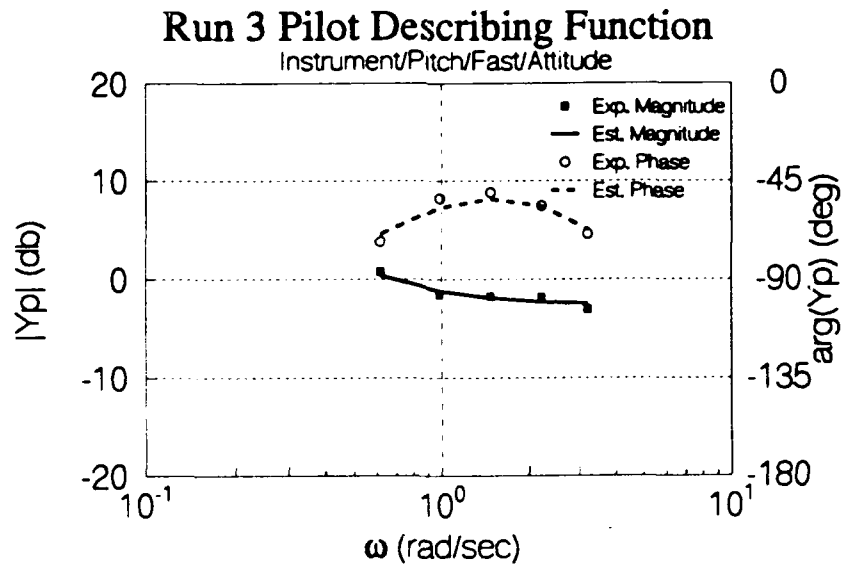
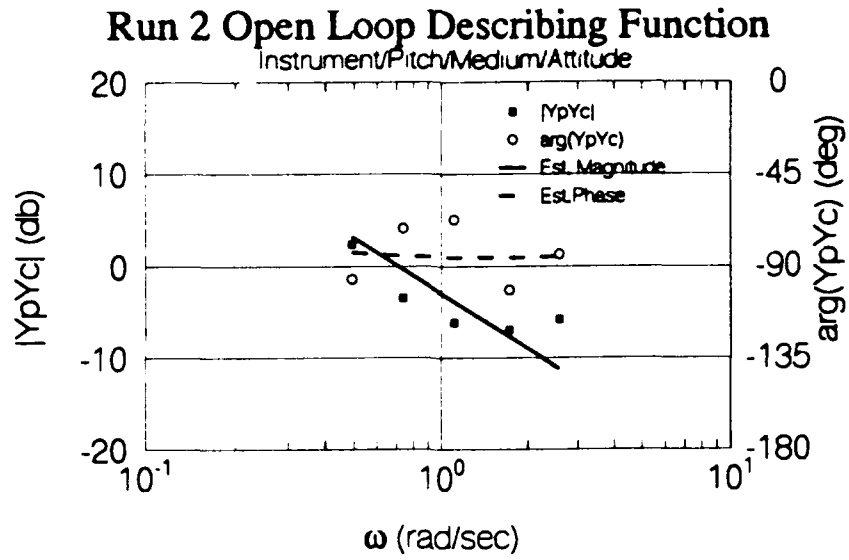


Figure B.2. continued.

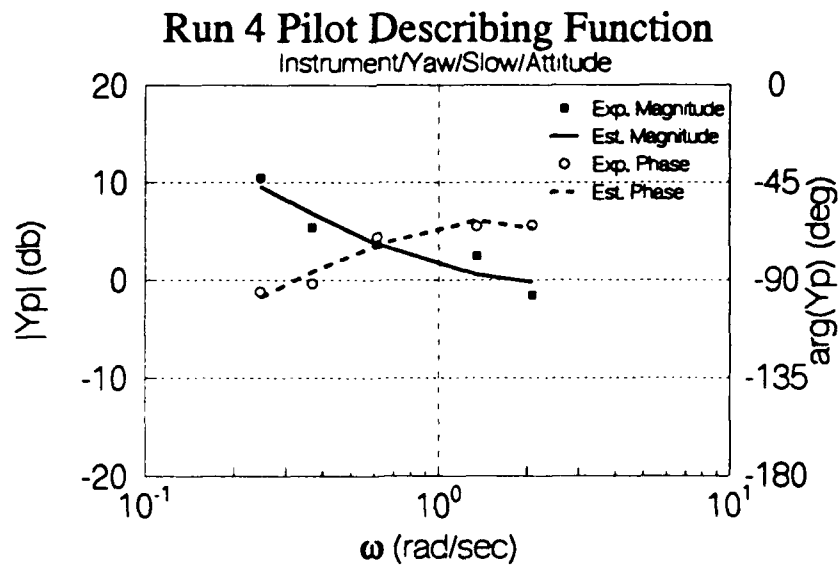
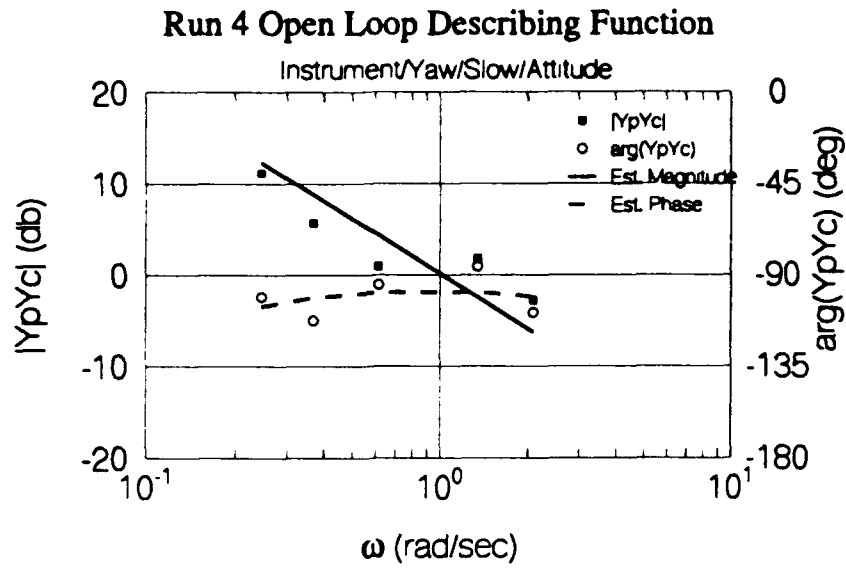


Figure B.2, continued.

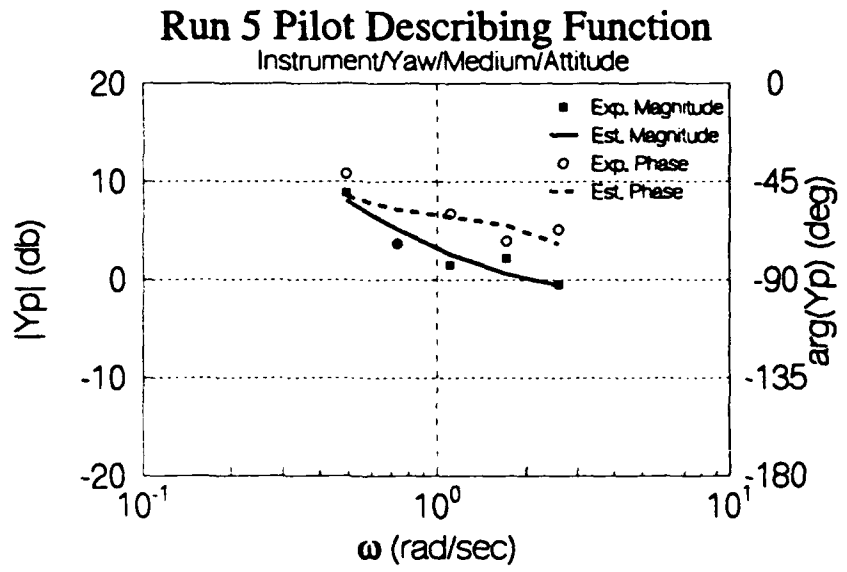
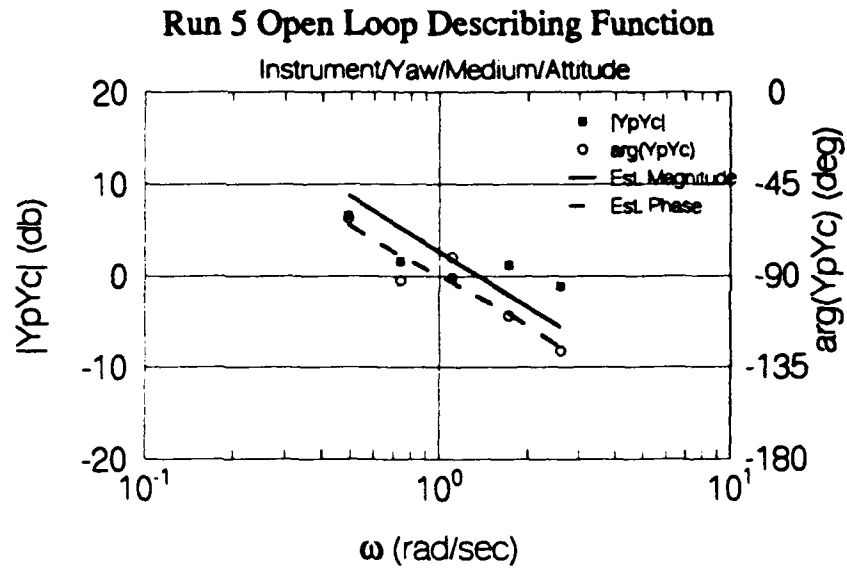


Figure B.2, continued.

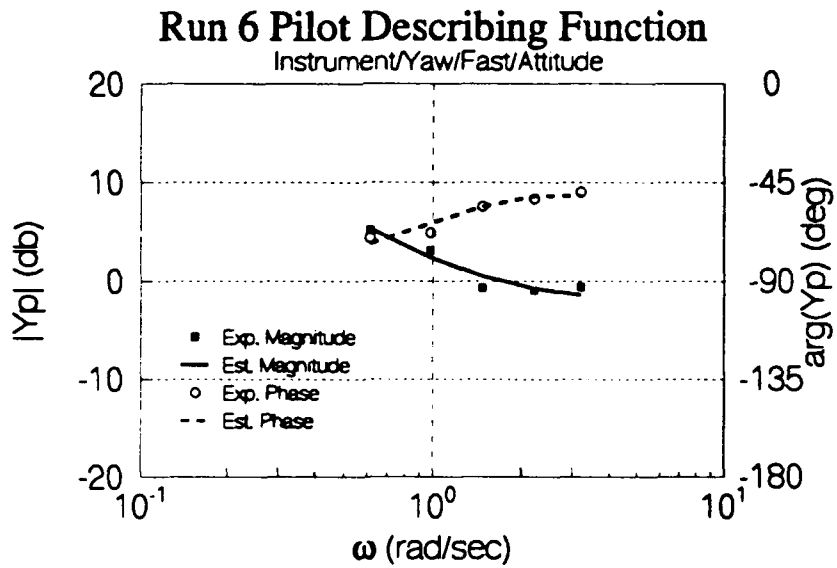
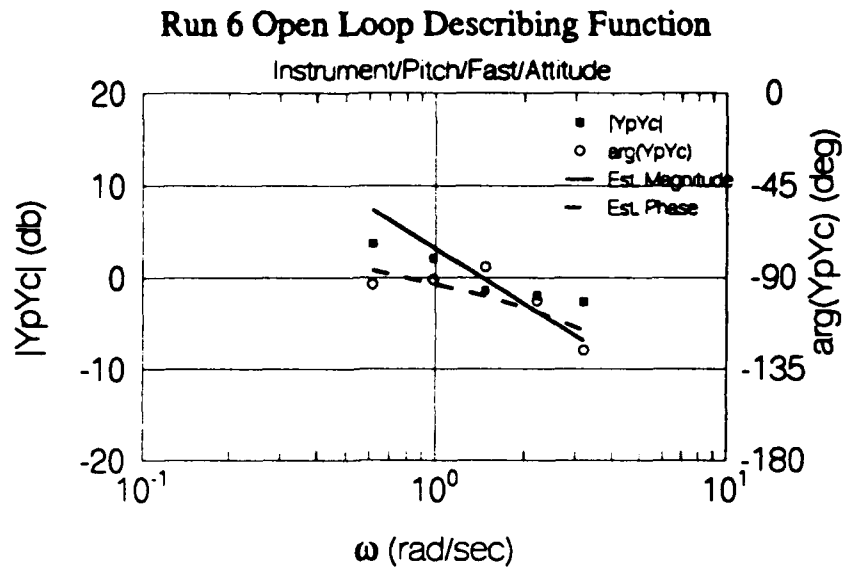
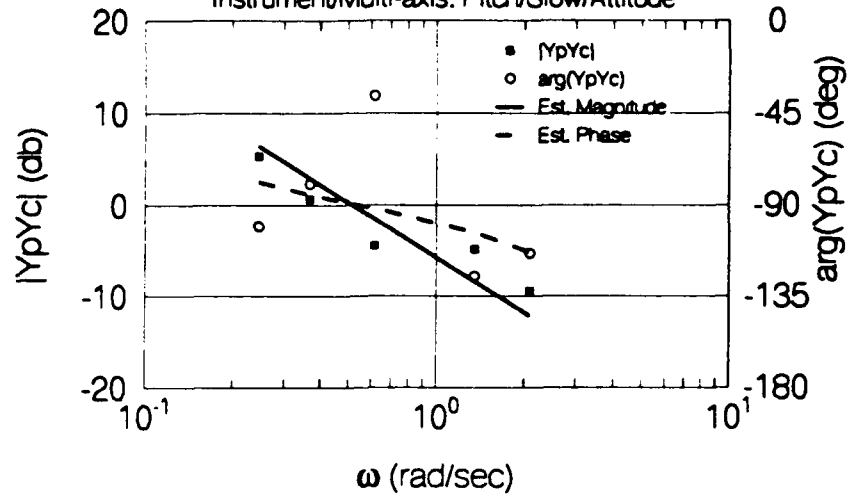


Figure B.2, continued.

Run 7 Open Loop Describing Function

Instrument/Multi-axis: Pitch/Slow/Attitude



Run 7 Pilot Describing Function

Instrument/Multi: Pitch/Slow/Attitude

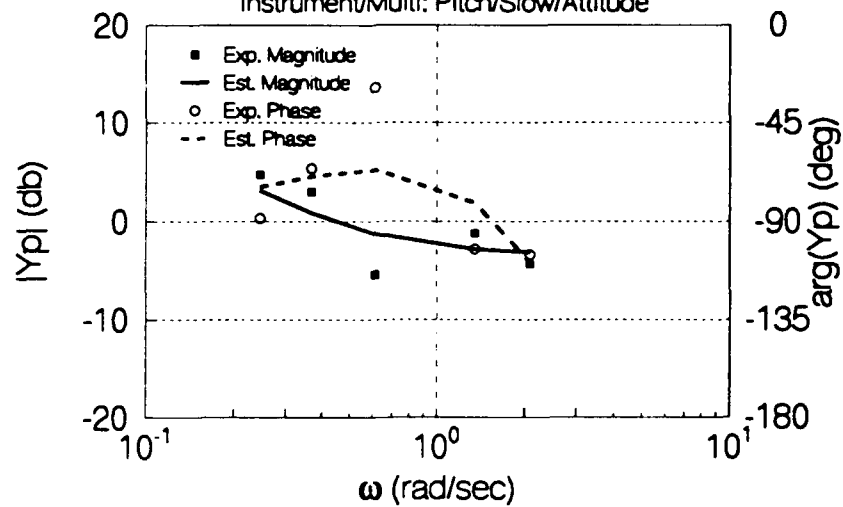


Figure B.2, continued.

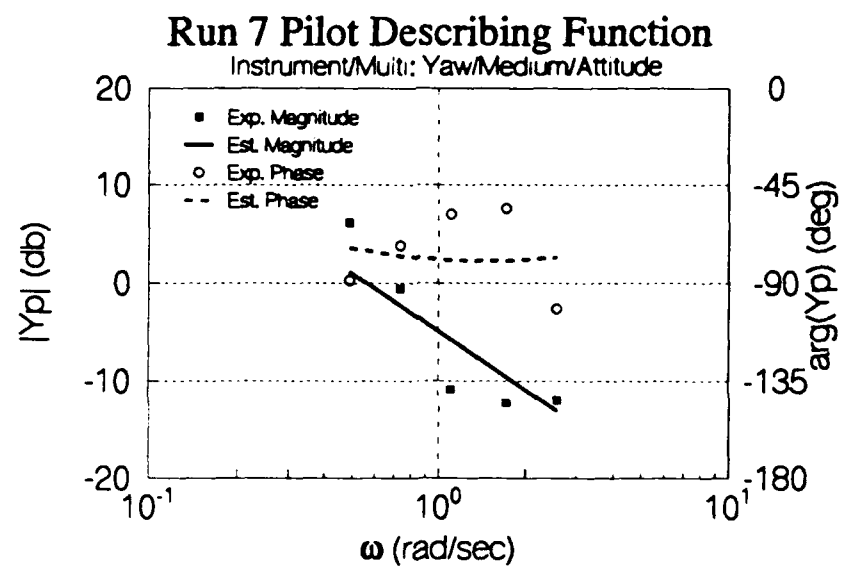
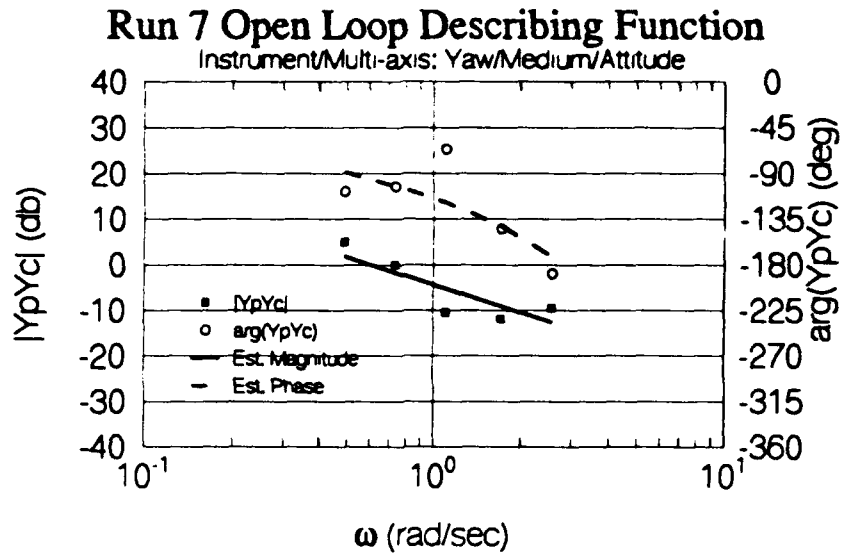


Figure B.2, continued.

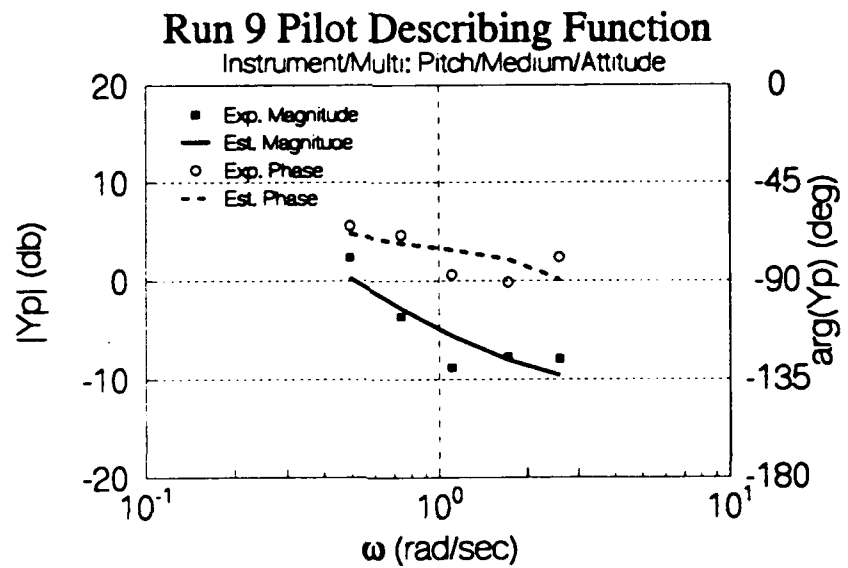
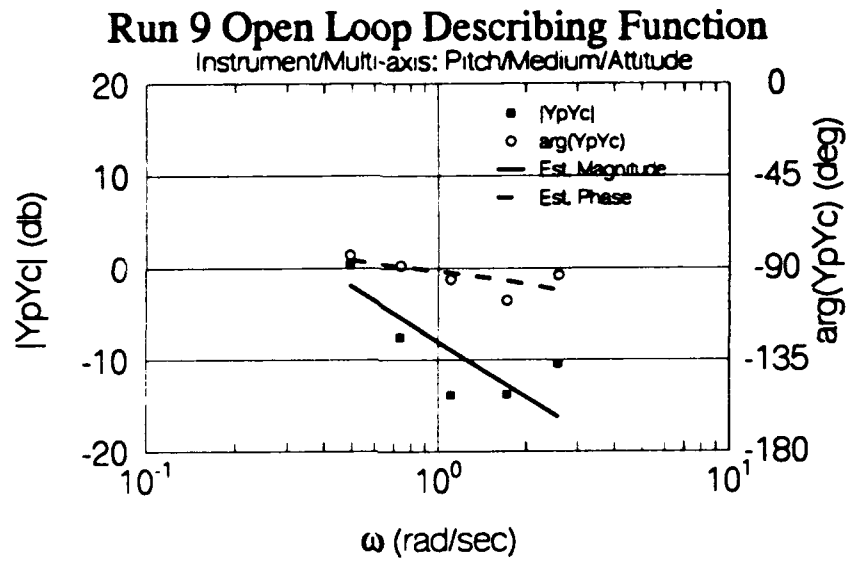


Figure B.2, continued.

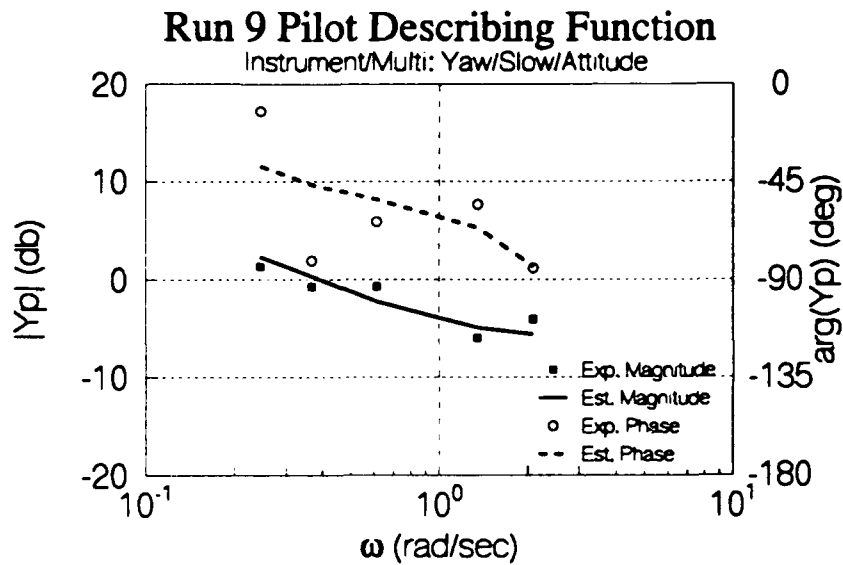
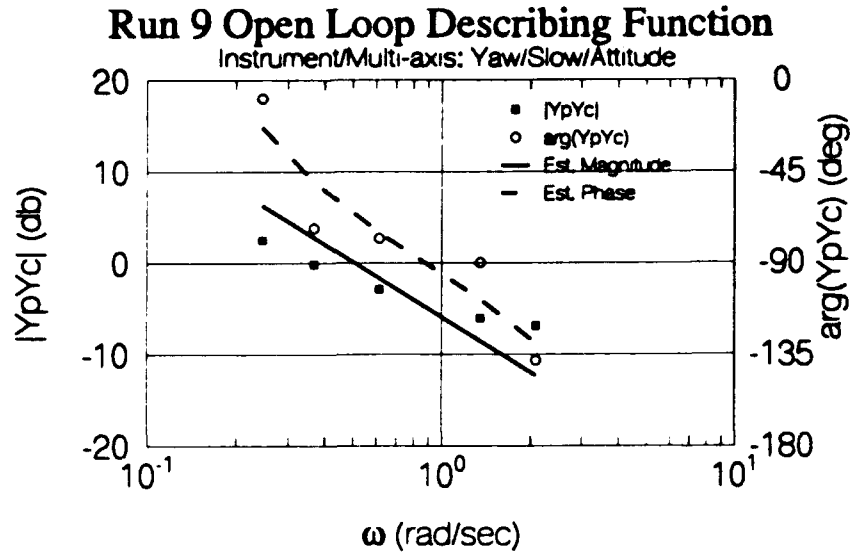
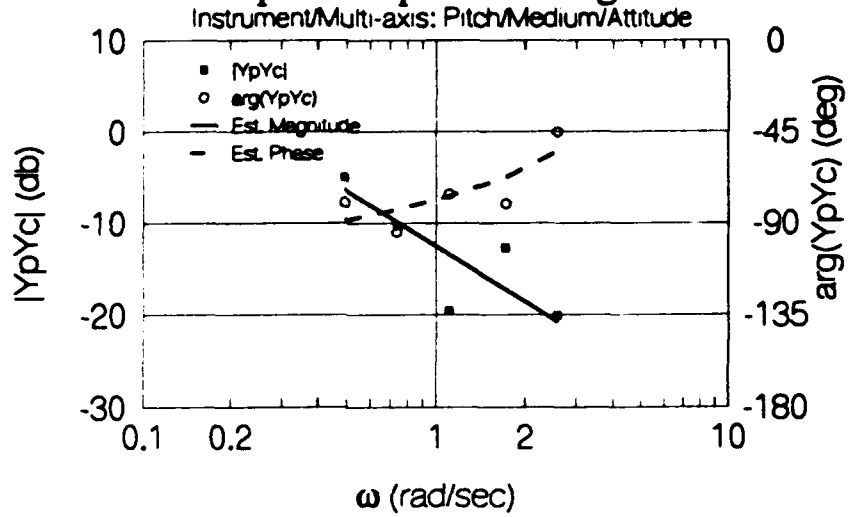


Figure B.2, continued.

Run 10 Open Loop Describing Function



Run 10 Pilot Describing Function

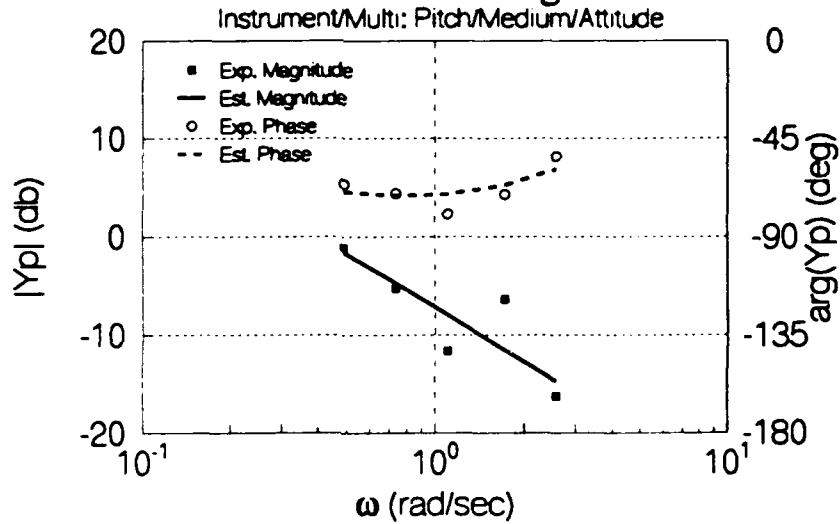


Figure B.2, continued.

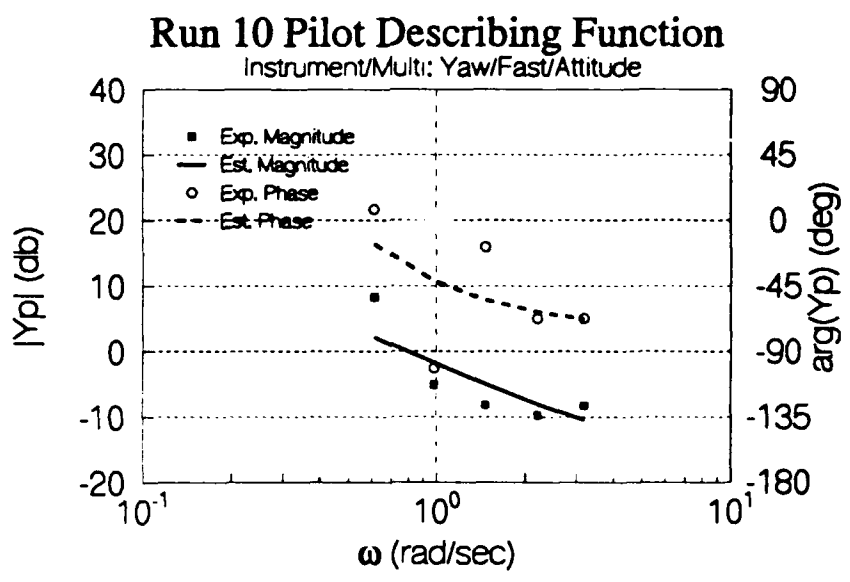
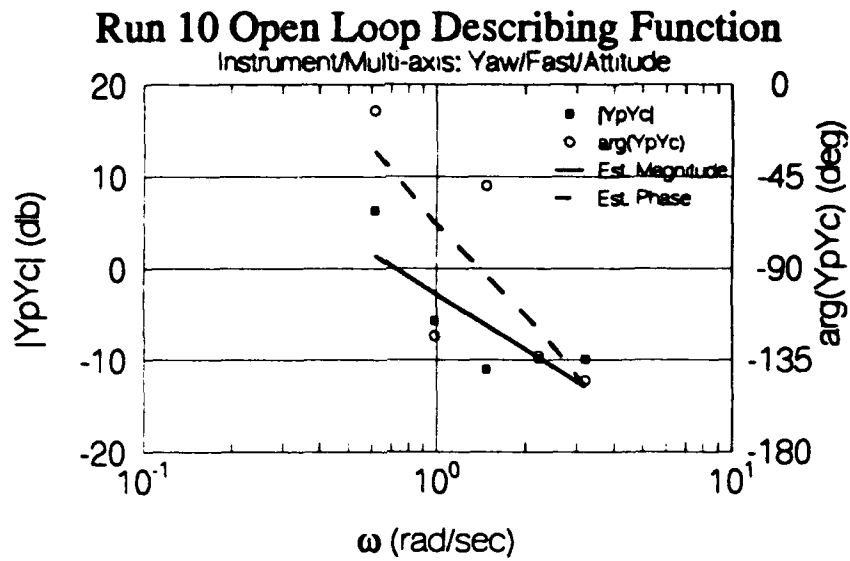


Figure B.2, continued.

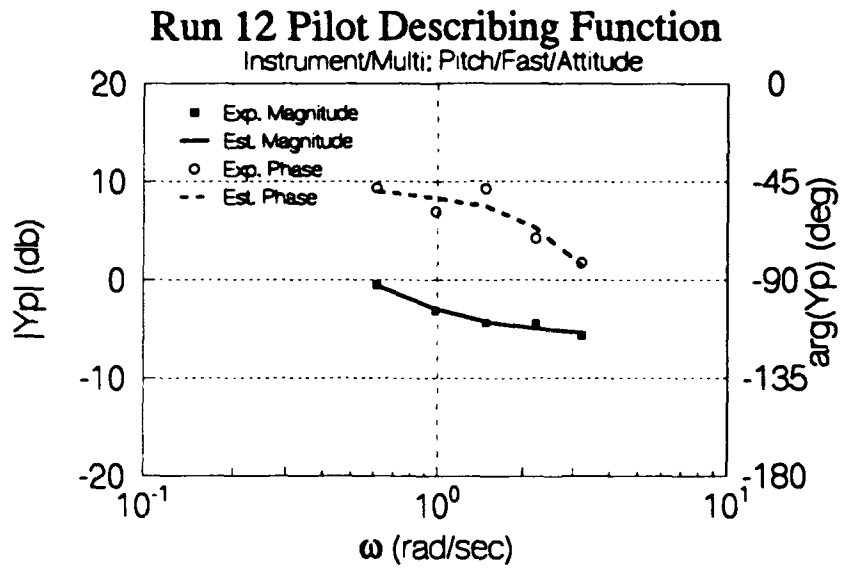
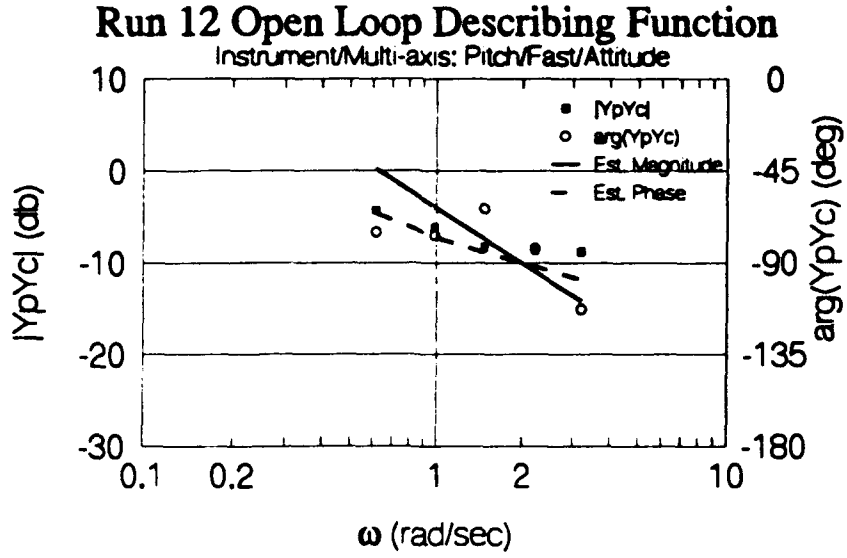
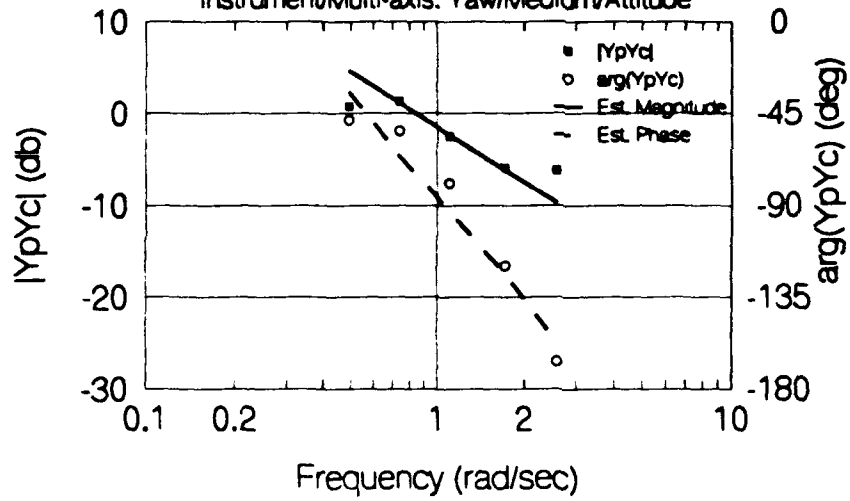


Figure B.2, continued.

Run 12 Open Loop Describing Function

Instrument/Multi-axis: Yaw/Medium/Attitude



Run 12 Pilot Describing Function

Instrument/Multi: Yaw/Medium/Attitude

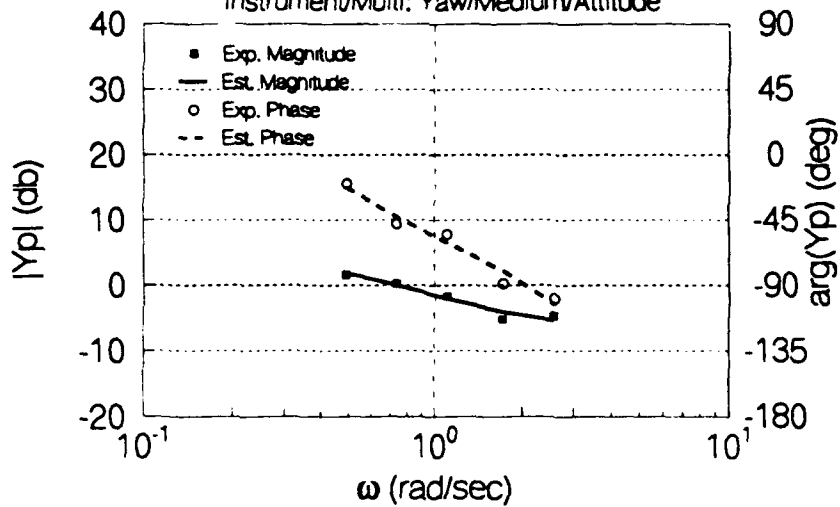


Figure B.2, continued.

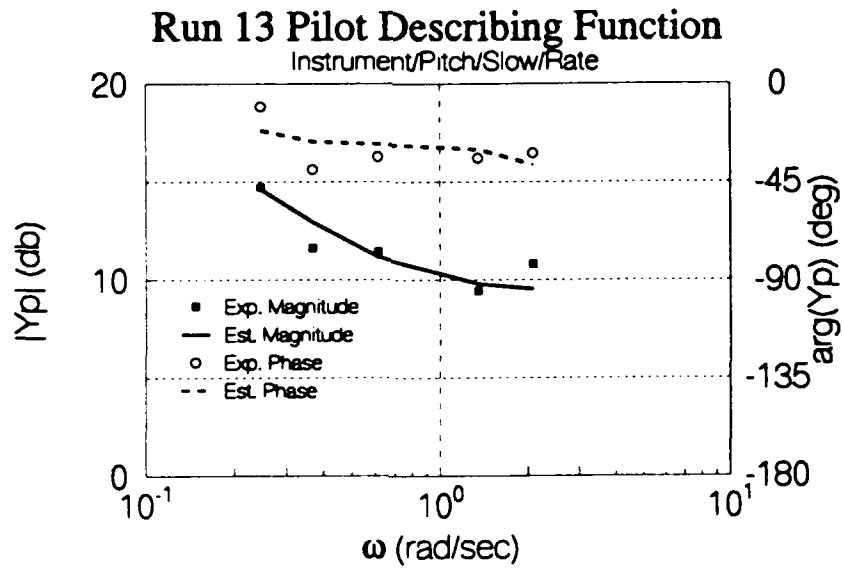
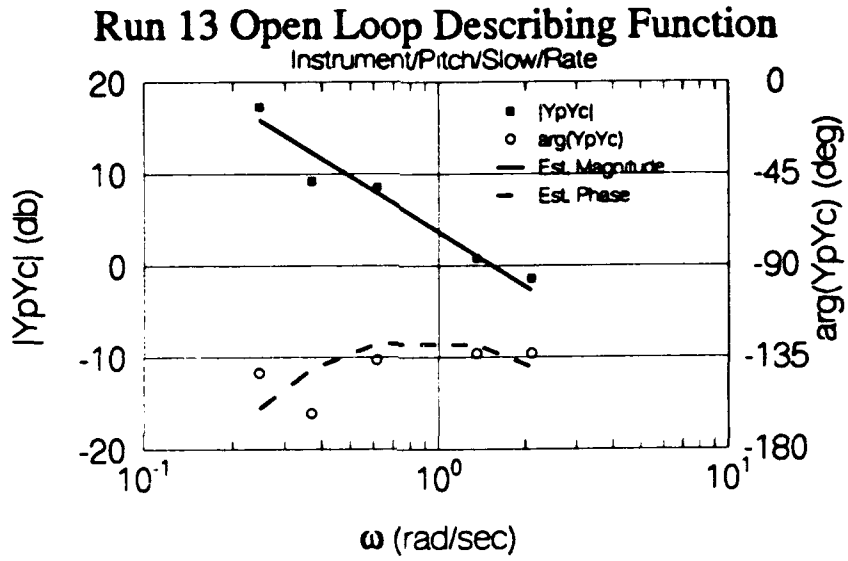
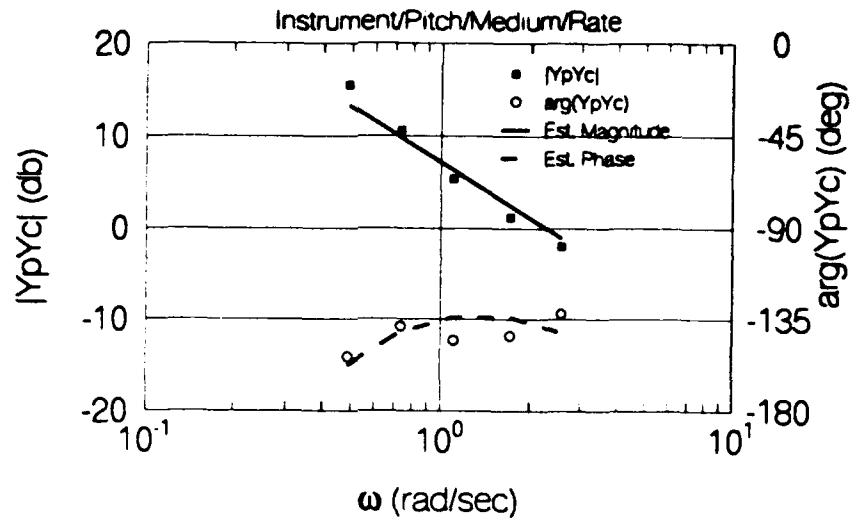


Figure B.2, continued.

Run 14 Open Loop Describing Function



Run 14 Pilot Describing Function

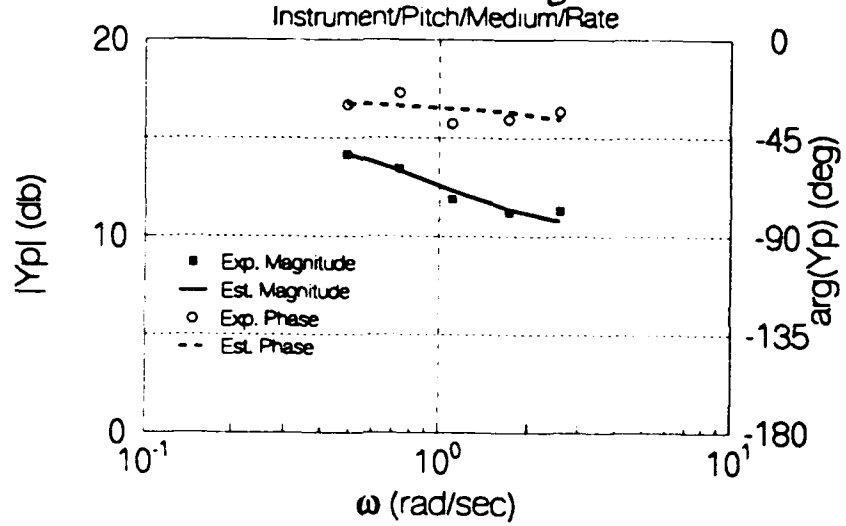


Figure B.2, continued.

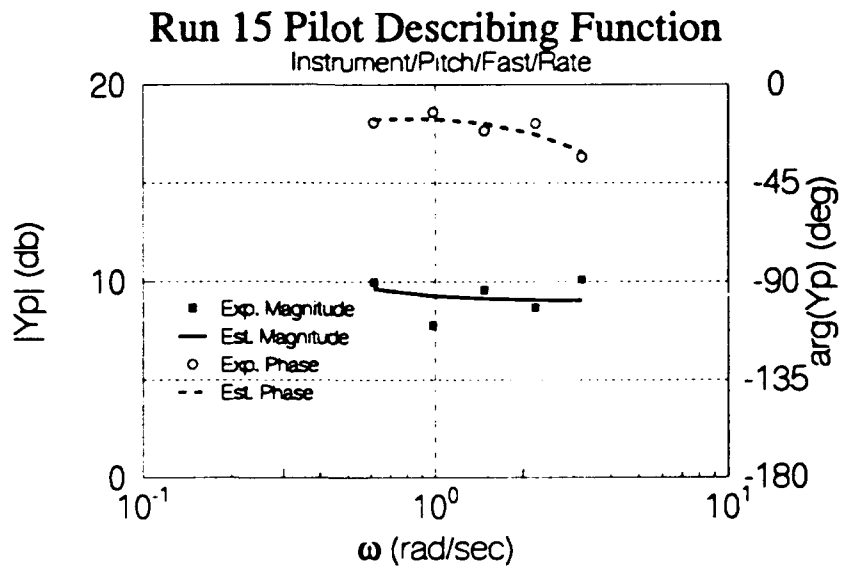
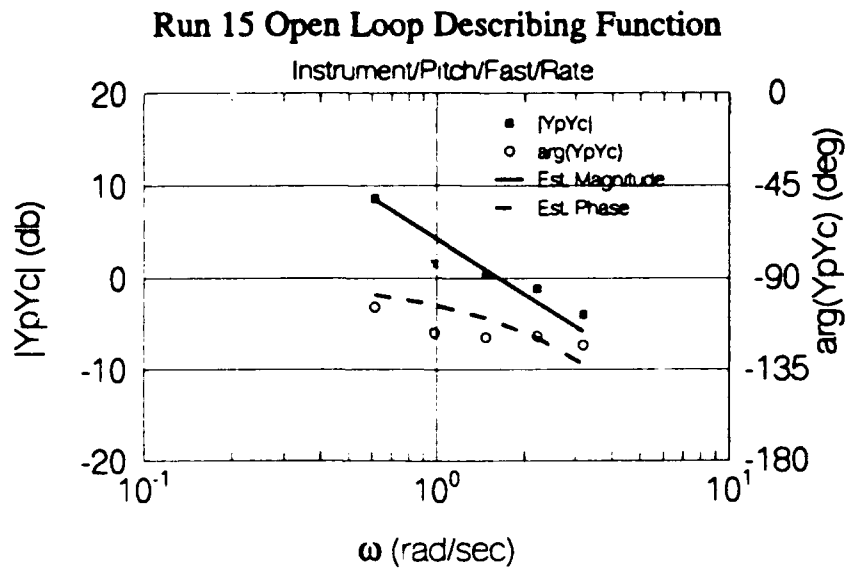


Figure B.2, continued.

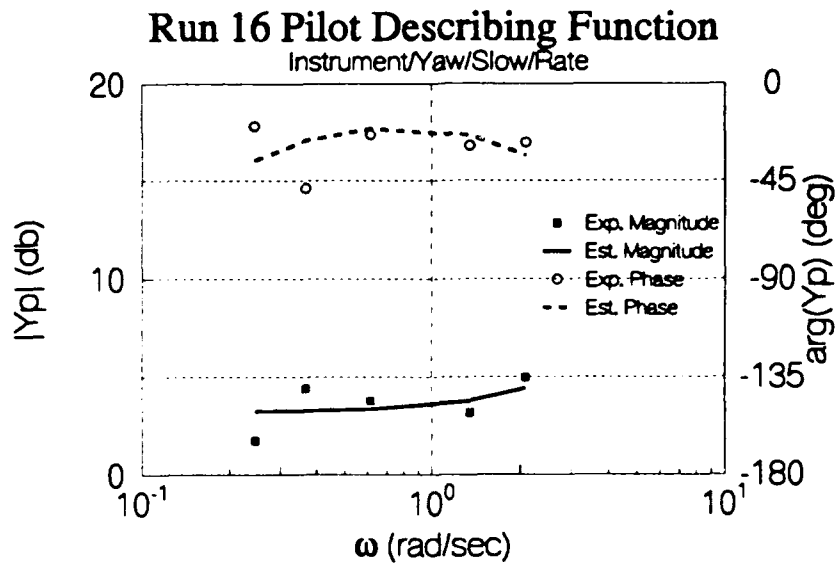
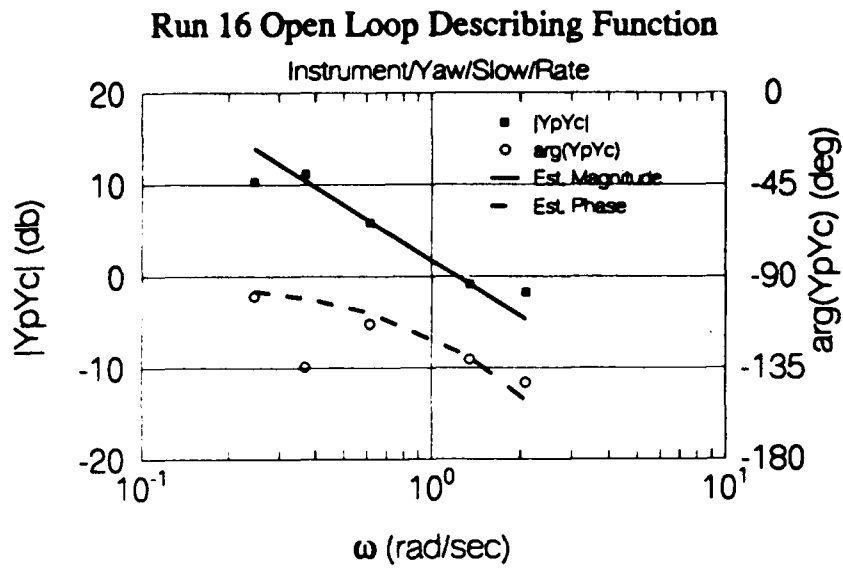


Figure B.2, continued.

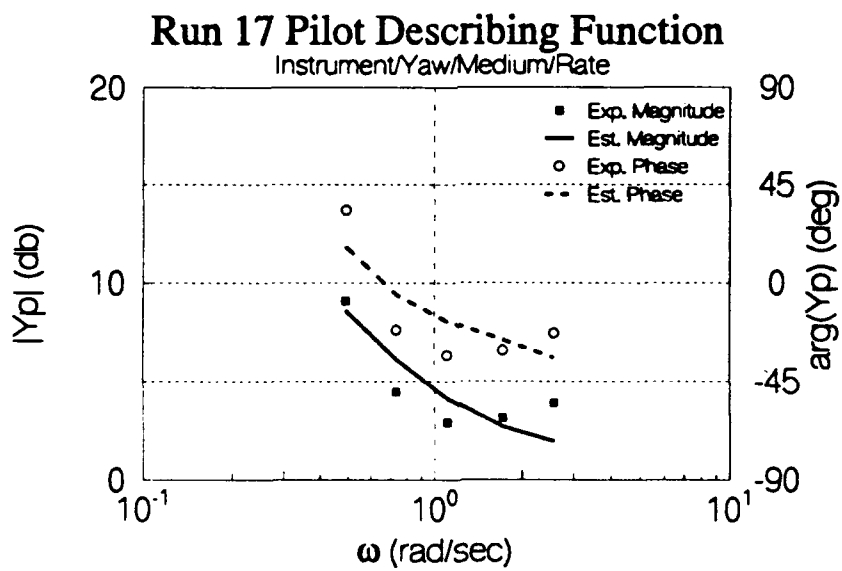
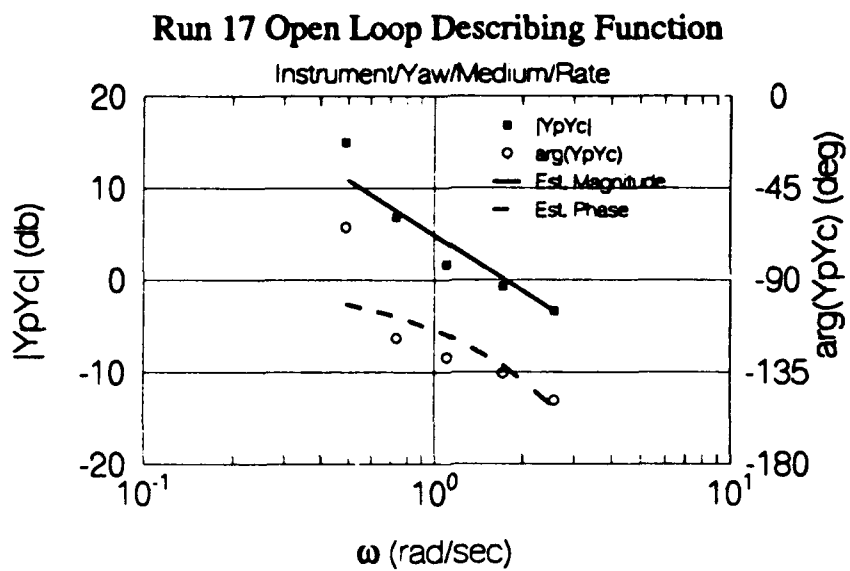
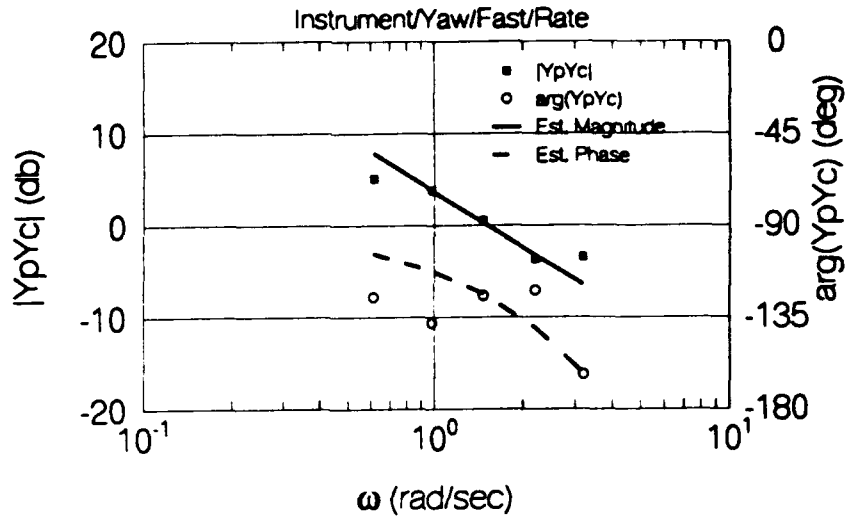


Figure B.2, continued.

Run 18 Open Loop Describing Function



Run 18 Pilot Describing Function

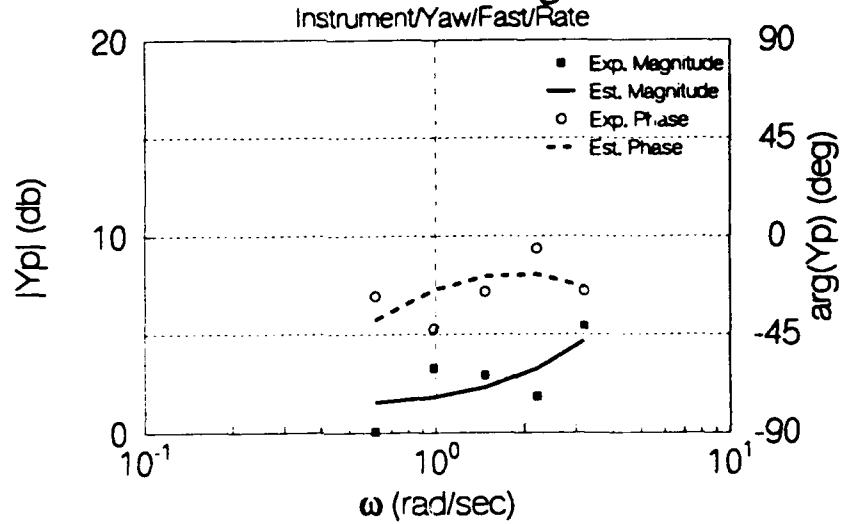


Figure B.2, continued.

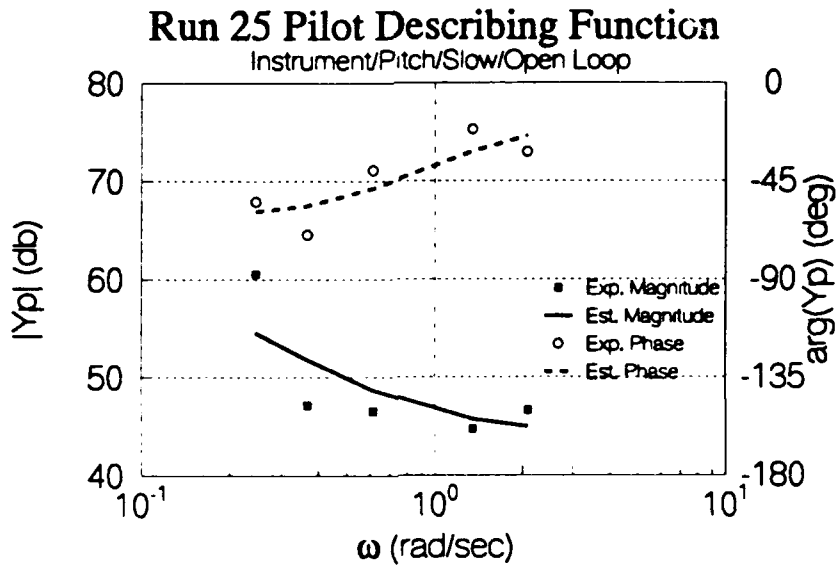
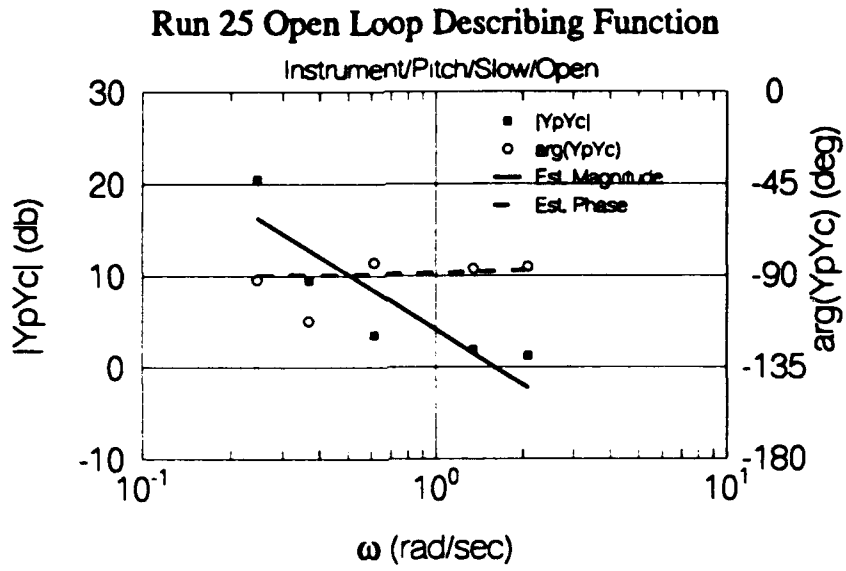


Figure B.2, continued.

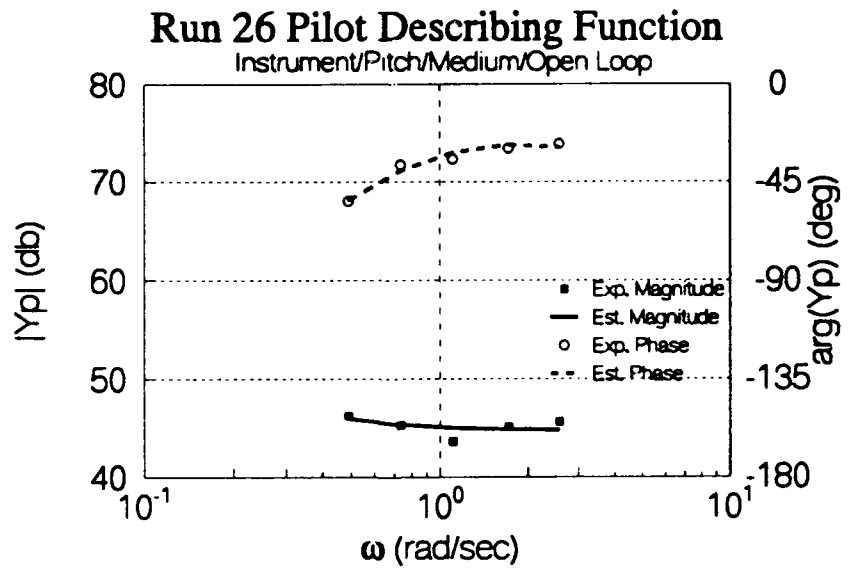
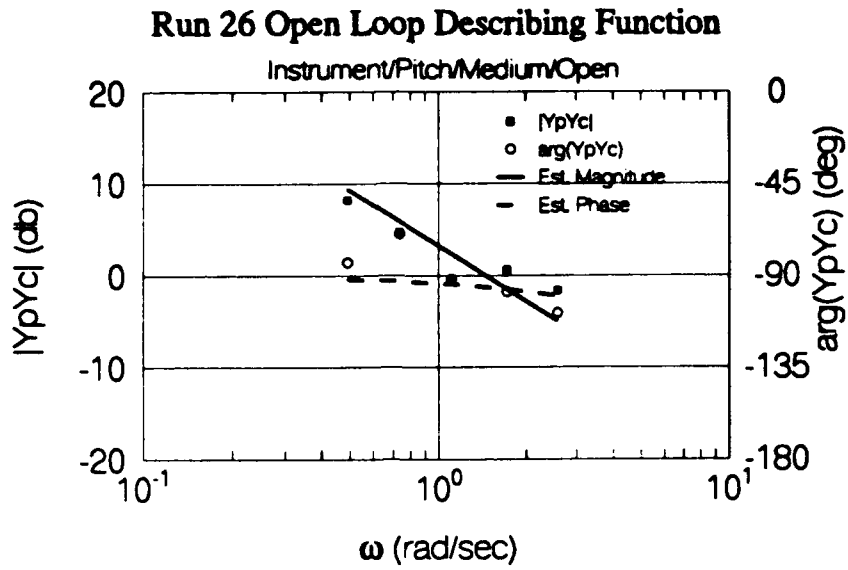


Figure B.2, continued.

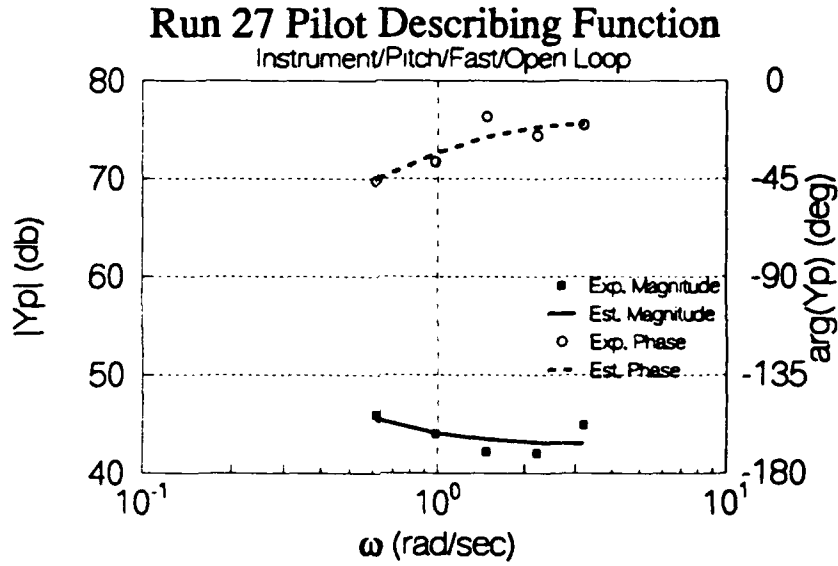
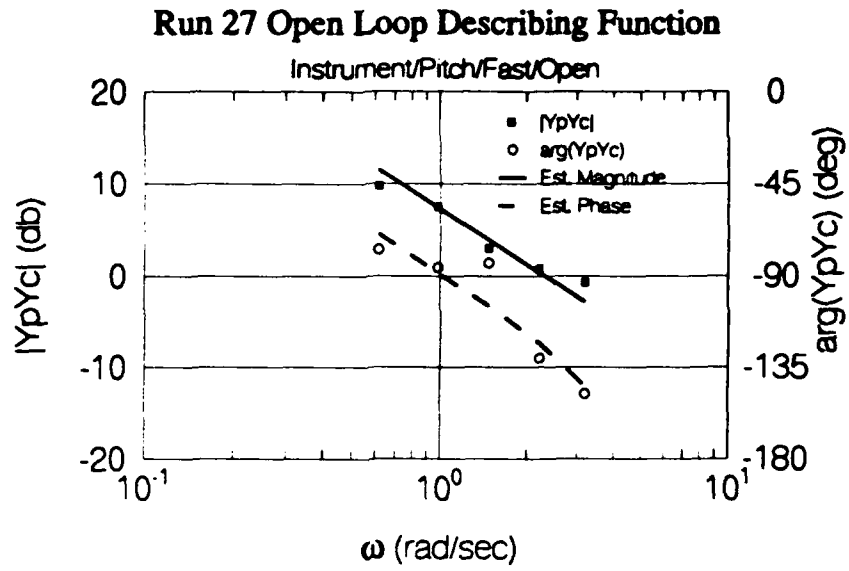


Figure B.2, continued.

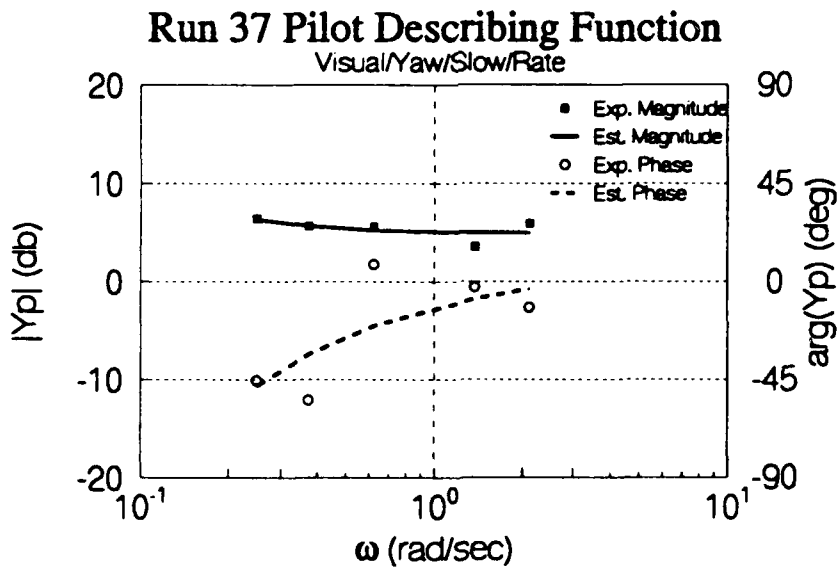
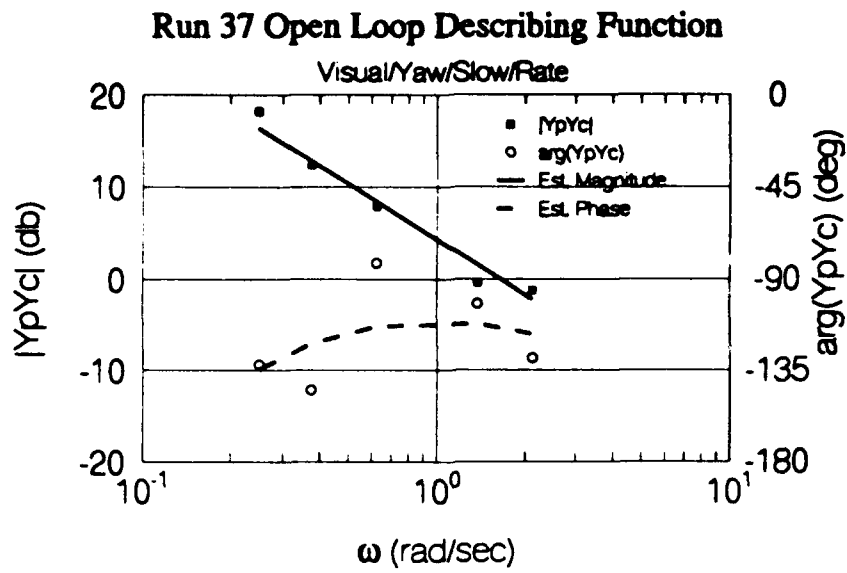
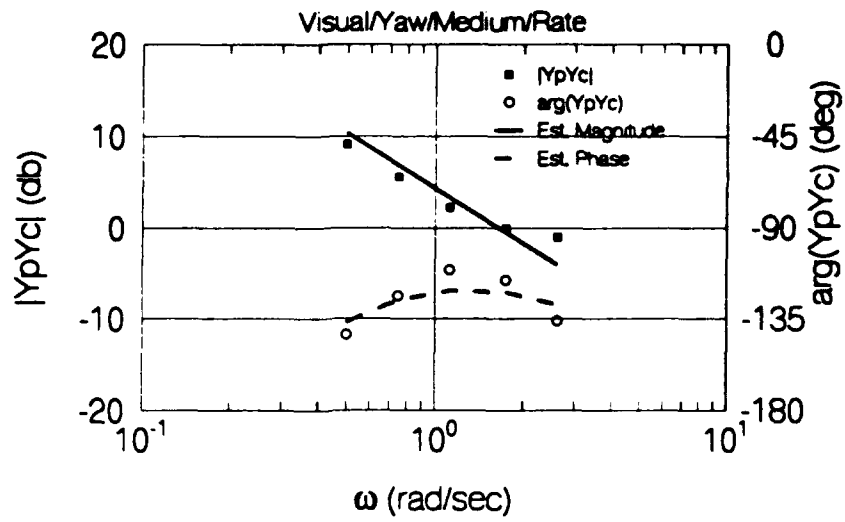


Figure B.2, continued.

Run 38 Open Loop Describing Function



Run 38 Pilot Describing Function

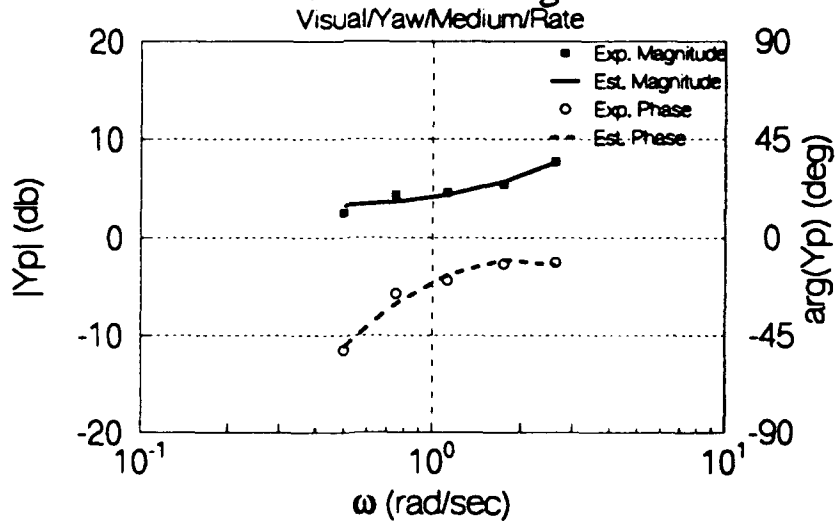
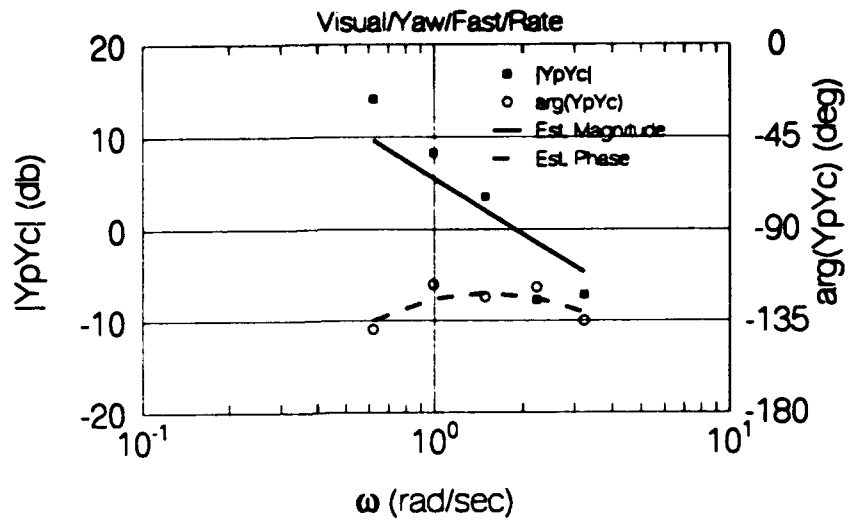


Figure B.2, continued.

Run 39 Open Loop Describing Function



Run 39 Pilot Describing Function

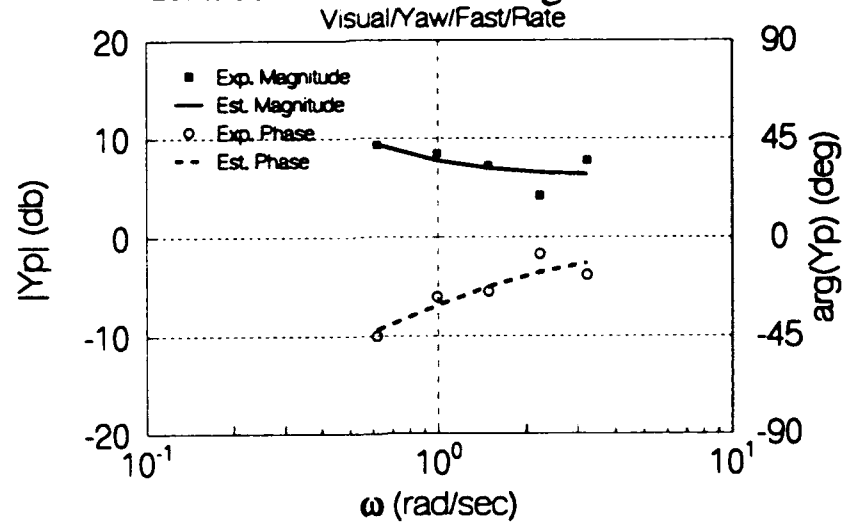
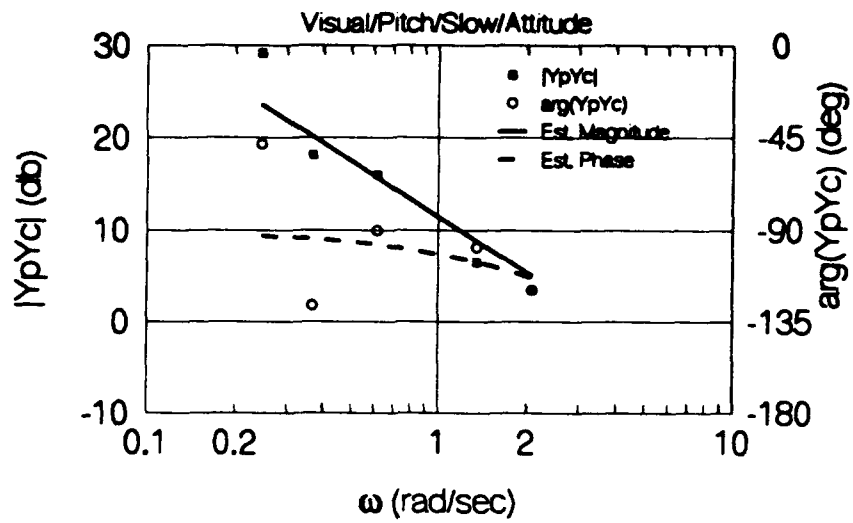


Figure B.2, continued.

Run 40 Open Loop Describing Function



Run 40 Pilot Describing Function

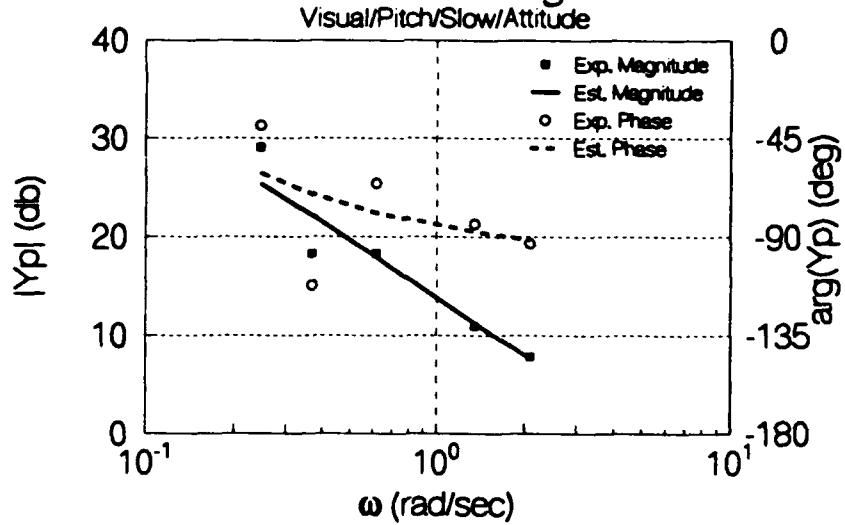


Figure B.2, continued.

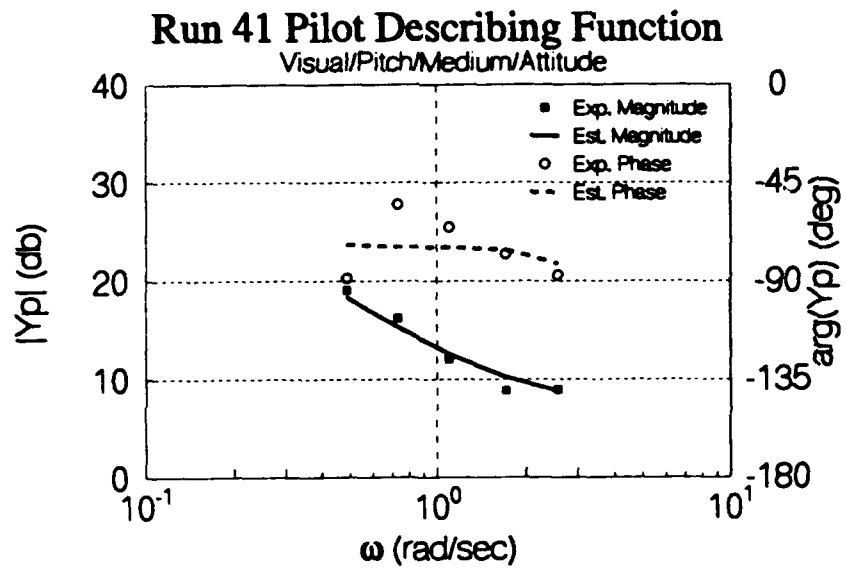
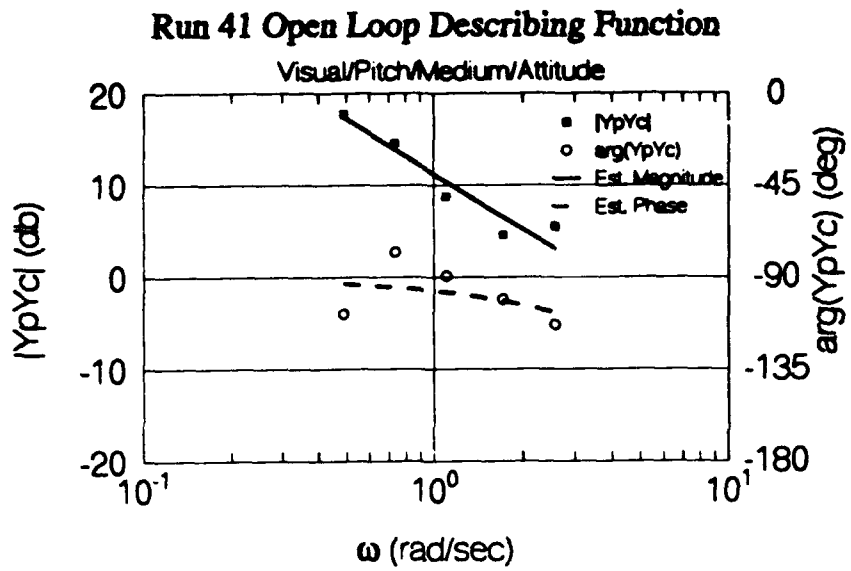


Figure B.2, continued.

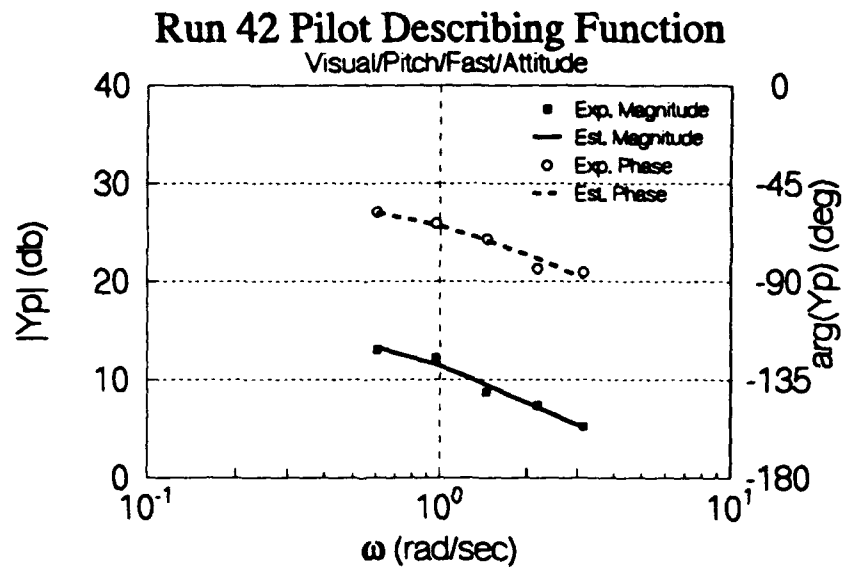
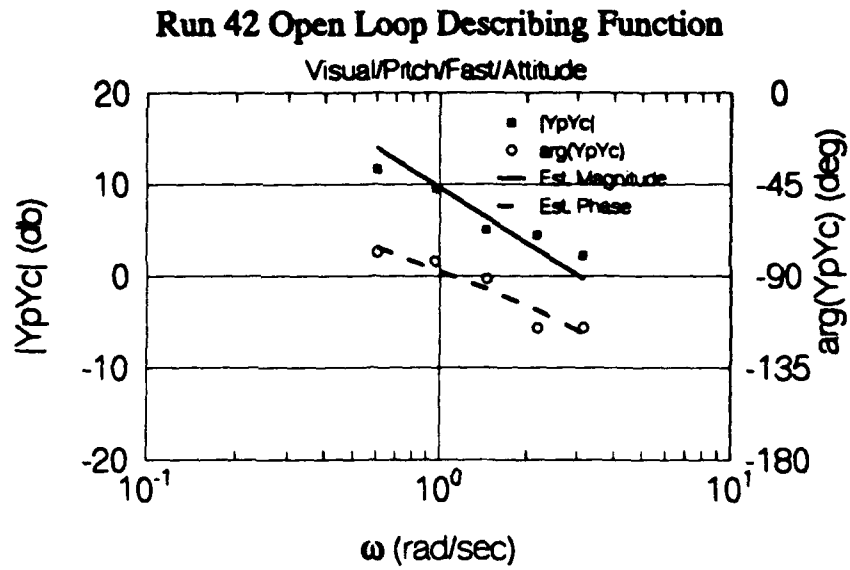
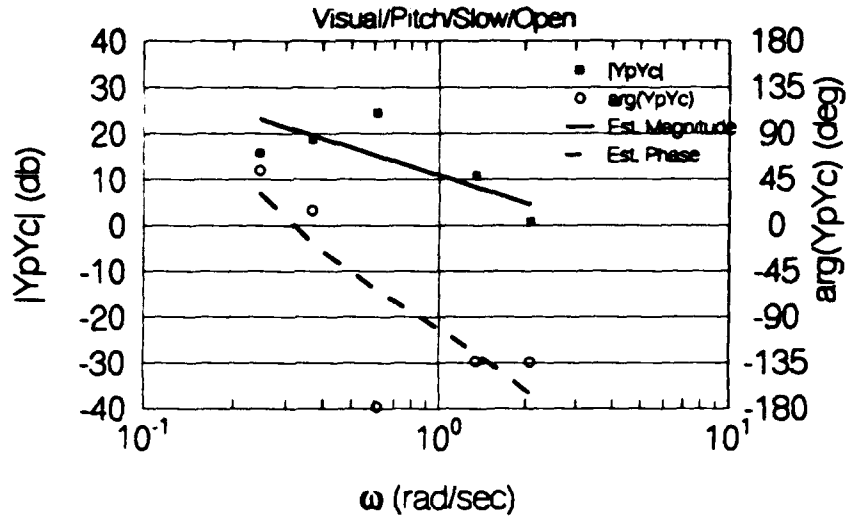


Figure B.2, continued.

Run 43 Open Loop Describing Function



Run 43 Pilot Describing Function

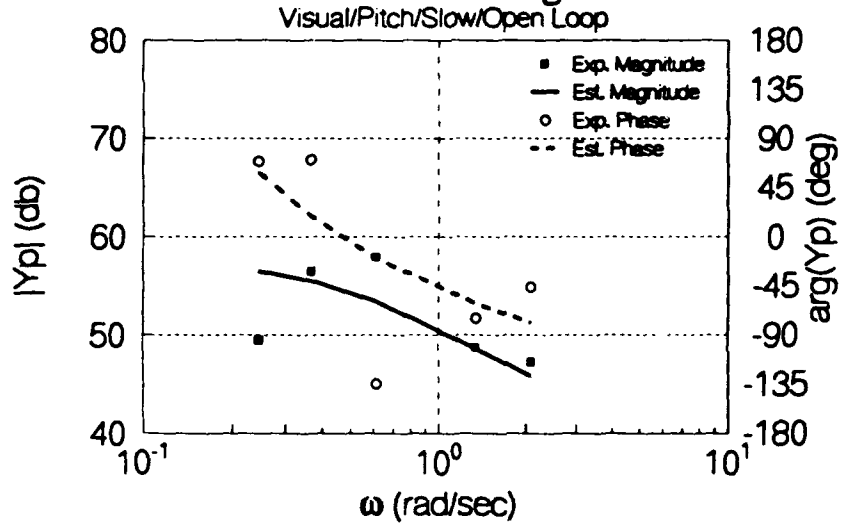


Figure B.2, continued.

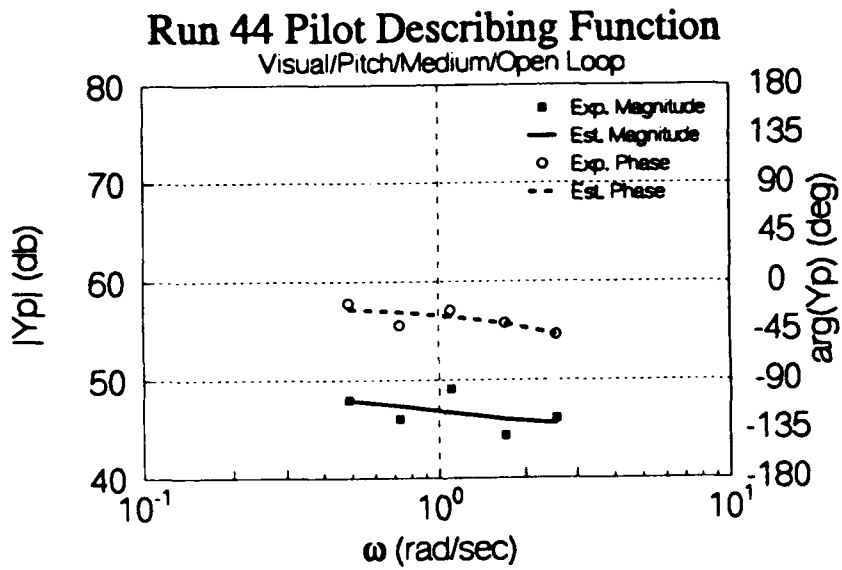
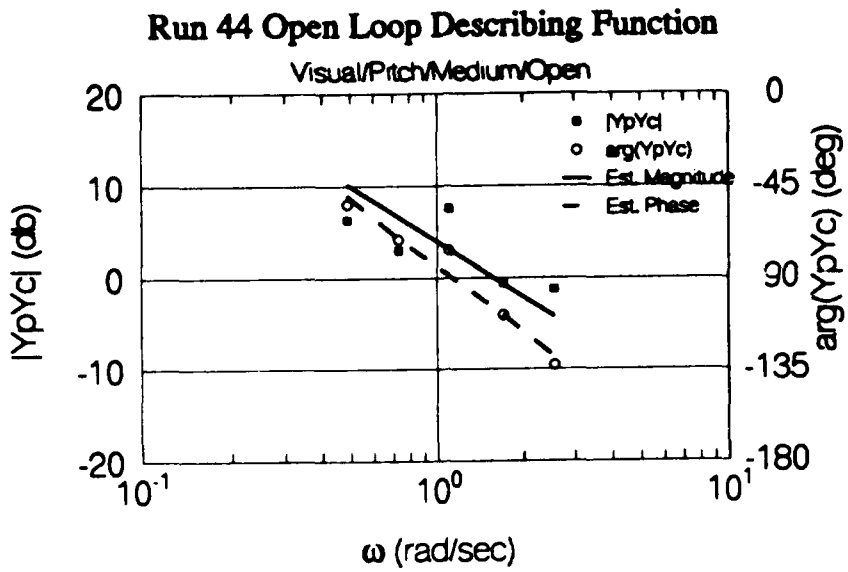
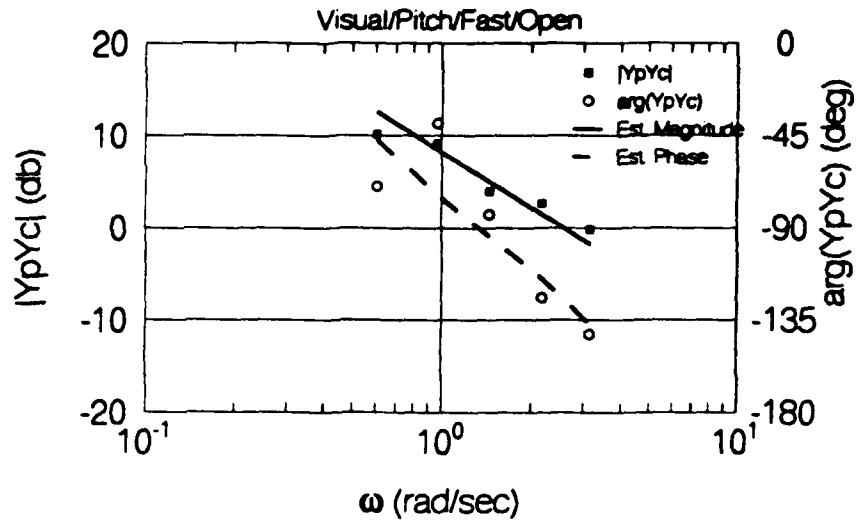


Figure B.2, continued.

Run 45 Open Loop Describing Function



Run 45 Pilot Describing Function

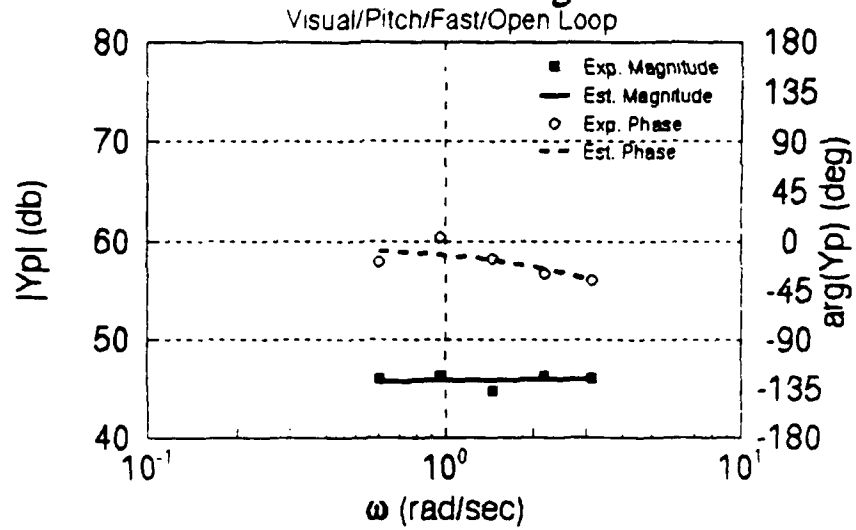
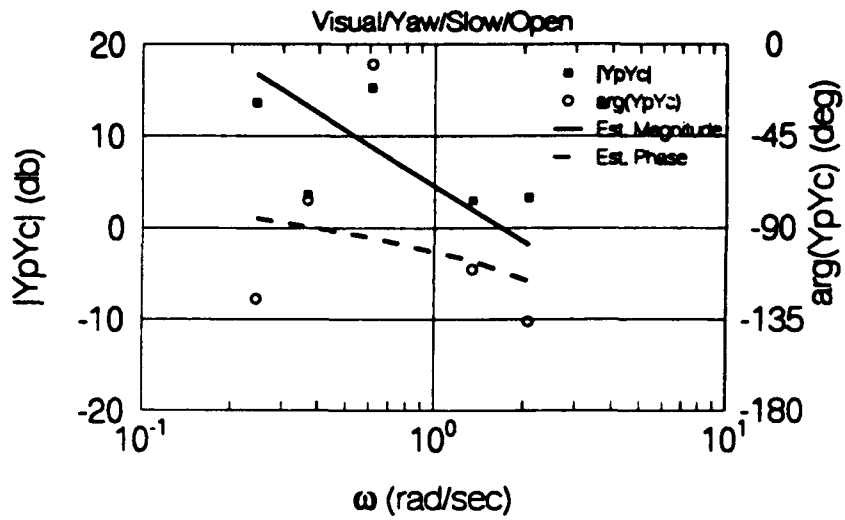


Figure B.2, continued.

Run 46 Open Loop Describing Function



Run 46 Pilot Describing Function

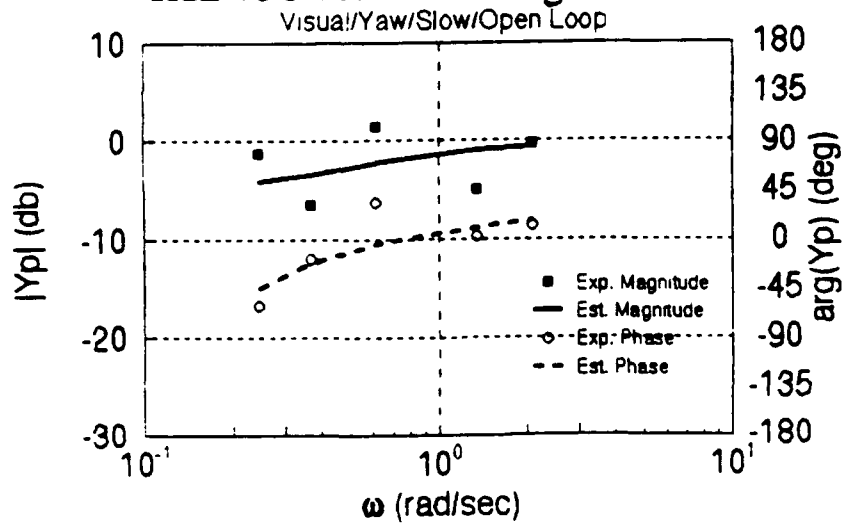
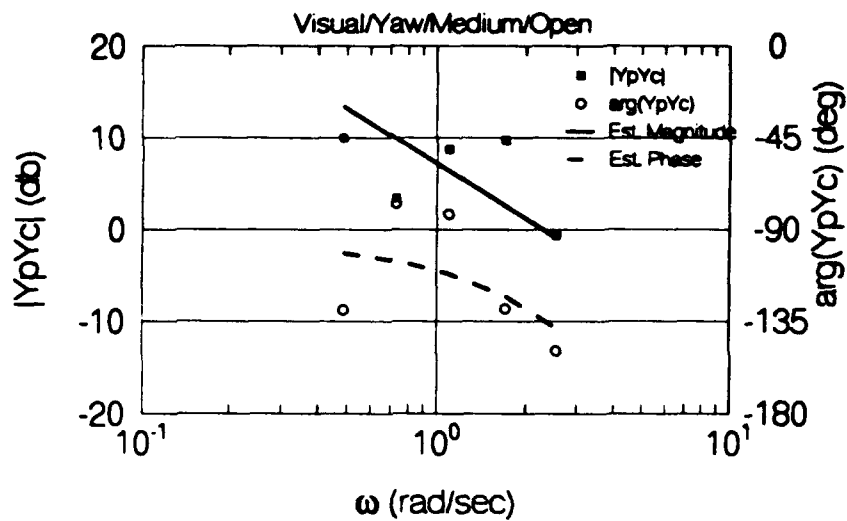


Figure B.2, continued.

Run 47 Open Loop Describing Function



Run 47 Pilot Describing Function

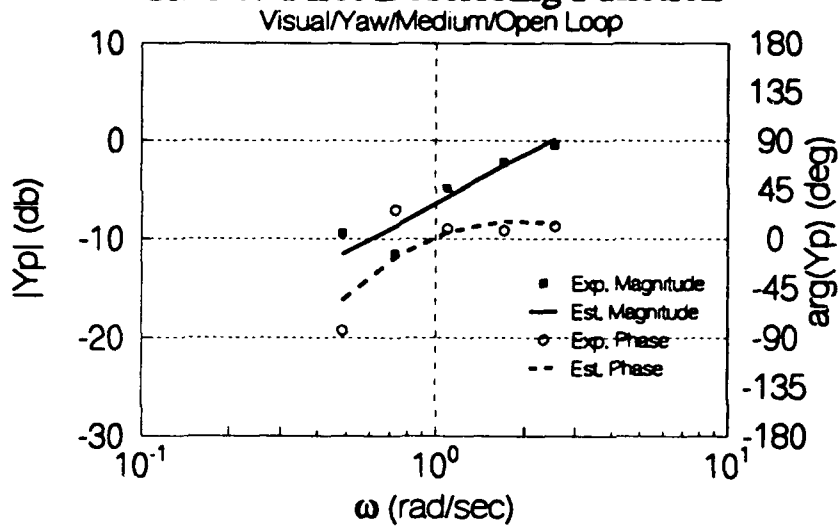
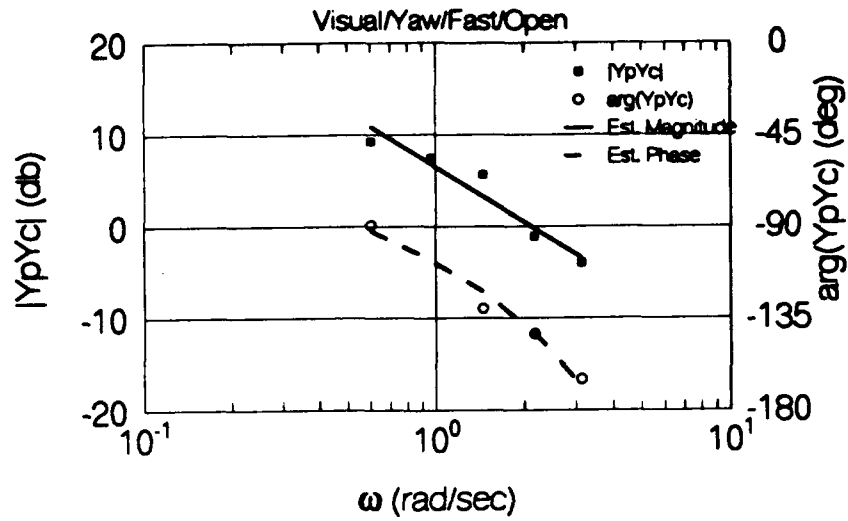


Figure B.2, continued.

Run 48 Open Loop Describing Function



Run 48 Pilot Describing Function

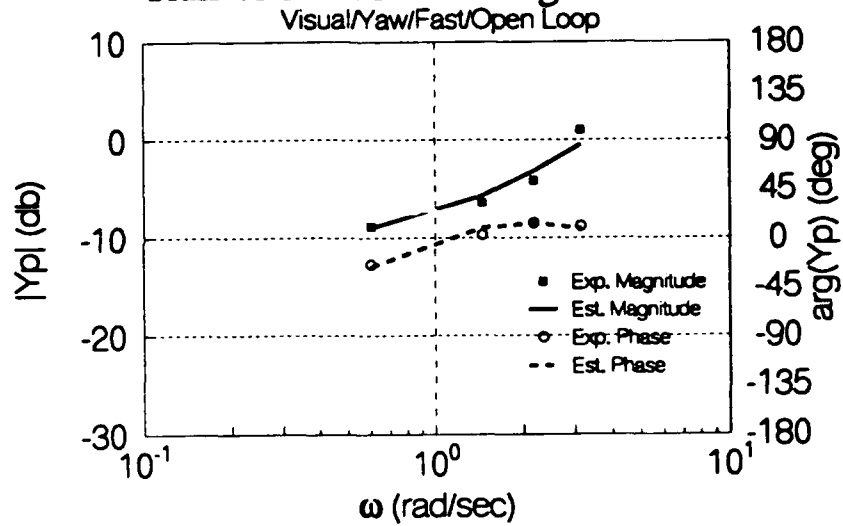


Figure B.2, continued.

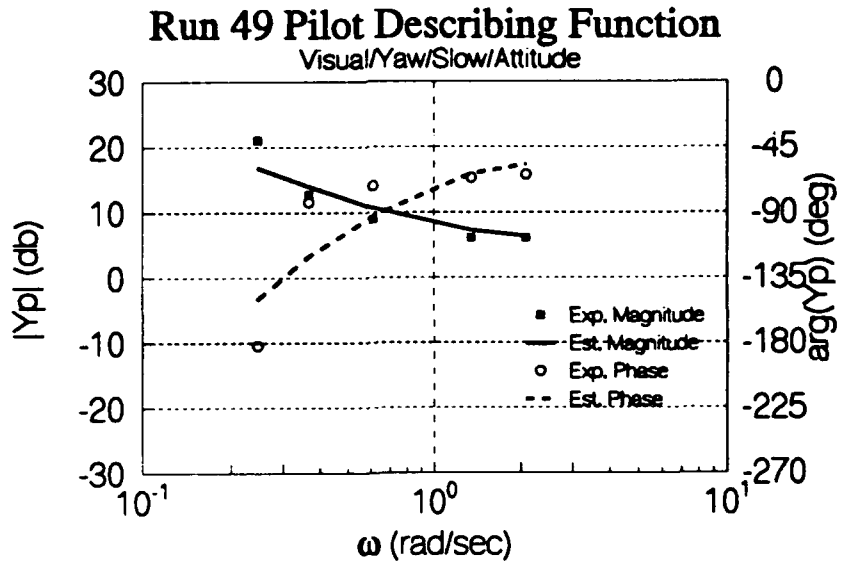
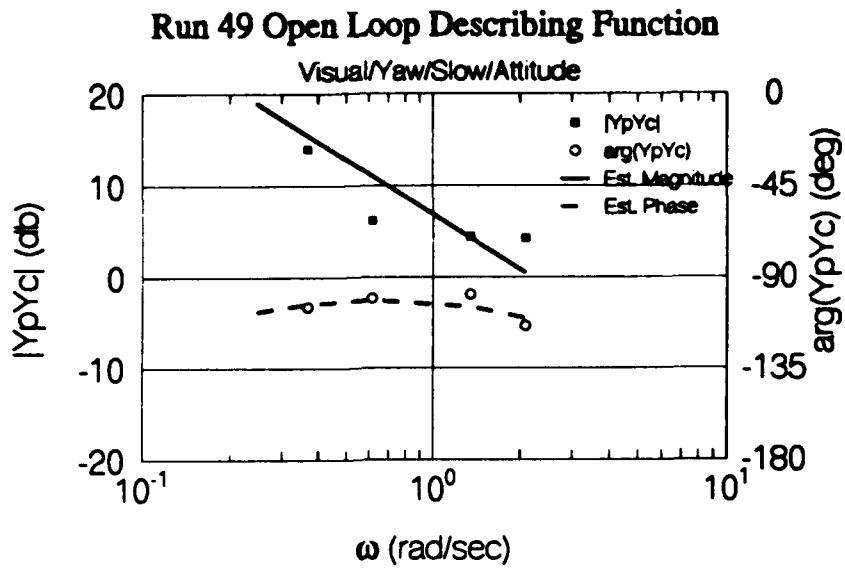
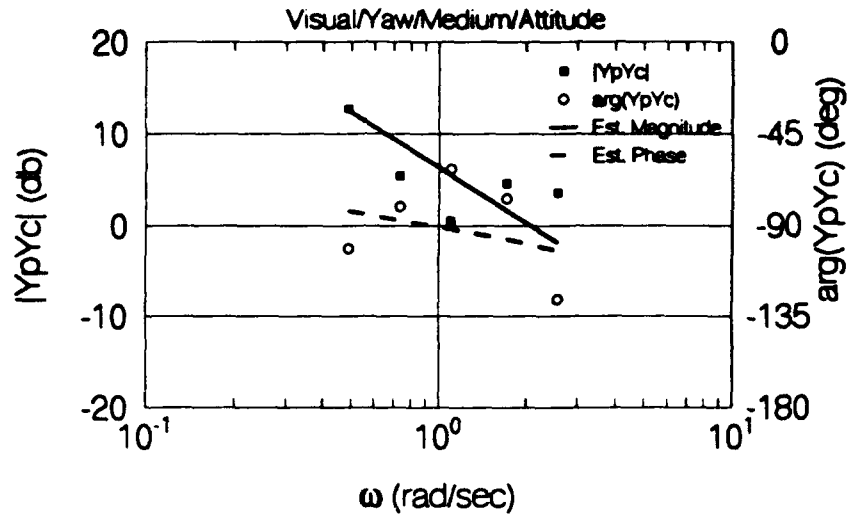


Figure B.2, continued.

Run 50 Open Loop Describing Function



Run 50 Pilot Describing Function

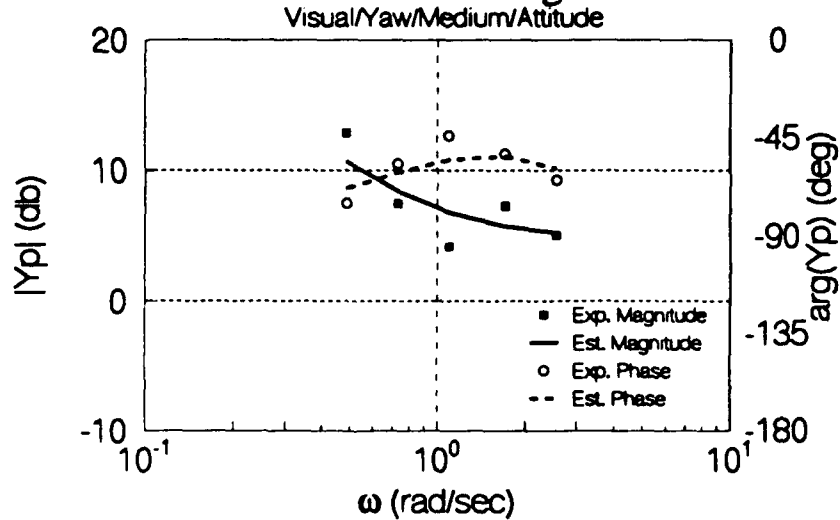


Figure B.2, continued.

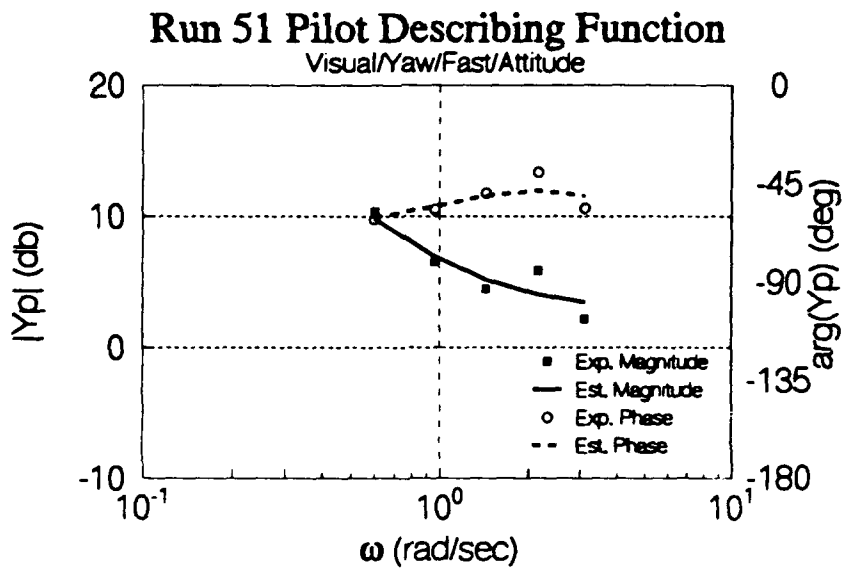
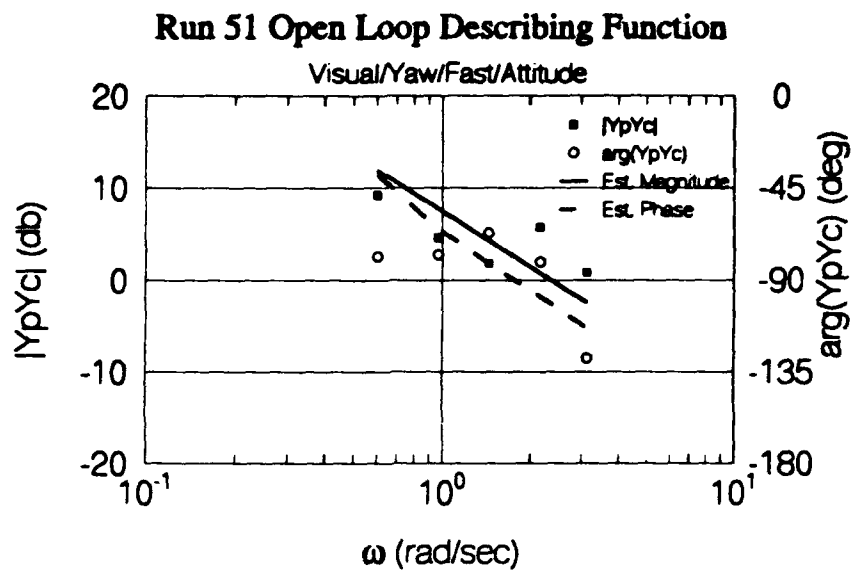


Figure B.2, continued.

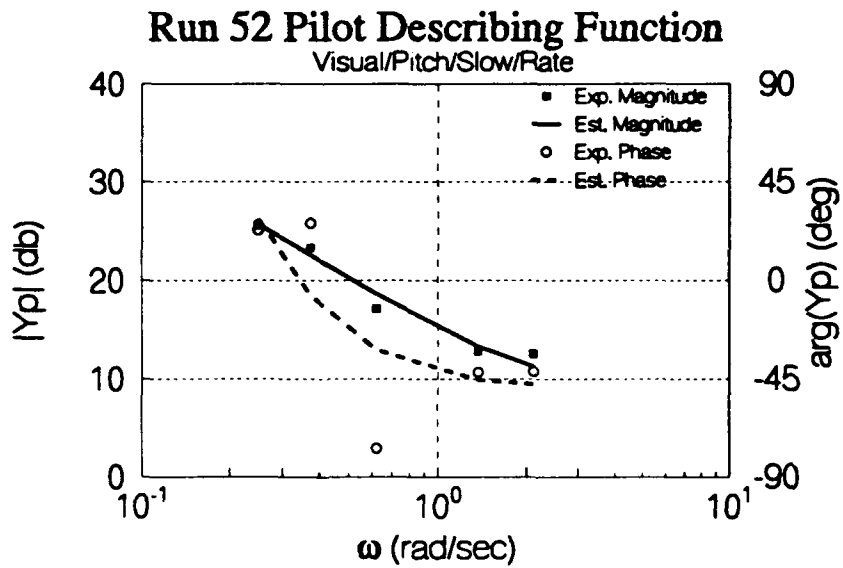
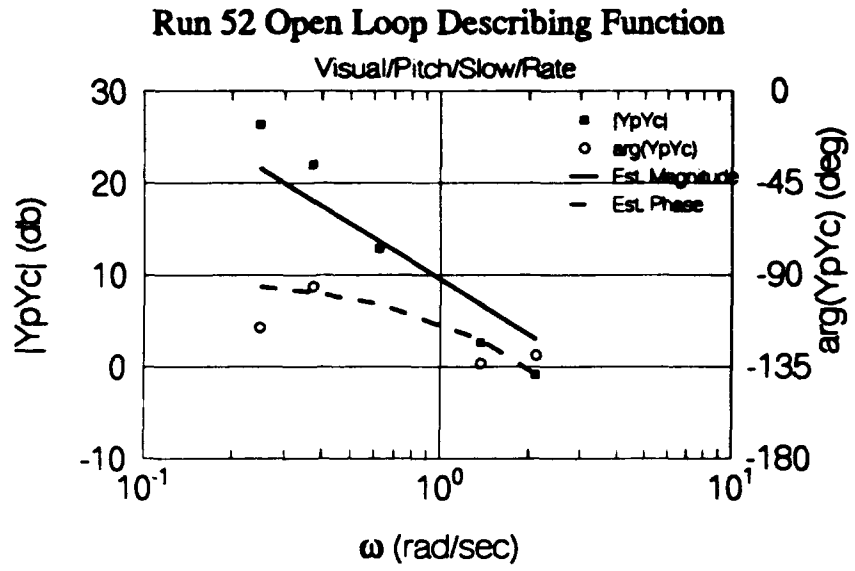


Figure B.2, continued.

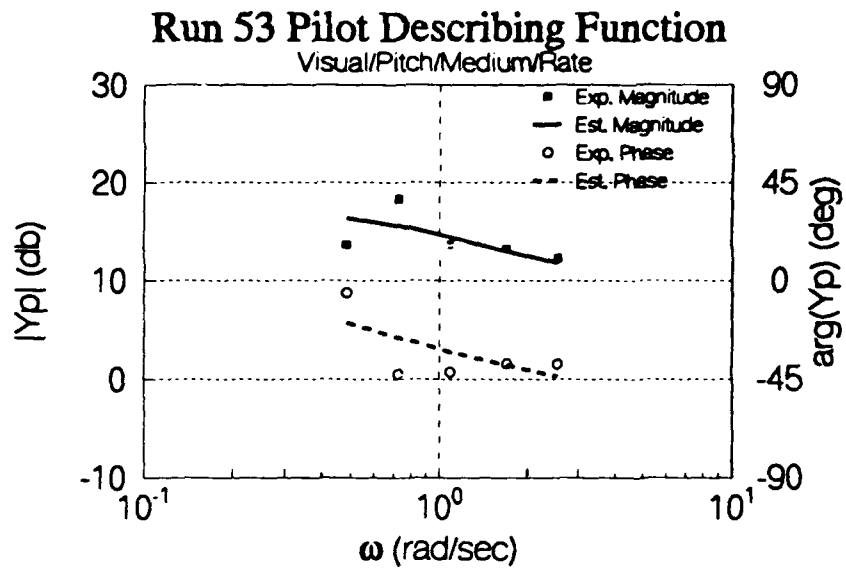
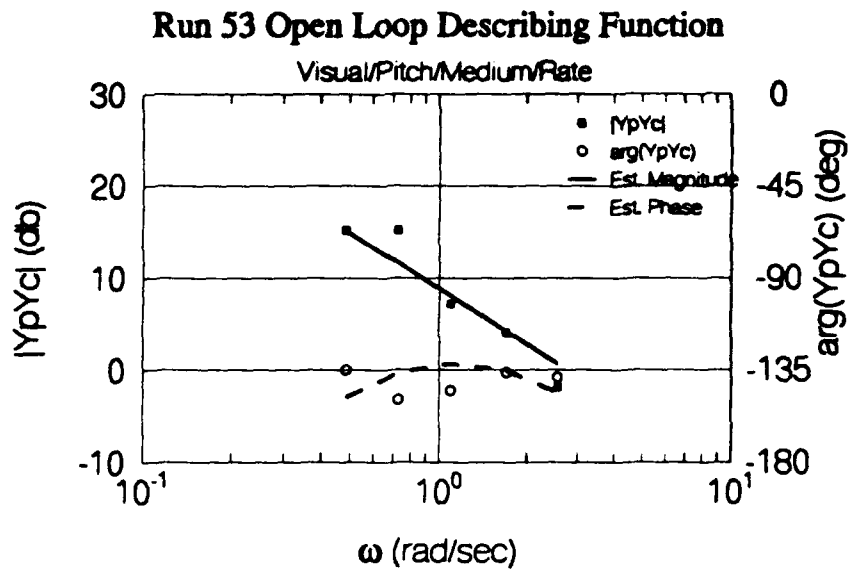


Figure B.2, continued.

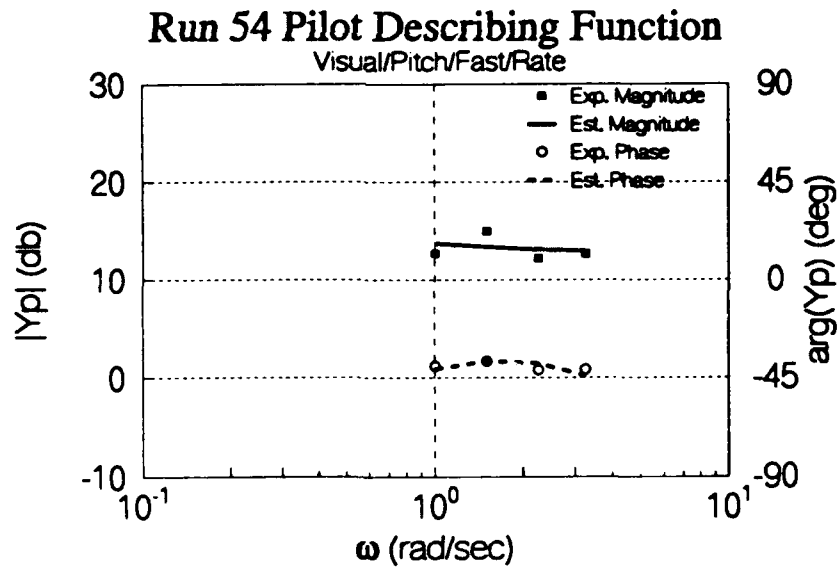
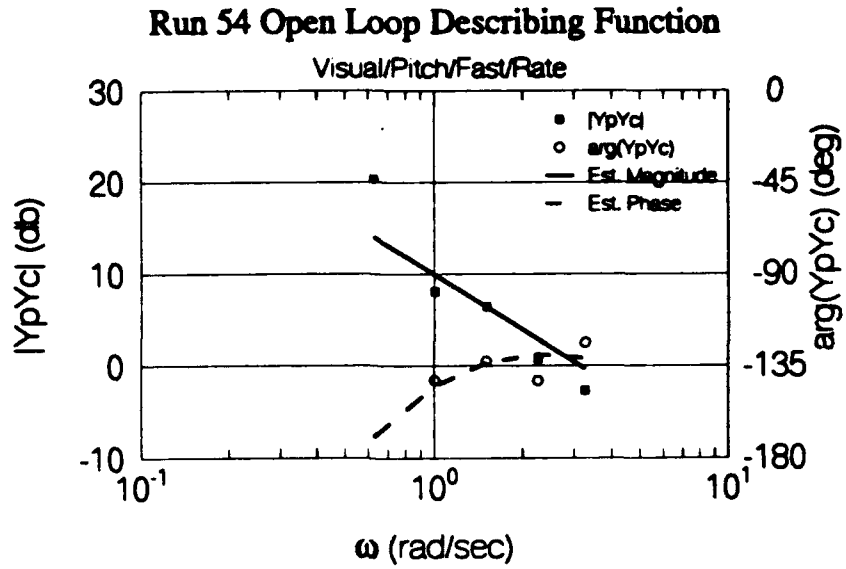


Figure B.2, continued.

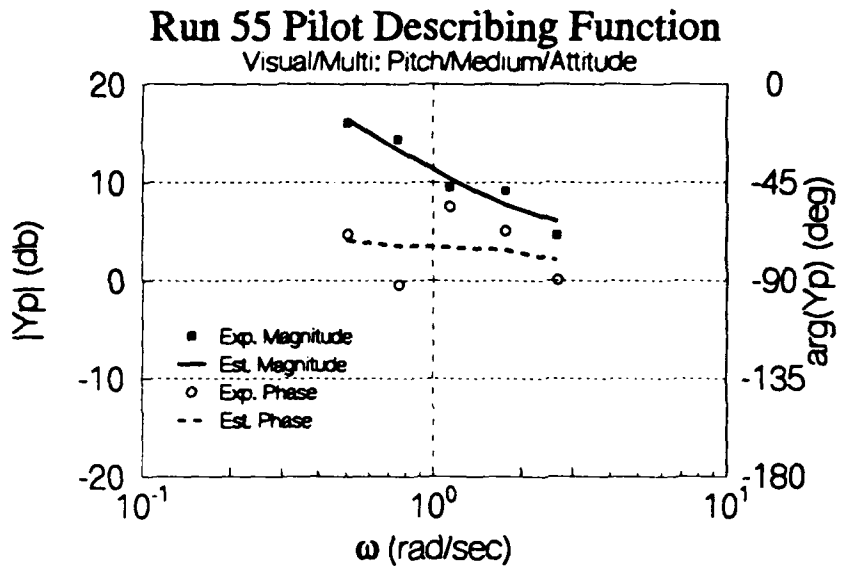
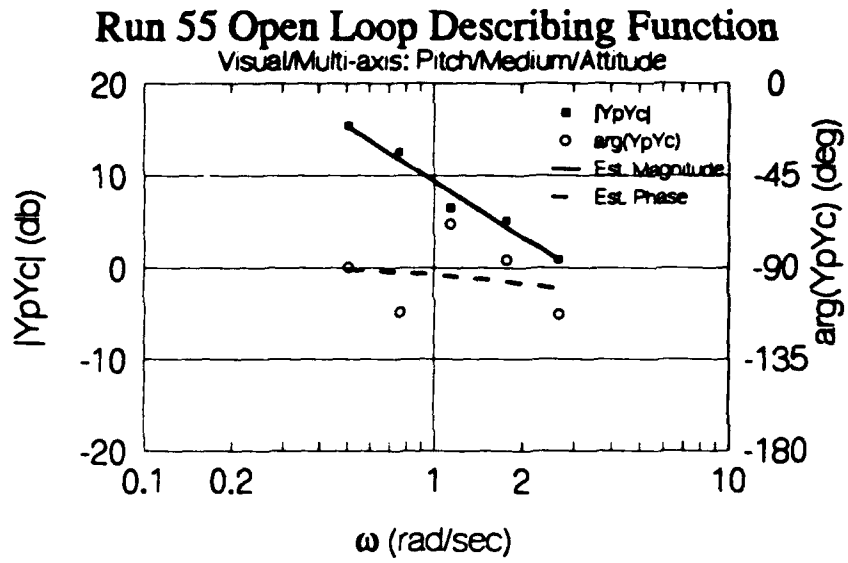
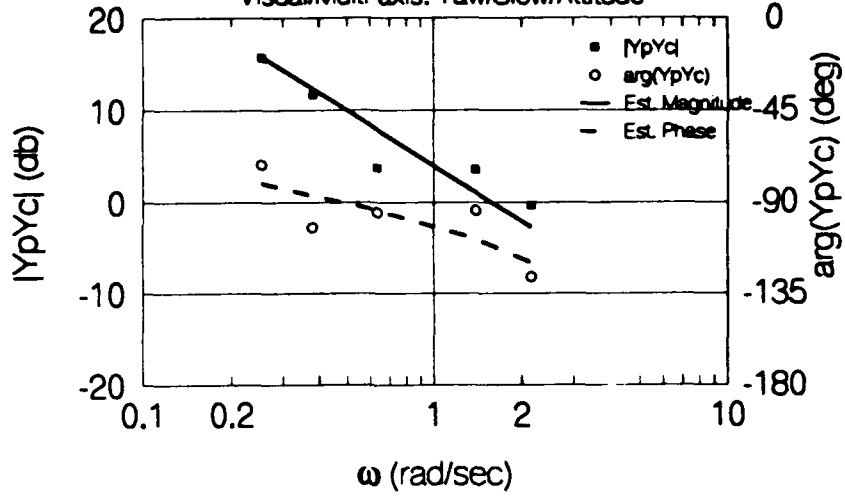


Figure B.2, continued.

Run 55 Open Loop Describing Function

Visual/Multi-axis: Yaw/Slow/Attitude



Run 55 Pilot Describing Function

Visual/Multi: Yaw/Slow/Attitude

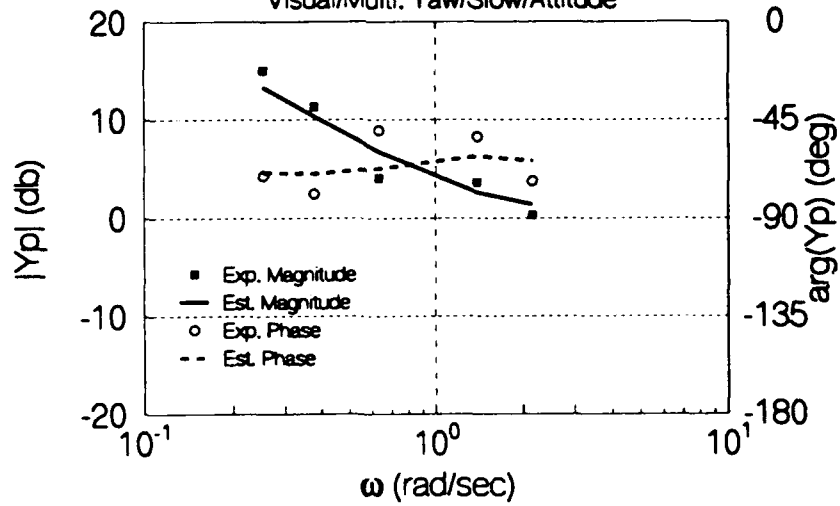
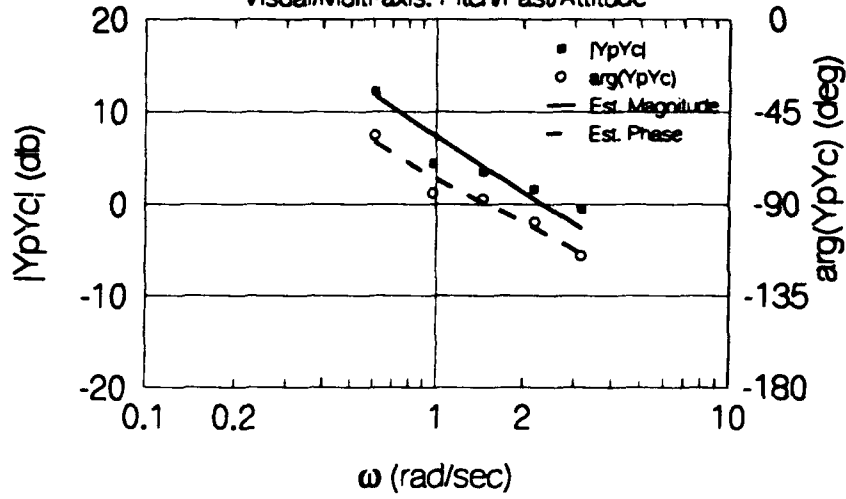


Figure B.2, continued.

Run 56 Open Loop Describing Function

Visual/Multi-axis: Pitch/Fast/Attitude



Run 56 Pilot Describing Function

Visual/Multi: Pitch/Fast/Attitude

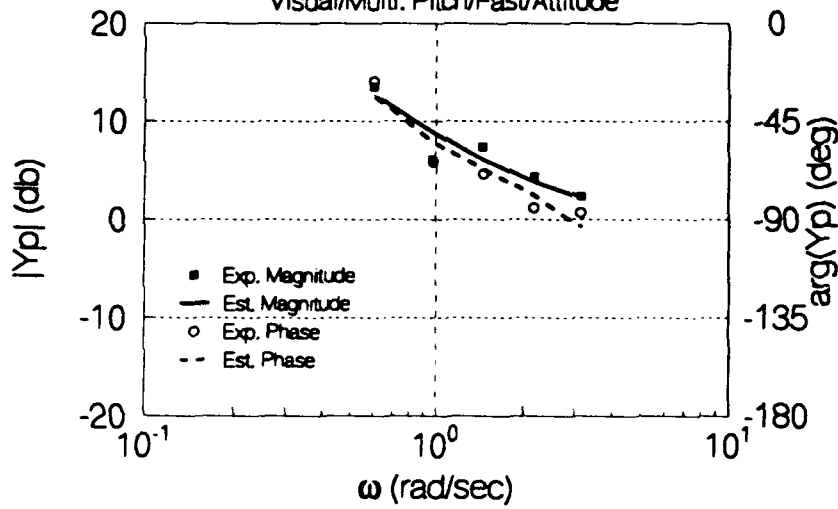
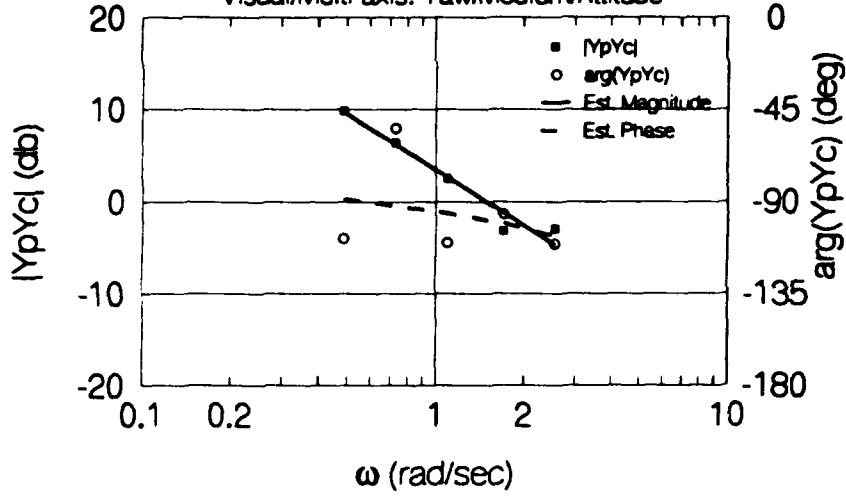


Figure B.2, continued.

Run 56 Open Loop Describing Function

Visual/Multi-axis: Yaw/Medium/Attitude



Run 56 Pilot Describing Function

Visual/Multi: Yaw/Medium/Attitude

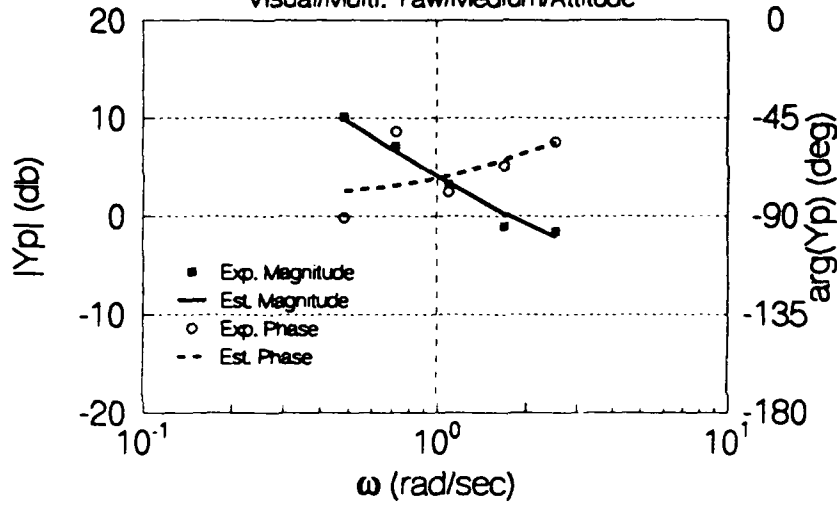
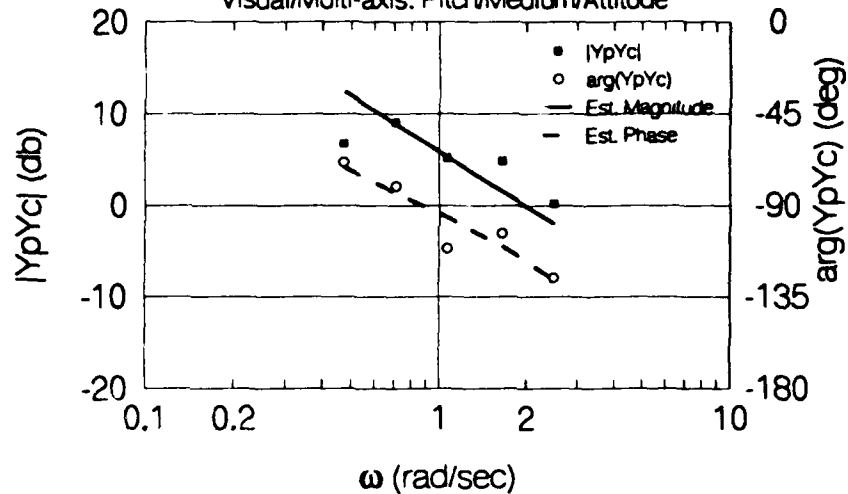


Figure B.2, continued.

Run 57 Open Loop Describing Function

Visual/Multi-axis: Pitch/Medium/Attitude



Run 57 Pilot Describing Function

Visual/Multi: Pitch/Medium/Attitude

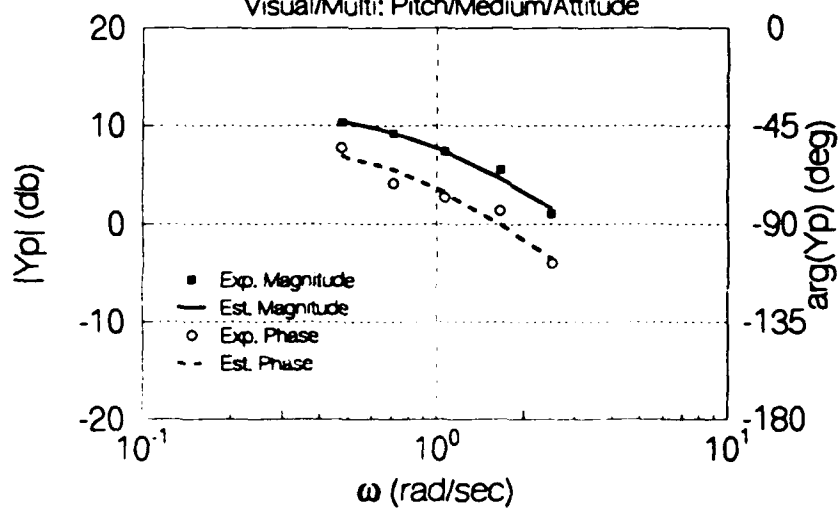
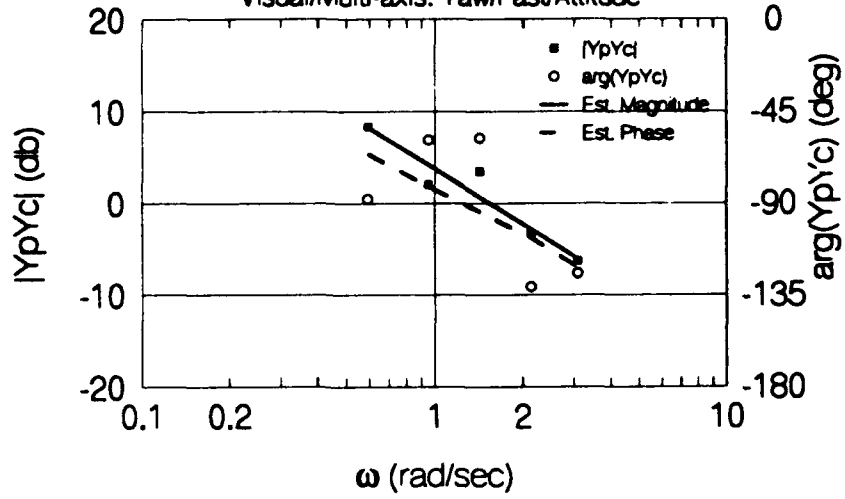


Figure B.2, continued.

Run 57 Open Loop Describing Function

Visual/Multi-axis: Yaw/Fast/Attitude



Run 57 Pilot Describing Function

Visual/Multi: Yaw/Fast/Attitude

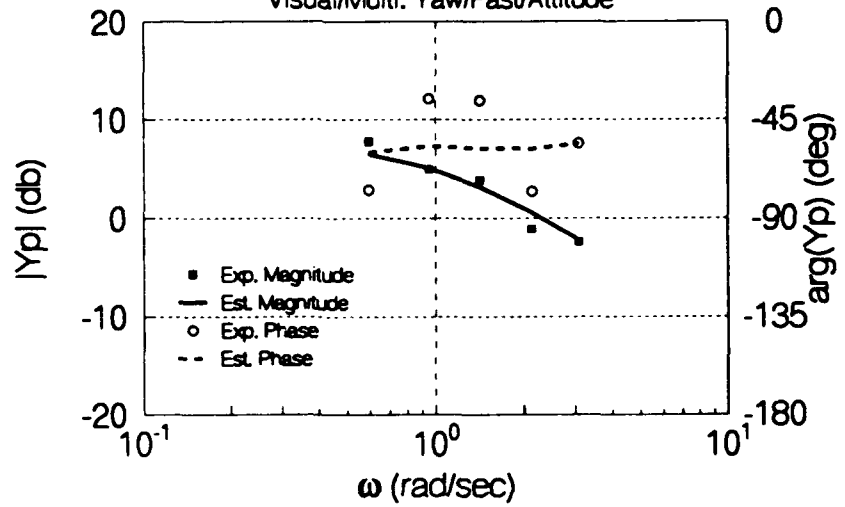
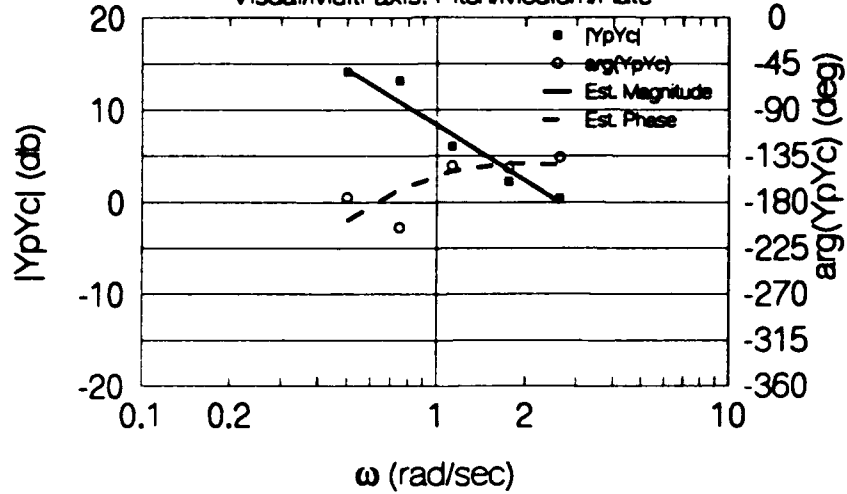


Figure B.2, continued.

Run 58 Open Loop Describing Function

Visual/Multi-axis: Pitch/Medium/Rate



Run 58 Pilot Describing Function

Visual/Multi: Pitch/Medium/Rate

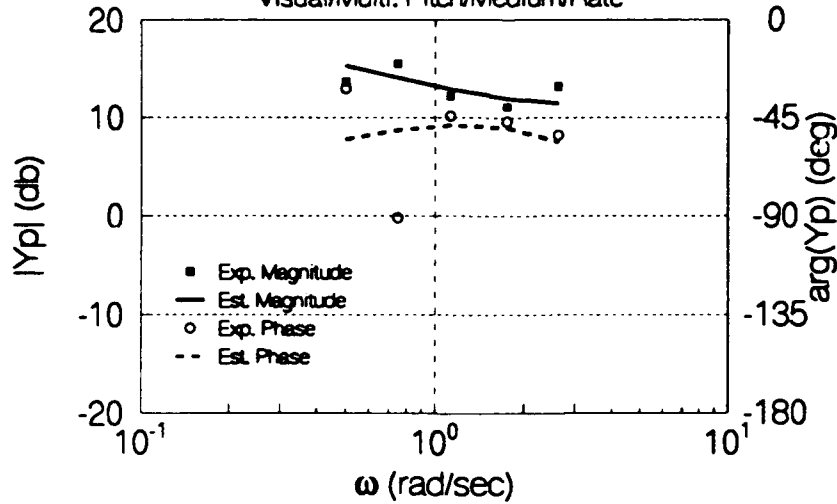


Figure B.2, continued.

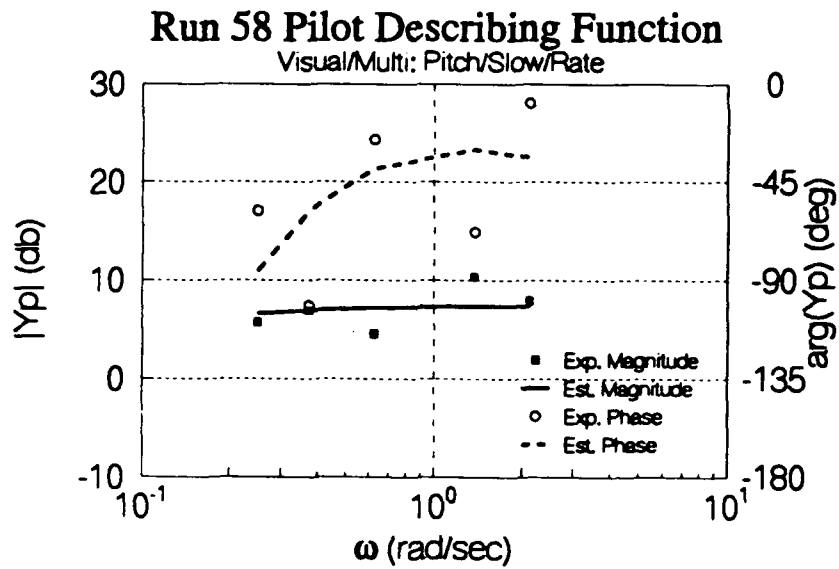
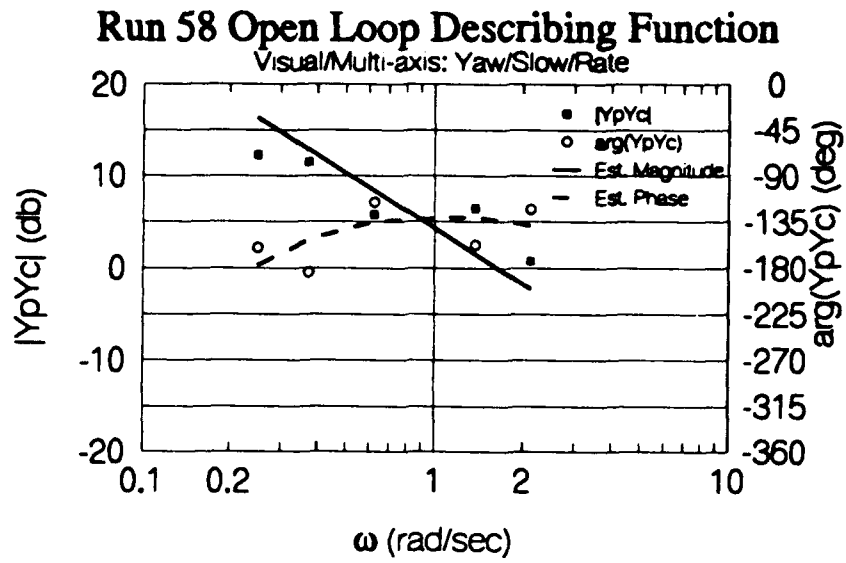
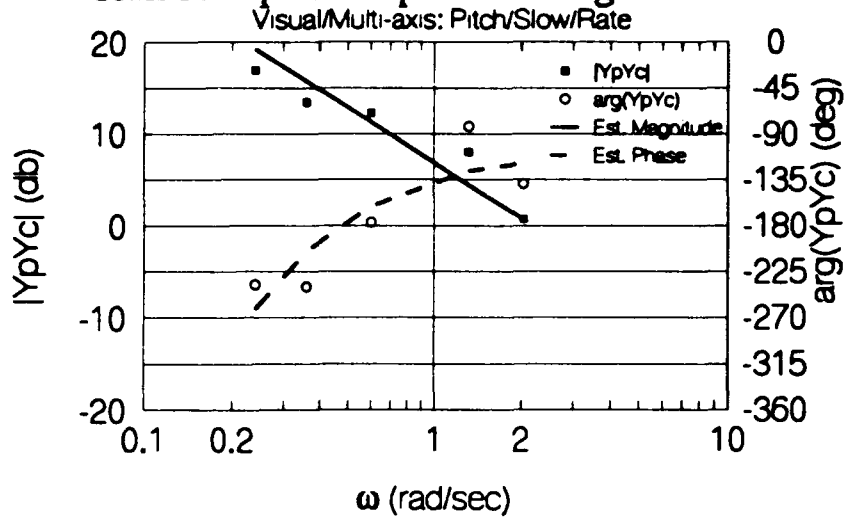


Figure B.2, continued.

Run 59 Open Loop Describing Function



Run 59 Pilot Describing Function

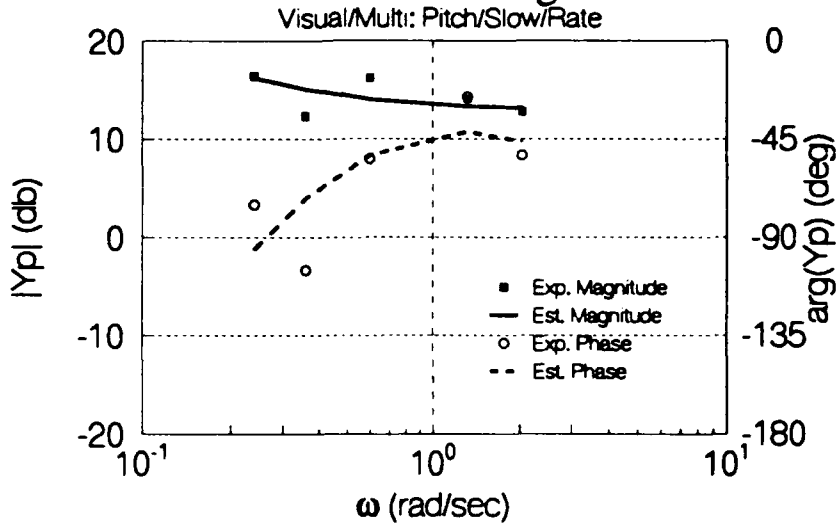
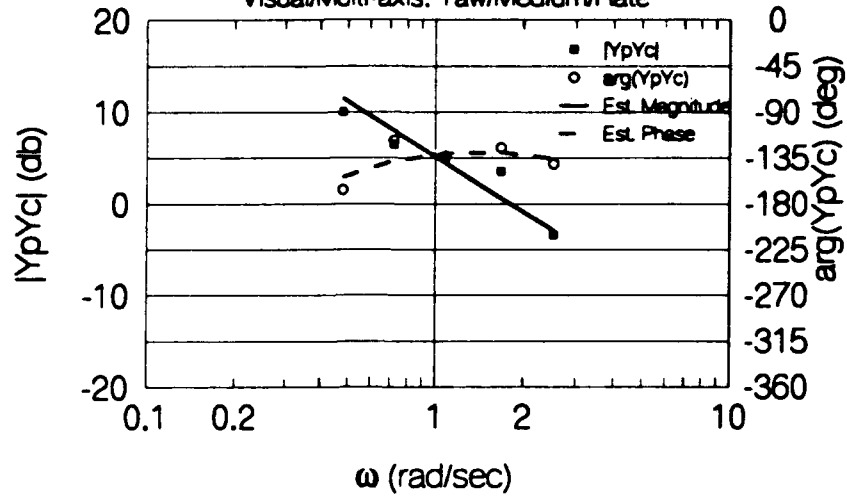


Figure B.2, continued.

Run 59 Open Loop Describing Function

Visual/Multi-axis: Yaw/Medium/Rate



Run 59 Pilot Describing Function

Visual/Multi: Yaw/Medium/Rate

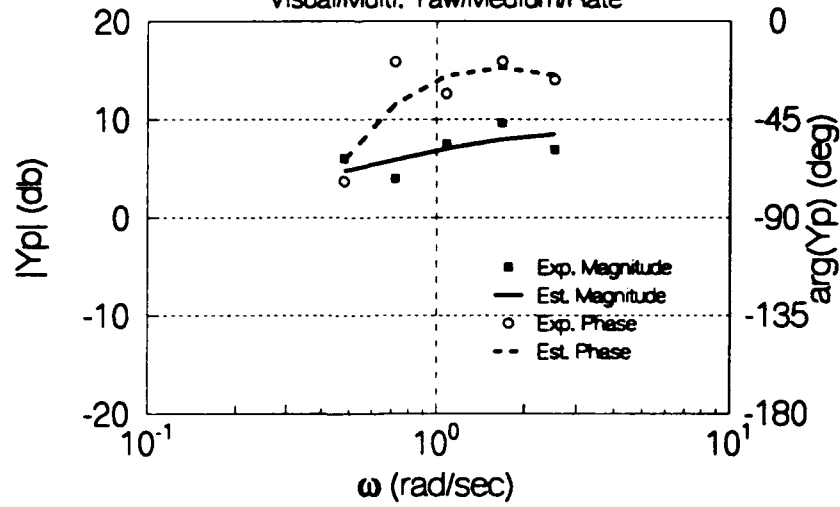


Figure B.2, continued.

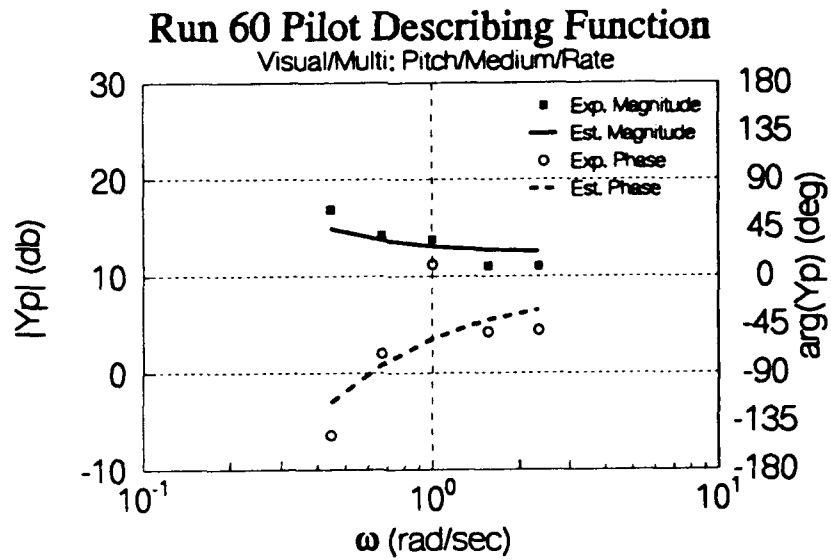
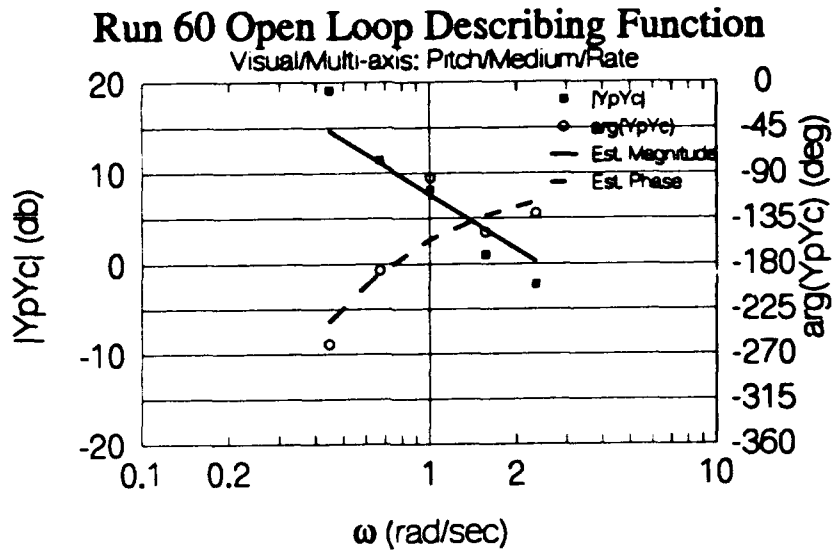
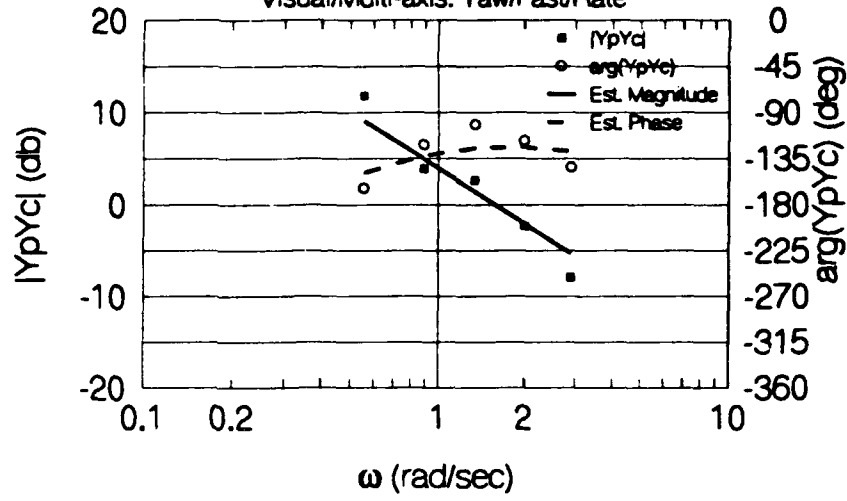


Figure B.2, continued.

Run 60 Open Loop Describing Function

Visual/Multi-axis: Yaw/Fast/Rate



Run 60 Pilot Describing Function

Visual/Multi: Yaw/Fast/Rate

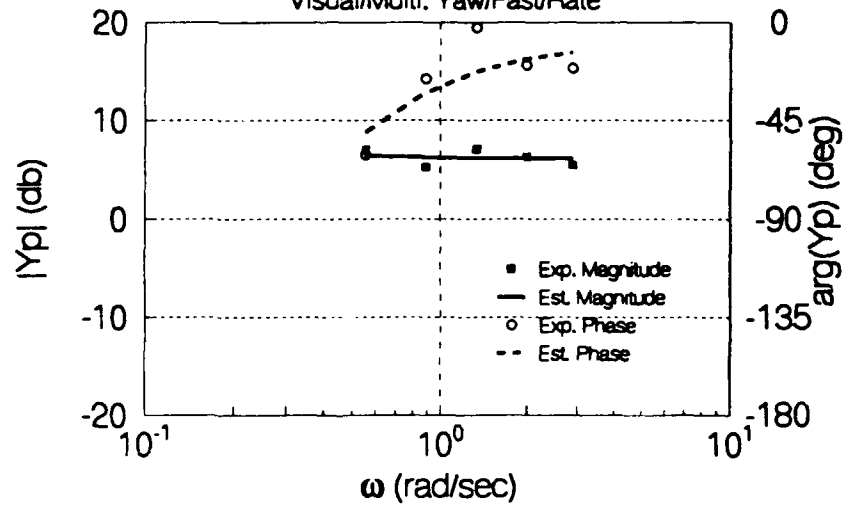
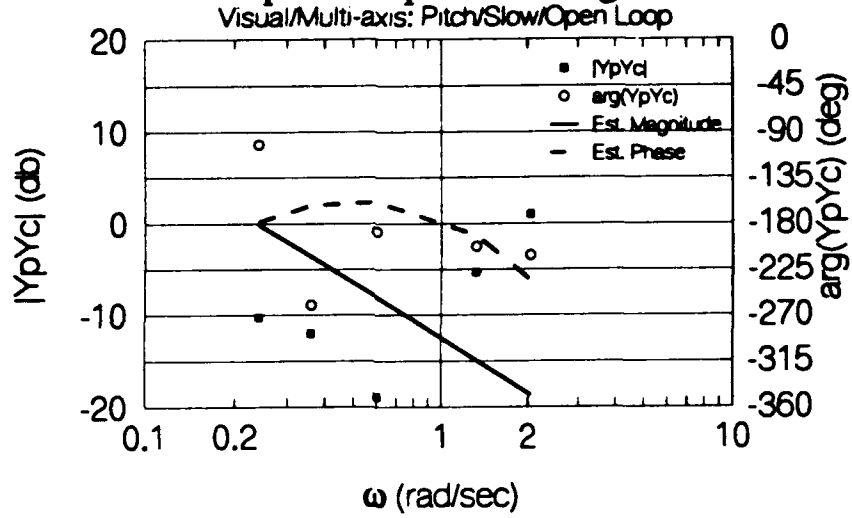


Figure B.2, continued.

Run 61 Open Loop Describing Function



Run 61 Pilot Describing Function

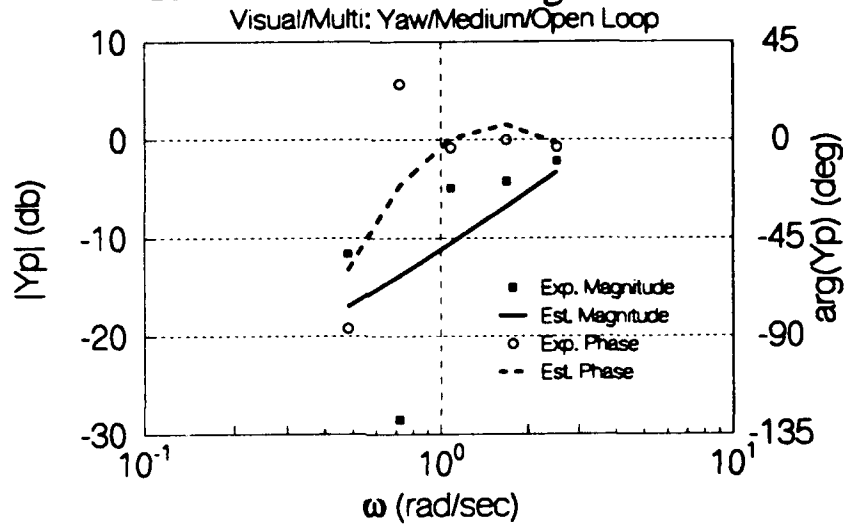
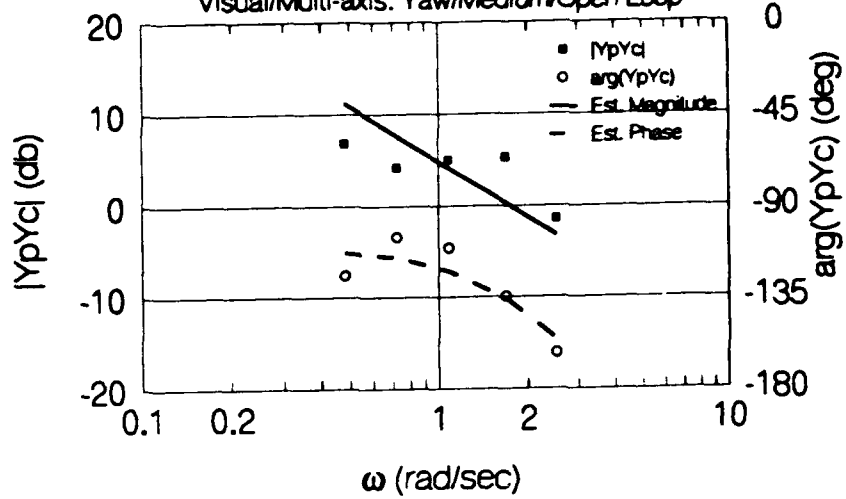


Figure B.2, continued.

Run 61 Open Loop Describing Function

Visual/Multi-axis: Yaw/Medium/Open Loop



Run 61 Pilot Describing Function

Visual/Multi: Yaw/Medium/Open Loop

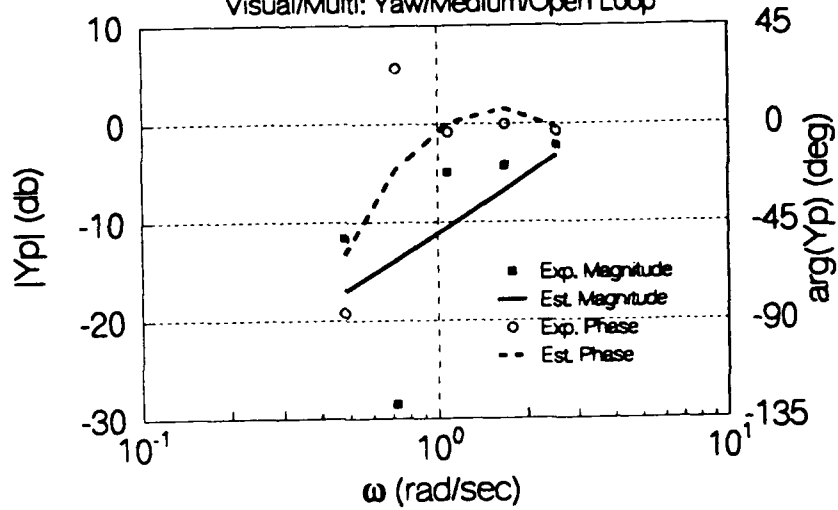
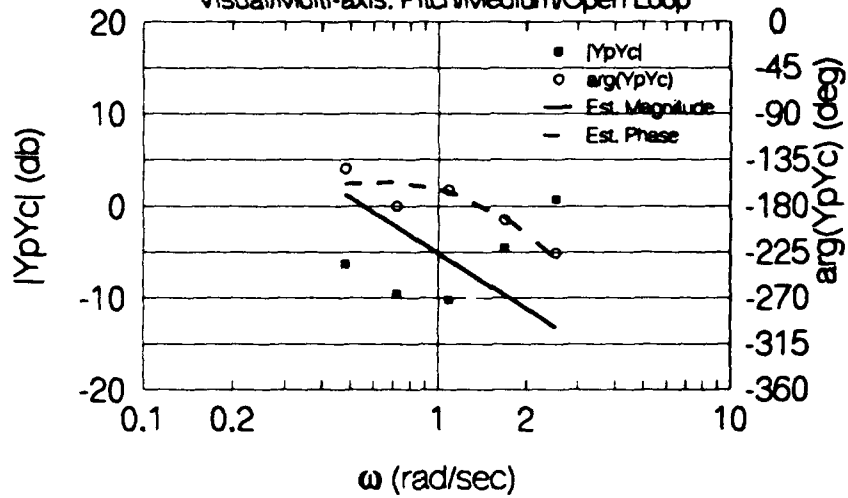


Figure B.2, continued.

Run 62 Open Loop Describing Function

Visual/Multi-axis: Pitch/Medium/Open Loop



Run 62 Pilot Describing Function

Visual/Multi: Pitch/Medium/Open Loop

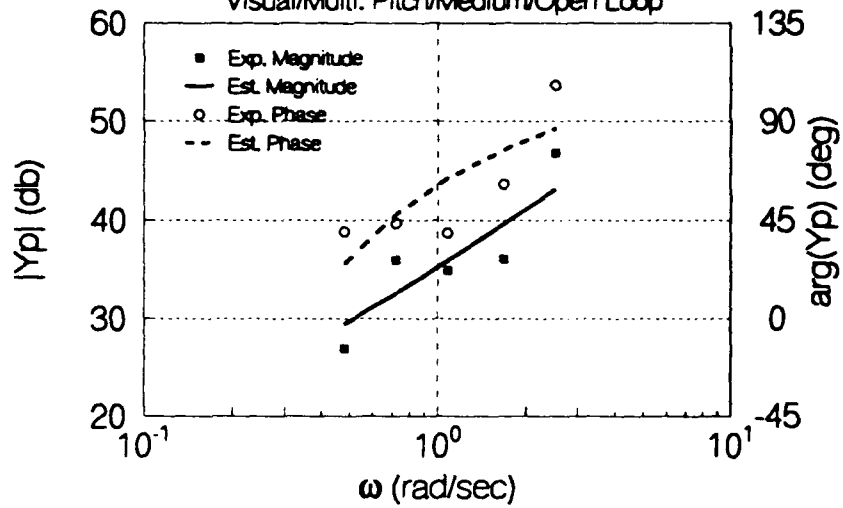
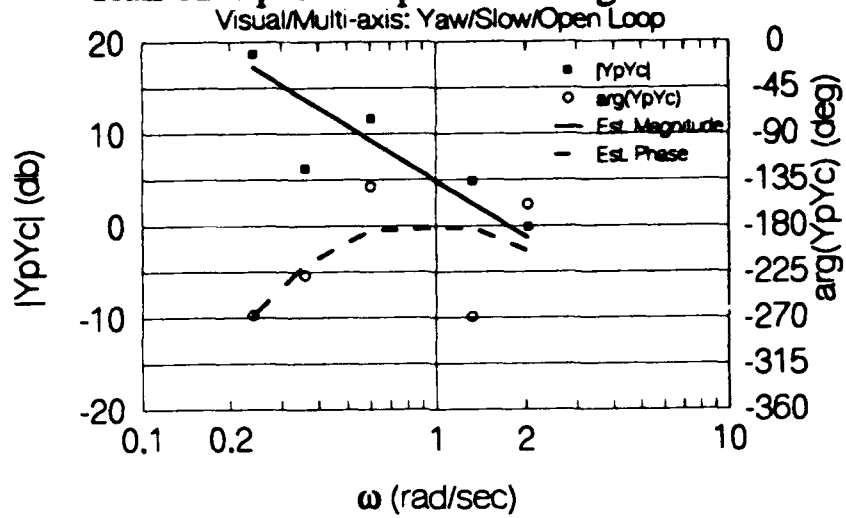


Figure B.2, continued.

Run 62 Open Loop Describing Function



Run 62 Pilot Describing Function

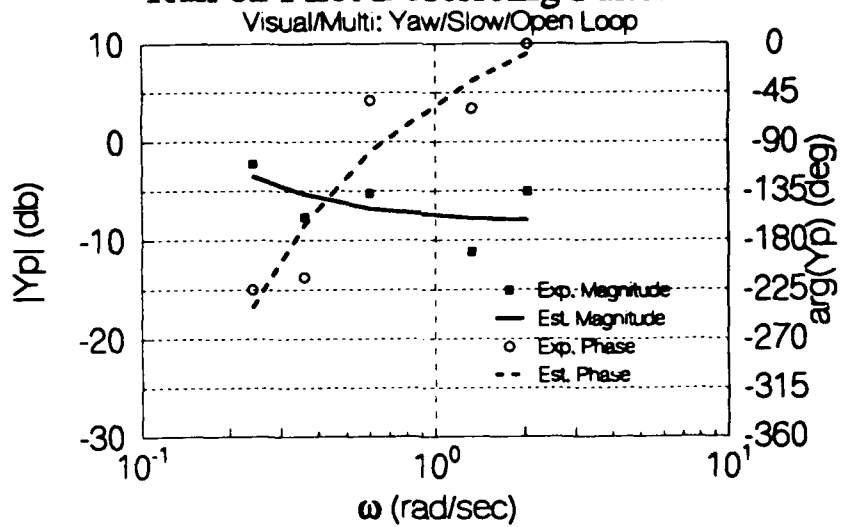
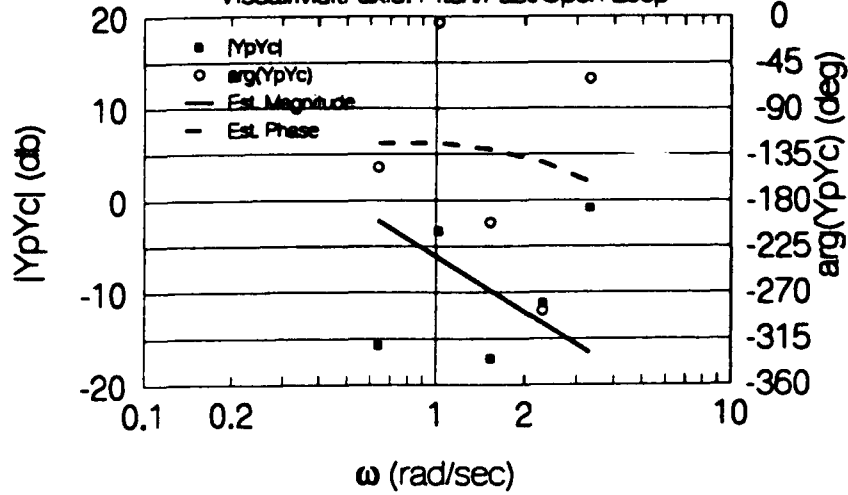


Figure B.2, continued.

Run 63 Open Loop Describing Function

Visual/Multi-axis: Pitch/Fast/Open Loop



Run 63 Pilot Describing Function

Visual/Multi: Pitch/Fast/Open Loop

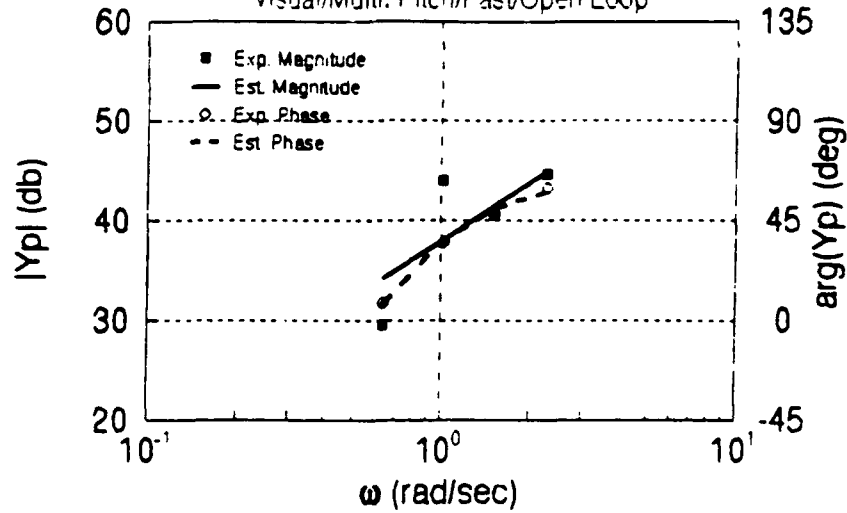
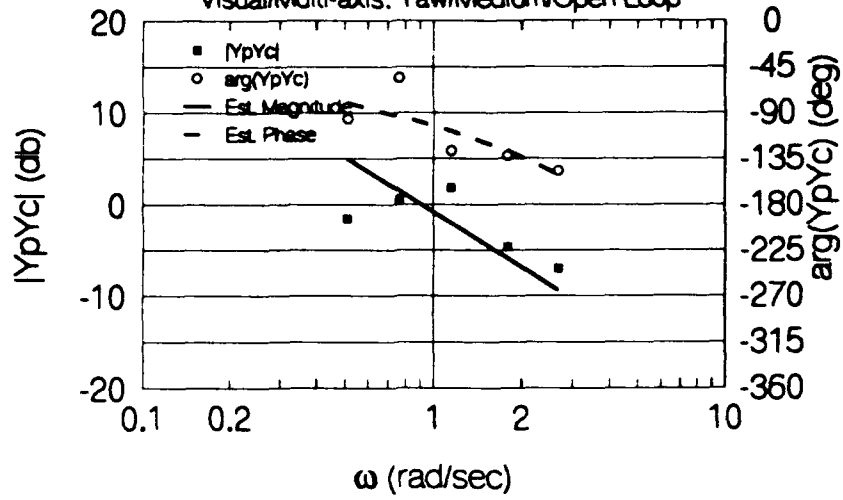


Figure B.2, continued.

Run 63 Open Loop Describing Function

Visual/Multi-axis: Yaw/Medium/Open Loop



Run 63 Pilot Describing Function

Visual/Multi: Yaw/Medium/Open Loop

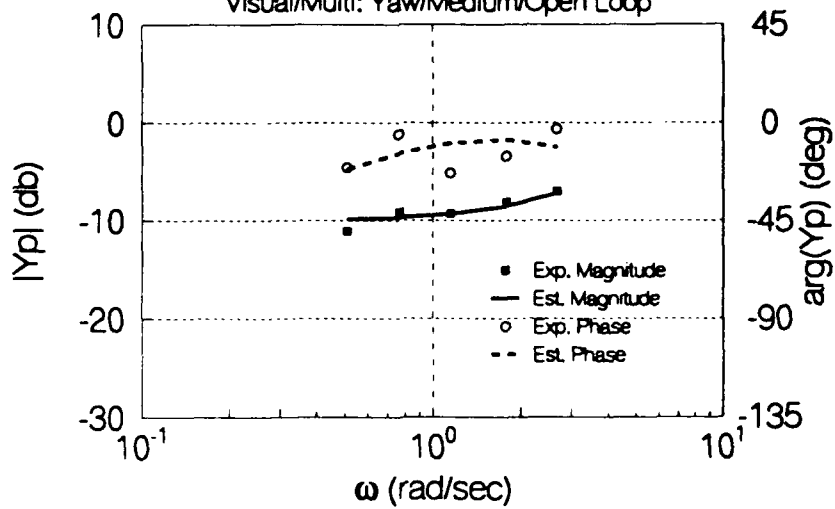


Figure B.2, continued.

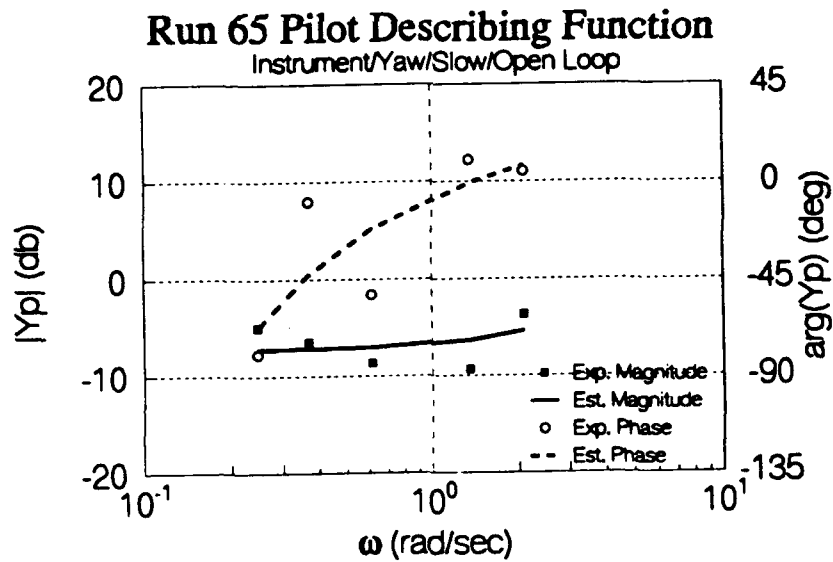
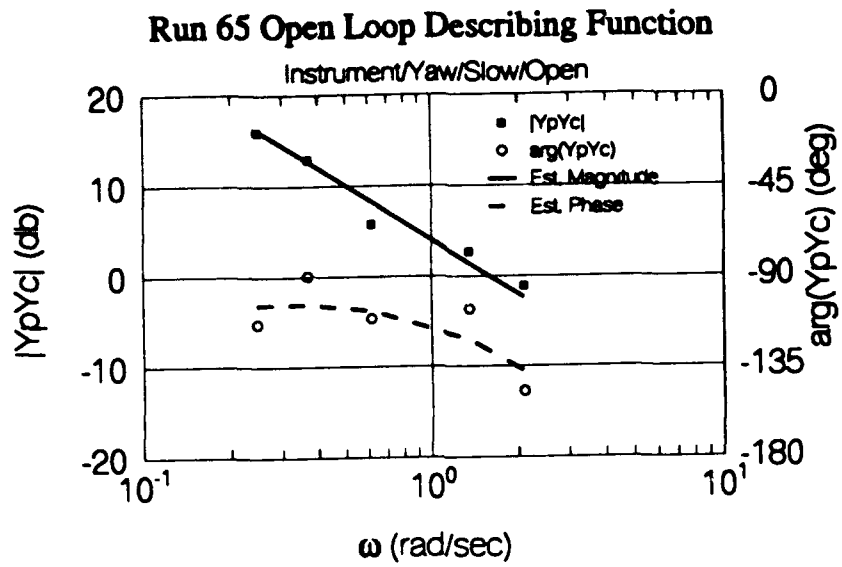


Figure B.2, continued.

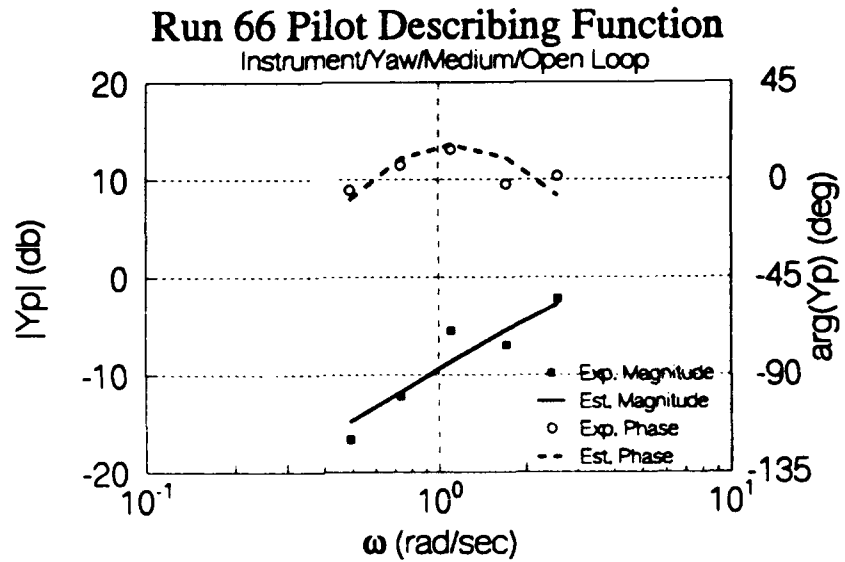
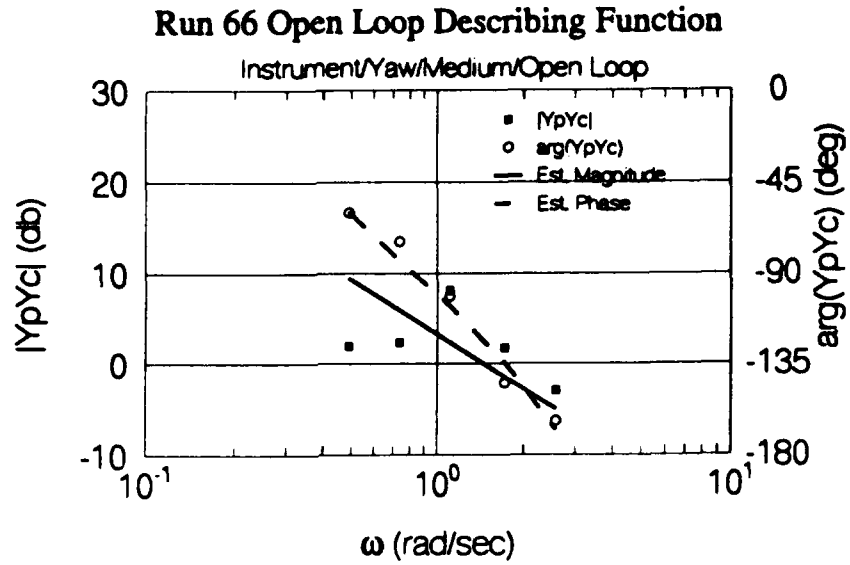
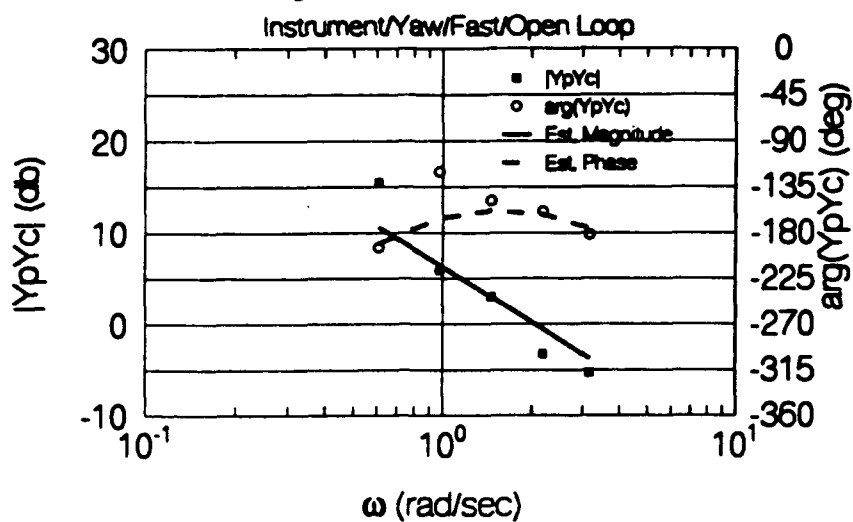


Figure B.2, continued.

Run 67 Open Loop Describing Function



Run 67 Pilot Describing Function

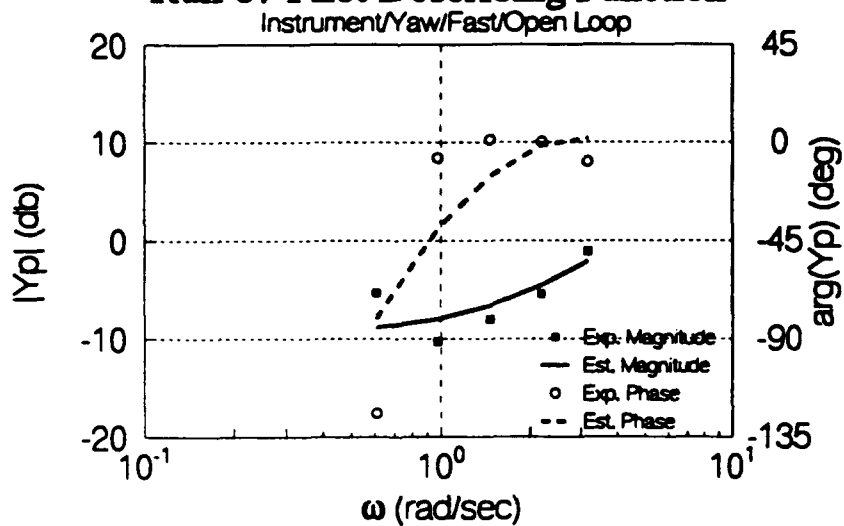


Figure B.2, continued.